Universidade de Brasília – UnB
Instituto de Geociências - IG

Tese de Doutorado nº 176
Área de Concentração: Geologia Regional

PALEOGEOGRAFIA E AMBIENTE DE DEPOSIÇÃO DA BACIA CARAJÁS: UMA ANÁLISE A PARTIR DE ESTUDOS GEOQUÍMICOS, PALEOMAGNÉTICOS E ISOTÓPICOS DAS ROCHAS VULCÂNICAS E JASPILITOS DO GRUPO GRÃO-PARÁ

PEDRO LUIZ GOMES MARTINS – 17/0130517

Orientadora:

Profa. Dra. Catarina L.B. Toledo

Coorientadora:

Profa. Dra. Adalene Moreira Silva

Banca Examinadora:

Prof. Dra. Catarina Labouré Bemfica Toledo (Presidente)

Prof. Dr. Leo Afraneo Hartmann

Prof. Dr. Candido Augusto Veloso Moura

Prof. Dra. Lucieth Cruz Vieira

Brasília, junho de 2021

Pedro Luiz Gomes Martins

PALEOGEOGRAFIA E AMBIENTE DE DEPOSIÇÃO DA BACIA CARAJÁS: UMA ANÁLISE A PARTIR DE ESTUDOS GEOQUÍMICOS, PALEOMAGNÉTICOS E ISOTÓPICOS DAS ROCHAS VULCÂNICAS E JASPILITOS DO GRUPO GRÃO-PARÁ.

Tese de doutorado elaborada junto ao curso de Pós-Graduação em Geologia (Área de concentração em Geologia Regional), Instituto de Geociências, Universidade de Brasília, como requisito parcial para a obtenção do título de Doutor em Geologia.

Orientadora: Prof. Dra. Catarina L.B. Toledo

Coorientadora: Profa. Dra. Adalene Moreira Silva

Banca examinadora:

Prof. Dra. Catarina Labouré Bemfica Toledo (Presidente)

Prof. Dr. Leo Afraneo Hartmann (UFRGS)

Prof. Dr. Candido Augusto Veloso Moura (UFPA)

Prof. Dra. Lucieth Cruz Vieira (UnB)

Brasília, junho de 2021

Ficha catalográfica elaborada automaticamente,
com os dados fornecidos pelo(a) autor(a)

GM386p

Gomes Martins, Pedro Luiz
Paleogeografia e ambiente de deposição da Bacia Carajás: Uma análise a partir de estudos geoquímicos, paleomagnéticos e isotópicos das rochas vulcânicas e jaspilitos do Grupo Grão Pará / Pedro Luiz Gomes Martins; orientador Catarina Labouré Bemfica Toledo; co-orientador Adalene Moreira Silva. -- Brasília, 2021.
261 p.

Tese (Doutorado - Doutorado em Geologia) -- Universidade de Brasília, 2021.

1. Cráton Amazônico. 2. Província Carajás. 3. Formação Ferrífera Bandada. 4. Quimioestratigrafia. 5. Paleomagnetismo. I. Bemfica Toledo, Catarina Labouré, orient. II. Moreira Silva, Adalene, co-orient. III. Título.

AGRADECIMENTOS

Agradeço inicialmente ao Instituto de Geociências representado aqui pelos professores, coordenadores e funcionários, e à Universidade de Brasília pela oportunidade de realizar este trabalho, bem como o apoio ao longo de todo doutorado.

Agradeço em especial às minhas orientadoras e amigas, Profas. Dra. Catarina L. B. Toledo e Dra. Adalene Moreira Silva, pela convivência, orientação, apoio e dedicação ao meu aprendizado nos últimos anos, horas de discussões geológicas e conversas casuais que possibilitaram a criação de uma relação de amizade, respeito e companheirismo. Aos Profs. Dr. Farid Chemale Jr e Dr. Ricardo I. F. pelas contribuições a este trabalho e pelas enriquecedoras discussões geológicas.

Ao CNPQ pela concessão da bolsa de doutorado e pelos auxílios à pesquisa concedidos tanto durante as etapas e usos de laboratórios, a Vale. S.A pelo apoio nas etapas de campo, coleta de material e no custeio das análises químicas. O presente trabalho foi realizado com apoio da Coordenação de Aperfeiçoamento de Pessoal de Nível Superior – Brasil (CAPES) – Código de Financiamento 001. Agradeço também à Fundação de Apoio à pesquisa do Distrito Federal (FAPDF) (23411.93.27701.29052018) pelo financiamento de parte da pesquisa.

Não esquecendo ainda dos amigos, especialmente Darielton, Thiago, Marcones, Cleiton, Jader e Deógenes que aturaram semanas de ausência todos esses últimos anos e puderam impulsionar e motivar a conclusão desta fase de minha vida.

Finalmente agradeço a minha mãe (Ana Maria), meu sobrinho (Kauã Lucas), minha irmã (Stella), minha esposa (Thássia) e minha sogra (Maria) pelo apoio e amor incondicional, respeito, confiança e amizade que tornaram a jornada mais leve e sem os quais não seria possível a realização de mais esta etapa de minha vida. Em especial, à minha esposa Thássia, pelo suporte e apoio incondicional, por aturar dias de sono e noites de insônia, e por embarcar comigo nessa aventura acadêmica. Dedico a vocês, juntamente com meu falecido pai (Luciano) esta tese de doutorado.

"*There are only two ways to live your life. One is as though nothing is a miracle. The other is a though everything is a miracle"*

Albert Einstein

RESUMO

O período de transição do Neoarqueano para o Paleoproterozoico (~ 2,80-2,20 Ga) testemunhou diversos eventos evolutivos ambientais e biológicos interligados, dentro eles o aumento do oxigênio atmosférico como deduzido pelo desaparecimento de pirita detrítica e uraninita em conglomerados, pelo advento de *red beds* e pela deposição das maiores formações ferríferas bandadas (FFB) do mundo. Estabelecer as posições dos continentes e as condições paleoambientais durante o arqueano são dois dos desafios mais importantes das geociências atualmente. Esses desafios ocorrem, principalmente, devido às diversas limitações existentes na obtenção de dados geológicos e/ou geofísicos do início da história evolutiva da Terra, particularmente dados paleomagnéticos robustos. Neste estudo, a investigação paleomagnética de rochas basálticas da sequência vulcanossedimentar do Grão-Pará (~ 2,75 Ga), situada na Província Mineral de Carajás, sudeste do Cráton Amazônico, permitiu apresentar a primeira reconstrução paleogeográfica para este bloco arqueano, com uma estimativa de paleolatitude para o bloco e a discussão de sua posição dentro das configurações dos supercontinentes arqueanos propostos anteriormente. A investigação paleomagnética foi conduzida em testemunhos de sondagens perfurados na mina de minério de ferro de Carajás, os quais interceptam os derrames de lava basáltica da Formação Parauapebas. Duas componentes de magnetização características, C1 e C2, foram isoladas e posteriormente usadas para calcular o pólo paleomagnético médio para cada uma: C1 (~ 2759 Ma; 40,5ºE, -44,6ºS A95 = 6,5º, K = 18,5) e C2 (~ 2745 Ma; 342,4ºE, -54,3ºS, A95 = 14,8º, K = 27,8). Nossos resultados, integrados às evidências geológicas, revelam que o bloco Carajás ocupava baixas latitudes na época, e poderia ter feito parte da configuração do supercráton Supervaalbara durante o Neoarqueano (~ 2,75 Ga), em uma posição mais próxima da linha do Equador. Além disso, foi possível identificar uma sequência de três eventos de reversão magnética na sequência de derrames basálticos da Formação Parauapebas, o que potencialmente sugere a existência de um geodínamo dinâmico pré-2,7 Ga.

Além disso, uma das ocorrências mais importantes de FFB no mundo está situada na Província de Carajás e está hospedada na sequência vulcanossedimentar do Grão-Pará. As formações ferríferas bandadas que tipificam muitas sucessões supracrustais arqueanas e paleoproterozóicas são excelentes arquivos da química da água do mar pré-cambriana e do ciclo de ferro. A FFB de Carajás presente no corpo N4Ws está bastante preservada da deformação e metamorfismo regional, com a mineralogia e as texturas primárias extremamente preservadas, e oferece uma excelente oportunidade para estudar a gênese, o ambiente de deposição e as condições paleoambientais durante sua formação há aproximadamente 2,75 bilhões de anos. A FFB de Carajás é constituída de intercalações milimétricas a centimétricas de bandas de hematita, jaspe e *chert*. Suas texturas e estruturas primárias ainda são preservadas como *soft-sediment deformation*, bandamento, microesferulitos, *microflame* e *pinch and swell*. A baixa quantidade de Al_2O_3 (<1,0% em peso) e *high field strength elements* (<1 ppm) para a maioria das amostras de FFB indicam um ambiente de deposição essencialmente livre de material detrítico. No geral, os padrões de elementos terras raras e de

ítrio (REY) mostram uma anomalia positiva fraca de La e uma anomalia positiva pronunciada de Eu (Eu / Eu $_{PAAS}$ = 1,86 - 5,05); embora a presença de anomalia verdadeira de Ce não seja evidente. Variações estratigráficas na composição isotópica de ferro, de até 0,80 ‰ (δ^{56}Fe = +1,10 a +1,90 ‰) ao longo de dezenas a centenas de metros, sugerem mudanças na composição de isotópica de ferro da água do mar de Carajás durante períodos de alguns milhões de anos. Dados isotópicos do sistema Sm–Nd para as amostras da FFB de Carajás plotam ao longo de uma linha de correlação em um diagrama de isócrono convencional, que resultou em uma idade de 2707 ± 118 Ma (MSWD = 230). Um subconjunto desses dados, com apenas amostras de FFB exibindo um melhor alinhamento (n = 20), forneceu uma idade isócrona mais velha de 2795 ± 77 Ma (MSWD = 56). Ambas as idades das isócronas Sm–Nd foram concordantes com a idade mínima proposta de formação para os jaspilitos de Carajás, ou seja, ~ 2745 Ma. Além disso, os jaspilitos mostram distribuição heterogênea da assinatura isotópica de Nd ao longo da sequência, sendo que as rochas amostradas perto do contato com os derrames basálticos (tipo II) tiveram valores negativos de εNd (t) (–4,97 a –0,90). Enquanto isso, valores predominantemente positivos de εNd (t) (-0,84 a +5,40) foram observados nas demais amostras (tipo I). O padrão dos REY e os dados isotópicos de Nd-Fe combinados sugerem que a deposição ocorreu principalmente em águas profundas distantes das massas continentais. A precipitação das BIFs ocorreu sob condições anóxicas e subóxicas em uma bacia do tipo rifte próxima aos centros de atividade vulcânica em um ambiente submarino com superimposição hidrotermal. Entretanto, uma quantidade considerável de oxigênio poderia estar presente em algumas porções do oceano evidenciada pela presença de anomalias negativas de Ce em algumas seções, sugerindo que as condições de oxidação emergentes poderiam ter influenciado a Bacia de Carajás antes do GOE.

Palavras-chave: Cráton Amazônico, Província Carajás, Formação Ferrífera Bandada, Quimioestratigrafia, Paleomagnetismo, Supervaalbara.

ABSTRACT

The Neoarchean to Paleoproterozoic transition (~2.80–2.20 Ga) witnessed several major interlinked environmental and biological evolutionary events, including the increase in atmospheric oxygen as deduced from the disappearance of detrital pyrite and uraninite in conglomerates, the advent of red beds, and the deposition of the largest banded iron formations (BIF) in the world. Establishing the positions of continents and paleoenvironmental conditions at this time are two of the most important challenges in geosciences today. These challenges are mainly due to the severe limitations on obtaining geological, and/or geophysical data from early Earth time, particularly robust paleomagnetic data. In this study, the paleomagnetic investigation of basaltic rocks from the Neoarchean volcano-sedimentary succession of the Grão Pará (~2.75 Ga), situated in the Carajás Mineral Province, southeastern Amazonian Craton, allowed the first paleogeographic constraints for this Archean block, yielding a paleolatitude estimate for the block and discussing its affiliation to previously proposed Archean cratonic assemblies. The paleomagnetic investigation was conducted on fresh drill cores drilled into the Carajás iron ore mine and cutting across the basaltic lava flows from Parauapebas Formation. Two characteristic components, C1 and C2, were isolate and further used to calculate the mean paleomagnetic pole for each: C1 (~2759 Ma; 40.5ºE, -44.6ºS A95 =6.5º, K = 18.5) and C2 (~2745 Ma; 342.4ºE, -54.3ºS, A95 = 14.8º, K = 27.8). Our results, integrated with geological evidence reveals that the Carajás block occupied low latitudes at the time, and could have been part of the Supervaalbara supercraton configuration during the Neoarchean (~2.75 Ga) in a position nearest the equatorial line. After rotating the drill core segments to geographic coordinates, a consistent sequence of three magnetic reversal events is identified in the lava flow sequence from the Parauapebas Formation, potentially suggesting an already dynamic geodynamo pre-2.7 Ga.

In addition, one of the most important occurrences of BIF worldwide is situated in Carajás Province and is hosted in the volcano-sedimentary sequence of the Grão-Pará. BIF represent an iron-rich rock type that typifies many Archaean and Paleoproterozoic supracrustal successions and are chemical archives of Precambrian seawater chemistry and post-depositional iron cycling. Given its well-preserved rock types, the Carajás BIF provide an excellent opportunity for studying the genesis, depositional environment, and paleoenvironmental conditions during the formation of BIF at approximately 2.75 billion years ago. The BIFs are jaspilites and are mostly composed of cm-thick intercalations of hematite, jasper, and chert ringed by hematite. Their primary textures and structures are still preserved (e.g., soft-sediment deformation, banding, micro-spherulites, microflame, and pinch and swell). The low abundance of Al2O3 (< 1.0 wt.%) and high field strength elements (< 1 ppm) for most BIF samples indicate an essentially detritus-free depositional environment. Overall, the rare earth elements and yttrium (REY) patterns show a weak positive La anomaly, and a pronounced positive Eu anomaly (Eu/Eu_{PAAS} = 1.86 – 5.05); although the presence of true Ce anomaly is not evident. Stratigraphic variations in iron isotope compositions, up to 0.80 ‰ ($\delta^{56}Fe$ = +1.10 to +1.90 ‰) over tens to hundreds of meters of stratigraphic section, hint towards relative changes

in the iron isotope composition of Carajás seawater over periods of few million years. Sm–Nd isotope data of the Carajás jaspilite plot along a correlation line in a conventional isochron diagram, which yielded an age of 2707 ± 118 Ma (MSWD = 230). A subset of these data, with only BIF samples displaying better alignment (n = 20), provided an older isochron age of 2795 ± 77 Ma (MSWD = 56). Both Sm–Nd isochrone apparent ages were concordant with the proposed minimum formation age of the Carajás jaspilites, i.e., ~2745 Ma. In addition, the jaspilites show heterogeneous distribution of Nd isotopic signature throughout the BIF sequence, and rocks sampled from near the basaltic flows/jaspilite contact (type-II) had negative εNd (t) values (–4.97 to –0.90). Meanwhile, predominantly positive εNd(t) values (–0.84 to +5.40) were widespread in the remaining samples (type-I). The REY distribution and Nd-Fe isotope data combined suggest that the deposition occurred mainly on deep-water, and in distal to continental landmasses. The precipitation of BIF occurred under anoxic and suboxic conditions in a rift basin near volcanic activity centers in a hydrothermal overprinted submarine environment. Nevertheless, considerable oxygen was probably present in the ancient ocean's water masses, evidenced by the presence of negative Ce anomalies in a few sections of the BIF sequence, thereby suggesting that the emerging oxidizing conditions could have influenced the Carajás Basin before the GOE.

Keywords: Amazonian Craton, Carajás Province, Banded Iron Formation, Chemostratigraphy, Paleomagnetism, Supervaalbara.

SUMÁRIO

AGRADECIMENTOS

RESUMO

ABSTRACT

1. INTRODUÇÃO 11

1.1 APRESENTAÇÃO E JUSTIFICATIVAS 11

1.2 OBJETIVOS 14

1.3 HISTÓRICO DA PESQUISA 15

1.4 LOCALIZAÇÃO DA ÁREA DE ESTUDO E ACESSO 15

1.5 SÍNTESE DO CONTEXTO GEOLÓGICO REGIONAL 17

1.5.1 Província Mineral de Carajás 17

1.5.2 Grupo Grão-Pará 19

1.6 MATERIAIS E MÉTODOS 23

1.7 ESTRUTURA DA TESE 26

2. FUNDAMENTAÇÃO TEÓRICA I: SÍNTESE SOBRE PALEOMAGNETISMO 28

2.1. CONCEITOS GERAIS 29

2.1.1 Campo geomagnético da Terra 29

2.1.2 Magnetismo dos sólidos 30

2.2. AMOSTRAGEM PALEOMAGNÉTICA 32

2.3. IDENTIFICAÇÃO DE MINERAIS PORTADORES DE MAGNETISMO ("FERROMAGNÉTICOS") 33

2.4. MAGNETIZAÇÃO REMANENTE NATURAL (MRN) 34

2.5. TESTES DE CAMPO DA ESTABILIDADE DE MAGNETIZAÇÃO 34

2.6. DETERMINAÇÃO DAS COMPONENTES CARACTERÍSTICAS DE MAGNETIZAÇÃO 35

2.7. PÓLO PALEOMAGNÉTICO 36

2.8. RECONSTRUÇÕES PALEOGEOGRÁFICAS 38

2.9. PALEOGEOGRAFIA EM ROCHAS ARQUEANAS 39

3. FUNDAMENTAÇÃO TEÓRICA II: FORMAÇÕES FERRÍFERAS: DESCRIÇÃO, CLASSIFICAÇÃO E GÊNESE.. 42

3.1. FORMAÇÕES FERRÍFERAS 43

3.2. GÊNESE DAS FORMAÇÕES FERRÍFERAS 45

3.2.1 Fontes hidrotermais de ferro para os oceanos 45

3.2.2 Fontes continentais de ferro para os oceanos 49

3.2.3 Fatores oxidantes na água do mar para oxidação do Fe^{2+} 50

3.2.4 Formações Ferríferas Neoproterozóicas 52

3.3. CONSIDERAÇÕES FINAIS 52

4. ARTIGO I: LOW PALEOLATITUDE OF THE CARAJÁS BASIN AT ~2.75 GA: PALEOMAGNETIC EVIDENCE FROM BASALTIC FLOWS IN AMAZONIA 54

ABSTRACT 55

1. INTRODUCTION 56

2. GEOLOGICAL SETTING 58

3. SAMPLING AND ANALYTICAL PROCEDURES 63

3.1 sampling 63

3.2 paleomagnetism 64

4. FIELD ASPECTS AND PETROGRAPHY 65

5. PALEOMAGNETIC RESULTS 68

5.1 baked contact test 75

6. ROCK MAGNETISM 77
6.1 THERMAL SUSCEPTIBILITY 77
6.2 HYSTERESIS AND ISOTHERMAL REMANENT MAGNETIZATION CURVES 79
7. DISCUSSION 81
7.1 RELIABILITY OF PALEOMAGNETIC POLES 81
7.1.1 C2 GROUP 81
7.1.2 C1 GROUP 83
7.2 AGE AND COEVAL MAGMATIC EVENTS 83
7.3 MAGNETOSTRATIGRAPHY 87
7.4 IMPLICATIONS FOR ARCHEAN SUPERCRATONS 90
8. CONCLUSION 96
ACKNOWLEDGMENTS 96
REFERENCES 97
SUPPLEMENTARY MATERIAL 114
5. ARTIGO II: CHEMOSTRATIGRAPHY OF THE CARAJÁS BANDED IRON FORMATION, BRAZIL: A RECORD OF NEOARCHEAN OCEAN CHEMISTRY 119
ABSTRACT 120
1. INTRODUCTION 121
2. GEOLOGICAL SETTING OF GRÃO-PARÁ GROUP 125
3. SAMPLING AND ANALYTICAL PROCEDURES 129
3.1 SAMPLING 129
3.2 WHOLE-ROCK GEOCHEMICAL ANALYSES 131
3.3 SM-ND ISOTOPIC ANALYSES 131
3.4 FE ISOTOPE ANALYSIS 132
4. RESULTS 134
4.1 PETROGRAPHY AND MINERALOGY 134
4.2 MAJOR AND TRACE ELEMENT GEOCHEMISTRY OF WHOLE-ROCK SAMPLES 140
4.3 SM–ND ISOTOPE SYSTEMATICS 146
4.4 FE ISOTOPE GEOCHEMISTRY 150
5. DISCUSSION 153
5.1 EFFECTS OF POST- AND SYN-DEPOSITIONAL PROCESSES ON REY PATTERNS IN CARAJÁS JASPILITES 153
5.2 HYDROTHERMAL FLUIDS INFLUENCE IN CARAJÁS BIF 155
5.3 REDOX STATE OF THE NEOARCHEAN SEAWATER IN CARAJÁS BASIN 162
5.4 IRON ISOTOPIC CONSTRAINTS 165
5.5 CONSTRAINTS FROM SM-ND ISOTOPIC COMPOSITION OF CARAJÁS JASPILITES 173
5.6 DEPOSITIONAL ENVIRONMENT AND TECTONIC SETTING 180
6. CONCLUSION 185
ACKNOWLEDGMENTS 188
REFERENCES 188
SUPPLEMENTARY MATERIAL 215
6. CONSIDERAÇÕES FINAIS 240
7. REFERÊNCIAS BIBLIOGRÁFICAS 250

CAPÍTULO 1 – INTRODUÇÃO

1. INTRODUÇÃO

1.1. Apresentação e justificativas

Investigar e desvendar os processos que modelaram o planeta Terra para o estágio que conhecemos hoje é um dos pilares das geociências atualmente. Entretanto, devido à antiguidade do nosso planeta, parte considerável de sua história foi obliterada do registro geológico, ou em diversos casos encontra-se profundamente modificada, ou limitada a poucos fragmentos de áreas cratônicas ao redor globo. Tal fato é ainda mais evidente quando se trata do registro da primeira metade da existência do planeta, ao longo da qual ocorreram mudanças significativas, que propiciaram as condições ideais para o nascimento, manutenção e proliferação da vida em larga escala (Bekker et al., 2004; Konhauser et al., 2011). Essas condições só foram possíveis após o estabelecimento da tectônica de placas e a oxigenação da atmosfera, que transcorreram ao longo do Arqueano e início do Paleoproterozóico.

A passagem entre o Neoarqueano e o Paleoproterozóico (~2.80–2.20 Ga) registra um dos períodos mais importantes da história da Terra, marcada por uma série de modificações paleoambientais, e paleoclimáticas (p.ex., o aumento do oxigênio na atmosfera) que permitiram dentre outras coisas o surgimento da vida e a melhoria das condições de habitabilidade na superfície. Neste contexto, depósitos minerais desenvolvidos durante este período registram informações valiosas sobre a evolução da atmosfera, hidrosfera, além da biosfera terrestre. Dentre esses depósitos, pode-se destacar os depósitos gigantes de minério de ferro (> 56% Fe), derivados de formações ferríferas bandadas (FFB).

As formações ferríferas bandadas são rochas sedimentares químicas ricas em ferro (15-40 % Fe) e sílica (40-60 % SiO_2) que precipitaram da água do mar durante o Éon Pré-cambriano, sendo que a maior concentração deste tipo de deposição situa-se no Neoarqueano e Paleoproterozóico (entre 2.80 e 1.85 Ga). Tais rochas têm sido amplamente estudadas nas últimas décadas (p.ex., Gross, 1980; Trendall, 2002; Bekker et al., 2010; Konhauser et al., 2017), porque, além da sua importância econômica, os modelos propostos para explicar sua gênese estão intimamente ligados à evolução do sistema terrestre. Entretanto,

a inexistência de processos deposicionais modernos análogos dificulta a formulação de modelos genéticos, de tal forma que não há consenso sobre os mecanismos de precipitação, taxa de sedimentação, gênese do bandamento, influência de processos biológicos, assim como a fonte do suprimento de ferro para explicar a origem destas sequências.

Neste contexto, as formações ferríferas bandadas (FFBs) da Província Mineral de Carajás (Fig. 1), que hospedam um dos maiores depósitos de ferro de alto teor do mundo (18 bilhões toneladas >65% Fe; DOCEGEO, 1988; Vasquez et al., 2008), se tornam de grande interesse para a compreensão da gênese das formações ferríferas, ambiente deposicional e condições paleoambientais durante o período de deposição cerca de 2,75 bilhões de anos atrás (Trendall et al., 1998; Martins et al., 2017). Ademais, estabelecer as posições dos continentes neste momento, quando a configuração continental ainda é pouco conhecida e intensamente debatida, é uma das questões mais importantes para decifrar a evolução geológica terrestre.

As FFBs de Carajás estão contidas na sequência vulcanossedimentar neoarqueana do Grupo Grão-Pará (~2.76 a 2.73 Ga; Fig. 1C). Estas são referidas usualmente como jaspilitos e correspondem ao protominério de ferro da região da Serra do Carajás, norte da Província Mineral de Carajás. Jaspilitos e minérios de alto teor (> 65% Fe) constituem a Formação Carajás, sobreposta e sotoposta por rochas, essencialmente, máficas das formações Parauapebas e Igarapé Bahia, respectivamente. Acima do Grupo Grão-Pará ocorrem as rochas sedimentares (~2.68 a 2.06 Ga) metamorfizadas em baixo grau das formações Serra Sul e Águas Claras (Macambira, 2003; Araújo & Nogueira, 2019; Araújo Filho et al., 2020; Rossignol et al., 2020).

Nas últimas décadas, os aspectos estratigráficos, estruturais, geoquímicos e geocronológicos do Grupo Grão-Pará foram investigados por vários pesquisadores (p.ex., Wirth et al., 1986; Gibbs et al., 1986; Olszewski et al., 1989; Meirelles & Dardenne 1991; Trendall et al., 1998; Lindenmayer et al., 2001; Macambira 2003; Cabral et al., 2013, 2017; Martins et al., 2017; Figueiredo e Silva et al., 2020). Entretanto, poucos trabalhos foram dedicados ao estudo dos aspectos paleoambientais, ao conhecimento dos mecanismos de deposição dos jaspilitos e à investigação do ambiente tectônico de formação da bacia. Neste

sentido, várias questões relativas à evolução desta sequência supracrustal, especialmente sobre as FFBs de Carajás, ainda permanecem em aberto, entre elas: (i) Qual é a fonte do ferro nas formações ferríferas bandadas de Carajás? (ii) Quais as condições paleoambientais na época de sua deposição? (iii) Qual a paleogeografia do proto-cráton Amazônico (Bloco Carajás) durante a deposição das formações ferrífera de Carajás? E, por fim, (iv) Qual seria o ambiente tectônico de formação da Bacia Carajás?

1.2. Objetivos

O objetivo desta pesquisa está centrado no estudo do ambiente tectônico de deposição, na reconstrução paleogeográfica e no estudo da gênese da formação ferrífera bandada que compõem o Grupo Grão Pará, a partir da integração de dados geológicos, geoquímicos, paleomagnéticos e isotópicos de alta precisão.

Os objetivos específicos incluem:

i. Estudar as relações estratigráficas originais entre as formações ferríferas bandadas e as rochas vulcânicas do Grupo Grão Pará, a partir da descrição de 11 furos de sondagem distribuídos nos Corpos N4WS e N5S;

ii. Caracterização petrográfica das rochas sedimentares (jaspilitos) e vulcânicas (basaltos) do Grupo Grão-Pará com o intuito de identificar as estruturas e a mineralogia primária, bem como caracterizar as assembleias metamórficas/hidrotermais secundárias;

iii. Reconhecer e caracterizar a mineralogia e as microestruturas mais importantes no jaspilito da Formação Carajás, com a aplicação de técnicas analíticas avançadas, como a microssonda eletrônica e microscopia eletrônica de varredura (MEV/EDS).

iv. Analisar a quimioestratigrafia da Formação Carajás utilizando de técnicas avançadas de geoquímica de elementos maiores e traços visando a reconstrução das condições paleoambientais que controlaram a deposição dos jaspilitos e a investigação dos fatores secundários que levaram a suas modificações;

v. Reconstruir o ambiente deposicional dos jaspilitos, a partir do estudo dos sistemas isotópicos Sm-Nd e $\delta^{56}Fe$;

vi. Aquisição de dados paleomagnéticos de alta qualidade nos basaltos da Formação Parauapebas, com foco na reconstrução paleogeográfica da Bacia Carajás.

1.3 Histórico da pesquisa

Esta tese de doutorado deu continuidade a vários projetos de pesquisa que tiveram o apoio da empresa VALE (Acordo de Cooperação e Apoio Técnico-Científico Entre a Vale S.A e a Fundação Universidade de Brasília – FUB) e da FAP-DF (EDITAL 03/2018 – Nº 23411.93.27701.29052018). Os projetos foram coordenados pelas orientadoras Catarina (FAP-DF) e Adalene (Vale-FUB). Os projetos tiveram início em 2012, cujo maior parte das etapas de campo e coleta de amostras foram realizadas em 2012 e 2013. Todas as pesquisas foram realizadas na região da Bacia Carajás, estudando tanto as rochas vulcânicas quanto as sedimentares (jaspilitos), que resultou dentre outras coisas em dissertações e artigos publicados em revistas cientificas internacionais (Qualis A1) (p.ex., Martins et al., 2017). A última pesquisa realizada (mestrado) aconteceu entre o período de 2015-2017 e estava centrada no estudo das rochas vulcânicas, obtendo dados, discussões e conclusões importantes sobre a petrogênese dos basaltos e ambiente tectônico da Bacia de Carajás (Martins, 2017).

1.4 Localização da área e acesso

A área de estudo localiza-se no distrito mineiro Serra Norte, Província Mineral de Carajás – PA, especificamente nos depósitos de ferro N4WS e N5S. O município de Parauapebas (Fig. 2), localizado a aproximadamente 550 km a sudoeste de Belém, serve como referência e apoio logístico. Os depósitos de ferro N4 e N5 fazem parte dos depósitos pertencentes à Companhia Vale do Rio Doce (CVRD), situados na parte norte da serra dos Carajás e nomeados de N1 a N9. O acesso pode ser feito pela rodovia PA-150, que liga Belém a Marabá e Cuiabá (MT), seguindo-se pela Trans-Carajás (PA-275) até o núcleo urbano de Carajás e, depois, para os depósitos de ferro, numa extensão de aproximadamente 700 km (Fig. 2). O

aeroporto de Carajás (CKS) é servido diariamente por voos diretos de/para Belém, Brasília, Belo Horizonte e para cidades menores do sul e do sudeste do Pará.

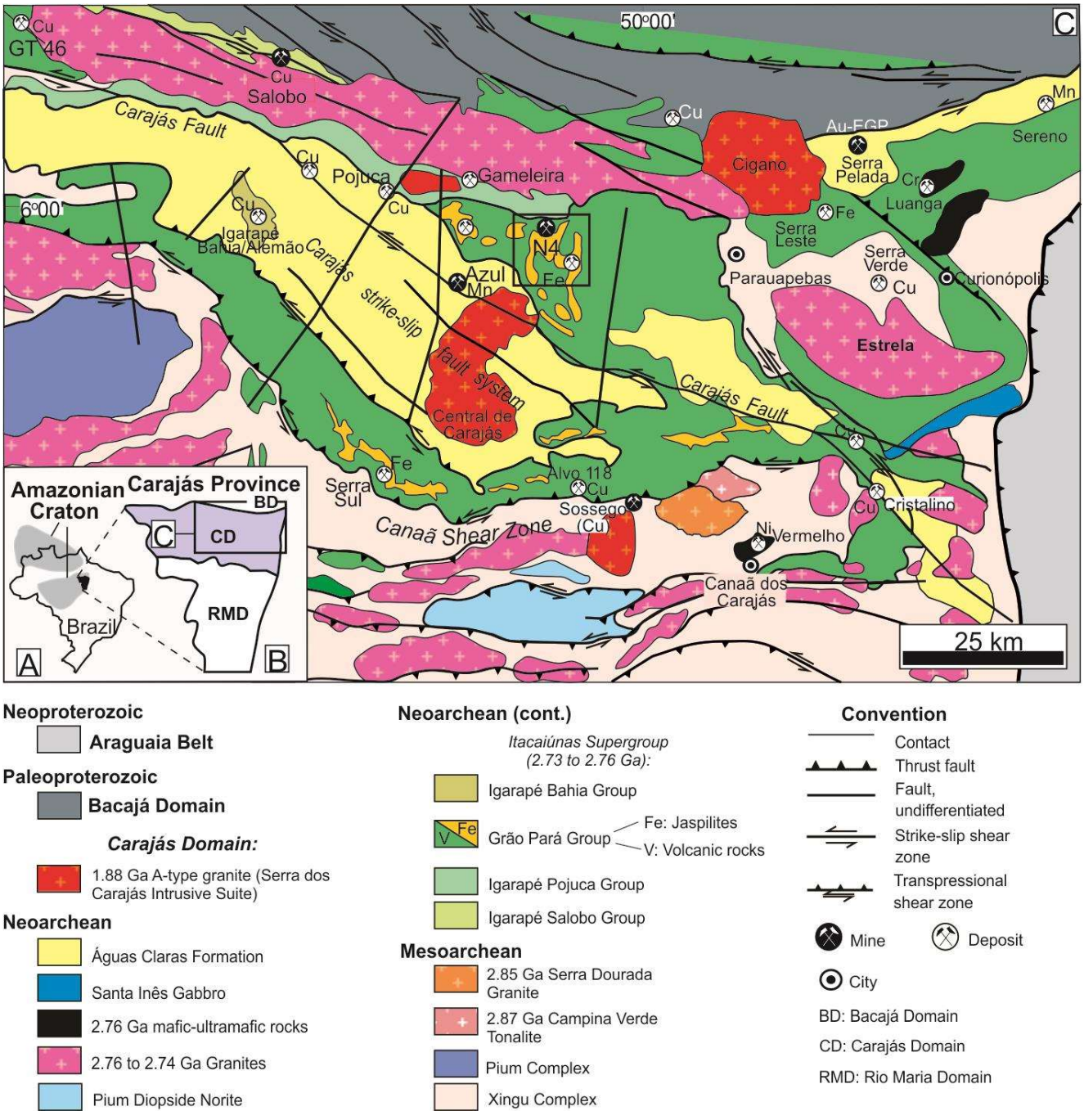

Figura 1. A) *Localização da Província Carajás no Brasil;* ***B)*** *Localização do Domínio Carajás dentro da Província Carajás; o retângulo corresponde aproximadamente a área detalhada na Fig. 1C;* ***C)*** *Mapa geológico simplificado da parte nordeste da província Carajás, Domínio Carajás (modificado de Vasquez et al., 2008); o retângulo preto indica a localização aproximada dos depósitos N4 e N5.*

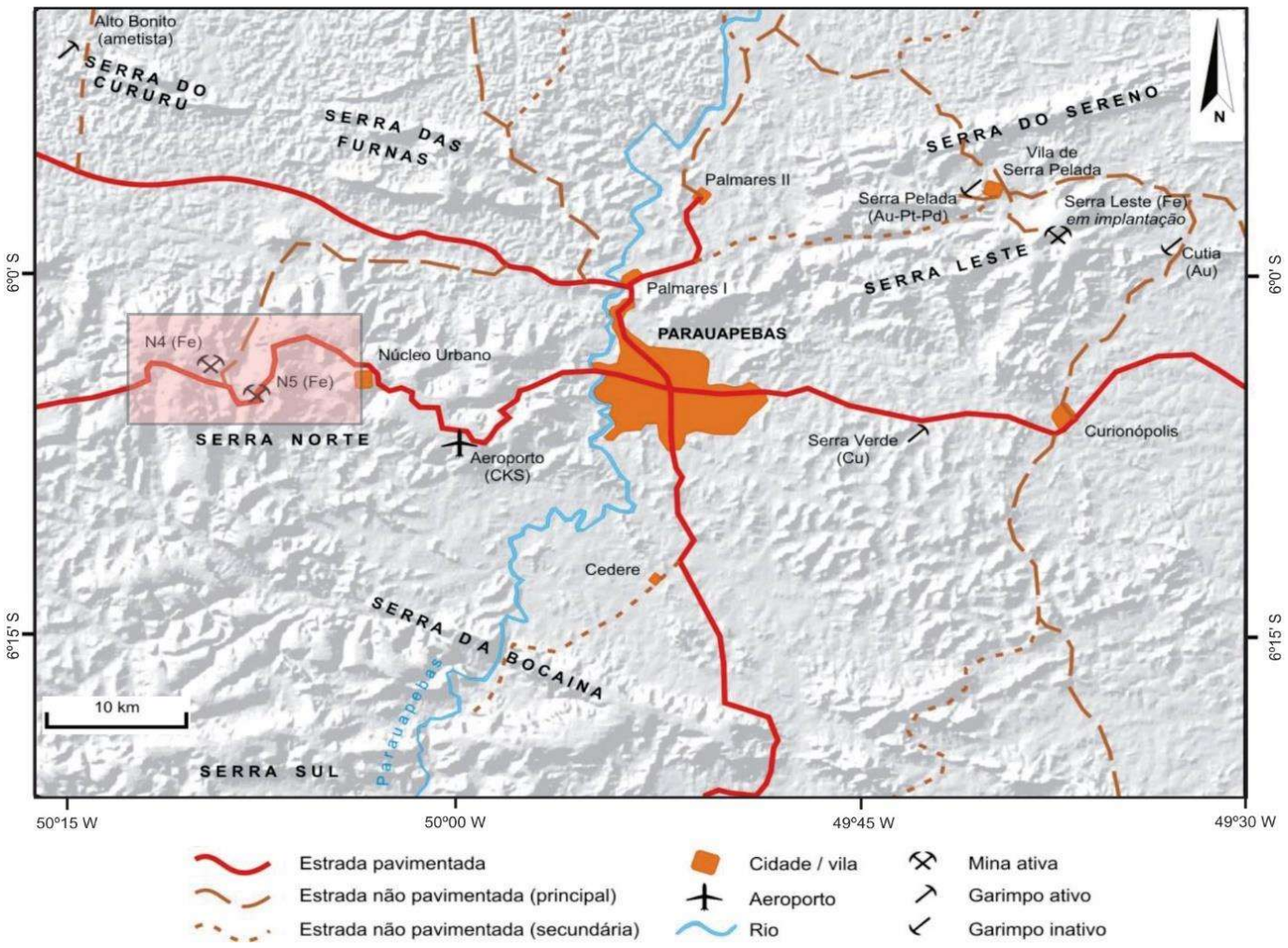

Figura 2. *Fusão do mapa planimétrico de parte da Serra de Carajás com imagem de relevo sombreado (SRTM), mostrando as principais feições geomorfológicas, acessos e localidades (modificado de Tavares, 2015). O polígono marcado representa as regiões da área de estudo, especificamente sobre os corpos N4 e N5.*

1.5 Síntese do contexto geológico regional

1.5.1 Província Mineral de Carajás

A Província Mineral de Carajás, localizada no setor sudeste do Cráton Amazônico (Fig. 1A), é o maior e mais bem preservado segmento arqueano do cráton. É conhecida por abrigar vários depósitos minerais de classe mundial (DOCEGEO, 1988; Vasquez *et al*., 2008), incluindo um dos maiores depósitos de minério de ferro do mundo, bem como vários depósitos de classe mundial de Cu-Au e Ni. A Província Mineral de Carajás é subdividida em dois domínios tectônicos distintos (Fig. 1B): Domínio Rio Maria ao sul e o Domínio Carajás ao norte, também conhecido como Domínio Itacaiúnas ou Bacia Carajás (Araújo

et al., 1988; Vasquez *et al*., 2008). Uma zona pouco definida e estudada, conhecida como Subdomínio Transicional, separa os domínios Rio Maria e Carajás (Dall'Agnol *et al*., 2006; Feio *et al*., 2013).

O Domínio Rio Maria (ou Terreno Granito-*Greenstone* Rio Maria) possui evolução mesoarqueana, caracterizada pela amalgamação de terrenos tipo granito-*greenstone* juvenis, com idades de formação entre 3,05 Ga e 2,82 Ga (DOCEGEO, 1988, Althoff *et al*., 2000; Dall'Agnol *et al*., 2006, dentre outros). A caracterização de komatiitos com textura *spinifex* em uma sequência *greenstone belt* dentro do Subdomínio Transicional (Siepierski & Ferreira Filho, 2016) sugere que os terrenos granito-*greenstone* se estendem mais para o norte do que indicado nos mapas regionais anteriores. A estruturação principal do Domínio Rio Maria é um resultado de encurtamento N-S durante processo acrescionário/colisional mesoarqueano, porém influenciado por tectonismo vertical do tipo domos-e-quilhas (Althoff *et al*., 2000).

Já o Domínio Carajás, também conhecido como Cinturão Itacaiúnas (Araújo *et al*., 1988), apresenta um cenário geológico mais complexo. Sem considerar as rochas mesoarquenas graníticas fortemente deformadas e gnáissicas do Subdomínio Transicional (2,96-2,83 Ga; Feio et al., 2012; Feio *et al*., 2013), o Domínio Carajás é composto essencialmente pelas rochas das sequências vulcanossedimentares da Bacia Carajás. Tendo como embasamento o Complexo Xingu (similar em idade e conteúdo ao Subdomínio Transicional), as principais assembleias da Bacia Carajás possuem idade neoarqueana a paleoproterozóica comumente segmentada na sequência vulcanossedimentar do Grupo Grão-Pará (2,76–2,73 Ga) recoberta por rochas sedimentares das formações Serra Sul e Águas Claras (~2,68-2,06 Ga; Araújo & Nogueira, 2019; Araújo Filho et al., 2020; Rossignol et al., 2020) (Fig. 3). A Formação Serra Sul compreende, da base para o topo, diamictitos glaciais foliados a maciços que ocorrem intercalados com camadas de *black-shale*, conglomerados polimíticos de origem glacial, que ocorrem intercalados com camadas de ritmito, e camadas espessas de ritmito no topo. Já a Formação Águas Claras consiste em pelitos, arenitos e rochas carbonáticas subordinadas de ambiente marinho raso na base, seguidos por um pacote espesso de arenitos fluviais e conglomerados no topo. Sua idade de deposição é incerta (neoarqueana ou paleoproterozóica) e ainda não está claro se esta sucessão sedimentar representa apenas uma ou mais sequências diferentes (Araújo Filho

et al., 2020). Ambas as unidades se sobrepõem em inconformidade ao Grupo Grão-Pará (Araújo & Nogueira, 2019; Araújo Filho et al., 2020) (Fig. 3).

Diversos complexos máfico-ultramáficos acamadados afloram perto das bordas da Bacia Carajás (Fig. 1C; Vasquez et al., 2008) e intrudem rochas do Complexo Xingu e do Grupo Grão-Pará (DOCEGEO, 1988; Ferreira Filho et al., 2007). Essas intrusões possuem idades neoarqueanas (Lafon et al., 2000; Machado et al., 1991) e representam um grande evento magmático coevo com o extenso vulcanismo basáltico do Grupo Grão-Pará (Machado et al., 1991; Ferreira Filho et al., 2007).

Três principais episódios de geração de rochas graníticas ocorrem na Bacia de Carajás ou em áreas adjacentes (Fig. 1C): (i) O mais antigo, de idade neoarqueana (~2.76-2.73 Ga), é intrusivo no Grupo Grão-Pará e marcado por corpos graníticos subalcalinos do tipo A, sendo representado pelas suítes Plaquê e Planalto, Complexo Estrela e granito Serra do Rabo (Feio et al., 2012, 2013); (ii) Intrusões mais novas (~ 2.56 Ga), como os granitos peralcalinos a metaluminosos Old Salobo e Itacaiúnas (Machado et al., 1991), que estão associados a magmatismo pouco expressivo, também do tipo A, aparentemente concentrado no extremo norte da Província Carajás, ao longo do Cinturão Norte do Cobre; (iii) O último episódio magmático promoveu a formação de vários plútons graníticos anorogênicos paleoproterozóicos (~1.88 Ga), dentre eles, o Central de Carajás, Young Salobo e Cigano que pertencem a uma extensão província magmática do tipo A espalhada por todo o Cráton Amazônico (Dall'Agnol et al., 2006).

1.5.2 Grupo Grão-Pará

A sequência vulcanossedimentar neoarqueana do Grupo Grão-Pará (~2.76 Ga; Gibbs et al., 1986; Olszewski et al., 1989; Machado et al., 1991; Trendall et al., 1998; Martins et al., 2017), localizada na porção norte do Domínio Carajás, é a principal sequência da Bacia Carajás. Possui aproximadamente 260 km de comprimento e 70 km de largura, com as rochas vulcânicas cobrindo uma área extensa de aproximadamente 11.000 km^2 (Macambira, 2003). Diferentes propostas estratigráficas foram apresentadas para a região de Carajás nas últimas décadas (DOCEGEO, 1988; Araújo et al., 1988; Araújo & Maia, 1991, Macambira, 2003; Tavares et al., 2018). Para a estratigrafia do Grupo Grão-Pará, seguimos o arcabouço

estratigráfico proposto por Araújo & Nogueira (2019) e Araújo Filho et al. (2020). Sendo assim, o Grupo Grão-Pará é composto pela Formação Parauapebas na base, constituída essencialmente por rochas vulcânicas máficas, seguida pelos jaspilitos da Formação Carajás (Lindenmayer et al., 2001; Macambira, 2003) e pela unidade vulcânica superior com sedimentação clástica associada denominada Formação Igarapé Bahia, a qual contem expressivos depósitos de Cu-Au (Tallarico et al., 2005; Galarza et al., 2008; Dreher et al., 2008).

A Formação Parauapebas, unidade basal do Grupo Grão-Pará (Fig. 3), é representada por derrames basálticos e basalto andesíticos maciços, amigdaloidais e porfiríticos, associados a riolitos, brechas e tufos vulcânicos (Macambira, 2003; Martins et al., 2017). Este extenso vulcanismo, essencialmente basáltico, é geralmente considerado como sendo o resultado de rifteamento da crosta continental mais antiga e fusão parcial do manto (p.ex., Gibbs et al., 1986; DOCEGEO, 1988; Olszewski et al., 1989; Macambira, 2003; Martins et al., 2017; Tavares et al., 2018), mas alguns autores (p. ex., Meirelles & Dardenne, 1991; Teixeira & Eggler, 1994; Lobato et al., 2005; Zuchetti, 2007; Figueiredo e Silva et al., 2020) sugeriram um ambiente relacionado à subducção. A idade do vulcanismo é determinada em 2758 ± 39 Ma, por meio de análises U-Pb em zircões de riolitos pertencentes à Formação Parauapebas, feitas por Wirth et al. (1986). Esta idade (~2,76 Ga) é ratificada por análises isotópicas por diversos autores (p. ex., Olszewski et al., 1989; Machado et al., 1991; Trendall et al., 1998). Recentemente, idades um pouco mais novas (2749 ± 6 e 2745 ± 5 Ma; U-Pb em SHRIMP), foram obtidas em zircões de rochas vulcânicas máficas (Martins et al., 2017).

Já a Formação Carajás é constituída por formações ferríferas bandadas de fácies óxidos (jaspilito) com camadas de espessura de até algumas centenas de metros, que em algumas regiões estão quase totalmente transformadas em minério hematítico. Esta unidade está em contato abrupto ou gradacional com a Formação Parauapebas e mostra intercalações com as rochas vulcânicas máficas (Macambira, 2003; Martins et al., 2017). A formação ferrífera bandada é descrita como jaspilito meso- e microbandado formado por bandas de jaspe e óxidos de ferro, sendo o jaspe caracterizado como um *chert* impregnado por hematita microcristalina (Lindenmayer et al., 2001; Macambira, 2003). Lindenmayer et al. (2001) concluem que os jaspilitos formaram-se por precipitação química em plataformas marginais de águas rasas,

em período de calma tectônica e perto de fumarolas com ampla distribuição areal. Diques e *sills* de gabro e diabásio cortam as unidades anteriormente descritas (Beisiegel et al., 1973; Lindenmayer et al., 2001; Macambira, 2003; Martins et al., 2016).

A sequência de jaspilitos é sobreposta por um conjunto de rochas vulcânicas intercaladas subordinadamente com rochas siliciclásticas finas (ritmitos) que ocorrem logo acima da Formação Carajás (Fig. 3) e na parte basal da mina do Igarapé Bahia (Tallarico et al., 2005; Dreher et al., 2008; Galarza et al., 2008; Araújo & Nogueira, 2019). Os dados de zircão U-Pb existentes restringem a idade das rochas vulcânicas em 2748 ± 34 Ma (Tallarico et al., 2005).

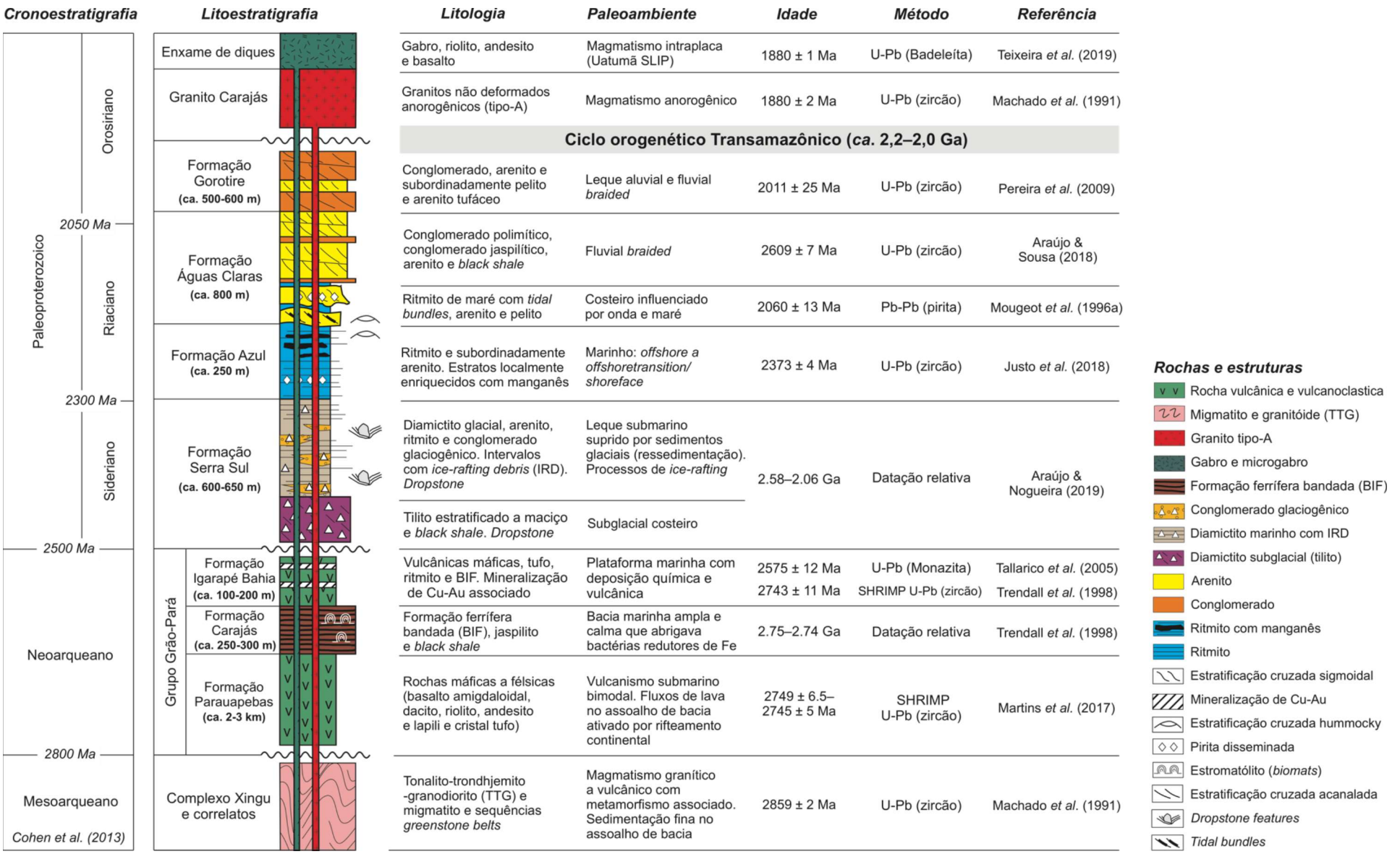

Figura 3. *Coluna estratigráfica da Bacia de Carajás (extraída de Araújo, 2020).*

1.6 Materiais e métodos

Inicialmente, o foco da pesquisa foi direcionado para revisões bibliográficas e estudos complementares a fim de aprofundar o conhecimento concernente ao contexto geológico da Província Carajás, à geodinâmica presente no arqueano, as reconstruções paleogeográficas em terrenos arqueanos, gênese das formações ferríferas e diferentes aspectos relacionados as sequências vulcanossedimentares arqueanas de Carajás. A caracterização das rochas vulcânicas e sedimentares do Grupo Grão-Pará foi efetuada por meio da descrição sistemática de 9 furos de sondagem, assim como estudos petrográficos por microscópio petrográfico, em luz transmitida e refletida, microssonda eletrônica (EDS e WDS), análises químicas e geocronológicas. Os resultados foram integrados para reconstituição paleoambiental, inferências paleoclimáticas, e construção de modelos geodinâmicos e paleogeográficos (Fig. 4).

O trabalho de campo foi realizado em novembro de 2017 e consistiu na descrição de testemunhos de sondagem e coleta de amostras de furos de sondagens dos Corpos N4WS e N5S e arredores. Amostras coletadas em etapas de campo anteriores ao desenvolvimento da tese (julho de 2012 e maio de 2013) forneceram a maioria das amostras utilizadas. Ambos as etapas contaram com o apoio da Empresa VALE S.A., incluindo discussões sobre o contexto geológico regional, seleção de testemunhos de sondagem e deslocamentos na área.

As amostras deste estudo foram coletadas em testemunhos correspondentes a cinco furos de sondagens, distribuídas em três seções na direção EW que seccionam o depósito de N4WS (Fig. 5). A amostragem foi realizada sistematicamente a cada dois metros, com amostras representativas de 15 cm, totalizando 1766 amostras (1051 amostras de jaspilitos, 346 amostras de minério e 369 amostras de basaltos). As amostras foram seccionadas ao meio, sendo que uma parte foi separada para análise geoquímica (XRF, ICP-MS, ICP-AES e Titulação) e a outra metade foi utilizada para medições e aquisição de dados geofísicos, incluindo o estudo paleomagnético e dados espectroradiométricos. Esses dados forneceram informações suficientes para a confecção de cinco dissertações de mestrado no âmbito do projeto.

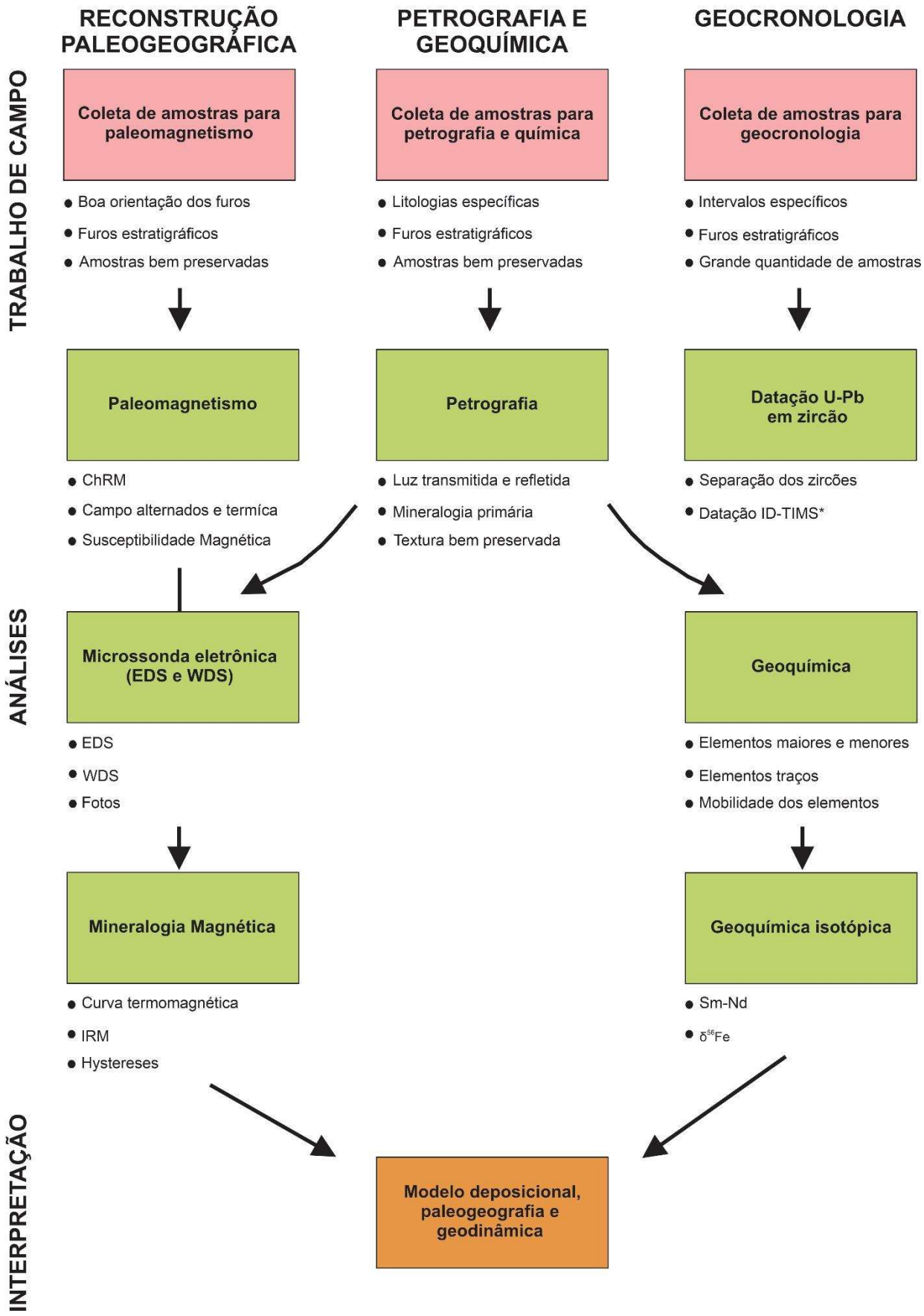

Figura 4. *Fluxograma de metodologias e técnicas empregadas na investigação da sequência vulcanossedimentar do Grão-Pará.*

As análises litogeoquímicas foram efetuadas no laboratório ALS Chemex (Canadá). Já as análises isotópicas de Sm-Nd foram realizadas utilizando um espectrômetro de massa com ionização termal (*TIMS – Thermal ionization mass spectrometer*) no laboratório de geocronologia da Universidade de Brasília. Por fim, as análises de isótopos de ferro foram adquiridas utilizando um espectrômetro de massa com multi-coletores (*MC-ICP-MS – Multi-collector inductively coupled plasma mass spectrometer*) Nu Plasma II, no Laboratório de Isótopos Estáveis do *Institute of Geochemistry and Petrology, Department of Earth Sciences, ETH Zürich* – Suíça. A descrição mais detalhada de todas técnicas utilizadas nas amostras de jaspilitos encontram-se no **Capítulo 5** "*Chemostratigraphy of the Carajás banded iron formation, Brazil: A record of chemical evolution of Neoarchean ocean"* deste documento.

A metodologia utilizada e a amostragem realizada para a aquisição dos dados paleomagnéticos nas rochas vulcânicas da Formação Parauapebas está detalhada no **Capítulo 4** "*Low paleolatitude of the Carajás Basin at ~2.7 Ga: Paleomagnetic evidence for basaltic flows in Amazonia".*

Além disso, amostras de rocha, com aproximadamente 10 kg, foram coletadas de afloramentos e testemunhos de sondagem para datação pelo método U-Pb em zircão. Devido a pandemia global do COVID-19 e consequente interrupção das atividades regulares dos laboratórios em todo o mundo, não foi possível a obtenção dos resultados a tempo de serem inseridos na tese de doutorado. Nesta etapa seria feito o cálculo da taxa de sedimentação dos jaspilitos por meio das idades U-Pb (ID-TIMS) de alta precisão nos derrames basálticos que intercalam o pacote de jaspilitos, fornecendo informações importantes sobre as condições de deposição da Bacia Carajás.

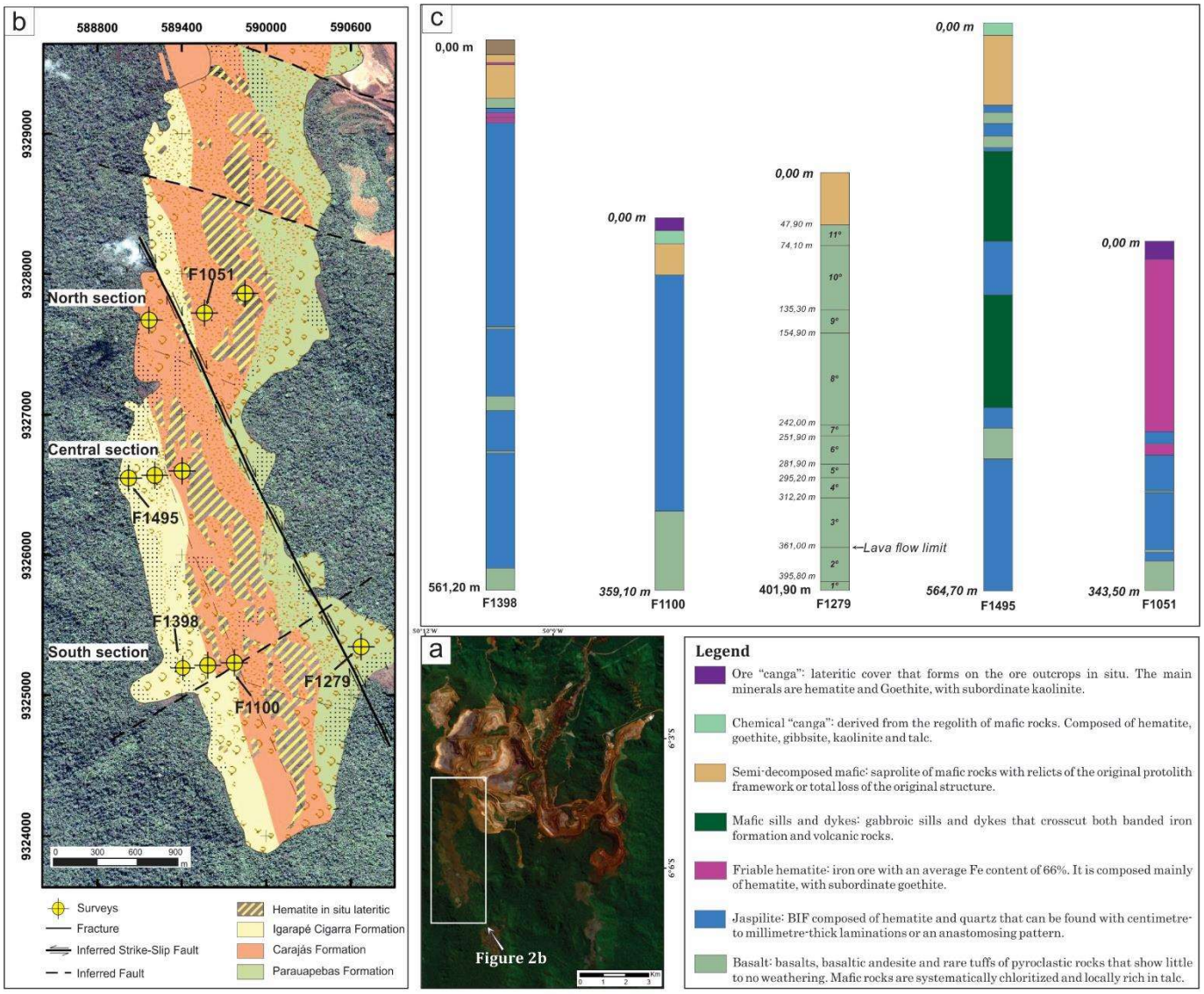

Figura 5. ***A****) Imagem de satélite Landsat 8 (OLI) mostrando a região do depósito N4, com destaque para a região do Corpo N4WS (3B);* ***B****) Mapa geológico do Corpo N4WS, com o posicionamento dos testemunhos de sondagens estudos nesta pesquisa;* ***C****) "Log" de alguns dos testemunhos de sondagens amostrados.*

1.7. Estrutura da Tese

A presente tese de doutorado foi desenvolvida no programa de pós-graduação em Geologia do Instituto de Geociências – Universidade de Brasília (UnB) e tem como base o estudo da paleogeografia, condições paleoambientais e ambiente tectônico da formação da Bacia Carajás, localizado na porção sudeste do Cráton Amazônico, a partir de dados geológicos, geoquímicos, paleomagnéticos e isotópicos de rochas do Grupo Grão-Pará.

O **primeiro capítulo** deste documento tem como finalidade apresentar as justificativas, objetivos, histórico da pesquisa, localização, síntese do contexto geológico regional da Bacia Carajás e metodologia. O **segundo capítulo** apresenta fundamentação teórica atualizada por meio de uma breve descrição e discussão sobre o paleomagnetismo com foco em reconstruções paleogeográficas. Já o **terceiro capítulo** abordará uma breve revisão bibliográfica sobre formações ferríferas tendo como foco a sua descrição, classificação e gênese.

Os resultados da tese estão redigidos no formato de artigos para divulgação em periódicos internacionais. Dessa forma, o **quarto capítulo** apresenta o artigo científico submetido ao periódico *Precambrian Research*, intitulado "*Low paleolatitude of the Carajás Basin at ~2.7 Ga: Paleomagnetic evidence for basaltic flows in Amazonia*". Esse estudo baseou-se na aquisição de dados paleomagnéticos de boa qualidade em diferentes porções dos basaltos neoarqueanos da Formação Parauapebas (2749 ± 6.5 Ma; Martins et al., 2017), base da sequência vulcanossedimentar do Grão-Pará. Com base nesses dados, é fornecida a primeira reconstrução paleogeográfica para um fragmento arqueano do Cráton Amazônico (Província Carajás), expandindo a configuração do supercráton Supervaalbara (Gumsley, 2017; Gumsley et al., 2017; Salminen et al., 2019) durante este período para um bloco do Cráton Amazônico pela primeira vez. Além disso, pelo menos cinco eventos de reversão magnética e uma mudança significativa na paleolatitude são identificados ao longo da sequência de derrames basálticos estudados.

Em seguida, o **quinto capítulo** apresenta o artigo científico submetido à revista *Gondwanna Research*, intitulado "*Chemostratigraphy of the Carajás banded iron formation, Brazil: A record of Neoarchean ocean chemistry*". Nesse estudo, foi apresentado um conjunto de dados quimioestratigráficos, isotópicos e de elementos maiores e traços, ao longo de uma seção completa do pacote de jaspilitos de Carajás. A partir dessas informações, são avaliadas as principais condições paleoambientais durante a precipitação dos jaspilitos, obtendo um importante registro da composição do mar durante o Neoarqueano.

Por fim, o **sexto capítulo** apresenta as considerações finais da tese, enquanto que na parte final da tese encontram-se as referências bibliográficas usadas nos capítulos 1, 2, 3 e 6.

CAPÍTULO 2 – FUNTAMENTAÇÃO TEÓRICA I: SÍNTESE SOBRE PALEOMAGNETISMO

2. SÍNTESE SOBRE PALEOMAGNETISMO

A maioria das informações sobre a evolução de supercontinentes advém de estudos dos crátons individuais em diversas partes do mundo (Fig. 6; Rogers & Santosh, 2003). Para se ter uma configuração confiável de um supercontinente e/ou supercráton, torna-se necessário obter com precisão, grande quantidade de informações geológicas, geocronológicas e paleomagnéticas dos fragmentos continentais hoje separados, visando fornecer meios de estabelecer estas ligações. O paleomagnetismo, em particular, torna-se ferramenta essencial para determinar a paleogeografia das diversas unidades cratônicas que participaram da formação e fragmentação destas grandes massas continentais (supercontinentes e/ou supercrátons).

Neste capítulo, de forma sintetizada, primeiramente será feita uma revisão quanto aos conceitos gerais inerentes ao paleomagnetismo. Em seguida, serão apresentados procedimentos e técnicas utilizadas em estudos paleomagnéticos (p.ex., amostragem, magnetização remanente natural, técnicas de desmagnetização e testes de campo da estabilidade de magnetização). No final, serão abordados a obtenção de polos magnéticos e as reconstruções paleogeográficas associadas. Os detalhes do estudo realizado nas rochas vulcânicas máficas neoarqueanas (~2.75 Ga) da Bacia Carajás será apresentado no próximo capítulo (Capítulo 4) em forma de artigo submetido à revista *Precambrian Research.*

2.1 Conceitos gerais

2.1.1 Campo geomagnético da Terra

O campo geomagnético é um campo vetorial e pode ser representado por meio de projeção tri-ortogonal (Fig. 7). Seus valores são positivos na direção Norte, Leste, e para baixo. A projeção horizontal do campo magnético H é dada pelo ângulo I, conhecido como inclinação magnética. O ângulo D formado entre o Norte geográfico e a projeção horizontal do campo H é denominado declinação magnética, D.

O campo geomagnético total é formado por três campos: 1) campo gerado no interior da Terra, proveniente do núcleo externo líquido; 2) o campo gerado na crosta terrestre, proveniente dos materiais

magnetizados; e 3) um campo de origem externa à Terra, relacionado à influência do campo magnético interplanetário sobre o campo geomagnético.

No paleomagnetismo o campo magnético terrestre é considerado como o de um dipolo geocêntrico e axial, ou seja, o campo magnético é gerado por dipolo magnético situado no centro da Terra e cujo eixo está alinhado com seu eixo de rotação. Nessa aproximação a declinação D em qualquer ponto da superfície da Terra sempre será nula e a inclinação I varia com a latitude λ ($\tan \mathrm{I} = 2 \tan \lambda$).

Variações do campo geomagnético (rápidas ou lentas) são observadas e cobrem intervalos de tempo da ordem de anos a milhões de anos. De forma geral, as variações rápidas estão relacionadas ao campo externo, enquanto as mais lentas se relacionam ao campo interno, gerado no núcleo externo. As variações de longo período podem ser divididas em: variação secular, excursões geomagnéticas e reversões.

2.1.2 Magnetismo dos sólidos

Os materiais quando submetidos à ação de um campo magnético podem apresentar propriedades magnéticas distintas em função de parâmetros como a natureza dos orbitais e spins dos elétrons. De acordo com suas características magnéticas, os minerais classificam-se em diamagnéticos, paramagnéticos e ferromagnéticos.

Diamagnetismo é uma propriedade encontrada em todos os minerais, mas somente será observado em minerais com átomos que não possuem momento magnético (p.ex. quartzo com susceptibilidade magnética de ~0,8 x 10^{-7} SI).

As substâncias paramagnéticas são aquelas em que os átomos possuem momento magnético resultante, causado pelos spins desemparelhados que agem como dipolos magnéticos. A susceptibilidade magnética dos materiais paramagnéticos é positiva, maior que a dos materiais diamagnéticos (geralmente duas ordens de grandeza), mas ainda assim, pequena. Assim como no diamagnetismo, a magnetização volta a ser nula quando o campo externo é retirado. Um exemplo de mineral paramagnético é a ilmenita ($FeTiO_3$).

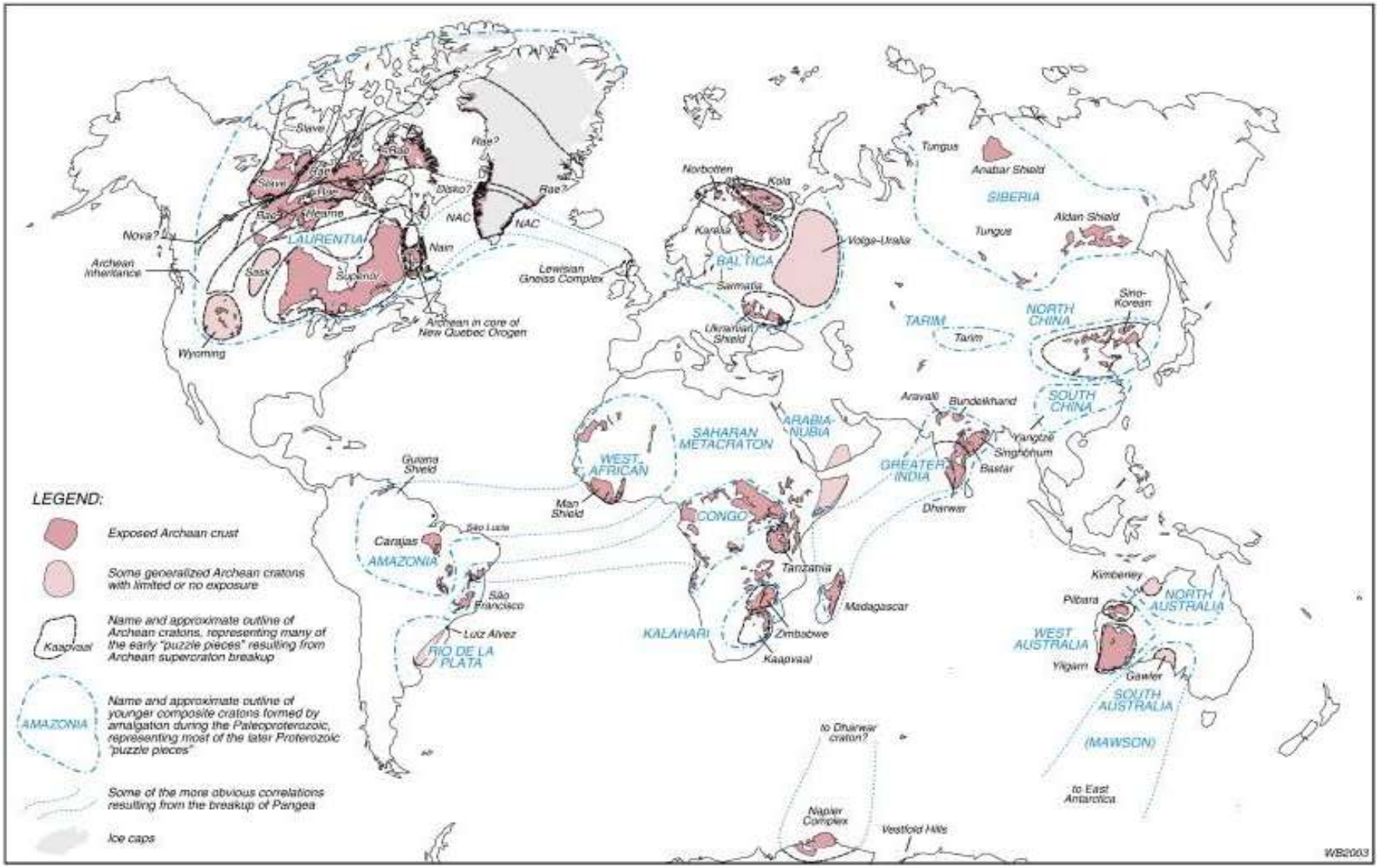

Figura 6. *Distribuição dos principais blocos cratônicos ao redor do mundo (modificado de Bleeker, 2003).*

Nas substâncias ferromagnéticas os átomos com momentos magnéticos resultantes interagem fortemente entre si, gerando magnetização mais forte que no paramagnetismo. Além disso, a magnetização permanece mesmo após a remoção do campo externo e é chamada de magnetização remanente. Para o paleomagnetismo, os minerais "ferromagnéticos" são os mais importantes.

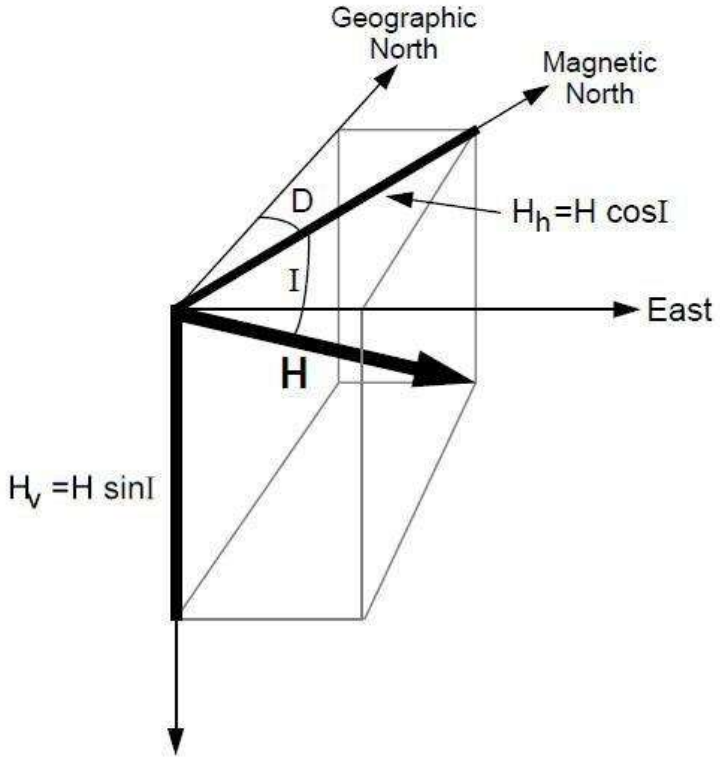

Figura 7. *Representação espacial de um campo H e suas componentes (extraído de Butler, 1992).*

2.2 Amostragem paleomagnética

Denomina-se sítio paleomagnético o afloramento de rocha escolhido para amostragem. Esta rocha deve estar necessariamente "*in situ*", ou seja, não houve qualquer tipo de deslocamento após sua formação, estando a rocha em seu local natural. Esta escolha deve ser realizada corretamente e de maneira muito criteriosa para que erros inerentes não afetem diretamente a obtenção dos resultados. Por isso, uma boa amostragem é essencial para o sucesso da investigação paleomagnética.

A coleta das amostras pode ser feita de duas formas diferentes, sendo que a escolha depende das condições do afloramento. A primeira é a coleta de cilindros orientados utilizando-se uma perfuratriz portátil, movida a gasolina, que possui uma broca diamantada. O diâmetro dos testemunhos cilíndricos é de 2.5 cm e o comprimento depende da dureza da rocha, das condições da broca e do operador da perfuratriz. A segunda é a coleta de blocos orientados que no laboratório são perfurados para a retirada de testemunhos cilíndricos, também de 2.5 cm de diâmetro. Os procedimentos de orientação das amostras são variados e não existe um padrão específico.

2.3 Identificação de minerais portadores de magnetismo ("Ferromagnéticos")

Para identificar os minerais magnéticos portadores das direções de magnetização nas rochas é preciso fazer experimentos de desmagnetização, estudar as propriedades magnéticas da rocha e analisar lâminas petrográficas. Este procedimento é importante para os resultados paleomagnéticos, porque quando associados às suas origens, se magmáticas ou pós-magmáticas, estes minerais podem indicar as idades relativas das magnetizações presentes na rocha.

Os minerais magnéticos podem ser identificados por meio de curvas termomagnéticas que fornecem a temperatura Curie e/ou de Néel dos mesmos, curvas de aquisição de magnetização remanescente isotérmica (MRI) e curvas de histerese. É importante conhecer as características dos portadores magnéticos dos espécimes, visto que minerais associados com intemperismo ou metamorfismo, por exemplo, são portadores de magnetização secundária, que, muitas vezes, apresenta estabilidade magnética igual à da magnetização primária (Tarling & Hrouda, 1983).

2.4 Magnetização Remanente Natural (MRN)

O magnetismo natural presente nas rochas é chamado de magnetização remanente natural (MRN), o qual pode ser entendido como a soma das magnetizações remanentes adquiridas (primárias ou secundárias) ao longo do tempo por diferentes processos naturais.

A magnetização remanente primária (MRP) é aquela adquirida durante sua formação. A magnetização primária adquirida por rochas ígneas durante sua formação é a magnetização termoremanente. Em rochas sedimentares a MRP é representada pela magnetização remanente detrítica, adquirida durante a deposição dos sedimentos. Qualquer magnetização adquirida posteriormente a formação de uma rocha é chamada de magnetização remanente secundária (MRS) e pode ser adicionada por diversos processos físicos e químicos ao longo do tempo geológico. Por exemplo, a MRN de uma lava vulcânica pode conter magnetização termoremanente (MTR) primária, magnetização secundária adquirida durante um metamorfismo de baixo grau (magnetização remanente química) e magnetização remanente viscosa adquirida do campo geomagnético atual.

2.5 Testes de campo da estabilidade de magnetização

Em diversos casos a análise petrográfica e das propriedades magnéticas das rochas podem trazer indícios importantes sobre a origem da magnetização presente nas rochas. Entretanto, alguns testes de campo podem ser o melhor método de verificar a estabilidade da magnetização remanente ao longo do tempo geológico.

Nem sempre é possível empregar testes de campo nos estudos paleomagnéticos, pois dependem de situações geológicas específicas. Os testes de campo mais comumente usados são: do conglomerado, da dobra, do contato cozido e o de reversão (Tauxe, 2002, 2009).

2.6 Determinação das Componentes Características de Magnetização

Nas investigações paleomagnéticas um dos maiores desafios é identificar e separar as componentes magnéticas presentes nas rochas. A componente de magnetização mais estável (com coercividades e/ou temperaturas de bloqueio mais altas) que é observada na maioria das amostras analisadas chama-se magnetização remanescente característica (MRC). Para analisar a composição vetorial da MRN e separar as componentes magnéticas, principalmente a MRC, é necessário a realização de processos de desmagnetização por etapas sucessivas, em campos magnéticos alternados (CA) ou desmagnetização térmica.

A desmagnetização CA consiste em submeter a amostra a um campo magnético alternado, de intensidade H_{CA}, que possui forma de onda senoidal e decresce com o tempo. Esse processo é repetido diversas vezes com valores de H_{CA} cada vez maiores. Ao final de cada etapa de desmagnetização, é realizada uma medida da magnetização remanente da amostra. Deste modo, os grãos magnéticos com coercividades menores ou iguais a H_{CA} são sucessivamente reorientados na direção do campo magnético alternado aplicado, fazendo com que a magnetização total associada a estes grãos seja nula. Assim, o resultado é a desmagnetização eficaz de todos os grãos magnéticos com coercividade menor que o pico do campo magnético aplicado, ou seja, tais grãos não contribuem mais para a medida da magnetização da amostra (Tarling & Hrouda, 1983). Geralmente, a desmagnetização por campos magnéticos alternados é bastante eficiente em eliminar componentes de magnetização secundárias e isolar a magnetização característica em rochas ígneas, onde predomina como principal mineral portador magnético a titanomagnetita. Já em rochas contendo minerais magnéticos com coercividades muito altas (p.ex. hematita) o tratamento térmico mostra-se mais eficaz.

Na desmagnetização térmica a amostra é submetida a ciclos de aquecimento e resfriamento sempre na ausência de campo magnético. Assim, todos os grãos portadores de

magnetismo com temperaturas de bloqueio menores ou iguais à temperatura utilizada no aquecimento serão termicamente afetados produzindo magnetização total nula. Um dos problemas desta técnica é o surgimento de alterações termoquímicas dos minerais presentes na rocha, em altas temperaturas, resultando na produção de novas fases minerais. Para monitorar essas possíveis mudanças, em cada etapa de aquecimento é medida a susceptibilidade magnética da amostra, pois qualquer mudança na susceptibilidade indica alteração (destruição e criação) de minerais magnéticos.

2.7 Polo paleomagnético

Para o paleomagnetismo, o campo geomagnético pode ser representado pelo campo de um dipolo geocêntrico e axial. Sendo assim, quando se obtém a média de magnetização remanente para um conjunto de sítios, ela deve representar a direção média do campo geomagnético na época em que as rochas adquiriram suas magnetizações.

O polo geomagnético determinado para cada direção média por sitio é denominado de Pólo Geomagnético Virtual (PGV) (Tauxe, 2002, 2009). A média dos PGVs determinada para cada sítio amostrado representa o pólo paleomagnético para a formação em estudo e, se a variação do campo geomagnético foi eliminada, ele deve coincidir com o pólo geográfico.

A posição de um polo magnético *(λp, φp)* é calculada a partir de uma direção média do campo magnético *(I_m, D_m)* em uma localidade particular *(λs, φs)* utilizando o modelo do dipolo axial geocêntrico e relações trigonométricas (Fig. 8).

Para se obter a latitude do pólo (λp) é preciso usar a relação: $\lambda p = sen^{-1}(sen\lambda s \cdot cos\ p + cos\lambda s \cdot sen\ p \cdot cos\ D_m)$, onde $p = tan^{-1}(\frac{2}{\tan Im})$.

Existem duas possibilidades para a longitude do pólo. Para $\cos p \geq sen\ \lambda s \cdot sen\ \lambda p$, $\theta p = \theta s + \beta$, mas, se $cos\ p < sen\ \lambda s \cdot sen\lambda p$, então, $\theta p = \theta s + 180° - \beta$.

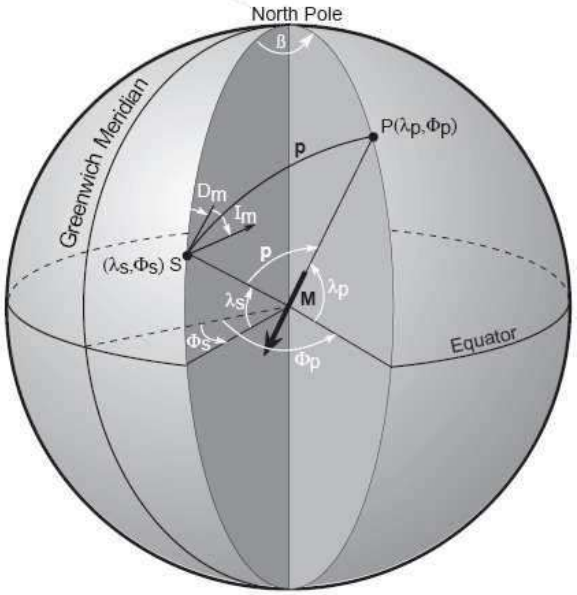

Figura 8. *Localização do Pólo Paleomagnético P (λp, φp), com declinação média (Dm) e inclinação média (Im) calculada para uma formação geológica (extraído de Butler, 1992).*

Em reconstruções continentais confiáveis ou na definição de curvas de deriva polar aparente são usados paleopólos que passam por critérios de qualidade. Estes paleopólos são denominados de pólos paleomagnéticos de referência (Buchan *et al*., 2000). Os critérios básicos que um pólo paleomagnético de referência deve atender são relacionados à qualidade da datação (idade do paleopólo) e dos paleopólos. Van der Voo (1990) estabeleceu alguns critérios de confiabilidade (7) para qualificar pólos paleomagnéticos, os quais vêm sendo utilizados com frequência na literatura para a classificação de pólos paleomagnéticos. De maneira geral, quanto maior é o número de critérios satisfeitos, mais confiável será o polo paleomagnético a ser usado nas reconstruções paleogeográficas.

Critérios de confiabilidade (Van der Voo, 1990):

i. A idade da unidade estudada deve apresentar erro inferior a ± 4%. Além disso, deve-se demonstrar que esta idade equivale à idade de aquisição da magnetização remanente;

ii. Apresentar parâmetros estatísticos satisfatórios: número de amostras (N) superior a 24, parâmetro K maior que 10,0 e α_{95} inferior a 16°;

iii. Apresentar desmagnetização adequada: a magnetização remanente característica deve ser obtida por meio da subtração de componentes secundárias em diagramas vetoriais.

iv. Apresentar testes de campo (testes da dobra, do contato cozido ou do conglomerado) positivos e estatisticamente significativos, que confirmem o caráter primário da magnetização;

v. Apresentar controle estrutural e tectônico coerentes para a unidade estudada;

vi. Presença de reversões, indicando intervalo de tempo significativo durante a aquisição da remanência.

vii. O paleopólo obtido não deve coincidir com a posição de polos paleomagnéticos mais jovens.

2.8 Reconstruções paleogeográficas

A maneira mais usual de sintetizar os resultados de estudos paleomagnéticos é determinar a posição de um polo paleomagnético a partir de um conjunto de PGVs. Nesse sentido e de acordo com o modelo do dipolo geocêntrico axial, os pólos paleomagnéticos de unidades geológicas com idades mais recentes estão agrupados próximos ao pólo geográfico. Em contrapartida, quando pólos paleomagnéticos são calculados para rochas mais antigas de um continente, eles situam-se, geralmente, distantes do pólo geográfico. Se o modelo de dipolo geocêntrico axial é válido para rochas de todas as idades e o pólo geográfico não mudou de posição no tempo geológico, conclui-se então, que é o continente que se move em relação ao pólo geográfico.

Diante dessa hipótese, pólos paleomagnéticos podem ser usados para determinar a paleogeografia dos continentes no passado. A reconstrução paleogeográfica pode ser feita por meio da rotação do pólo paleomagnético fazendo-o coincidir com o pólo geográfico, realizando a mesma rotação para o continente. Além disto, utilizar a média da direção obtida para a formação em estudo pode também determinar a posição antiga do continente.

Nesta reconstrução, a declinação média (Dm) representa a rotação do corpo em torno do sitio de amostragem, enquanto que a paleolatitude, determinada por meio da inclinação média (Im) ($\tan \mathrm{I} = 2 \tan \lambda$), define a latitude do sítio de amostragem na época em que a rocha adquiriu sua magnetização remanente. A paleolongitude do continente é indeterminada devido à simetria do campo de dipolo geocêntrico axial.

A ambiguidade na polaridade e a indefinição na paleolongitude dificultam a perfeita reconstrução paleogeográfica dos vários blocos continentais. Assim, tentativas podem ser feitas para melhorar e aproximar as reconstruções paleogeográficas analisando possíveis similaridades geológicas e estruturais (p.ex., cinturões orogênicos, lineamentos tectônicos, enxames de diques, províncias magmáticas, províncias geotectônicas/geocronológicas, etc.).

2.9 Paleogeografia em rochas arqueanas

Em épocas mais antigas na história da Terra (p.ex., pré-Columbia) é ainda mais complicado definir a paleogeografia crustal, visto que, alguns blocos continentais da Terra ainda estavam se formando nesse período, como é o caso da Laurentia, Báltica e Cráton Amazônico, fazendo com que paleogeografias construídas para essa época sejam muito mais especulativas.

Nesse sentido o paleomagnetismo pode ajudar nesta tarefa, pois representa a única ferramenta que pode estabelecer a paleolatitude e a paleorientação de blocos continentais.

Entretanto, algumas dificuldades são inerentes, pois a maioria dos dados paleomagnéticos para este intervalo de tempo (Arqueano-Paleoproterozóico) são de baixa qualidade e/ou possuem baixa precisão na idade geocronológica. Assim, poucos pólos paleomagnéticos podem ser considerados como de referência e curvas de deriva polar aparente das várias unidades cratônicas existentes nessa época são mais difíceis de serem definidas.

A existência de um supercontinente durante o Arqueano (~2.70 Ga), conhecido como *Kenorland* (Fig. 9A), foi sugerida por diversos autores (p.ex., Evans *et al*., 2016; Meert, 2014). Entretanto, os dados paleomagnéticos existentes não corroboram a ideia de um único supercontinente. Um modelo alternativo foi proposto, em que se acredita que durante este intervalo de tempo, existiam vários supercrátons dispersos ao redor da Terra (Fig. 9B; 9C): i) Superia que seria um supercráton formado pelo bloco Superior-Hearne-Wyoming (Laurentia) associado ao bloco Karelia-Kola (Baltica) (Bleeker, 2003); ii) Sclavia (também conhecido como Nunavutia) associado com o "*Slave clan*", um conjunto de crátons que inclui o "*Slave craton*" (Bleeker, 2003); iii) Crátons Kaapvaal (África) e Pilbara (Austrália) fazendo parte do supercráton Vaalbara (Zegers *et al., 1998;* de Kock *et al., 2009);* iv) Supercráton Zimgarn formado pelos crátons de Zimbabwe (África) e Yilgarn (Austrália) (Smirnov *et al*., 2013).

Importantes trabalhos têm sido publicados no mundo todo utilizando dados paleomagnéticos, mesmo em períodos mais antigos (p.ex., Biggin *et al*., 2011; de Kock *et al*., 2009; Denyszyn *et al*., 2013; Kumar *et al*., 2017). No entanto, as interpretações e implicações dos estudos paleomagnéticos na reconstrução desses terrenos devem ser feitas de maneira criteriosa e, desta forma, podem fornecer dados valiosos no entendimento da formação dos continentes e até mesmo da tectônica da Terra primitiva.

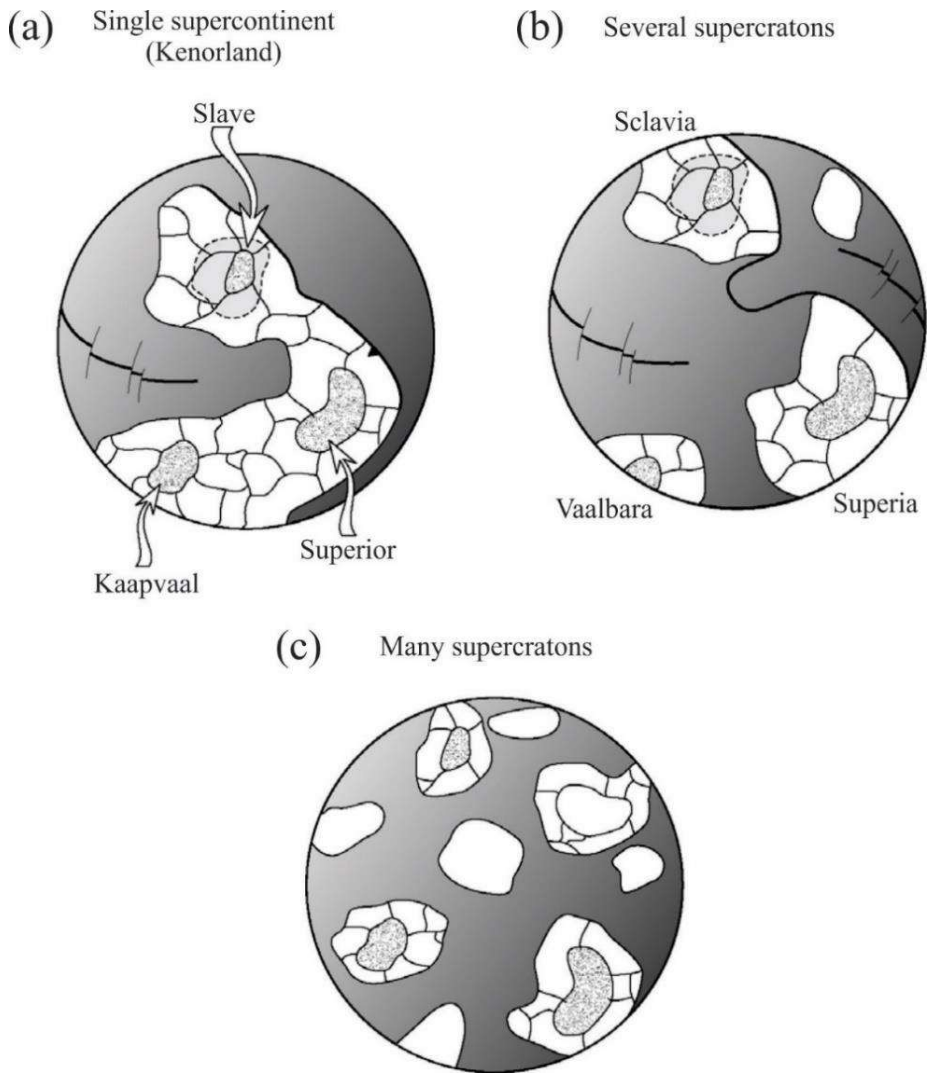

Figura 9. *Propostas para a organizações dos blocos continentais durante o Arqueano (Modificado de Bleeker, 2003).* ***A)*** *Único supercontinente, conhecido como Kenorland;* ***B)*** *e* ***C)*** *Vários supercrátons dispersos.*

CAPÍTULO 3 – FUNDAMENTAÇÃO TEÓRICA II: FORMAÇÕES FERRÍFERAS (SÍNTESE): DESCRIÇÃO, CLASSIFICAÇÃO E GÊNESE

3. FORMAÇÕES FERRÍFERAS (SÍNTESE): DESCRIÇÃO, CLASSIFICAÇÃO E GÊNESE

Depósitos gigantes de ferro, derivados de formações ferríferas bandadas, estão entre os maiores depósitos minerais conhecidos. Além da sua imensa importância econômica (p.ex., principal fonte de ferro para a indústria siderúrgica mundial), o estudo de sua gênese tem implicações fundamentais para compreensão da evolução da atmosfera, hidrosfera e biosfera terrestre (Konhauser *et al*., 2017).

O presente capítulo abordará revisão bibliográfica contendo: (i) breve descrição, classificação e distribuição no tempo geológico das formações ferríferas; e (ii) síntese sobre conhecimento atual da gênese das formações ferríferas, que inclui os tipos mais comuns no período entre o Arqueano-Paleoproterozóico (tipo Superior e Algoma).

3.1 Definição e principais características

Formações Ferríferas (*Iron Formations – IFs*) são rochas sedimentares químicas ricas em ferro (15-40 wt% Fe) e sílica (40–60 wt% SiO_2) que precipitaram da água do mar durante o Éon Pré-cambriano, sendo que a maior concentração deste tipo de deposição situa-se no Neoarqueano e Paleoproterozóico (entre 2.80 e 1.85 Ga; Fig. 10). Com base no seu ambiente deposicional e tipos de rochas associadas, *IFs* são subdivididas em tipo Superior (*Superior-type*) ou Algoma (*Algoma-type*) (Gross, 1980), embora seja mais prático considerar essas classificações como membros finais em um espectro de variedades intermediárias (Bekker *et al*., 2012). Formações ferríferas neoproterozóicas (~0.715 Ga), conhecidas como do tipo Rapitan (*Rapitan-type*), estão associadas a depósitos glaciais (Gross, 1983).

Texturalmente, as formações ferríferas são divididas em dois grupos – *BIF* (maioria) e *GIF*. *Banded iron formation (BIFs)* são rochas bandadas/laminadas, constituídas por bandas alternadas de *chert*/jaspe e óxidos de ferro (hematita e magnetita), e foram, em geral,

depositadas em ambientes de águas relativamente profundas, abaixo do nível de base de onda ou tempestade. Já as g*ranular iron formations (GIFs)* não apresentam bandamento e são constituídas por grânulos de *chert*, óxidos de ferro e silicatos, com cimento, formado por *chert*, carbonato ou hematita, preenchendo os poros. Considera-se que os *GIFs* foram depositados em águas rasas, produto do retrabalhamento de formações ferríferas bandadas.

As formações ferríferas mais antigas datam por volta de 3,7 Ga, no entanto a grande maioria se depositou entre 2,8 Ga e 1,5 Ga, refletindo as mudanças evolutivas nos mares e à emergência de oxigênio na atmosfera terrestre (Fig. 10). Em geral, formações ferríferas mais antigas que 3.0 Ga são descritas como do tipo Algoma, ainda que ocorram algumas ocorrências de ferro com essa classificação de idade entre 2,7 e 2,6 (Konhauser *et al*., 2017). A maioria das formações ferríferas depositadas entre 2,3 e 0,6 são granulares (*GIF*), enquanto aquelas com 2,5 Ga ou mais são geralmente bandadas (*BIF*). As formações ferríferas do tipo Rapitan possuem pico de deposição por volta de 850 Ma e 630 Ma, e estão relacionadas principalmente as mudanças climáticas ocorridas no final do Neoproterozóico (Konhauser *et al.,* 2017).

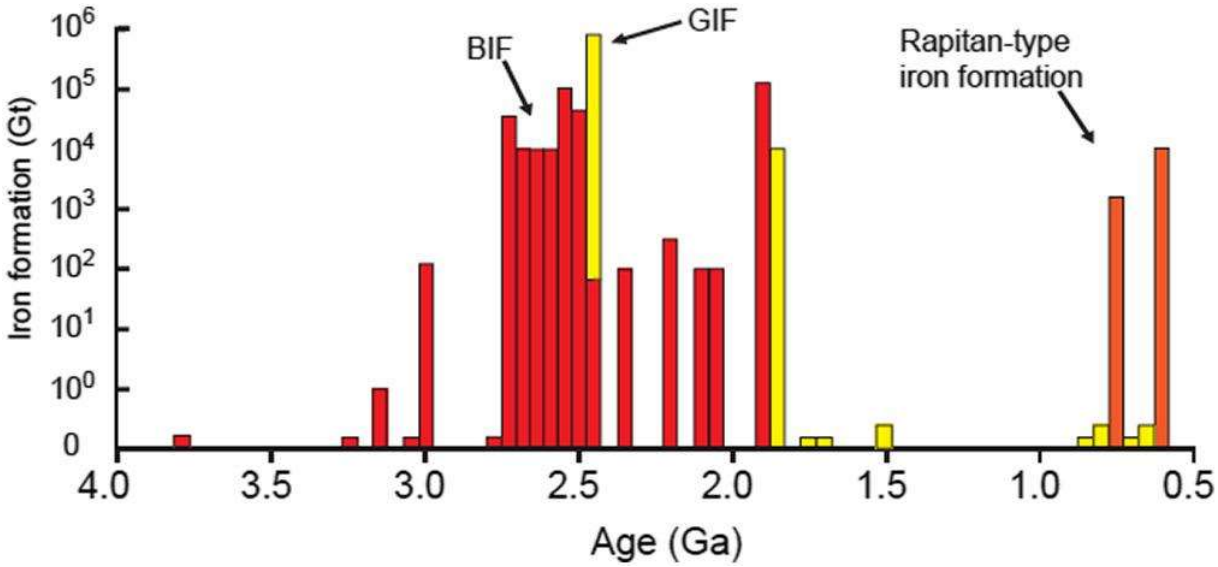

Figura 10. *Distribuição de formações ferríferas em bilhões de toneladas pelo tempo geológico, com cada coluna correspondendo ao período de 50 milhões de anos (modificado de Bekker et al., 2010).*

Maioria dos depósitos mais antigos que 2,4 Ga compreendem a formações ferríferas bandadas. Entre 2,3 Ga e 0,8 Ga predominam as formações ferríferas granulares. Os depósitos Neoproterozóicos (~0,75 Ga) são do tipo Rapitan, e estão associados a depósitos sedimentares glaciais. Figura extraída de Konhauser et al. (2017).

3.2 Gênese das Formações ferríferas

A origem das formações ferríferas exige que grandes quantidades de Fe estejam em solução como espécie reduzida (Fe^{2+}), que é então oxidado (Fe^{3+}) e precipitado como óxidos e carbonatos de ferro. Entretanto, a inexistência de ambientes modernos de deposição de formações ferríferas dificulta a formulação de modelos genéticos, de tal forma que não há consenso sobre os mecanismos de precipitação, gênese do bandamento, influência de processos biológicos, assim como a respeito da procedência do suprimento de ferro.

3.2.1 Fontes hidrotermais de ferro para os oceanos

Para a fonte do ferro, duas possibilidades são consideradas: origem continental por meio da lixiviação de rochas ricas em ferro; ou origem hidrotermal marinha profunda, onde o Fe é introduzido por descargas hidrotermais subaquosas, em mar profundo. Em ambas as teorias, há a necessidade de um sistema de densidade estratificado, em que correntes de ressurgência trazem o ferro reduzido de águas anóxicas mais profundas para um ambiente oxigenado em águas mais rasas, como em uma plataforma continental, onde o Fe^{2+} é oxidado e precipitado como óxidos e carbonatos.

Os primeiros estudos sugeriram que o Fe seria derivado da lixiviação de rochas ricas em ferro (e.g. basaltos continentais), onde o Fe^{2+} se tornaria móvel na ausência de O^2 na atmosfera. A ideia de que os primeiros continentes eram formados por grande quantidade de rochas máficas e, portanto, ricos em ferro favorecia tal ideia. No entanto, estudos detalhados realizados na Província de Hamersley, Austrália, identificaram que a quantidade de ferro depositado era

da ordem de 1 x 10^{13} g/ano (Trendall & Blockley, 1970), exigindo rios do tamanho ou maiores que o rio Amazonas para transportar tal quantidade de ferro. Além disso, a ausência de contribuição detrítica significativa na deposição das formações ferríferas argumenta contra a possibilidade de que o Fe fosse transportado pelos rios.

A ideia de fonte hidrotermal de ferro para os oceanos se firmou com a descoberta dos sistemas hidrotermais modernos de fundo oceânico, onde foi possível observar um alto fluxo de ferro dissolvido derivado do espalhamento lento do assoalho oceânico (*slow-spreading mid-ocean ridges*), e da constatação de que mesmo os sistemas hidrotermais modernos podem contribuir com 75% da quantidade de Fe dissolvido nos oceanos modernos. Além disso, foi demonstrado que, mesmo em oceanos modernos, partículas de ferro e ferro dissolvido podem ser transportados por mais de 2000 km a partir do eixo de espalhamento (*ridge axis*) nos sistemas hidrotermais do assoalho oceânico, e essa variabilidade no sistema de entrada e mistura com a água dos oceanos tem influenciado a extensão do transporte de ferro mesmo em um passado recente (Konhauser et al., 2017). De maneira similar, também foi proposto que o ferro dissolvido poderia ter sido fornecido diretamente por plumas hidrotermais aos níveis mais altos da coluna de água. As regiões de abertura do assoalho (*ridge crests)* no arqueano eram provavelmente mais rasas que atualmente, refletindo temperaturas mais altas do manto e, sob tais condições, o material hidrotermal efluente, rico em ferro, poderia ter subido através da coluna de água até a zona fótica, onde o Fe^{2+} poderia ter sido oxidado e precipitado como óxidos e carbonatos. Embora as concentrações (1-3 nM) de entrada de Fe^{2+} de origem hidrotermal em oceanos modernos estejam significativamente abaixo do que seria necessário para formar um *IF*, esse sistema fornece evidências de que o transporte de ferro a longo prazo e a formação de *IF* do tipo Superior são mecanicamente possíveis. As condições menos oxidantes, como as previstas para o Arqueano e o Paleoproterozóico, favorecem o transporte de Fe^{2+} dissolvido por

distâncias ainda maiores do que as observadas hoje. Além disso, as temperaturas mais elevadas das reações água-rocha observadas no Arqueano e a baixa concentração de sulfato marinho (o qual afeta o Eh dos fluidos hidrotermais, limitando a precipitação de sulfato de ferro) sugerem que a quantidade de Fe^{2+} dissolvido nos efluentes hidrotermais foi muito maior do que atualmente.

Elementos terras raras e ítrio (*REE+Y*) em fluidos hidrotermais apresentam distribuições características que corroboram a ideia de fonte hidrotermal de Fe^{2+} para as formações ferríferas. Os oceanos modernos, bem como as *IFs* pós-arqueanas, geralmente, exibem enriquecimento em terras raras pesados (*HREE*), anomalias positivas de La, Gd e Y e anomalias negativas acentuadas de Ce quando normalizadas para o *PAAS* (*post-Archaean average shale*). Entretanto, as formações ferríferas arqueanas (>2.5 Ga) também exibem anomalias positivas La, Gd e Y, mas não apresentam anomalias negativas de Ce e, em vez disso, apresentam anomalias positivas de Eu.

As anomalias do európio em padrões de *REE + Y* têm sido fundamentais no rastreamento de fontes de Fe. O enriquecimento do európio em rochas sedimentares químicas que precipitaram a partir da água do mar, indica uma forte influência de fluídos hidrotermais de alta temperatura na água do mar. A anomalia positiva de Eu observada em fluidos hidrotermais está ligada a quebra do plagioclásio presente nas rochas vulcânicas subjacentes às fissuras por onde estes fluidos saem (*hydrothermal vents*), uma vez que o plagioclásio durante a sua cristalização é enriquecido em Eu em relação aos outros *REE +Y.* Ademais, o Eu permanece solúvel na forma de Eu^{2+} nos fluidos hidrotermais, devido a forma Eu^{2+} ser mais estável em temperaturas mais altas. Presume-se que o Fe e os REE + Y não são fraccionados durante o transporte a partir dos *spreading ridges* ou outros centros exalativos, devido à alta capacidade de sorção (adsorção e absorção) dos hidróxidos de Fe^{3+}, ou seja, uma anomalia de

európio muito acentuada (>2) indica que o Fe presente na rocha sedimentar química foi derivado de origem hidrotermal. Alguns *trends* ao longo do tempo da magnitude da anomalia de Eu observada nas formações ferríferas do tipo Superior (*Superior-type*) foram usadas para identificar variações no fluxo hidrotermal. O tamanho das anomalias positivas de Eu diminui de forma constante a partir do Arqueano, o que pode ser explicado tanto pelo aumento na entrada de fluidos hidrotermais e/ou pela baixa quantidade de oxigênio dissolvido, oxigênio este necessário para estabilizar Eu^{2+} para o transporte nos oceanos antes de se tornarem oxigenados. Há um pico muito alto entre 2.7 e 2.5 Ga, provavelmente, relacionado a uma grande entrada de fluidos ricos em ferro de origem hidrotermal (Fig. 11).

Portanto, o consenso atual é que o ferro foi introduzido no oceano a partir de fontes hidrotermais, seguido pela deposição de formações ferríferas na plataforma continental e talude superior, em uma coluna de água estratificada óxido-anóxico. Um fato interessante e também de consenso geral, que a deposição dos grandes depósitos de *IF* tem relação com grandes eventos de geração de magma, ligados as grandes províncias ígneas (*LIPs*).

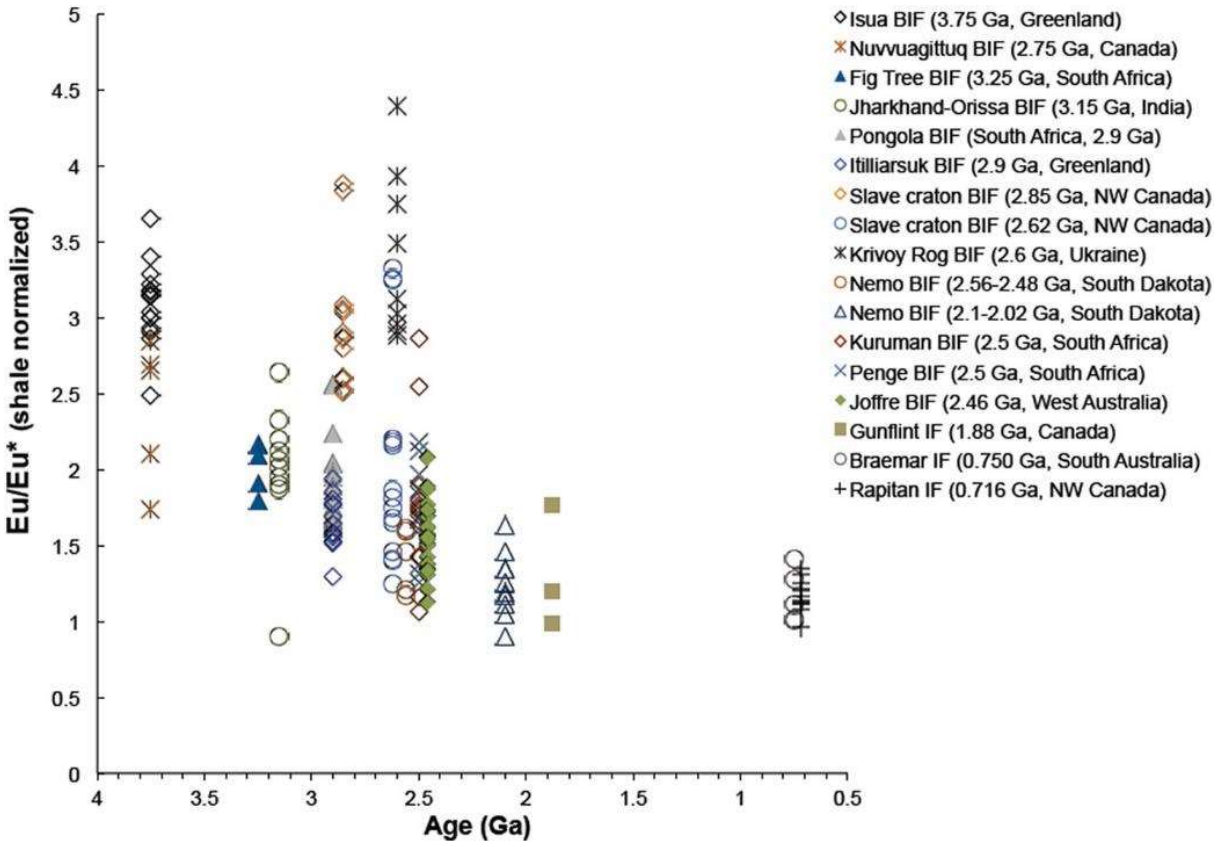

Figura 11. *Anomalia de Eu (Eu/Eu*) normalizado segundo PAAS (McLennan, 1989) pela idade de algumas das mais importantes formações ferríferas. Dados de Isua de Frei & Polat (2007); Nuvvuagittuq de Mloszewska et al. (2012, 2013); Fig Tree de Derry & Jacobsen (1990) e Hofmann (2005); Jharkhand-Orissa de Bhattacharya et al. (2007); Pongola de Alexander et al. (2008); Itilliarsuk de Haugaard et al. (2013); Slave Craton de Haugaard et al. (2016a, 2017); Krivoy Rog de Viehmann et al. (2015); Joffre de Haugaard et al. (2016b). Kuruman de Bau & Dulski (1996); Nemo de Frei et al. (2008); Gunflint de Danielson et al. (1992); Braemar de Lottermoser & Ashley (2000); Rapitan de Halverson et al. (2011). Figura extraída de Konhauser et al., 2017.*

3.2.2 Fontes continentais de ferro para os oceanos

Compilações de dados isotópicos de Nd das formações ferríferas arqueanas até as paleoproterozóicas demonstram que a maioria das *IFs* têm valores de εNd (t) intermediários entre os do manto empobrecido (*depleted mantle*) e a crosta continental antiga (*older continental crust*). Supondo que as fontes de REE + Y acompanham as fontes de Fe^{2+}, os dados

de isótopos de Nd nessas formações ferríferas sugerem uma contribuição significativa de ferro de origem continental. Em diversas formações ferríferas dessa idade, por exemplo as relacionadas a bacia de Hamersley, os dados isotópicos de Nd indicam que as *IFs* contêm uma mistura de Nd derivado de fonte hidrotermal e continental, ou seja, o ferro possui uma origem híbrida, continental e hidrotermal.

3.2.3 Fatores oxidantes na água do mar para oxidação do Fe^{2+}

Embora os mecanismos predominantes permaneçam incertos, a mineralogia encontrada e as composições isotópicas de Fe nas formações ferríferas demonstram que alguma oxidação do Fe^{2+} foi necessária para ocorrer a precipitação química. No início da terra primitiva, antes do aumento do oxigênio atmosférico e do desenvolvimento da camada de ozônio, a superfície terrestre era alvo de altos índices de radiação ultravioleta. Nesta mesma época, as águas dos oceanos eram anóxicas e "guardavam" altas concentrações de Fe^{2+} dissolvido. Sob estas condições, o ferro ferroso (Fe^{2+}) ou $Fe(OH)^{+}$ absorve radiação na faixa de 200-400 nm, levando a formação fotoquímica de ferro férrico dissolvido [reação 1], que por sua vez, se hidrolisa para formar óxi-hidróxidos de Fe^{3+}.

$2Fe^{2+}_{(aq)} + 2H^{+} + hv \rightarrow 2Fe^{3+}_{(aq)} + H_2$, onde hv representa a radiação ultravioleta. **(1)**

No entanto, diversos estudos demonstram que mesmo que seja possível que a fotoxidação por radiação ultravioleta (UV) tenha contribuído para a precipitação das *IFs*, parece improvável que este mecanismo tenha sido o principal mecanismo gerador de Fe^{3+} para a deposição dos grandes depósitos de formações ferríferas.

Como alternativa ao modelo abiótico, a oxidação do Fe^{2+} foi atribuída à atividade metabólica das bactérias em zonas fóticas oceânicas (Fig. 12). Embora tenha sido sugerido um papel biológico na precipitação dos óxi-hidróxidos de Fe^{3+} cerca de um século atrás (p.ex.,

Leith, 1903; Gruner, 1922), a importância das bactérias neste processo começou a receber maior aceitação com a descoberta de microfósseis nas formações ferríferas paleoproterozóicas (ca. 1.88 Ga) da Bacia Animikie, região do Lago Superior. Baseando-se no pressuposto de que os microfósseis eram cianobactérias, ou seus predecessores, Cloud (1973) propunha que essas bactérias fotossintetizadoras, produtoras primitivas de O_2, possuíam enzimas mediadoras de oxigênio adequadamente avançadas e, consequentemente, requeriam Fe^{2+} para a produção de oxigênio. Portanto, esses microrganismos teriam crescidos quando havia a disponibilidade de Fe^{2+} (e outros nutrientes), permitindo a oxidação indireta e precipitação de óxi-hidróxidos de Fe^{3+} e, em contrapartida, a população dos microrganismos teria diminuído quando a disponibilidade de Fe^{2+} era limitada.

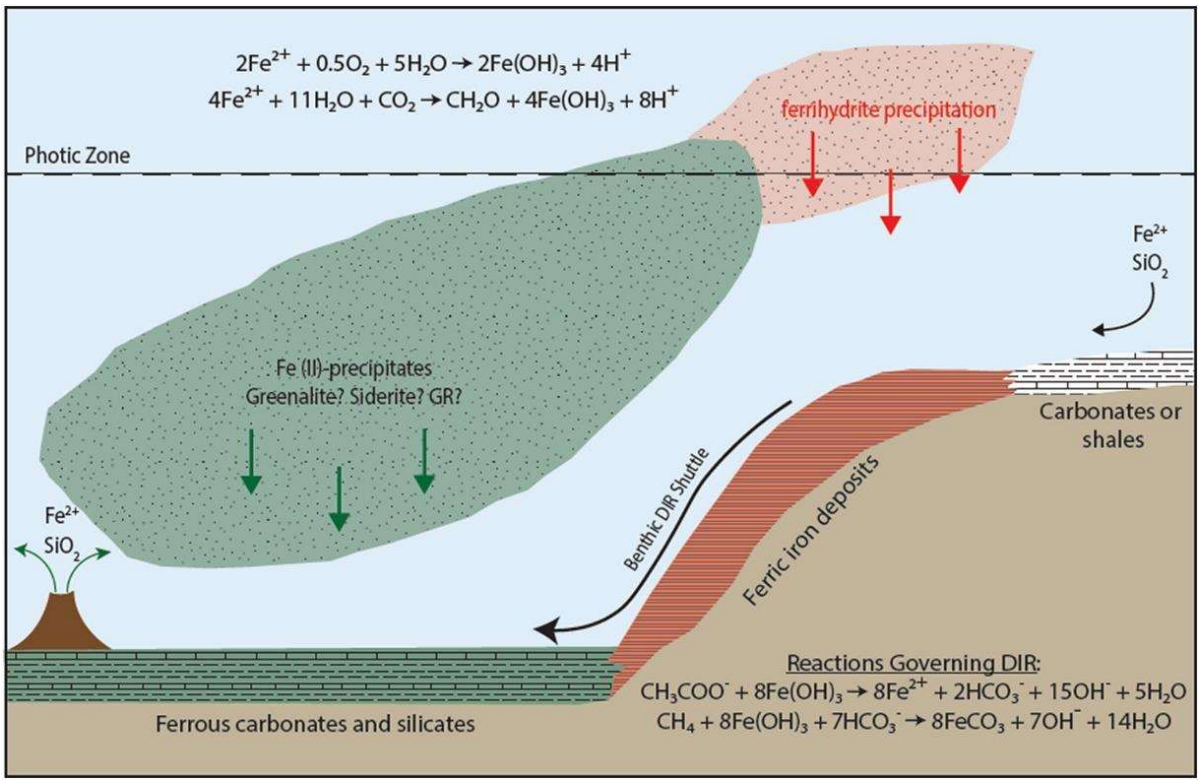

Figura 12. *Mecanismos de oxidação de Fe(II) em oceanos Pré-cambrianos. Dois mecanismos biologicamente controlados são previstos: (1) reação da cyanobactéria gerando 0_2 dissolvido com Fe(II), e/ou (2) oxidação direta via fotossíntese anaeróbica (fotoferrotrofia). O Fe(II) é proveniente*

tanto de sistemas hidrotermais de água profundas, como do intemperismo continental, enquanto que o Fe(III) é formado na zona fótica e precipitado como hidrato de ferro, $Fe(OH)_3$, e depositado no assoalho oceânico como precursor das formações ferríferas. Alguns hidratos de ferro são reduzidos através redução direta bacteriana (DIR) de Fe(III), utilizando carbono orgânico ou por meio de um potencial de redução metabólico pelo acoplamento de Fe(III) e oxidação de metano. Figura extraída de Konhauser et al. (2017).

3.2.4 Formações Ferríferas Neoproterozóicas

O ressurgimento de formações ferríferas após quase um hiato de 1 bilhão de anos no registro sedimentar representa um retorno as condições anóxicas e ferruginosas nos oceanos, o que é constantemente relacionado às mudanças climáticas extremas ocorridas no Neoproterozóico (Isley & Abbott, 1999; Klein, 2005). Ao contrário das ocorrências de ferro do Paleoproterozóico e do Arqueano, as formações ferríferas neoproterozóicas (*neoproterozoic iron formation – NIF*) teriam se desenvolvido num período em que a atmosfera já continha níveis elevados de O_2 e estão associadas à depósitos sedimentares glaciais (Klein & Beukes, 1993; Hoffman *et al*., 1998).

3.3 Considerações finais

Nas últimas décadas foi possível avançar significantemente em nosso entendimento sobre a gênese das formações ferríferas. Alguns desses avanços veio por meio da revisão da importância e comportamento das reações microbiais metabólicas na deposição e diagênese das formações ferríferas, gerando uma compreensão melhor sobre o ciclo microbial do Fe. Outros avanços, como esperado, vieram da aplicação de estudos isotópicos mais aprofundados (p.ex., isótopos de Fe, Cr, U, Mo, Cu), aplicado tanto em rocha total quanto *in situ,* que permitem correlacionar tais isótopos dentro da paragênese mineral. Com estas novas descobertas e avanços, existe aceitação generalizada que a oxidação de Fe^{2+} microbial exerceu papel

fundamental na deposição de muitos depósitos de formações ferríferas. Também é claro que a deposição das formações ferríferas não representaria uma sedimentação marinha muito profunda e que um forte fluxo hidrotermal de ferro junto com alguma entrada de ferro a partir da erosão de sedimentos epiclásticos seriam as principais fontes de ferro para a posterior deposição das formações ferríferas.

CAPÍTULO 4 – ARTIGO I: *LOW PALEOLATITUDE OF THE CARAJÁS BASIN AT ~2.75 GA: PALEOMAGNETIC EVIDENCE FROM BASALTIC FLOWS IN AMAZONIA.*

Observação

Este capítulo trará o artigo científico submetido ao periódico *Precambrian Research*, intitulado "*Low paleolatitude of the Carajás Basin at ~2.7 Ga: Paleomagnetic evidence for basaltic flows in Amazonia*". Os tópicos foram divididos e resumidos para se adequar a exigência da revista que o trabalho foi submetido. Os anexos citados no artigo foram acrescentados no final do capítulo.

LOW PALEOLATITUDE OF THE CARAJÁS BASIN AT ~2.75 GA: PALEOMAGNETIC EVIDENCE FROM BASALTIC FLOWS IN AMAZONIA.

Pedro L.G. Martins [a,*]*; Catarina L.B. Toledo*[a]*; Adalene M. Silva*[a]*; Paul Y.J. Antonio*[b]*, Farid Chemale Jr*[c]*, Luciano M. Assis*[d]*; Ricardo I.F. Trindade*[b]

[a] Universidade de Brasília, Instituto de Geociências, 70910-900 Brasília, DF, Brazil

[b] Instituto de Astronomia, Geofísica e Ciências Atmosféricas, Universidade de São Paulo, 05508-090 São Paulo, SP, Brazil

[c] Universidade do Vale do Rio dos Sinos, Departamento de Geologia, 93022-000 São Leopoldo, RS, Brazil

[d] Diretoria de Geociências, Planejamento de longo prazo e Uso futuro, Vale S.A., Mina de Águas Claras, Av. Dr. Marco Paulo Simon Jardim, 3580, Nova Lima, MG, Brazil

*Corresponding author. Tel: +55 61 993181098

Email address: plgmartins@gmail.com (P.L.G. Martins)

Abstract

Establishing the positions of continents during the initial stages of Earth's evolution is one of the most important challenges in geosciences today. This challenge is mainly due to the severe limitations on obtaining geological and/or geophysical data from early Earth time, particularly robust paleomagnetic data. Here, we report the first paleomagnetic data from an Archean block in the Amazonian craton, the Carajás Province, for ~2.76–2.74 billion years ago (Ga), when extensive dominantly mafic volcanism (Parauapebas Formation) covered an area of ~18,000 km^2. The paleomagnetic investigation was conducted on fresh drill cores drilled into the Carajás iron ore mine and cutting across the Parauapebas Formation. Two characteristic components, Carajás 1 and 2, were isolate and further used to calculate the mean paleomagnetic pole for

each: C1 (~2759 Ma; 40.5ºE, -44.6ºS A95 =6.5º, K = 18.5) and C2 (~2745 Ma; 342.4ºE, -54.3ºS, A95 = 14.8º, K = 27.8). Our results, integrated with geological evidence reveals that the Carajás block occupied low latitudes at the time, and could have been part of the Supervaalbara supercraton configuration during the Neoarchean (~2.75 Ga) in a position nearest the equatorial line. After rotating the drill core segments to geographic coordinates, a consistent sequence of three magnetic reversal events is identified in the lava flow sequence from the Parauapebas Formation, potentially suggesting an already dynamic geodynamo pre-2.7 Ga.

Keywords: Amazonia; Paleomagnetism; Supervaalbara; Carajás Province.

1. Introduction

The Archean cratons stabilized at different times worldwide from 3.1 to 2.5 Ga, and its peak in craton's heralded the transition from a mafic to a more evolved intermediate composition (Hawkesworth et al., 2020). Also, the Neoarchean to Paleoproterozoic transition (~2.80–2.20 Ga) witnessed several major interlinked environmental and biological evolutionary events, including the increase in atmospheric oxygen as deduced from the disappearance of detrital pyrite and uraninite in conglomerates, the advent of red beds and the deposition of the largest banded iron formations (BIF) in the world (Bekker et al., 2004; Konhauser et al., 2011). Establishing the positions of continents at this time, when the continental configuration is yet poorly known and intensely debated, is one of the most important tasks in deciphering the geological evolution of the planet at its youth. Specifically, two mains' questions concerning the arrangement of late Archean blocks related to their latitudinal distribution and whether they were amalgamated into a single mass of primitive continental crust (e.g., Williams et al., 1991) or if they were dispersed into several smaller supercratons such as Superia, Zimgarn and Vaalbara (e.g., Bleeker, 2003; Smirnov et al., 2013; Liu et al., 2021). This challenge is mainly due to the paucity of high-quality paleomagnetic data, which makes paleogeographic

reconstruction for these times very speculative (Buchan et al. 2000, Pesonen et al. 2003). Nevertheless, this task, particularly during the so-called Archean-Proterozoic transition, is becoming tractable by the increasing numbers of refined paleomagnetic data and geochronologic studies (e.g., Denyszyn et al. 2013; Gumsley, 2017; Gumsley et al., 2017).

South American cratons, such as São Francisco and Amazonia, have been absent from most of the Archean supercraton reconstructions. Recently, Salminen et al. (2019), based on paleomagnetic data and comparison of magmatic barcodes, demonstrated that the Uauá block, a fragment of the São Francisco craton, could have been part of a much larger supercraton named Supervaalbara by Gumsley (2017). Meanwhile, the paleogeography of the Amazonian Craton (Fig. 1A), one of the largest cratonic areas in the world (~5,600,000 km^2; Almeida et al., 1981), remains a challenging task especially during Archean-Paleoproterozoic times, being one of the least studied Archean cratons (D'Agrella-Filho et al., 2016).

Here, we focus on the paleomagnetic record of an Archean block in the Amazonian craton, the Carajás Province (Fig. 1B) for the ~2.76–2.74 Ga interval, when extensive volcanism, dominantly mafic, covered an area of approximately 18,000 km^2 (Macambira, 2003). This volcanism produced the Parauapebas Formation, the lowermost unit of the Neoarchean volcanic-sedimentary sequence of the Grão-Pará Group (Vasquez et al., 2008; Martins et al., 2017). Here, we report new paleomagnetic data for basaltic lava flows from two well-preserved deep drill cores sampled from the Carajás Basin in the northern Carajás Province. Our goal is to provide the first paleogeographic constraints for this Archean block, yielding a paleolatitude estimate for the block and discussing its affiliation to previously proposed Archean cratonic assemblies (e.g., Gumsley et al., 2017; Salminen et al., 2019). Furthermore, the thick sequence of basalts in the Carajás Basin has a good potential to provide evidence for geomagnetic reversals across the succession.

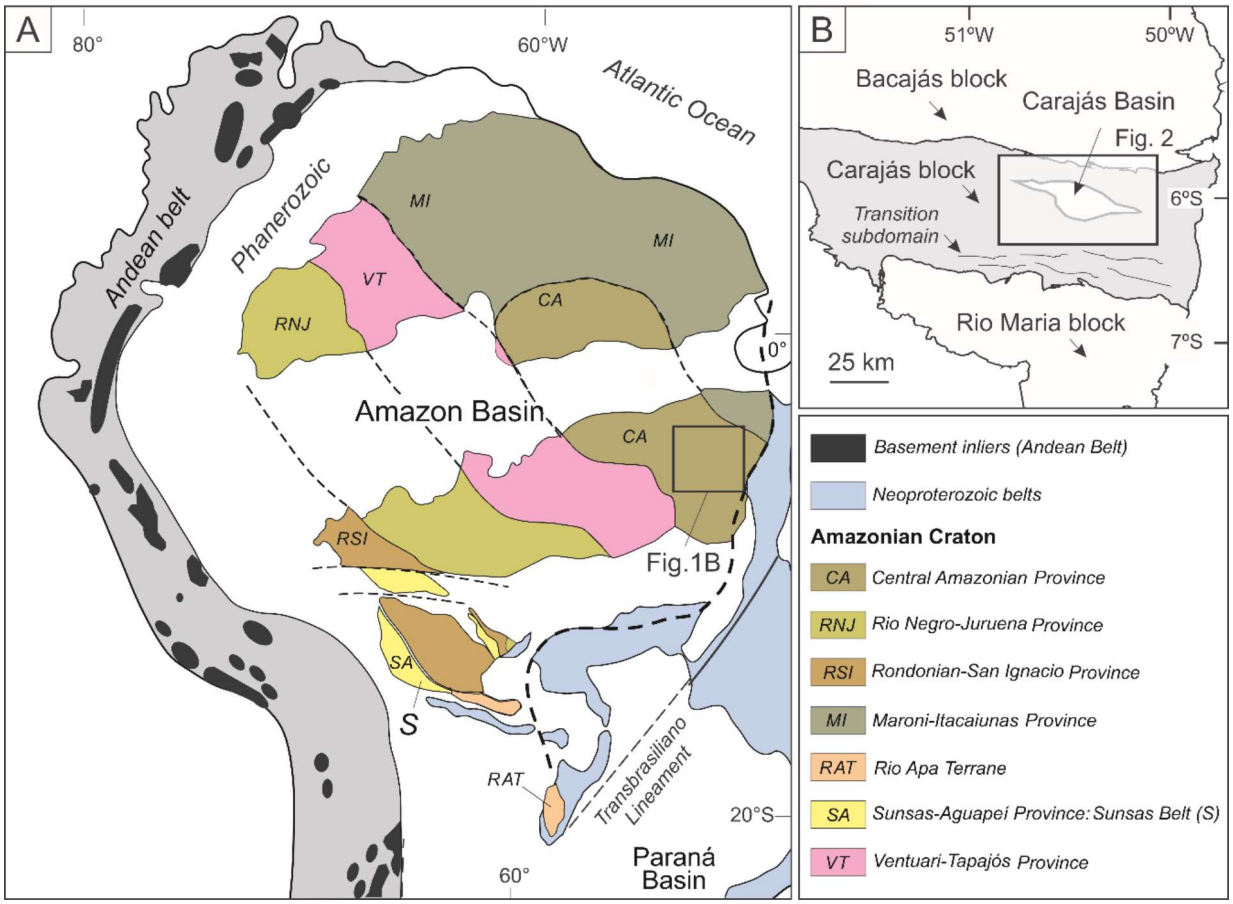

Fig. 1. A) *Amazonian Craton and its geologic/geochronological provinces (adapted from Cordani & Teixeira 2007 and Teixeira et al., 2019);* ***B)*** *Carajás province map showing the location of the Carajás Basin in the Carajás block (from Araújo Filho et al., 2020); the black rectangle indicates the approximate location of Carajás Basin (Fig. 2).*

2. Geological setting

The tectonic framework of the Amazonian Craton essentially consists of one ancient nucleus, the Central Amazonia Province (> 2.60 Ga), and adjacent Paleo- and Mesoproterozoic provinces (see Teixeira et al., 2019 for review). The eastern portion of the Central Amazonia Province (Fig. 1A) is comprised of the Carajás Province, which is renowned for hosting several world-class mineral deposits of Fe and Cu-Au, as well as Mn an Ni mines (Vasquez et al., 2008; Moreto et al., 2015). The Carajás Province is divided in two domains, the northern Carajás and

the southern Rio Maria (Fig. 1B) (Vasquez et al., 2008). A broad E-W striking shear zone (known as "Transition" subdomain), mostly within the Carajás Domain, occurs between the volcano-sedimentary Carajás Basin sequence and rocks of the Rio Maria Domain (Fig. 1B). The Rio Maria Domain is a typical granite-greenstone terrane, mainly composed of tonalite–trondhjemite–granodiorite (TTG) associations, surrounded by greenstone belts, with formation ages between ca. 3.00–2.85 Ga (e.g., Almeida et al., 2011; 2013 and references therein).

Apart from the strongly deformed granitoids and gneissic rocks of the Transition subdomain, the Carajás Domain (Carajás block) is composed essentially of the Carajás Basin (Vasquez et al., 2008; Fig. 1B; 2A), also known as the central sigmoid of Carajás (Holdsworth & Pinheiro, 2000). The basement of the Carajás Basin comprises 2.98–2.86 Ga Mesoarchean granitoids of the Xingu Complex (similar in age and lithological content to the Transitional subdomain; Machado et al., 1991). The main assemblages of the Carajás Basin are of Neoarchean to Paleoproterozoic age and it is commonly segmented into the lowermost volcanic–sedimentary Grão-Pará Group (2.76–2.73 Ga; Fig. 2) overlain by sedimentary rocks of the ca. 2.68–2.06 Ga Serra Sul and Águas Claras formations (Araújo & Nogueira, 2019; Araújo Filho et al., 2020; Rossignol et al., 2020) (Fig. 2).

The Neoarchean Grão-Pará Group (2.76-2.73 Ga) is the main volcano-sedimentary sequence of the Carajás Basin, and is approximately 260 km long and 70 km wide, with its rocks covering an area of approximately 18,000 km^2 (Macambira, 2003; Vasquez et al., 2008; Fig. 2A). For the Grão-Pará Group stratigraphy, we follow the stratigraphic framework proposed by Araújo & Nogueira (2019) and Araújo Filho et al. (2020), who defined that the group is composed, from the base to the top, of the following units: Parauapebas, Carajás, and Igarapé Bahia formations (see Fig. 2B). The oldest unit of the group is represented by the Parauapebas Formation, which is the focus of our paleomagnetic study. It consists of basalts

and basaltic andesites with minor pyroclastic rocks and rhyolites (Gibbs et al., 1986; Martins et al., 2017; Figueiredo e Silva et al., 2020), and is usually considered to be the result of an intraplate rifting of older continental crust (e.g., Gibbs et al., 1986; Olszewski et al., 1989; Martins et al., 2017; Tavares et al., 2018; Teixeira et al., 2021). However, a subduction-related environment is also suggested (e.g., Meirelles & Dardenne, 1991; Teixeira & Eggler, 1994; Zucchetti, 2007; Figueiredo e Silva et al., 2020). The age of this extensive volcanism is well constrained between ca. 2.77 and 2.75 Ga, using U-Pb analyses of zircon from rhyolites and basalts of the Parauapebas Formation (e.g., Olszewski et al., 1989; Machado et al., 1991; Trendall et al., 1998; Martins et al., 2017).

The Carajás Formation is mainly constituted by layers and discontinuous lenses of banded iron formations (jaspilites) and iron ore, intruded by sills and mafic dykes. The base of the Carajás Formation is interlayered with volcanic rocks of the underlying Parauapebas Formation (Gibbs et al., 1986; Martins et al., 2017), showing the gradual and conformable contact between these two formations, which reflects the contemporaneity of them. The BIFs sequence is overlain by a set of volcanic and volcaniclastic rocks, as well as subordinate deep-water marine turbidite strata belonging to the Igarapé Bahia Formation (Tallarico et al., 2005; Dreher et al., 2008; Galarza et al., 2008; Fig. 2B). Existing U–Pb zircon data constrain the age of the volcanic rocks at 2743 ± 11 Ma (Trendall et al., 1998).

The most conspicuous structural feature of the Carajás Basin is an S-shaped syncline-anticline pair (Rosière et al., 2006), the Carajás fold, and partially disrupted by the Carajás strike-slip system (Fig. 2A). The latter divides the Serra dos Carajás in two main blocks, named Serra Norte and Serra Sul. We sampled for paleomagnetism two exceptionally well-preserved, deep drill cores of the Serra Norte region (N4 deposit).

Forty-five geochemical analyses of Parauapebas basaltic flows are reported by Martins et al. (2017), including sampling localities and brief descriptions. Several of these flows were sampled for paleomagnetism in this study (e.g., N4WS-F1279). These geochemical investigations on basaltic rocks of the Parauapebas Formation show 51.12–55.26 wt.% SiO_2, 0.69–0.92 wt.% TiO_2, 7.02–12.35 wt.%. FeO, and MgO ranging from 4.38 to 7.38 wt.%. Moreover, the Parauapebas flows are sub-alkaline, plot in the transitional and calc-alkaline fields, and show either arc-like trace element patterns or similar to those of the upper continental. Geochemically, this is apparent in their LILE and LREE enrichment and Nb and Ti depletion, supporting the idea that the basaltic rocks from Parauapebas Formation derived from the subcontinental lithospheric mantle affected by upper continental crustal components.

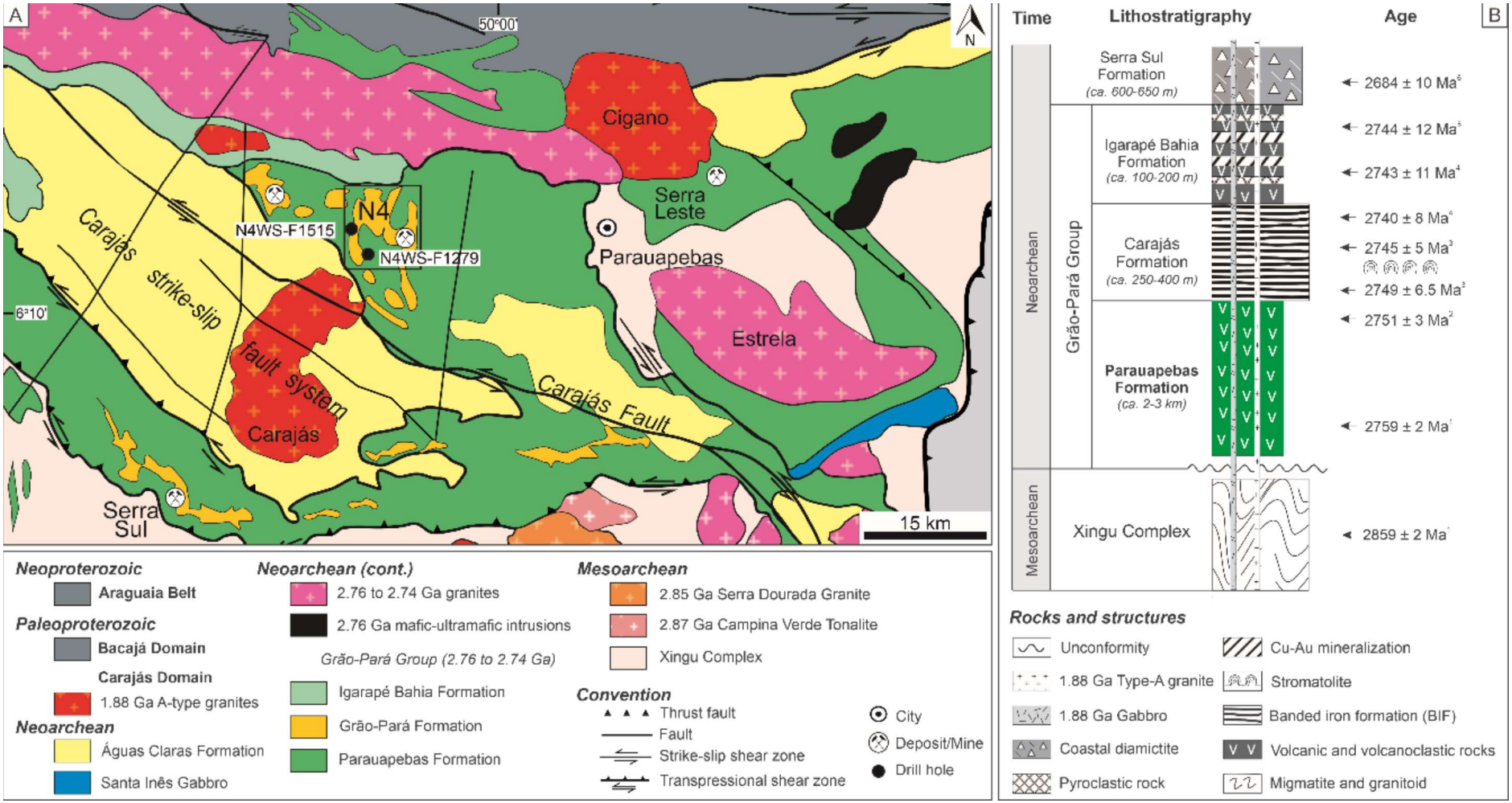
A
50°00'
N
Cigano
Serra Leste
N4
N4WS-F1515
N4WS-F1279
Parauapebas
Carajás strike-slip fault system
6°10'
Estrela
Carajás
Carajás Fault
Serra Sul
15 km
Neoproterozoic
Araguaia Belt
Paleoproterozoic
Bacajá Domain
Carajás Domain
1.88 Ga A-type granites
Neoarchean
Águas Claras Formation
Santa Inês Gabbro
Neoarchean (cont.)
2.76 to 2.74 Ga granites
2.76 Ga mafic-ultramafic intrusions
Grão-Pará Group (2.76 to 2.74 Ga)
Igarapé Bahia Formation
Grão-Pará Formation
Parauapebas Formation
Mesoarchean
2.85 Ga Serra Dourada Granite
2.87 Ga Campina Verde Tonalite
Xingu Complex
Convention
Thrust fault
Fault
Strike-slip shear zone
Transpressional shear zone
City
Deposit/Mine
Drill hole
Time
Lithostratigraphy
Age
B
Neoarchean
Grão-Pará Group
Serra Sul Formation
(ca. 600-650 m)
Igarapé Bahia Formation
(ca. 100-200 m)
Carajás Formation
(ca. 250-400 m)
Parauapebas Formation
(ca. 2-3 km)
Mesoarchean
Xingu Complex
2684 ± 10 Ma
2744 ± 12 Ma
2743 ± 11 Ma
2740 ± 8 Ma
2745 ± 5 Ma
2749 ± 6.5 Ma
2751 ± 3 Ma
2759 ± 2 Ma
2859 ± 2 Ma
Rocks and structures
Unconformity
1.88 Ga Type-A granite
1.88 Ga Gabbro
Coastal diamictite
Pyroclastic rock
Cu-Au mineralization
Stromatolite
Banded iron formation (BIF)
Volcanic and volcanoclastic rocks
Migmatite and granitoid

Fig. 2. A) *Location of drill cores (black dots inside black rectangle) over simplified geological map of the northeastern part of Carajás Province (modified from Vasquez et al., 2008);* ***B)*** *Stratigraphy of the basal part from Carajás Basin with indication of geochronological constraints (adapted from Araujo & Nogueira, 2019 and Araújo Filho et al., 2020). Geochronological data compiled from: 1—Machado et al. (1991); 2—Krymsky et al., 2002; 3—Martins et al. (2017); 4—Trendall et al. (1998); 5—Galarza et al. (2008); 6—Maximum depositional age from Rossignol et al. (2020). The time column was adapted from the International Chronostratigraphic Chart v2020/01 (Cohen et al., 2013).*

3. Sampling and analytical procedures

3.1. Sampling

Due to the challenging conditions of outcrops in the densely forested Amazonia, well-preserved, not weathered rocks are difficult to observe in the Carajás Basin. Therefore, we must rely on mining pits and drilled cores to obtain fresh rocks samples. Rock samples were collected from two well-preserved deep drill cores of the N4 deposit region (see Figs. 2A and S1). These fresh cores were selected for their remarkable well-preserved succession of basaltic flows, and apparent absence of post-depositional deformation and high-grade metamorphism (Figs. 3 and 4).

The core samples were obtained at the Vale core library in Serra dos Carajás, Pará. Core samples ~15 cm long and 8 cm in diameter were collected every 2 m in each drill core. The orientation of the Grão-Pará Group at N4WS-F1279 strikes 184º and dips 9º. At N4WS-F1515 core the bedding is opposed and strikes 352° and dips 14.2° (Fig. S1). The drill holes were performed for N4WS-F1279 with a plunge angle of 81° toward 94° azimuth and for N4WS-F1515 with a plunge of 75.8º toward 262º azimuth, in both cases nearly perpendicular to the bedding in each sector. The strike and dip of the beds remained constant from the surface to the bottom of the drilled core from the N4WS body.

At the N4WS-F1279 drill hole, a continuous ~350 m long core was obtained from the Parauapebas Formation, composed of basaltic rocks. Meanwhile, the N4WS-F1515 drill hole is stratigraphically superjacent and the samples were obtained through a total core length of 360 m (200–560 m depth). The

core is divided into mafic volcanic/subvolcanic rocks and banded iron formations (BIFs) corresponding to the Parauapebas and the Carajás formations (Fig. 7).

3.2. Paleomagnetism and rock magnetism

Preparation and magnetic demagnetization of the samples were performed in the Paleomagnetic Laboratory of the Instituto de Astronomia e Geofisica of the University of São Paulo (USPMag, Brazil). Cylindrical specimens of 1.0×2.0 cm were cut from each core sample (total of 318 specimens). We reconstructed the in-situ sample orientation using the recent viscous magnetizations, that need to be aligned with the present magnetic field at the location (Audunsson & Levi, 1989; Rolph et al., 1998; Rapalini et al., 2013). At least four specimens from each core sample were subjected to detailed stepwise alternating magnetic field (AF) and thermal demagnetization techniques to isolate the characteristic remanent magnetization (ChRM). Steps of 2.5 mT (up to 15 mT) and 5 mT (15–100 mT) were selected for AF demagnetization. Devices used were a tumbler Molspin AF demagnetizer coupled to a JR-6A spinner magnetometer (AGICO, Czech Republic); an automated three-axis AF demagnetizer coupled to a horizontal 2G-Enterprises™ DC-SQUID magnetometer or to a vertical 2G-Enterprises™ DC-SQUID magnetometer with RAPID sample changer (Kirschvink et al., 2008). Thermal demagnetization was performed using a Magnetic Measurements TD-48 furnace in steps of 50ºC (from 150 °C up to 500ºC) and 20ºC (from 500 ºC up to 600ºC/700ºC). Magnetic components for each specimen were identified in orthogonal plots (Zijderveld, 1967), and calculated using principal component analysis (Kirschvink, 1980). Line-fit was filtered using an upper limit of 8° for mean angular deviation (MAD), although vectors were generally very-well defined. For some sites, remagnetization great circles analysis (Halls, 1978) was also employed to determine high coercivity/high-blocking temperature components. Fisherian statistics (Fisher, 1953) were used to calculate vector mean directions and paleomagnetic poles. Paleomagnetic data processing was carried out using Paleomac software (Cogné, 2003). The GPlates software was used for paleogeographic reconstructions (Müller et al., 2018). In addition, the magnetic mineralogy of each site was investigated to determine the carriers of magnetic remanence. These analyses were performed at the

Laboratory of Geochronological, Geodynamic and Environmental Studies (LabGEO) of Instituto Oceanográfico da Universidade de São Paulo. Magnetic hysteresis and Isothermal remanent magnetization (IRM) measurements were performed at room temperature by using a MicroMag-VSM, Model 3900 (Princeton Measurements Corporation, USA) with a maximum magnetic field of 1T. The thermomagnetic curves were measured on powdered samples during continuous heating to 700 ºC and cooling to room temperature by using a CS-4 apparatus coupled to the KLY-4S Kappabridge instrument (AGICO, Czech. Republic).

A total of 24 thin sections were also examined using reflected and transmitted light microscopy. In addition, Scanning Electron Microscopy (SEM) analysis and X-ray energy dispersive spectroscopy (EDS) using a JEOL JXA-8230 SuperProbe at the Electron Microprobe Laboratory of the University of Brasília (Brazil) was used to constrain the nature and textures associated with the magnetic carriers.

4. Field aspects and petrography

The Parauapebas Formation in the studied drill cores consists of extensive successions of massive or amygdaloidal lava flows with at least 370 m in thickness. The basaltic lavas display different textures (amygdaloidal, massive, aphanitic, fine-grained and porphyritic; Figs. 3 and 4). Twelve lava flows cycles were identified by massive texture at the bottom and amygdaloidal and spilitized (seawater metasomatic alteration) zones at the top (Fig. 3). The base and central portions of each lava flows are massive to coarse-grained, respectively. However, amygdaloidal (Fig. 3C; 4D) and spilitized zones are common in the boundary between each lava flow unit (Fig. 3A). Primary mineral assemblages and igneous textures (largely amygdaloidal, intergranular and intersertal and rarely microporphyritic) are preserved (Fig. 3; 4A-E). The basalts consist predominantly of clinopyroxene (Fig. 4B; 4C) and plagioclase with minor quartz, K-feldspar, ilmenite, magnetite and rare pyrite. Titanite and zircon are present as accessory minerals. Common alteration in these rocks is the replacement of calcic plagioclase to sodic plagioclase, and the major replacement of glass and augite by chlorite (Fig. 4A). Alteration of both pyroxene, glass and plagioclase has been attributed to seafloor hydrothermal activity (Martins et al., 2017; Figueiredo e Silva et al., 2020).

The Fe-oxides were examined using a Scanning Electron Microscope (SEM) to explore their primary character. Fe-oxides observed in thin section include fine (>10 μm) grains of primary titanomagnetite (Fig. 4F-H) with typical sizes of 10–150 μm containing ilmenite alteration in some cases (Fig. 4H), and ilmenite. Although, titanomagnetite grains exhibit a small size, it was possible to detect the primary character of octahedral magnetite (Fig. 4G). Different types of sulfides (sphalerite, pyrrhotite) are also observed (Fig. 4H). The magnetic mineralogy analyses are discussed further.

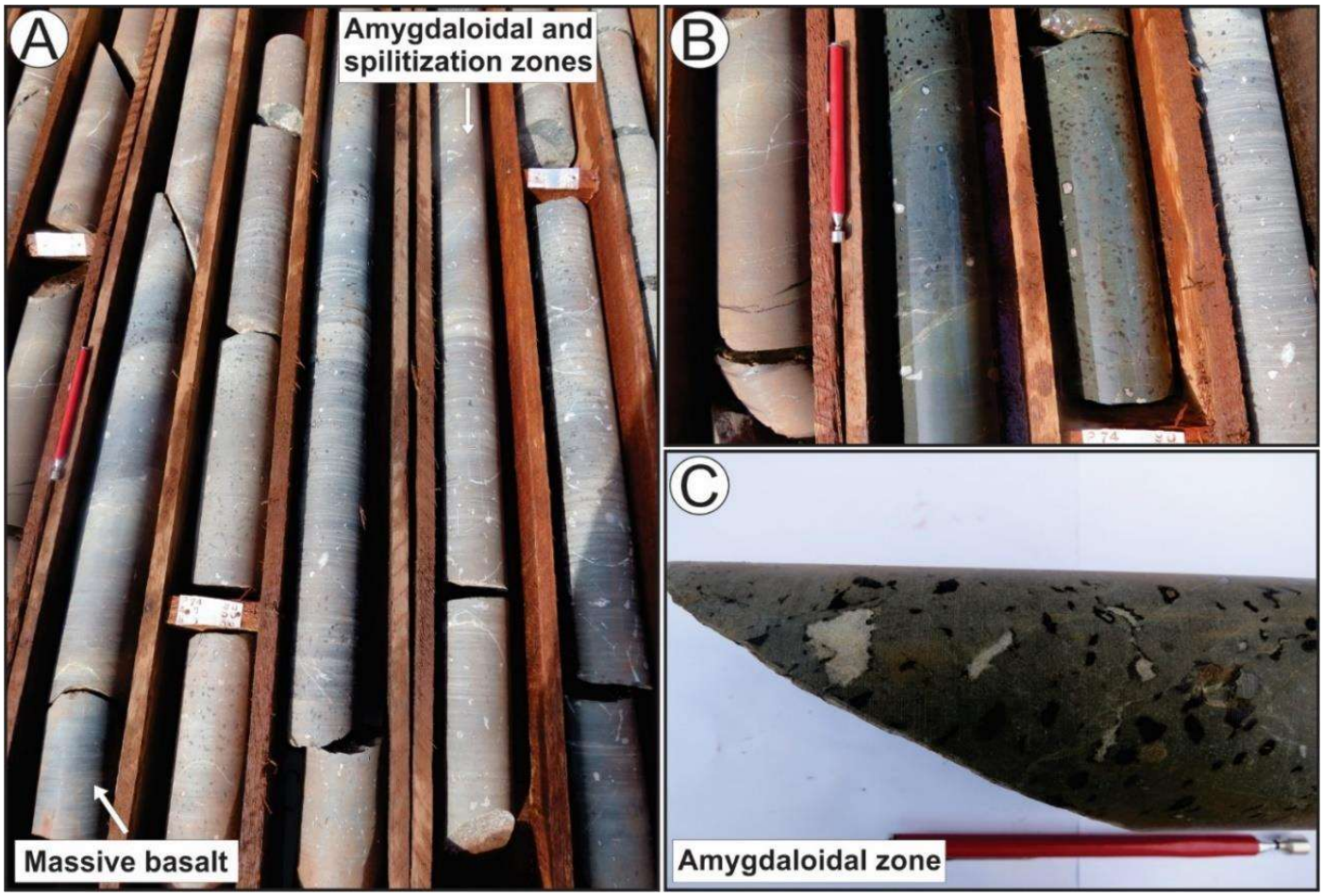

Fig. 3. *Macroscopic aspects of the basalts from Parauapebas Formation:* ***A)*** *and* ***B)*** *Overview of sampled drilling cores showing the basaltic lava flow, characterized by massive texture on the bottom and amygdaloidal and spilitization zones at the top;* ***C)*** *Amygdaloidal zone; amygdules are mainly filled with calcite and chlorite.*

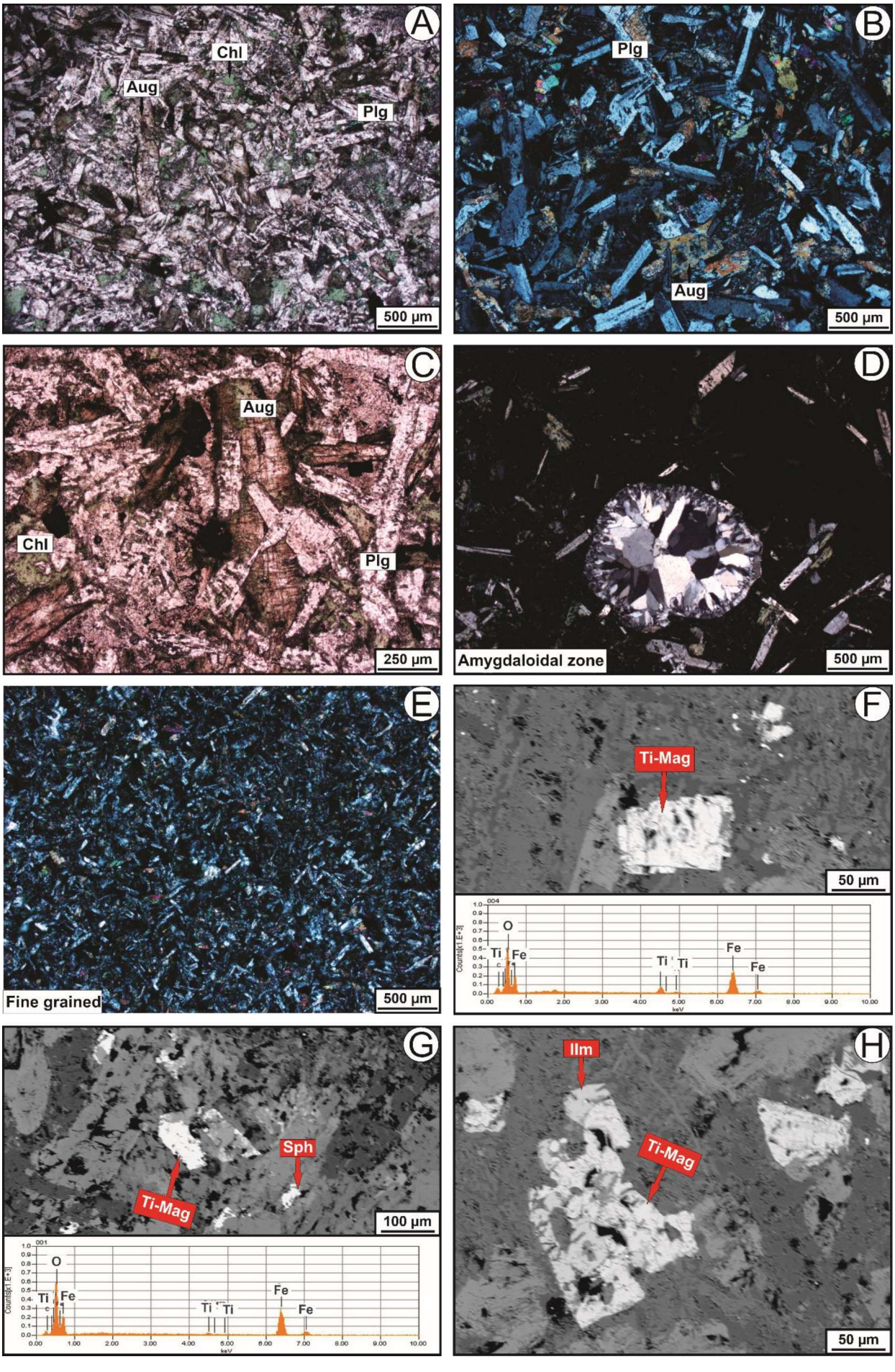
A
Chl
Aug
Plg
500 µm
B
Plg
Aug
500 µm
C
Aug
Chl
Plg
250 µm
D
Amygdaloidal zone
500 µm
E
Fine grained
500 µm
F
Ti-Mag
50 µm
O
Ti
Fe
Ti
Ti
Fe
Fe
G
Sph
Ti-Mag
100 µm
O
Ti
Fe
Ti
Ti
Fe
Fe
H
Ilm
Ti-Mag
50 µm

Fig. 4. *Photomicrographs of representative basalts of Parauapebas Formation:* ***A)*** *Basalt exhibits preserved primary igneous texture (intergranular/intersertal);* ***B)*** *Intergranular texture;* ***C)*** *Primary mineral assemblage still preserved, mainly composed by plagioclase and augite;* ***D)*** *Amygdule with subcircular form filled with quartz in a fine-grained groundmass of augite, plagioclase and glass (replaced by chlorite);* ***E)*** *Fine-grained basalt;* ***F)*** *and* ***G)*** *Backscatter electron image of representative basaltic sample, showing primary Fe-Ti oxides and EDS spectra associated titanomagnetite with ilmenite alteration;,* ***H)*** *Backscatter electron image showing primary titanomagnetite with ilmenite alteration; Mineral abbreviations: (Aug) augite, (Chl) chlorite, (Ilm) ilmenite, (Plg) plagioclase, (Sph) sphalerite, and (Ti-Mag) titanomagnetite.*

5. Paleomagnetic results

The paleomagnetic data were obtained from U-Pb–dated volcanic rocks in the Carajás Basin (Parauapebas Formation). In the studied rocks, AF demagnetization was more efficient than thermal demagnetization. In all specimens it as possible to identify a low-coercivity viscous remanent magnetization (VRM) component below 16 mT. This magnetic component was used to rotate the drill core sections to the true north position, assuming the orientation of the VRM coincides with the recent dipolar field (Fig. 6).

AF demagnetizations for the N4WS-F1279 drill hole reveal a ChRM of southeastern direction and low inclination (Fig. 5A, 5E) or of northwestern direction and low inclination (Fig. 5B, 5C). The remanence is carried mostly by magnetite as showed by thermal demagnetization with a high blocking temperature (~540°C; Fig. 5D). At the bottom part of the core, from 0 m to 54 m, the inclination values are greater than 30º (Fig. 5F). Specimens from the N4WS-F1515 core show a similar ChRM than the top part of N4WS-F1279 with a northeastern direction of low inclination (Fig. 5G, 5H).

Table 1. *Paleomagnetic results for 2.75 Ga Carajás basalts and associated baked contact tests.*

Site	Lithology	Depth (m)	Characteristic remanent magnetization					VGP	
			n/N	Dec (°)	Inc (°)	k	α95 (°)	Plat (ºN)	Plong (ºE)
F1279 (6.095°S / 50.184°W; strike: 184º and dip: 9º)									
F1279-E	Basalt	52.20	5/6	162.5	53.6	65.4	4.8	-57.6	337.5
F1279-F	Basalt	49.00	11/12	132.7	39.5	53.6	10.8	-41.6	15.1
F1279-G	Basalt	35.00	6/9	175.3	53.8	94.9	9.5	-61.4	317.9
F1279-ZD	Basalt	14.00	16/17	342.6	-62.5	28.5	7.1	-49.3	329.1
F1279-ZE	Basalt	7.00	4/5	336.9	-56.1	30.6	16.9	-52.9	341.2
Mean sites C1			*5*	*156.4*	*54.1*	*38.4*	*12.5*	*-54.3*	*342.4*
F1279-A	Basalt	347.20	12/13	146.1	4.6	43	6.7	-56	44.7
F1279-B	Basalt	340.30	8/9	150.8	0.1	93.5	5.8	-60.2	50.5
F1279-C	Basalt	334.05	4/4	132	3.9	36.3	15.5	-42	42.7
F1279-H	Basalt	298.10	9/9	116	-4.9	96.6	6.3	-25.5	45.5
F1279-I	Basalt	294.70	8/11	154.5	-7.2	108.5	6.9	-62.7	60
F1279-J	Basalt	285.00	15/18	144.8	18	33.4	5.3	-55	32.4
F1279-L	Basalt	265.20	13/15	148.6	3.1	28.1	5.3	-58.4	46.8
F1279-M	Basalt	264.50	5/5	152.2	5.1	30.4	6.7	-62.1	45.9
F1279-O	Basalt	238.40	6/7	115.6	13.2	55.3	8.1	1.7	32.9
F1279-P	Basalt	226.85	8/11	313.7	-14	40.3	14.5	-16.3	34.2
F1279-Q	Basalt	196.15	5/5	332.4	-18.3	20.3	9.1	-34.9	32.6
F1279-R	Basalt	184.20	4/5	143.4	20.3	36.7	9.4	-53.5	30.4
F1279-S	Basalt	171.10	10/15	130.3	-8.1	36.3	17.4	-39.3	50.2

F1279-T	Basalt	143.95	11/14	103.9	-13.6	24.7	13.9	14.7	45.4
F1279-U	Basalt	125.40	4/6	122.6	-17.2	197.5	8.5	-30.9	53.9
F1279-V	Basalt	120.35	6/6	302.5	-17.4	26.2	9.4	-5.4	31.4
F1279-X	Basalt	102.90	13/15	294.6	8.2	39.5	6.6	3.8	43.6
F1279-Y	Basalt	90.90	14/14	129.8	-13.3	95.1	13.3	-38.3	53.4
F1279-Z	Basalt	81.95	6/6	134.3	7.9	62	6.8	-16.6	37.5
F1279-ZB	Basalt	75.00	5/5	115.6	-20.8	81.5	4.1	3.5	50.3
F1279-D	Basalt	67.9	8/9	315.4	-31.9	27.2	8.6	-18.4	23.6
F1279-ZC	Basalt	57.80	15/15	162.7	22.8	66.2	8.5	-72	19.9
F1515 (6.082°S / 50.195°W; strike: 352.1º and dip: 14.2º)									
F1515-E-D*	Basalt	728.55	4/4	140.7	39.5	G.C.	10.3	-48.7	12.4
F1515-E-B*	BIF	728.55	4/8	151.5	39.4	G.C.	21.9	-58.1	6.4
F1515-M	Basalt	611.60	18/18	301	-31.8	65.9	4.3	-31.4	23.3
F1515-Y	Basalt	417.55	9/9	289.8	16.9	70.9	6.5	-18.5	51
F1515-Z	Basalt	416.10	14/14	301.7	22.6	25.2	8.4	-29.3	57
F1515-ZB	Basalt	402.25	14/15	159	26.2	54.1	5.5	-67.9	17.7
Mean sites C2			*28*	*134.3*	*6.8*	*11.3*	*8.5*	*-44.6*	*40.5*

n/N = number of analyzed samples/number of samples used in the mean; Dec. = declination; Inc. = inclination; α95 and k = Fisher's confidence cone and precision parameter (Fisher, 1953); G.C –Great circles analysis; VGP – Virtual Geomagnetic Pole; P. Long – Paleolongitude; P. Lat – Paleolatitude. * = Samples from baked.

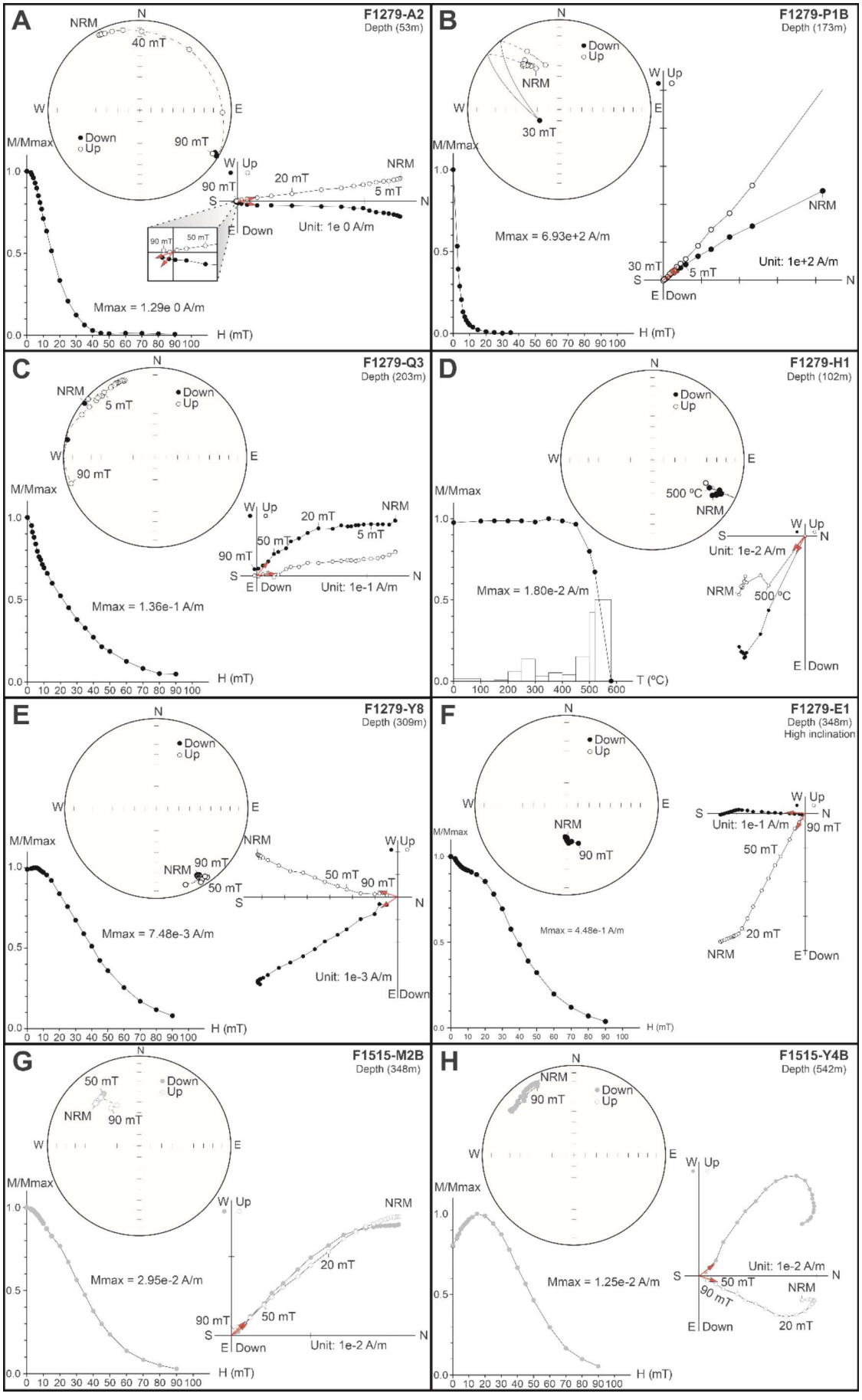
A
F1279-A2
Depth (53m)
NRM
40 mT
90 mT
Down
Up
M/Mmax
Mmax = 1.29e 0 A/m
H (mT)
20 mT
5 mT
Unit: 1e 0 A/m
B
F1279-P1B
Depth (173m)
30 mT
Mmax = 6.93e+2 A/m
Unit: 1e+2 A/m
C
F1279-Q3
Depth (203m)
Mmax = 1.36e-1 A/m
Unit: 1e-1 A/m
D
F1279-H1
Depth (102m)
500 ºC
Mmax = 1.80e-2 A/m
T (ºC)
Unit: 1e-2 A/m
E
F1279-Y8
Depth (309m)
Mmax = 7.48e-3 A/m
50 mT
Unit: 1e-3 A/m
F
F1279-E1
Depth (348m)
High inclination
Mmax = 4.48e-1 A/m
Unit: 1e-1 A/m
G
F1515-M2B
Depth (348m)
Mmax = 2.95e-2 A/m
Unit: 1e-2 A/m
H
F1515-Y4B
Depth (542m)
Mmax = 1.25e-2 A/m
Unit: 1e-2 A/m

Fig. 5. *Examples of AF and thermal demagnetization from the Parauapebas Formation basalts. A-F are examples for basaltic rocks from N4WS - F1279 drill hole (black); G and H are examples from N4WS - F1515 (grey). Demagnetization results are presented with stereographic projections, orthogonal projections and normalized magnetization intensity curves (M/Max versus alternating field H or thermal T).*

The ChRM direction and latitude of Virtual Geomagnetic Pole (VGP Lat) are plotted along the stratigraphy in Figure 7 after deleting the samples with MAD >8°. Whereas the top part of N4WS-F1515 is not well-defined due to the intercalation of BIFs (not sampled), the N4WS-F1279 drill hole shows several inversions of polarity (three) along the stratigraphy indicating that our sampling averages the secular variation of the geomagnetic field. As we mentioned before, at the bottom part of the N4WS-F1279 core (ca. 56 m), the inclination's plot shows a change in its values, showing values greater than 30º. For this reason, we divide the results into two groups, Carajás 1 (steep inclination) and Carajás 2 (low inclination), and calculate the mean paleomagnetic pole for each (C1 and C2, respectively) (Fig. 6).

For the C2 group, eight sites show "NW" direction and twenty sites "reverse" direction, both showing low inclination values, so that a reversal test was performed between these clusters. A primary approach is graphic showing that the mean normal (NW) and reverse polarity directions are statistically undistinguishable when corrected to the paleohorizontal (Fig. 7). Due to the low inclinations, we preferred a bootstrap reversal test (Koymans et al., 2016) (Fig. S2) to calculate the mean directions for the two distributions: Dm = 306.5°, Im = -6.8° (N = 8, k = 10.2) for the NW direction, and Dm = 137.9°, Im = 7.1° (N = 20, k = 12.6) for the SE direction. When performing the statistical test from McFadden and McElhinny (1990), statistical parameters are: N = 28 and critical angle = 15.1°, which classifies it as class-C. The C2 group is constituted of two different cores (N4WS-F1279 and N4WS-F1515) but as the dip of the both side of the fold are really low, the fold test is inconclusive (Tauxe et al., 1994). Overall, using both normal and reverse site mean directions, 28 sites (C2) in the almost entire section (lava flows 3 to 12; 57 to 728 m) yield a mean site directions cluster around the mean Dm = 134.3º, Im = 6.8 º (N = 28, α95 = 8.5º, k = 11.3), corresponding to the paleomagnetic pole at 40.5ºE, -44.6ºS (A95 =6.5º, K = 18.5) (Fig. 6A).

The second group (C1) consists of only 5 sites from the bottom section of N4WS-F1279 (<57 m; Fig. 7), which is below the limit to perform a reversal test (McFadden and McElhinny (1990). The C1 component is characterized by remanent magnetizations southerly directed and with medium downward inclinations. Their site means directions group around Dm = 156.4◦, Im = 54.1º (N = 5, α95 = 12.5º, k = 38.4) and the C1 paleomagnetic pole is located at 342.4ºE, -54.3ºS (A95 = 14.8º, K = 27.8) (Table 1; Fig. 6B).

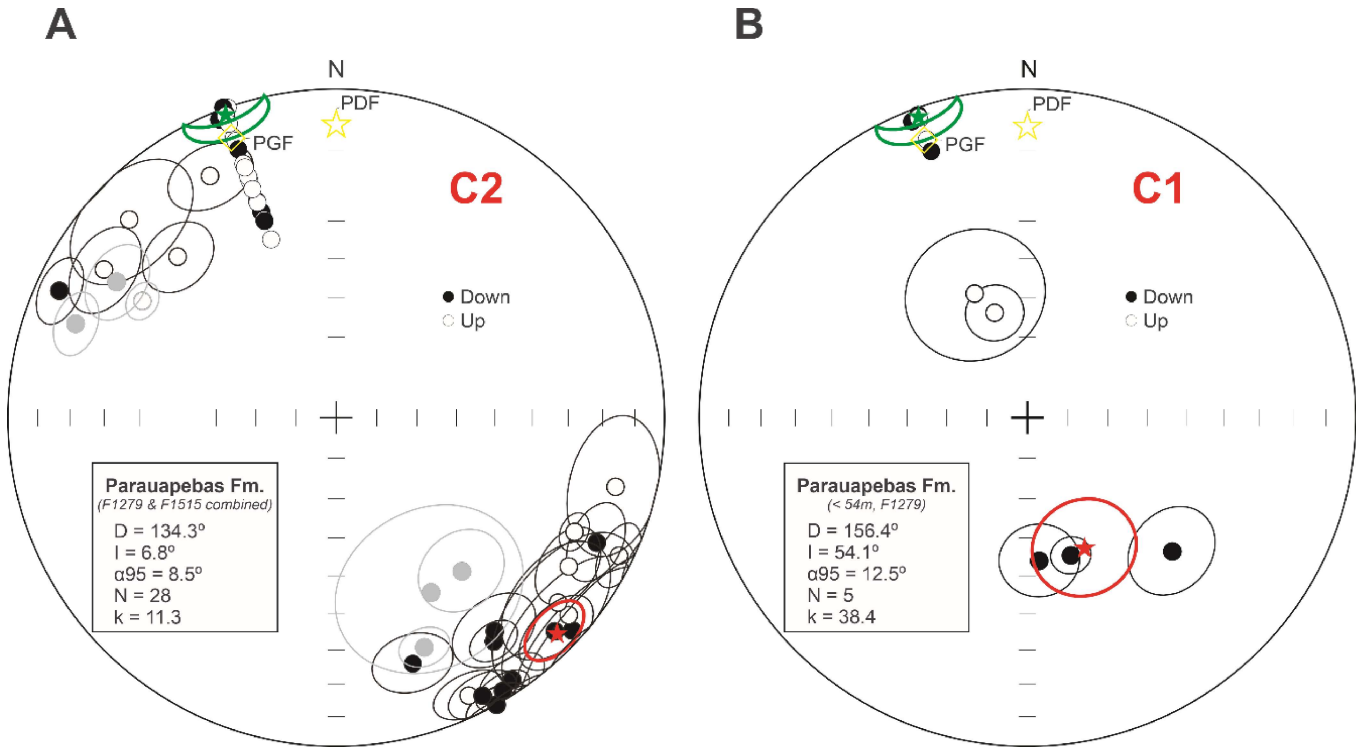

Fig. 6. *Stereoplots showing paleomagnetic data for Parauapebas Formation, Carajás Basin. Site mean characteristic remanence directions with circles of 95% confidence for 26 sites from C2 (A) and 5 sites from C1 (B). Site means are represented as black (N4WS - F1279) and grey (N4WS – F1515) circles; red and green stars in each stereogram represents the grand mean and viscous for each set of sites, respectively. We reconstructed the in-situ sample orientation using the recent viscous magnetizations that need to be aligned with the present magnetic field at the location. Viscous yield a mean directions cluster around the mean Dm = -20.0º, Im = -2.7º, α95 = 8.0º. PDF – Present Dipolar Field; PGF – Present Geomagnetic Field.*

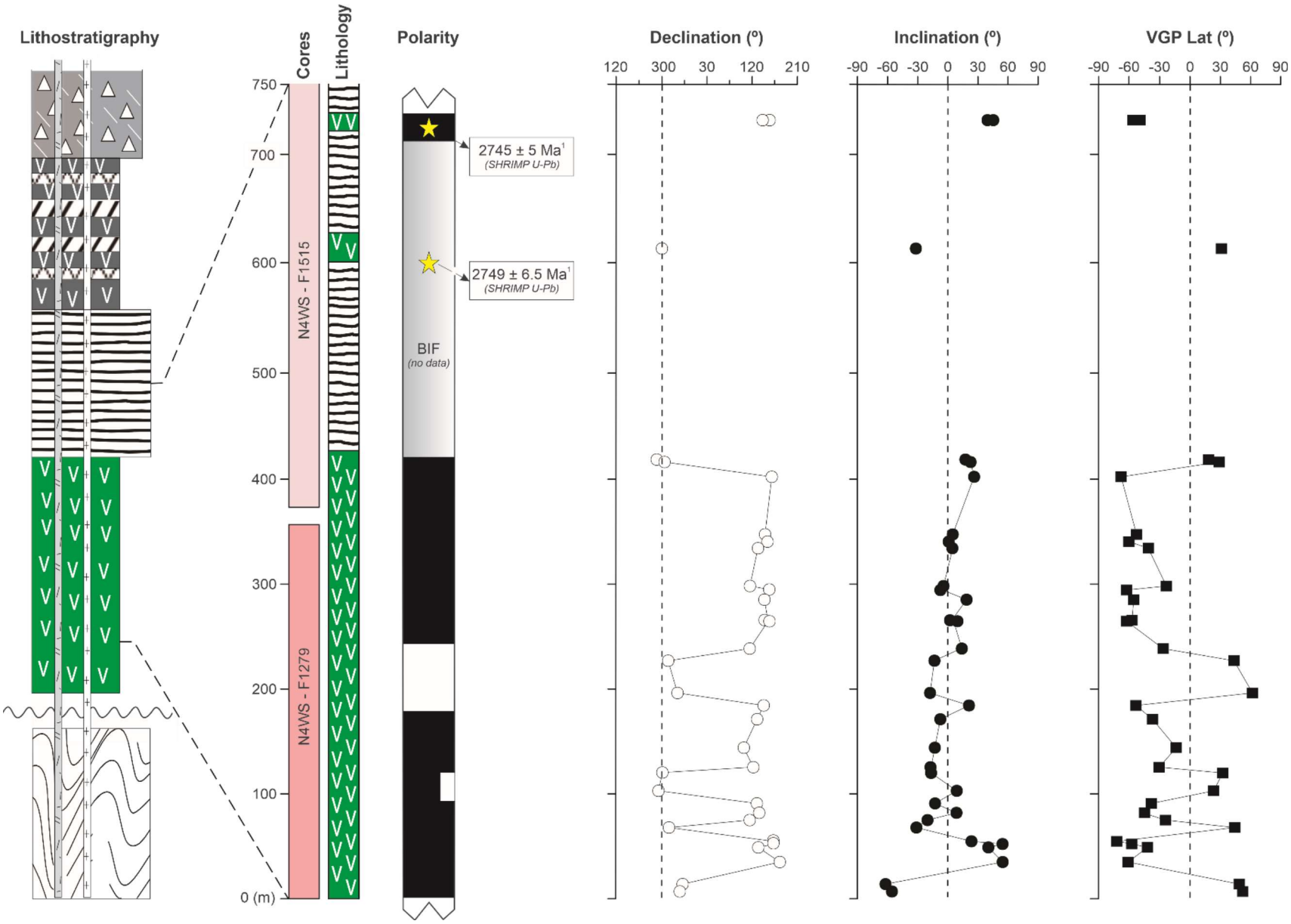
Lithostratigraphy
Cores
Lithology
Polarity
Declination (º)
Inclination (º)
VGP Lat (º)
750
700
600
500
400
300
200
100
0 (m)
N4WS - F1515
N4WS - F1279
2745 ± 5 Ma[1]
(SHRIMP U-Pb)
2749 ± 6.5 Ma[1]
(SHRIMP U-Pb)
BIF
(no data)
120 300 30 120 210
-90 -60 -30 0 30 60 90
-90 -60 -30 0 30 60 90

Fig. 7. *Lithostratigraphy, litholog, paleomagnetic sites, ChRM directions, VGP latitudes and magnetostratigraphy from the Parauapebas Formation basaltic section. The magnetostratigraphy shows reversal polarity directions up the stratigraphy and a major shift in paleolatitude across the flow 3 to 4 boundary (~55m). Reverse and normal (NW direction) polarity are white and black zones, respectively. 1 = Age correlated from Martins et al. (2017). Lithostratigraphy's legend is the same from Fig. 2.*

5.1. Baked contact test

Secondary magnetization in igneous (volcanic) rocks may result from physicochemical changes that somehow influence the composition and/or structure of magnetic minerals and must leave an imprint in rock-magnetic properties. Despite the difficulty to describe dykes/sills in drill core samples, it was possible to perform a reversal baked contact test between a small ramification of the Parauapebas magmatism and the host Carajás BIFs where the contact was visible. Fig. 8A is a schematic sketch showing a Parauapebas-associated gabbroic dyke cross-cutting the Carajás BIF sample. Correlation with SHRIMP dating of zircon grains in the same mafic dyke/sill that cuts the Carajás Formation suggests an age of 2745 ± 5 Ma (Martins et al., 2017) for this subvolcanic rock. The baked host rock sample (Carajás BIF) taken directly from bottom contact (Fig. 8A) of 1 m wide transversal mafic dyke shows a ChRM similar to that of the dyke (Fig. 8B; Table 1), and consequently, similar mean direction. The gabbroic dyke shows mean site directions around the mean Dm = 140.7º, Im = 39.5º, α95 = 10.3º) (Fig. 8B; Table 1). At contact (<5 cm), the Carajás BIF samples show a similar direction (Dm = 151.5º, Im = 39.4º, α95 = 21.9º) (Fig. 8B; Table 1). In contrast, samples collected far away from the contact (>100 m downwards) have distinct mean direction (Dm = 301.0º, Im = -31.8º, α95 = 4.3º) (Fig. 8B; Table 1). This preliminary baked contact test indicates that these BIF samples near the contact were baked during the intrusion of the dyke at ~2.745 Ma. The different remanent magnetization direction, with unblocking temperatures >450 ◦C, isolated for samples far away of the dyke contact (see Fig. 5) indicates that this was not thermally affected by the intrusion of dyke. While the mean directions from the baked host rocks are well defined (Fig. 8B), we interpret these data only as a preliminary-positive baked contact test due to the small number of samples, which prevents calculating the

statistics of mean directions for the baked or unbaked host rocks. Unfortunately, no paleomagnetic study were perform in the BIF section to assert its primary direction and no constrain of the depositional timing between the dyke and the BIFs are available but our test indicates a reheating of the BIF at contact. Such features indicate that the nature of magnetization recorded by the lava flows and dyke reported here was acquired at the time of their cooling and emplacement.

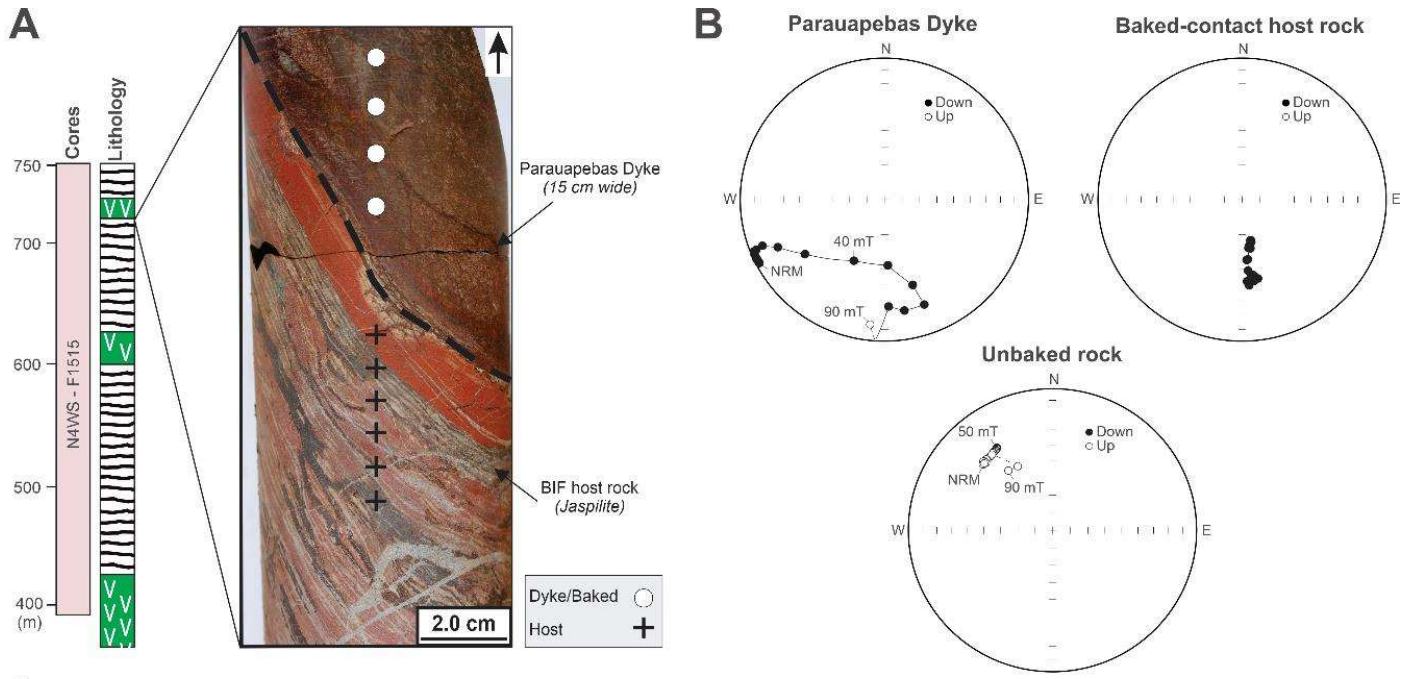

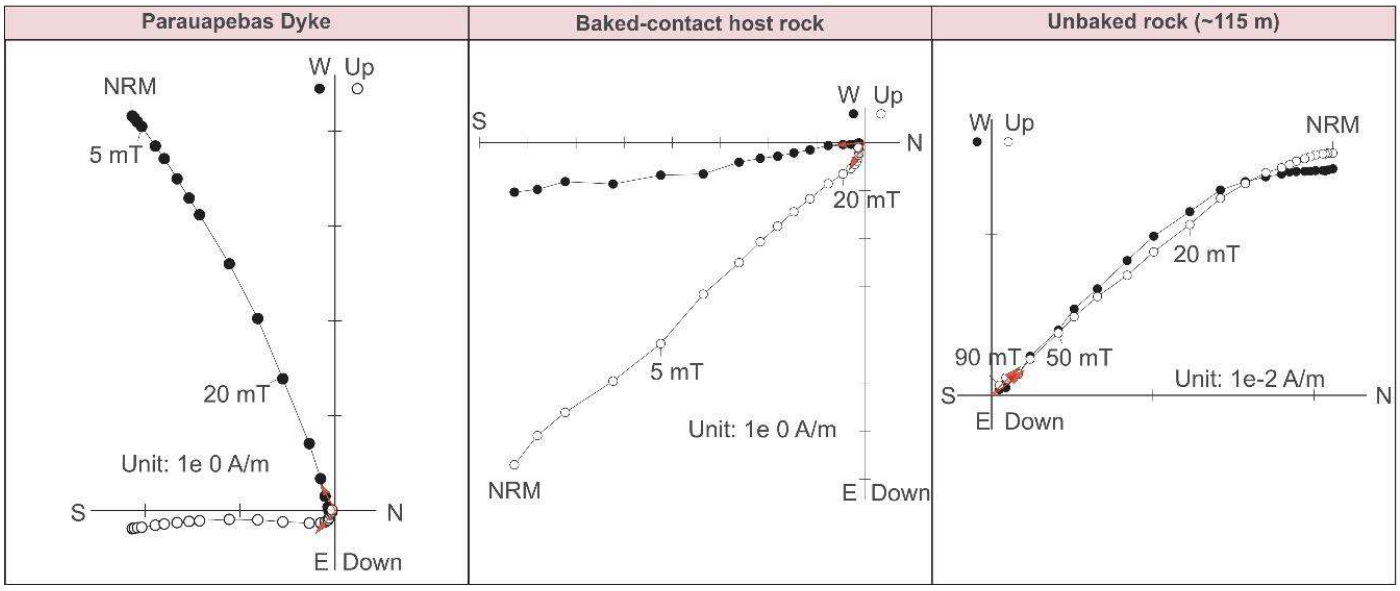

Fig. 8. *Parauapebas formation baked contact profile test at location F1515-E (~728 m):* ***A)*** *Location and sampling profile at samples used at baked contact test;* ***B)*** *Stereonet projections showing characteristic behavior of natural remanence to AF demagnetization for three representative samples, near dyke contact (samples F1515-E4Ba and F1515-E5) and unbaked rock sample at ~115 m from the contact (F1515-M2);* ***C)*** *Orthogonal projections (Zijderveld plot) for these representative samples.*

6. Rock magnetism

Identifying magnetic carriers provides crucial information about the magnetization, timing and information about the geological processes involved during the magnetization of the rock. We applied several rock magnetic analyses to the Neoarchean basalts from Parauapebas Formation, including thermomagnetic curves (bulk susceptibility k versus temperature T), hysteresis measurements and isothermal remanent magnetization. Because the rock magnetic characteristics of the studied volcanic rocks were very similar across the basins sampled, we describe their magnetic mineralogy collectively.

6.1. Thermal susceptibility

Thermomagnetic curve (low-field susceptibility versus temperature is a very useful tool to identify the minerals that carry the magnetic remanence (Hrouda, 1994), as it gives precise information about the Curie Temperature of ferromagnetic materials, characteristic for each mineral (Dunlop & Özdemir, 1997). Thus, high temperature curves were performed in representative samples. High-temperature thermomagnetic curve in the sample F1279-P shows Curie temperature around 575 ºC (Fig. 9A), typical of thermally stable magnetite grains (Dunlop & Özdemir, 1997). In all irreversible curves (Fig. 9) susceptibility increases during the cooling phase, indicating that probably magnetite is being formed during heating, producing a new magnetic phase. The sample F1279-P also suggests the development of hematite (Fig. 9A). This behavior was also observed during the thermal demagnetizations. Sample F1279-X shows a curve with irreversible behavior characterized by different trajectories during heating and cooling and small fall between 500 and 600 ºC indicating the presence of magnetite in small quantity (Fig. 9B).

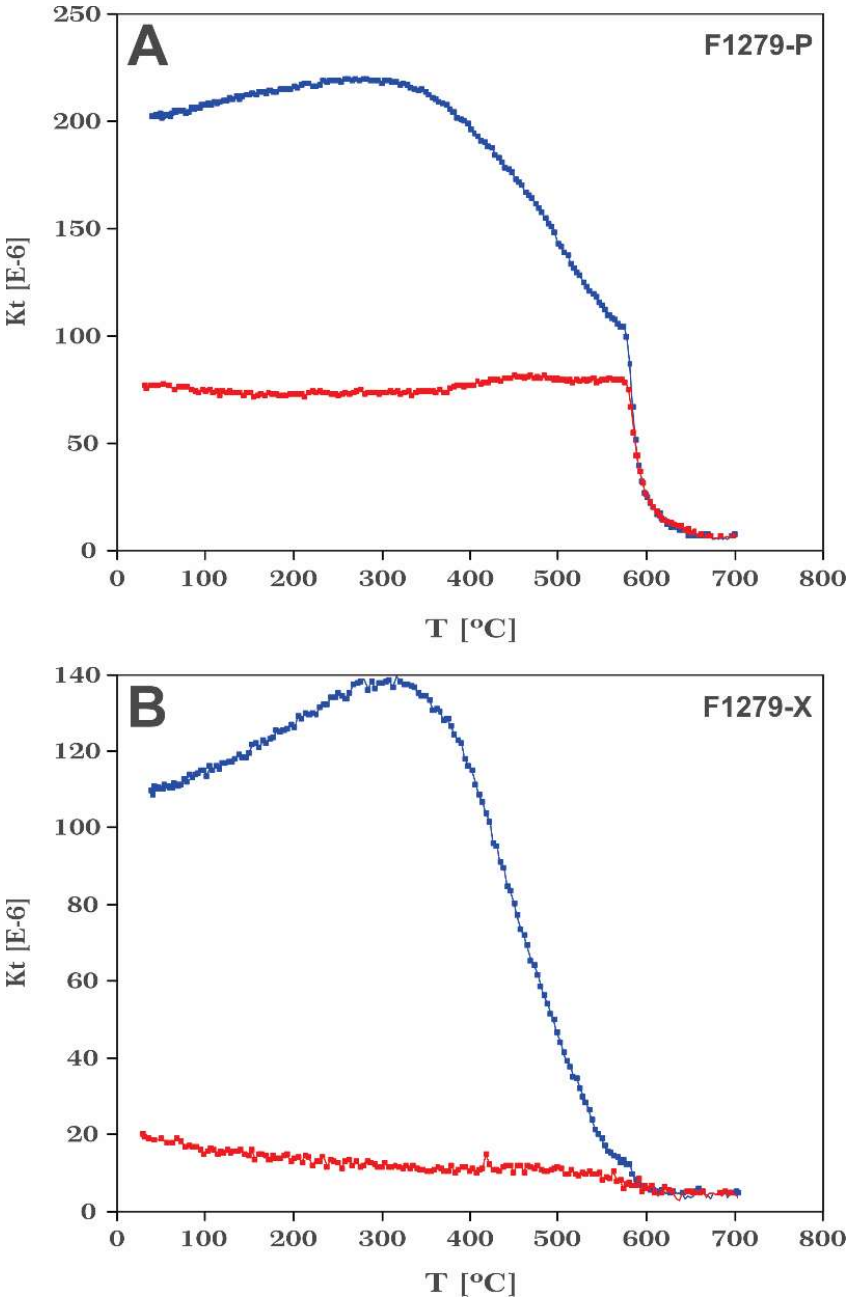

Fig. 9. *High temperature thermomagnetic curves from Parauapebas formation. Red and blue curves for heating and cooling, respectively. Kt is bulk susceptibility in International System (SI) units. See main text for details.*

6.2. Hysteresis and isothermal remanent magnetization curves

Hysteresis loops of the Parauapebas samples show typical behaviors of PSD magnetite characterized by narrow-waisted hysteresis curves (Fig. 10A-C). IRM curves were acquired for 15 specimens and three representative examples are illustrated in Fig. 10D-E. Presence of magnetite in the Parauapebas lava flows is confirmed by IRM curves, which reach at saturation without presence of hematite or hard-coercivity minerals. Based on thermomagnetic curves, IRM acquisition curves and demagnetization diagrams (Fig. 5) we interpret that the remanence is carried mostly by Ti-poor magnetite. Furthermore, the petrographic observations also support magnetite as the predominant magnetic carrier in these rocks (see Section 4).

Day plot diagram (Day et al., 1977; Dunlop, 2002) is a powerful tool to visualize the domain state of magnetic minerals, especially magnetite. The Day plot values can be found in the Supplementary Material (Table S1). All studied samples fall into pseudosingle domain (PSD) range or along a trend parallel to the theoretical SD/MD mixing curves of Dunlop (2002) (Fig. 11). According to the Day's diagram, the studied samples contain about 10–40% of SD grains, except for sites F1279-J, F1279-ZB, F1279-ZD and F1279-ZE, which has less (~10%) SD grain contribution (Fig. 12). This behavior is consistent with the good magnetic stability obtained during AF and thermal treatment. For the studied basaltic flows, the PSD magnetite is formed during the magmatic stage, and no evidence of secondary magnetite was observed.

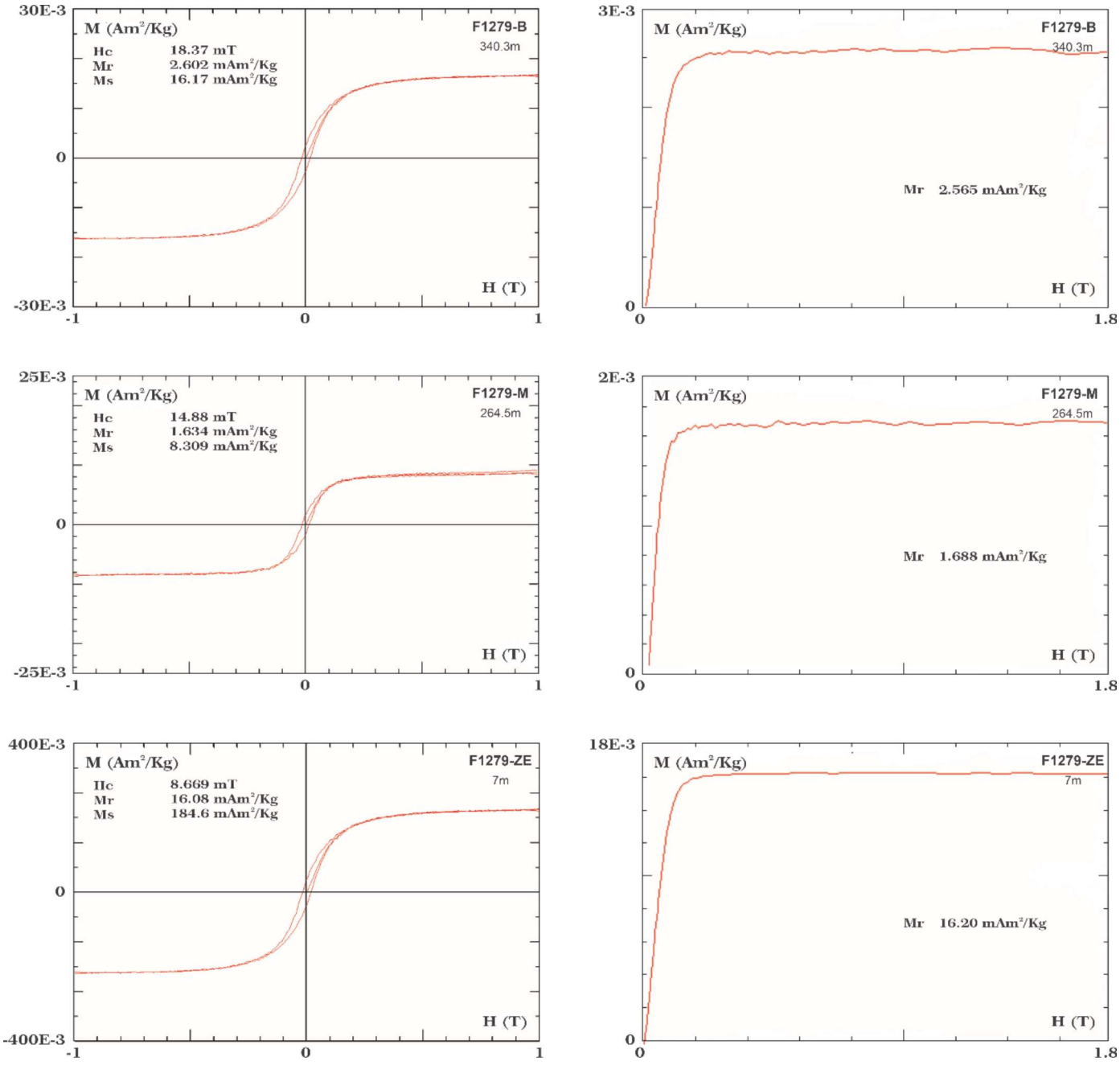

Fig. 10. *Representative hysteresis loops and isothermal remanent acquisition (IRM) curves of the Parauapebas Formation after paramagnetic slope correction.*

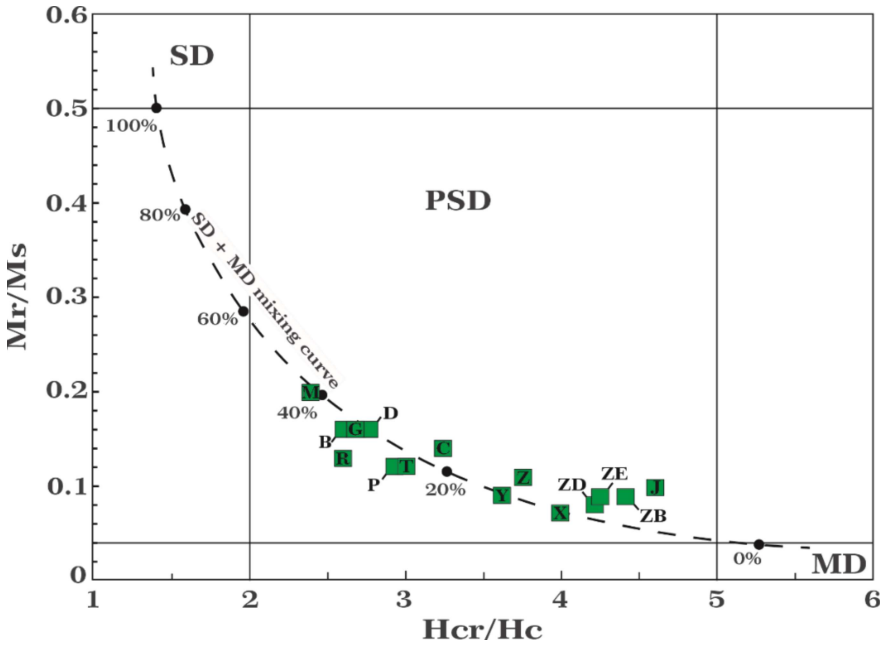

Fig. 11. *Day diagram modified by Dunlop (2002), indicating the state of domain of magnetites. Samples from Parauapebas Formation correspond to the pseudo-single domain (PSD) field. Dashed line represents the theoretical mixing curve for MD grains at different percentages (black dots) with SD magnetite (Dunlop, 2002). Magnetic parameters used to construct this diagram are given in Supplementary Table 1.*

7. Discussion

7.1. Reliability of paleomagnetic poles

7.1.1 C2 group

The C2 group is defined using two different drill cores (N4WS-F1279 and N4WS-F1515) as two different locations. Similarities between these two cores strengthens the use of this component as characteristic of the Parauapebas Formation. The Parauapebas Formation C2 pole (-44.6ºS, 40.5ºE, A95= 6.5º) satisfies 5 (Q = 5) out of the 6 quality criteria proposed by Meert et al. (2020), if we discard his seventh criterion as suggested in the Paleomagia database for Precambrian rocks (Pivarunas et al., 2018). (1) The age is well-defined at 2749 ± 6.5 Ma by correlation with the NAWS-F1338 and the N4WS-F1515 cores which are on the same sequence (Martins et al., 2017). (2) Stable southeastern, low downward/upward inclination (C2 component group) were determined for 171 specimens from 20 out of 28 analyzed sites of

the Parauapebas volcanic rocks, and has adequate Fisher's statistical parameters (A95= 8.5º, K = 11.3) (Table 1). Remanence vectors were well-isolated using stepwise AF treatments, and thermal demagnetizations. They were calculated by the principal component analysis (Kirschvink, 1980) through the visualization of magnetic directions plotted in the Zijderveld diagrams and stereographic projections; (3) The dominant magnetic phase in Parauapebas samples is magnetite, which is supported by the Curie temperature (580–590 °C) determined in the thermomagnetic susceptibility experiments (Fig. 9) and by rock magnetic experiments (Fig. 10; 11). (4) An inverse preliminary positive baked contact test was obtained for a Neoarchean dyke/sill cutting across the upper banded iron formations. This test indicates that reheating of the BIFs at contact which can constrain the age of magnetization of this dyke during its emplacement. (5) No significant metamorphism or deformation is observed in the Parauapebas lava flows and neither in the banded iron formation (upper sequence) in the area (see Martins et al., 2017 for details). The inconclusive fold test does not allow to satisfy this criterion. Further studies will have to sample these formations on different flanks of more inclined folds. (6) Both polarities were observed in the studied samples and the components pass a reversal test (Table 1), which implies the secular variation was averaged out. (7) Also, the ca. 1890-1850 Ma Uatamã dykes that crosscut basement rocks from Carajás Province show a very different ChRM direction (e.g., Dm= 132.8º, Im= 76º, N = 26, α95 = 5º, k = 32.7, yielding the paleomagnetic pole at 328.7ºE, 23.3ºS, A95 = 8.7º, K = 11.7), for which a positive baked contact test was obtained (Antonio et al., 2017; 2021).

Furthermore, the reliability of the results is indicated by the well-preserved primary mineral assemblages and igneous textures from the samples (see section 4), in which the secondary alteration observed (mainly chloritization) is attributed to seafloor hydrothermal activity (Martins et al., 2017; Figueiredo e Silva et al., 2020). It implies that these basaltic lava flows could not have been heated beyond the blocking temperature of magnetite (~450–550 °C) after their emplacement.

7.1.2 C1 group

Although more scattered, the C1 directions were isolated in the investigated rocks (Fig. 6B) yielded a paleomagnetic pole (-54.3ºS, 342.4ºE, A95 = 14.8º) different to the C2 pole. This paleomagnetic pole was calculated for 3 basaltic flows and is located at bottom part of Parauapebas Formation(<57m). The age of the bottom part of the N4WS-F1279 is not defined but the U-Pb older age on zircon of the Parauapebas Formation was given by Machado et al. (1991) at 2759 ± 2 Ma. We can speculate that this age can be assigned to the bottom of this unit to represent the C1 group.

7.2. Age and correlation of magmatic events

Well-exposed and preserved Archean cratons and cratonic fragments typically display numerous episodes of mafic events associated or not with LIPs (Large Igneous Provinces), and therefore a well-defined rock record of mafic magmatism is recorded. Bleeker & Ernst (2006) introduced the concept of a magmatic 'barcode' record of mafic magmatism through time for specific cratonic blocks which can be easily visualized. Age magmatic barcodes provide a convenient graphical representation of the magmatic events within cratons. Each mafic magmatic event from a mafic dyke swarm, sill province, layered intrusion or indeed a continental flood basalt province is defined by a temporal line in the barcode. Similar magmatic barcode and paleogeographic position indicate if the cratons were a part of a common crustal framework, whereas divergent magmatic barcodes and paleogeographic position indicate the cratons were presumably dispersed during this time interval (e.g., Bleeker & Ernst, 2006).

Due to post-eruption tectonic fragmentation and erosion, the preserved volume of the Parauapebas basalts is less than minimum required size for a LIP (100,000 km^3) (e.g., Ernst, 2014). However, the available precise geochronological data revealed that the thick volcanic lava sequence was formed in a short duration (Machado et al., 1991; Olszewski et al., 1989; Martins et al., 2017). The huge thickness of the basalts from Parauapebas Formation (2–3 km; Cabral et al., 2013) is comparable with those of Siberia and Emeishan LIPs (Zhang et al., 2019). As already mentioned, we consider that the tectonic setting of the

Parauapebas Formation results from the rifting of older continental crust. However, it is unclear whether the rift-related setting attributed to Parauapebas volcanism may be linked to a mantle plume event or a transition from a collisional to the post-collisional environment, followed by rifting (Martins et al., 2017; Tavares et al., 2018). This latter is considered to result from delamination of lithospheric mantle and lower crust or slab breakoff (e.g., Rudnick & Gao, 2003) accompanied by upwelling of asthenospheric mantle. One step ahead from the indication that this rift-related setting is a result of a post-collisional environment, and therefore not directly associated to mantle plume breakouts events, is the absence of plume signature on the geochemical data from the Parauapebas formation basalts. These rocks preserve characteristics related to a previous collision or metasomatic mantle event (Martins et al., 2017). Nevertheless, the hypothesis that this volcanism originated by mantle plume activity cannot be entirely ruled out (Teixeira et al., 2021). If it is correct, the ca. 2750 Ma igneous activity in Carajás Basin meets at least three characteristics for a LIP, i.e., short duration, huge thickness and typical rift-like geochemical signatures. Thus, we incorporate Carajás block in the followed magmatic barcode as a LIP fragment within Amazonian craton (Teixeira et al., 2021; Rossignol et al., 2021).

Magmatic age barcodes for the southeastern part of the Amazonia craton, Carajás Province, were compared with age barcodes for the Pilbara, Kaapvaal, Superior, Karelia, and Singhbhum cratons (Fig. 12). As we have mentioned before, the ages for the oldest and youngest Parauapebas Formation lava flows vary from 2759 ± 2 Ma (zircon U-Pb age; Machado et al., 1991) to 2749 ± 6.5 (zircon U-Pb age; Martins et al., 2017) (Fig. 2B). The age of 2749 ± 6.5 was obtained in the same dataset (C2) used in this study. Ca. 2.75 Ga magmatism coeval with the Parauapebas basalts exist in the stabilized Pilbara (the Fortescue group), Kaapvaal (the Ventersdorp group) and Singhbhum (NNE dyke swarm) cratons, and in the non-stabilized Karelia (Panozero) and Superior (Wabigoon tholeiitic dykes) cratons (Fig. 12). Moreover, Pilbara, Kaapvaal and Carajás show similarities between their magmatism as a bimodal affinity. The next magmatic age barcode (do not shown) match for the Amazonia craton is at ca. 2.0 - 1.8 Ga (Uatumã event) with other widespread throughout world cratonic areas (e.g., Laurentia, Zimbabwe, Kalahari, Baltica, São Francisco).

The age of the rifting event (~2.7 Ga) in the Carajás basin broadly coincides in time with the break-up of one of the first documented supercontinent (Eriksson & Condie, 2014; Pesonen et al., 2003; Reddy & Evans, 2009; Salminen et al., 2019; Rossignol et al., 2020; Fig. 12). For instance, the onset of rifting in the Pilbara and Kaapvaal cratons occurred during the course of the Neoarchean, at ~ 2.7 Ga (Blake, 1993; Olsson et al., 2010). Continental rifting event also affected the Karelian-Kola and Superior cratons, which had started around the Neoarchean-Paleoproterozoic boundary at ~2.50 Ga (Amelin et al., 1995; Ernst & Bleeker, 2010). Furthermore, Rossignol et al. (2020) also illustrated that the Neoarchean to Paleoproterozoic tectonic setting of the eastern Amazonia Craton compares with those documented in other major cratons across the world, and suggest that it could record the break-up of one of the first documented supercontinent (Gumsley et al., 2017; Salminen et al., 2019). They suggested that the eastern Amazonia Craton (Carajás Province) could have been part of a much larger supercraton named Supervaalbara during the Archean, along with the São Francisco, Superior, Wyoming, Kola and Karelia, Zimbabwe, Kaapvaal, Tanzania, Yilgarn, and Pilbara cratons (Gumsley, 2017; Gumsley et al., 2017; Salminen et al., 2019).

Therefore, based on matching ca. 2.75 Ga magmatic barcode with similar cratonization ages, it is possible to conclude that Kaapvaal, Pilbara, Singhbhum cratons, and perhaps Carajás Province were nearest neighbors in the late Archean. Furthermore, based on coeval 2.75-2.68 Ga magmatism and tectonics similarity in Pilbara, Kaapvaal, Singhbhum, Karelia and Superior cratons, and Carajás block, we could propose that these blocks were parts of the same supercraton at this time. As the location of the Carajás block during the Neoarchean could be constrained by the new paleomagnetic data showed, this hypothesis will be discussed further.

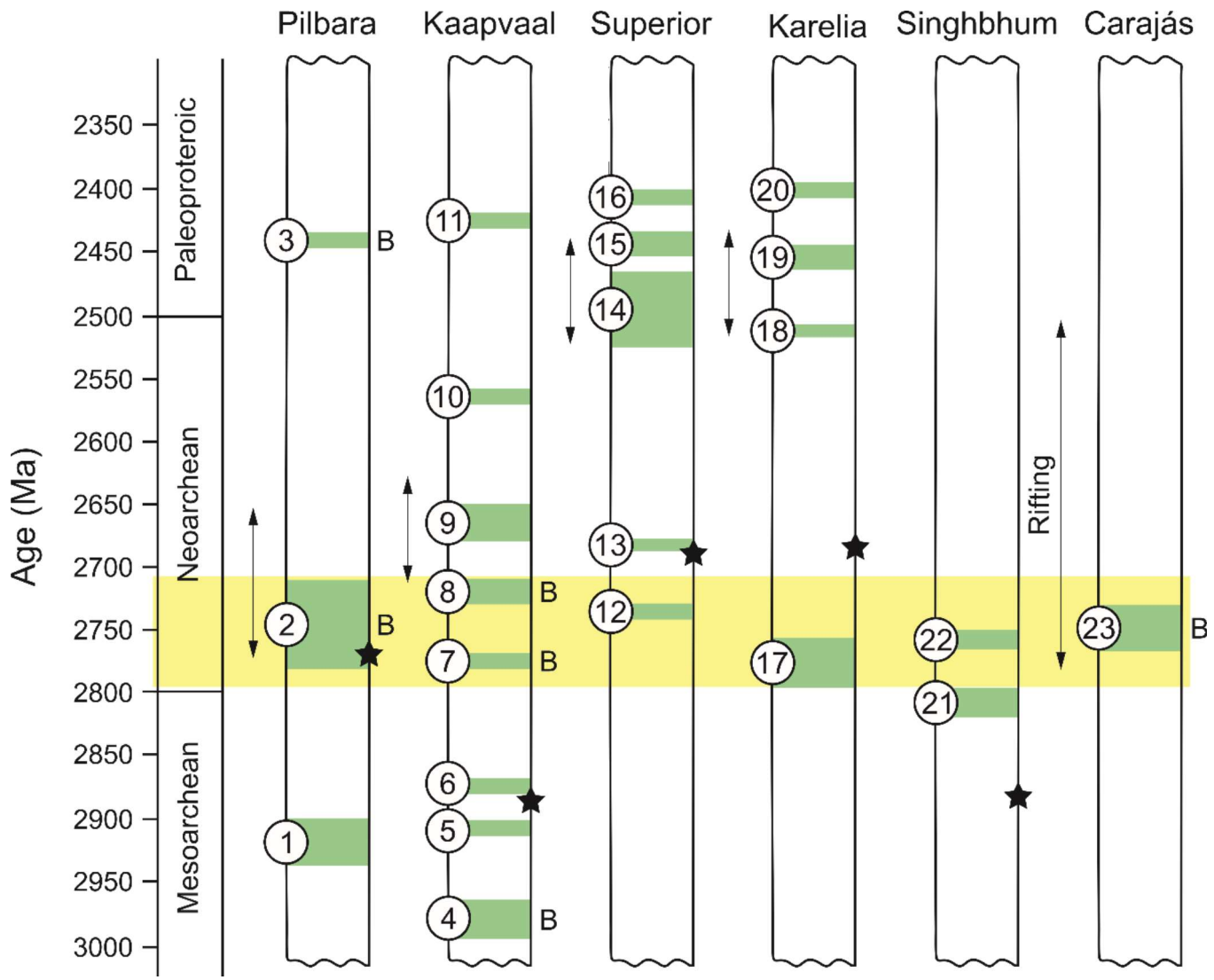

Fig. 12. *Magmatic barcode for some of the Archean cratons, with each individual magmatic event denoted. These include the following events (dyke swarms, sill provinces, and other components of LIPs): 1 - Munni Munni; 2 - Fortescue; 3 - Woongarra; 4 - Nsuze; 5 - Crown; 6 - Hlagothi; 7 - Derdepoort; 8 - Ventersdorp; 9 - Rykoppies-White Mfolozi; 10 – Mvunyana; 11 - Ongeluk, 12 - Wabigoon; 13 - Otto; 14 - Ptarmigan-Mistassini; 15 – Matachewan R; 16 – Matachewan N; 17 -Panozero; 18 - Shalskiy; 19 - Burakovka; 20 - Taivalkoski; 21 – Malaigiri; 22 – Singhbhum NNE dykes; 23 – Parauapebas. The width of individual bars corresponds to the 2σ error in radiometric ages and 'B' denotes bimodal magmatism. Star denotes the end of cratonization (Bleeker, 2003; Halla, et al., 2017). Data mostly from Ernst & Buchan, 2001. The arrow indicates the range of rifting ages. Pilbara Craton after Blake, (1993), Kaapvaal Craton after Olsson et al. (2010), Karelian-Kola Craton after Amelin et al. (1995) and Superior Craton after Ernst & Bleeker (2010).*

7.3. Magnetostratigraphy

The ChRM directions and VGP latitudes of the individual site means for the Parauapebas Formation are plotted from oldest to youngest in Fig. 7. Two particular components of this scheme may prove useful in assisting stratigraphic correlations within the Parauapebas Formation basaltic flows across the Carajás Basin: (i) reversal polarity directions up the stratigraphy and (ii) the major shift in paleolatitude across the flow 3 to 4 boundary (~55m). At least three possible magnetic reversal events are identified in the lava flow sequence from the Carajás Basin (Fig. 7). Although these reversal events have not been useful in stratigraphic divisions, we tried to correlate with to those observed by Strik et al. (2003) in the 2775-2715 Ma rocks from the East Pilbara Basin. The best fit between both magnetostratigraphic scales is achieved in the lower part of Parauapebas interval, bearing dominant normal at the base (Fig. 13). The thicker reversal zone at sites 16–27 would then correlate with that of P2 package, and the following large "NW direction" that comprises the boundary between upper basalts and lower BIF with that of normal interval in P4-P7 packages. Given the scarcity of well-defined paleomagnetic data from some parts of the sequence in both areas (Carajás Basin and Pilbara Craton), it is possible to correlate only one Archean magnetic reversal events (Fig. 13). Nevertheless, our results also corroborated with the possibility that these geomagnetic reversals represent the oldest known geomagnetic field, as previously proposed by Strik et al. (2003).

The reconstructed paleolatitudes from the Carajás Basin reveal a major change in the paleolatitude position (average of 31.2°; Fig. 13) across the flow 3 to 4 boundary (~55m, C1 to C2). However, this significant change is not observed in petrographic and geochemical data from previous studies (e.g., Martins et al., 2017). If the adopted SHRIMP zircon ages are correct, this suggest that the difference from above and below the boundary between sites 28 and 29 (~55 m) is 10 million years (Myr) with an error range of ± 8.5 Myr (ages from Machado et al., 1991 and Martins et al., 2017). Thus, assuming an Earth with the current radius, the average shift is ~3466 km, which gives an average rate of shift in paleolatitude of ~34.6 cm/year (3.12°/Ma) in a period of 10 Myr. Within the 95% confidence errors of both the geochronology and the paleomagnetic study, the minimum apparent drift rate (latitudinal velocity) is

approximately ≥6 cm/year. Each pole's paleolatitude uncertainty is normally distributed about its mean with 2σ = α95. Importantly, because the longitude of the Carajás block during the relevant time interval is unknown, the discussed drift rates are lower bounds. Since this time-averaged rate of horizontal motion is faster than typical of modern plates (~4cm/year; Zahirovic et al., 2015), the paleomagnetic record is suggestive of either uniformitarian or episodic rapid operation of plate tectonics (Gerya et al., 2019) in the Carajás before ~2.7 Ga. This hypothesis is not well constrained, and represents another opportunity for further work. In additional, the discrepancy in the Carajás paleomagnetic poles could also be explained by a true polar wander event and/or nondipole magnetic fields. Constraining the relative contributions of each of these components in Carajás block and other cratons is also necessary to resolve these issues. Furthermore, the mean paleolatitude positions of the remaining sites (1-28; 57 to 728 m) have similar average paleolatitudes with overlapping errors, which implies that either no significant latitudinal movement occurred or that it cannot be resolved with the current amount of data.

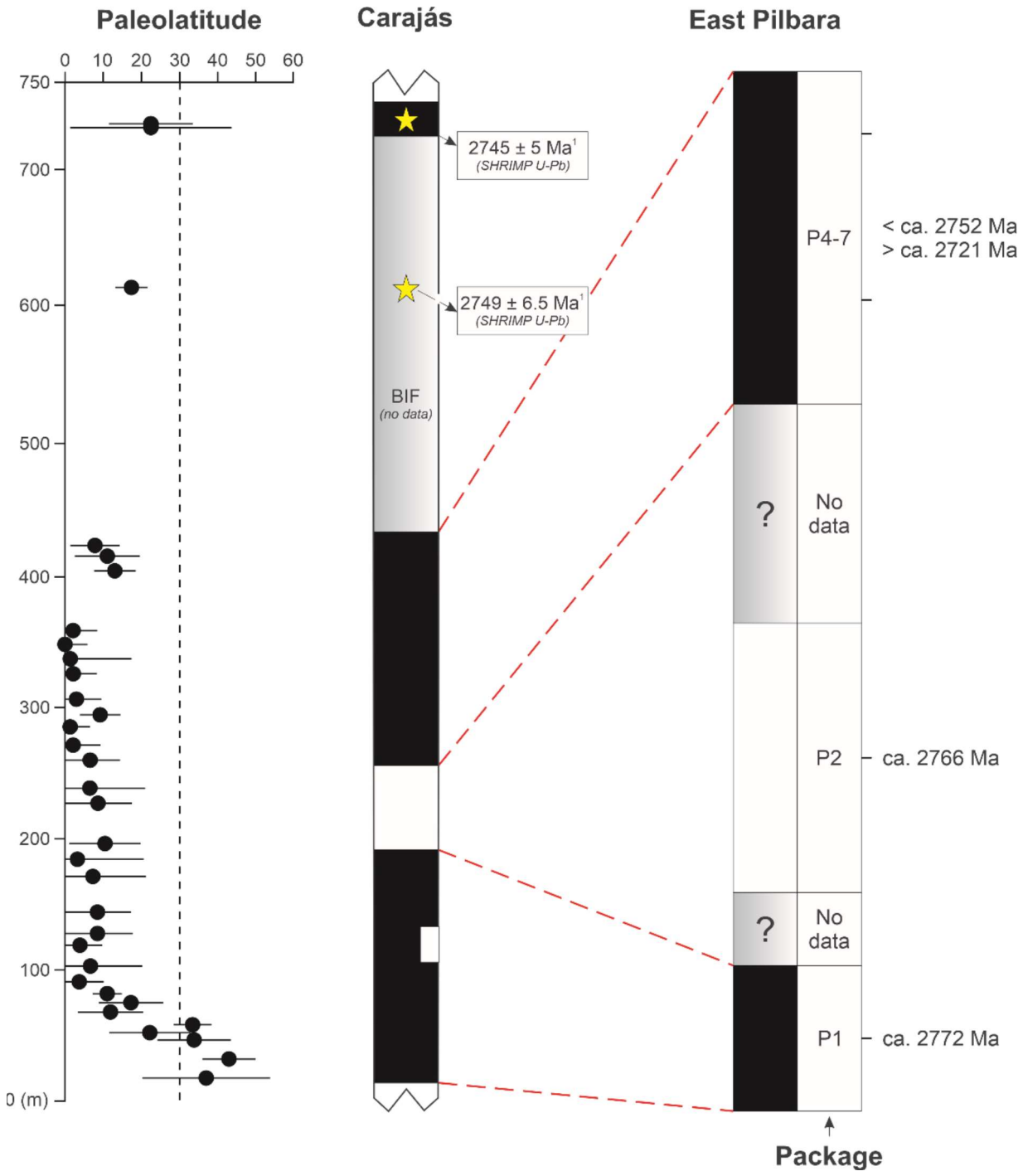

***Fig. 13**. Paleolatitude vs. schematic stratigraphy, and correlation between Carajás Basin (Parauapebas Fm.) and the East Pilbara Basin (P1 to P7). A major change in the paleolatitude position (average of 31.2°) across the 28-29 boundary (C1 to C2) is noteworthy. We interpret that the best fit between both magnetostratigraphic scales is achieved in the lower part of Parauapebas interval, bearing dominant normal (NW direction) at the base following a subsequent large reversal period, thus restricting its age to 2.77-2.76 Ga. Interpreted East Pilbara polarity with approximate ages extracted from Strik et al. (2003).*

7.4. Implications for Archean Supercratons

The hypothetical supercontinent formed by the end of the Neoarchean has been given the name Kenorland. The name was suggested for the first time by Williams et al. (1991) after the 2.7 Ga Kenoran orogeny consolidating the Superior craton in North America. The alternative to a united Kenorland supercontinent is a paleogeographic model of distinct, freely drifting, continent-sized supercratons, including Superia, Sclavia and Vaalbara – each containing several modern cratons with characteristic ages of amalgamation, ca. 2.7, 2.6 and 2.9 Ga, respectively (Bleeker, 2003: Evans et al., 2016).

One of the earliest known potential Archean crustal configurations is that of Vaalbara (e.g., Cheney, 1996; de Kock et al., 2009), which incorporates ancient crust in southern Africa (Kaapvaal) and Western Australia (Pilbara). The connection between the Pilbara and Kaapvaal cratons begins with a comparison between the geology and geochronology of both cratons, and the parallel development of the Neoarchean-Paleoproterozoic stratigraphy that is the core of the Vaalbara hypothesis. In particular, good indicators are the Paleoproterozoic iron formations (Trendall, 1968), but there are also broader links between the 3.5 Ga and 1.8 Ga volcano-sedimentary basins and mineral deposits (e.g., Button, 1976; Cheney, 1996). Since these early contributions, new paleomagnetic data have become available that can both support (e.g., Strik et al., 2003, de Kock et al., 2009. Denyszyn et al., 2013) and discredit (e.g., Wingate, 1998) the concept of Vaalbara. Recently, Kumar et al. (2017) shows the broad geochronological and paleomagnetic similarity between the Kaapvaal with that of Singhbhum Craton in India at 2.81-2.76 Ga. It implies that Singhbhum Craton was also likely part of Vaalbara configuration at this time. Later, Gumsley (2017) and Gumsley et al. (2017) proposed that these cratons were not nearest neighbors but were instead parts of a much larger supercraton named Supervaalbara. This supercraton included the Superior, Wyoming, Hearne, Kola + Karelia, Kaapvaal, Pilbara, and perhaps Singhbhum cratons. Furthermore, Salminen et al. (2019) follow these authors and demonstrated that Uauá block, a fragment of São Francisco craton, could have been part of the Supervaalbara supercraton by 2.62 Ga.

Table 2. *Selected high-quality ca. 2780-2700 Ma global paleomagnetic poles.*

Code	Rock Unit	Age (Ma)	Age References	Plat (ºN)	Plong (ºE)	A_{95}	R	References
CARAJÁS (C)								
C1	Parauapebas Fm. 1	2759 ± 2	Machado et al. 1991	-54.3	342.4	14.8	6	This study
C2	Parauapebas Fm. 2	2749 ± 6.5	Martins et al. 2017	-44.6	40.5	6.5	4-5	This study
KAAPVAAL (K)								
K1	Modipe gabbro	2784 ± 1	Denyszyn et al. 2013	-47.6	12.4	8.6	5	Denyszyn et al. 2013
K2	Derdepoort basalt	2782 ± 5	Wingate, 1998	-39.6	4.7	17.5	6	Wingate, 1998
K3	Allanridge basalts	2718–2713	Armstrong et al.1991	-69.8	345.6	5.8	5	de Kock et al. (2009)
KARELIA (Ka)								
Ka1	Panozero sanukitoids	2765 ± 8	Sergeyev et al. 2007	-10.2	226.1	4.1	5	Lubnina & Slabunov 2009
Ka2	Koitere sanukitoids	2684 ± 2	Halla 2002	-67.5	192.5	21.5	5	Mertanen & Korhonen 2011
PILBARA (P)								
P1	Mount Roe Basalts	2772 ± 2	Wingate, 1999	-52.4	178.0	7.6	7	Schmidt & Embleton, 1985
P2	Pilbara Package 1	2771 ± 7	Arndt et al. 1991	-41.0	160.0	3.7	6	Strik et al. 2003
P3	Pilbara Package 2	2766 ± 2	Blake et al. 2004	-46.5	152.7	15.2	3	Strik et al. 2003; Blake et al. 2004
P4	Pilbara Package 4-7	2720–2740	Blake et al. 2004	-50.4	138.2	12.5	4	Strik et al. 2003; Blake et al. 2004
SINGHBHUM (Si)								
Si	NNE Dykes	2762 ± 2	Kumar et al. 2017	14.0	78.0	11	5	Kumar et al. 2017
SUPERIOR (Su)								

Su1	Dobie Lake batholith	2747 ± 3	Corfu & Stott (1989)	87.3	307.1	27.8	4	Hale & Lloyd, 1990
Su2	Wabigoon gabbro	2732 ± 1	Morrison et al. (1985)	-10.7	200.2	7.5	4	Dunlop, 1983
WYOMING (W)								
W1	Stillwater complex	2705 ± 4	Premo et al. 2000	-83.6	335.8	4.0	5	Selkin et al. 2008
ZIMBABWE (Z)								
Z1	Belingwe komatiites	2692 ± 9	Chauvel et al. (1993)	-44.0	302.0	17.0	4	Yoshihara & Hamano 2004

Code, corresponds to the code in Fig. 14. Plat, Plong are pole latitude and longitude. A_{95}, 95% confidence circle of the pole. N: number of sites studied. R: Reliability criteria (Meert et al., 2020). For Superior, Wyoming, and Karelia, the north poles are used.

Integrating our new paleomagnetic data (C2 and C1) with the comparison of magmatic barcodes (see section 7.2) and paleopoles compiled from the major Archean cratons (Table 2) that could have been part of the Supervaalbara configuration, we illustrate a plausible Archean position for the Carajás block with respect to these cratons during 2760-2740 Ma (Fig. 14). The details of selected high-quality 2800-2700 Ma paleomagnetic poles are shown in Table 2. The new ~2760 Ma Carajás pole (C1) locates the southeastern part of the Amazonia Craton at low latitudes of 34.6 ± 12.5º (upper globe in Fig. 14). Because of some similar geological records (e.g., coeval bimodal magmatism), we reconstruct the Carajás block close to the Kaapvaal, Pilbara, Superior and Wyoming cratons. Singhbhum is reconstructed at steep latitudes and could have been proximal during this time (Kumar et al., 2017). The matching ~2760 Ma magmatism and overlapping paleolatitudes also support the proximity with the Karelia craton (Fig. 14). This reconstruction is further supported by geological observations (Fig. 12). Note that since longitude is not constrained in paleolatitude reconstructions, these cratons could still have been situated up to 180° away from each other. Our speculative Neoarchean reconstruction based on a modest amount of paleomagnetic data and comparison of magmatic barcodes demonstrates that the Carajás block could have been part of the Supervaalbara supercraton.

After 2750 Ma, the paleolatitudes of the Carajás block and the abovementioned cratons diverge over a large distance, indicating that rifting and separation of these blocks had started. The expressive rift-related volcanism of the Carajás basin represented by the Parauapebas Formation (Gibbs et al., 1986; Olszewski et al., 1989; Martins et al., 2017; Tavares et al., 2018) and the onset of rifting in other major cratons across the world during the course of the Neoarchean to early Paleoproterozoic also supports this hypothesis. It could record the break-up of one of the first documented supercontinent (Gumsley et al., 2017; Salminen et al., 2019; Rossignol et al., 2020). In the second stage at ~2749 Ma (lower globe in Fig. 14), Carajás

Province is reconstructed to the lowest latitudes (C2 = 3.4 ± 8.5°). However, encouraged by the overlap of paleolatitude data for ~2740-2730 Ma, the Carajás block and Superior Craton are reconstructed as nearest neighbors (Fig. 14) at this time. This juxtaposition could indicate that the Carajás block was still connected in the Supervaalbara configuration at a lower latitudinal position. Due to the limited amount of Archean-Paleoproterozoic paleomagnetic data for the Amazonia craton, we are currently unable to test the duration of this configuration more precisely.

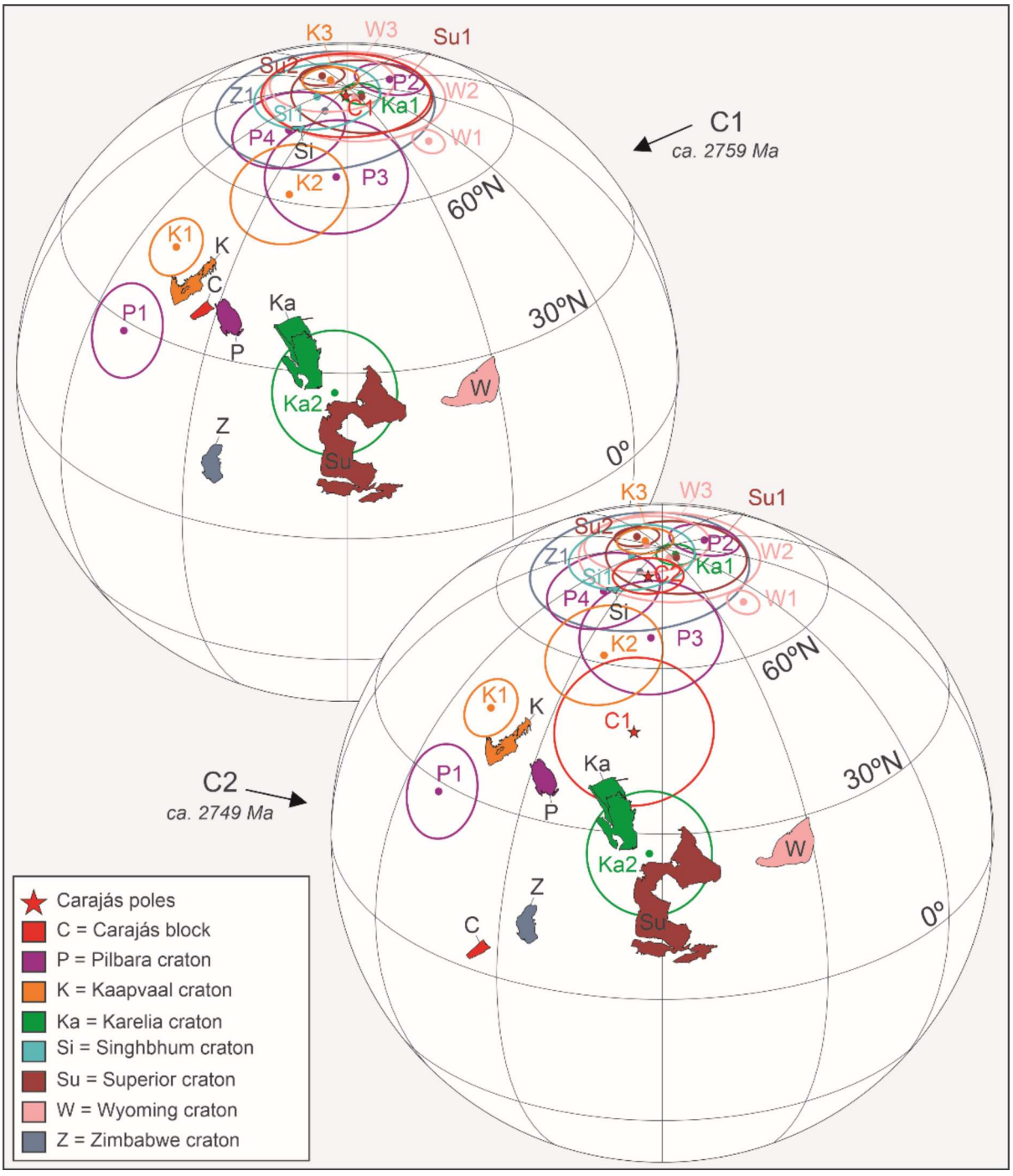

***Fig. 14**. A plausible paleogeographic reconstruction for the Carajás block with respect to the Pilbara + Kaapvaal (Vaalbara), Karelia, Singhbhum, Superior cratons, Wyoming and Zimbabwe at ca. 2780-2700 Ma after Strik, 2003, Denyszyn et al. 2013, Kumar et al., 2017 and Salminen et al., 2019. The upper globe and lower globe correspond to the possible range of Carajás block paleoposition at ~2759 Ma (Carajás 1 – C1) and ~2749 Ma (Carajás 2 – C2), respectively. Paleopole numbers are as in Table*

2 and indicate a key pole (well-defined rock age and proven primary magnetization direction, Buchan 2014).

8. Conclusion

The first robust paleomagnetic data were obtained for the Carajás Province during the Neoarchean (~2750 Ma). The results reduce the unsampled period in the available paleomagnetic record from a fragment of Amazonia craton. We use paleomagnetic methods to isolate two characteristic components, Carajás 1 and 2, and calculate the mean paleomagnetic pole for each: C1 (~2759 Ma; 40.5ºE, -44.6ºS A95 =6.5º, K = 18.5) and C2 (~2745 Ma; 342.4ºE, -54.3ºS, A95 = 14.8º, K = 27.8). The restored paleomagnetic directions pass a provisionally baked contact test within the ~2740 Ma Carajás banded iron formation. These observations, combined with petrography and rock magnetic results, suggest a primary origin for the magnetization. At least three possible magnetic reversal events are identified in the lava flow sequence from the Carajás Basin. Although these reversal events have not been useful in stratigraphic divisions, they could be correlative to those observed in the 2775-2715 Ma rocks from the East Pilbara Basin.

Our paleomagnetic investigation integrated with the comparison of geological features reveals that the Carajás block could have been part of the Supervaalbara supercraton configuration during the Neoarchean (~2750 Ma) in a position nearest the equatorial line. Due to the limited amount of Archean-Paleoproterozoic paleomagnetic data for the Amazonia craton, we are currently unable to test the duration of this configuration more precisely.

Acknowledgements

The authors wish to extend their special thanks to Vale S.A. mining company for permitting the use of geological data and access to the N4 deposit, as well as providing research

funding. This study was financed in part by the Coordenação de Aperfeiçoamento de Pessoal de Nível Superior - Brasil (CAPES) - Finance Code 001. We also would like to thank the Fundação de Apoio à Pesquisa do Distrito Federal (FAP-DF) (23411.93.27701.29052018) for supporting this research. Catarina L.B. Toledo, Adalene M. Silva, Farid Chemale Jr. and Ricardo I.F. Trindade thank Conselho Nacional de Desenvolvimento Científico e Tecnológico (CNPq) for their respective research grants. The first author Pedro L. G. Martins thanks CNPq for the PhD scholarship.

References

Almeida, F.F.M., Hasui, Y., Neves, B.B.D., Fuck, R.A., 1981. Brazilian structural provinces: an introduction. Earth Sci. Rev. 17, 1–29. https://doi.org/10.1016/0012-8252(81)90003-9.

Almeida, J.A.C., Dall'Agnol, R., Oliveira, M.A., Macambira, M.J.B., Pimentel, M.M., Rämö, O.T., Guimarães, F.V., Leite, A.A.S., 2011. Zircon geochronology and geochemistry of the TTG suites of the Rio Maria granite-greenstone terrane: implications for the growth of the Archean crust of Carajás Province, Brazil. Precambrian Res. 187, 201–221. https://doi.org/10.1016/j.precamres.2011.03.004.

Almeida, J.A.C., Dall'Agnol, R., Leite, A.A.S., 2013. Geochemistry and zircon geochronology of the Archean granite suites of the Rio Maria granite-greenstone terrane, Carajás Province, Brazil. J. S. Am. Earth Sci. 42, 103–126. https://doi.org/10.1016/j.jsames.2012.10.008.

Amelin, Y.V., Heaman, L.M., Semenov, V.S., 1995. U-Pb geochronology of layered mafic intrusions in the eastern Baltic Shield: implications for the timing and duration of Paleoproterozoic continental rifting. Precambrian Res. 75, 31–46. https://doi.org/10.1016/0301-9268(95)00015-W.

Antonio, P.Y.J., D'Agrella-Filho, M.S., Trindade, R.I.F., Nédélec, A., de Oliveira, D.C., da Silva, F.F., Roverato, M., Lana, C., 2017. Turmoil before the boring billion: Paleomagnetism of the 1880–1860Ma Uatamã event in the Amazonian craton. Gondwana Res. 49, 106–129. https://doi.org/10.1016/j.gr.2017.05.006.

Antonio, P.Y.J., D'Agrella-Filho, M.S., Trindade, R.I.F., Nédélec, A., Poujol, M., Sanchez, C., Dantas, E.L., Dall'Agnol, R., Teixeira, M.F.B., Proietti, A., Martínez Dopico, C.I., Oliveira D.C., Silva, F.F., Marangoanha, B., Trindade, R.I.F., 2021. New constraints for paleogeographic reconstructions at ca. 1.88 Ga from geochronology and paleomagnetism of the Carajás dyke swarm (eastern Amazonia). Precambrian Res. 353, 106039. https://doi.org/10.1016/j.precamres.2020.106039.

Araújo, R., Nogueira, A., 2019. Serra sul diamictite of the Carajás Basin (Brazil): a Paleoproterozoic glaciation on the Amazonian craton. Geology 47, 1166–1170. https://doi.org/10.1130/G46923.1.

Araújo Filho, R., Nogueira, A.C.R., Araújo, R.N., 2020. New stratigraphic proposal of a Paleoproterozoic siliciclastic succession: implications for the evolution of the Carajás Basin, Amazonian craton, Brazil. J. S. Am. Earth Sci. 102, 102665. https://doi.org/10.1016/j.jsames.2020.102665.

Armstrong, R.A., Compston, W., Retief, E.A., Williams, I.S., Welke, H.J., 1991. Zircon ion microprobe studies bearing on the age and evolution of the Witwatersrand triad. Precambrian Res. 53, 243–266. Zircon ion microprobe studies bearing on the age and evolution of the Witwatersrand Triad. https://doi.org/10.1016/0301-9268(91)90074-K.

Arndt, N.T., Nelson, D.R., Compston, W., Trendall, A.F., Thorne, A.M., 1991. The age of the Fortescue Group, Hamersley Basin, Western Australia, from ion microprobe zircon U-Pb results. Aust. J. Earth Sci. 38, 261–281. https://doi.org/10.1080/08120099108727971.

Audunsson, H., S. Levi, 1989. Drilling-induced remanent magnetization in basalt drill cores. Geophysical Journal International, 98, 613-622. https://doi.org/10.1111/j.1365-246X.1989.tb02294.x.

Blake, T.S., 1993. Late Archaean crustal extension, sedimentary basin formation, flood basalt volcanism and continental rifting: the Nullagine and Mount Jope Supersequences, Western Australia. Precambrian Res. 60, 185–241. https://doi.org/10.1016/0301-9268(93)90050-C.

Bekker, A., Holland, H.D., Wang, P.L., Rumble III, D., Stein, H.J., Hannah, J.L., Coetzee, K.O. L.L., Beukes, N.J., 2004. Dating the rise of atmospheric oxygen. Nature 427, 117–120. https://doi.org/10.1038/nature02260.

Blake, T.S., Buick, R., Brown, S.J.A., Barley, M.E., 2004. Geochronology of a Late Archaean flood basalt province in the Pilbara Craton, Australia: constraints on basin evolution, volcanic and sedimentary accumulation, and continental drift rates. Precambrian Res. 133, 143–173. https://doi.org/10.1016/j.precamres.2004.03.012.

Bleeker, W., 2003: The late Archean record: a puzzle in ca. 35 pieces. Lithos 71, 99–134. https://doi.org/10.1016/j.lithos.2003.07.003.

Bleeker, W., Ernst, R., 2006. Short-lived mantle generated magmatic events and their dyke swarms: the key unlocking Earth's paleogeographic record back to 2.6 Ga. In: E. Hanski, S. Mertanen, T. Rämö, J. Vuollo (eds.), Dyke Swarms - Time Markers of Crustal Evolution, 3-26. Taylor & Francis, London.

Buchan, K.L., Mertanen, S., Park, R.G., Pesonen, L.J., Elming, S.-Å., Abrahamsen, N., Bylund, G., 2000. Comparing the drift of Laurentia and Baltica in the Proterozoic: the importance of key palaeomagnetic poles. Tectonophysics 319, 167–198. https://doi.org/10.1016/S0040-1951(00)00032-9.

Buchan, K.L., 2014. Reprint of "Key paleomagnetic poles and their use in Proterozoic continent and supercontinent reconstructions: a review". Precambrian Res. 244, 5–22. https://doi.org/10.1016/j.precamres.2014.01.010.

Button, A., 1976. Transvaal and Hamersley Basins – review of basin development and mineral deposits. Miner. Sci. Eng. 8, 262–290.

Cabral, A.R., Creaser, R.A., Nagler, T., Lehmann, B. Voegelin, A.R., Beltasky, B., Pasava, J., Gomes, A.A.S., Galbiatti, H., Bottcher, M.E., Escher, P., 2013. Trace-element and multi-isotope geochemistry of Late-Archean black shales in the Carajás iron-ore district, Brazil. Chem. Geol. 362, 91 – 104. https://doi.org/10.1016/j.chemgeo.2013.08.041.

Chauvel, C., Dupré, B., Todt, W., Arndt, N.T., 1993. Pd and Nd isotopic correlation in Belingwe komatiites and basalts. In: Bickle, M.J., Nisbet, E.G. (Eds.) The Geology of the Belingwe Greenstone Belt, Zimbabwe: A Study of the Evolution of Archaean Continental Crust. Geol. Soc. Zimbabwe Spec. Pub. 2, Rotterdam, Balkema, pp. 167–174.

Cheney, E.S., 1996. Sequence stratigraphy and plate tectonic significance of the Transvaal succession of southern Africa and its equivalent in Western Australia. Precambrian Res. 79, 3–24. https://doi.org/10.1016/0301-9268(95)00085-2.

Cohen, K.M., Finney, S.C., Gibbard, P.L., Fan, J.-X., 2013. The ICS international chronostratigraphic chart (updated). Episodes 36, 199–204.

Cogné, J.P., 2003. PaleoMac: A Macintosh™ application for treating paleomagnetic data and making plate reconstructions. Geochem. Geophys. Geosyst. 4, 1007. https://doi.org/10.1029/2001GC000227.

Cordani, U.G., Teixeira, W., 2007. Proterozoic accretionary belts in the Amazonian Craton. Geological Society of America Memoirs 200, 297–320. https://doi.org/10.1130/2007.1200(14).

Corfu, F. and Stott, G.M., 1989. U-Pb geochronology of the central Uchi subprovince, NW Ontario. Geol. Assoc. Can. Annu. Mtg., Program with Abstracts, 14: A55. https://doi.org/10.1139/e93-100.

D'Agrella-Filho, M.S., Bispo-Santos, F., Trindade R.I.F., Antonio, P.Y.J., 2016. Paleomagnetism of the Amazonia Craton and its role in paleocontinents. Brazilian Journal of Geology 46, 275-299. https://doi.org/10.1590/2317-4889201620160055.

Day, R., Fuller, M., Schmidt, V.A., 1977. Hysteresis properties of titanomagnetites: grainsize and compositional dependence. Phys. Earth Planet. Inter. 13, 260–267. https://doi.org/10.1016/0031-9201(77)90108-X.

de Kock, M.O., Evans, D.A.D., Beukes, N.J., 2009. Validating the existence of Vaalbara in the Neoarchean. Precambrian Res. 174, 145–154. https://doi.org/10.1016/j.precamres.2009.07.002.

Denyszyn, S.W., Feinberg, J.M., Renne, P.R., Scott, G.R., 2013. Revisiting the age and paleomagnetism of the Modipe Gabbro of South Africa. Precambrian Res. 238, 176–185. https://doi.org/10.1016/j.precamres.2013.10.002.

Dreher, A.M., Xavier, R.P., Taylor, B.E., Martini, S.L., 2008. New geologic, fluid inclusion and stable isotope studies on the controversial Igarapé Bahia Cu-Au deposit, Carajás Province, Brazil. Miner. Deposita 43, 161–184. https://doi.org/10.1007/s00126-007-0150-6.

Dunlop, D.J., 1983. Paleomagnetism of Archean rocks from northwestern Ontario: Wabigoon gabbro, Wabigoon Subprovince. Can. J. Earth Sci. 20, 1805-1817. https://doi.org/10.1139/e83-172.

Dunlop, D.J., Özdemir, Ö., 1997. Rock Magnetism: Fundamentals and Frontiers. Cambridge Univ. Press, Cambridge, U.K. (572 pp.).

Dunlop, D.J., 2002. Theory and application of the Day plot (Mrs/Ms versus Hcr/Hc) 1. Theoretical curves and tests using titanomagnetite data. J. Geophys. Res.: Solid Earth 107, B3. https://doi.org/10.1029/2001JB000486.

Eriksson, P.G., Condie, K.C., 2014. Cratonic sedimentation regimes in the ca. 2450–2000Ma period: relationship to a possible widespread magmatic slowdown on Earth? Gondwana Res. 25, 30–47. https://doi.org/10.1016/j.gr.2012.08.005.

Ernst, R.E., 2014. Large Igneous Provinces, 1–653. Cambridge University Press, Cambridge.

Ernst, R.E., Bleeker, W., 2010. Large igneous provinces (LIPs), giant dyke swarms, and mantle plumes: significance for breakup events within Canada and adjacent regions from 2.5 Ga to the present. Can. J. Earth Sci. 47, 695–739. https://doi.org/10.1139/E10-025.

Ernst, R.E., Buchan, K.L., 2001. Large mafic magmatic events through time and links to mantle plume-heads. In: Ernst, R.E., Buchan, K.L., (eds.) Mantle Plumes: Their Identification

Through Time, Geological Society of America Special Paper, 352, pp. 483–575. https://doi.org/10.1130/0-8137-2352-3.483.

Evans, D.A.D., Li, Z.X. and Murphy, J.B., 2016. Four-dimensional context of Earth's supercontinents. Geological Society, London, Special Publications, 424, pp.1-14. https://doi.org/10.1144/SP424.12.

Figueiredo e Silva, R.C., Lobato, L.M., Zucchetti, M., Hagemann, S., Vennemann, T., 2020. Geotectonic signature and hydrothermal alteration of metabasalts under-and overlying the giant Serra Norte iron deposits, Carajás mineral Province. Ore Geology Reviews 120, 103407. https://doi.org/10.1016/j.oregeorev.2020.103407.

Fisher, R., 1953. Dispersion on a sphere. Proc. R. Soc. Lond. A 217, 295–305. https://doi.org/10.1098/rspa.1953.0064.

Galarza, M.A., Macambira, M.J.B., Villas, R.N.N., 2008. Dating and isotopic characteristics (Pb and S) of the Fe oxide-Cu-Au-U-REE Igarapé Bahia ore deposit, Carajás mineral province, Pará state, Brazil. J. S. Am. Earth Sci. 25, 377–397. https://doi.org/10.1016/j.jsames.2007.07.006.

Gerya, T., 2019, Geodynamics of the early Earth: Quest for the missing paradigm: Geology, v. 47, p. 1006–1007, https://doi.org/10.1130/focus102019.1.

Gibbs, A.K., Wirth, K.R., Hirata, W.K., Olszewski Jr., W.J., 1986. Age and composition of the Grão Pará Group volcanics, Serra dos Carajás. Revista Brasileira de Geociências 16, 201–211.

Gumsley, A.P., 2017. Validating the existence of the supercraton Vaalbara in the Mesoarchaean to Palaeoproterozoic. Doctoral dissertation, Lithosphere and Biosphere Science, Department of Geology, Lund University. Litholund theses 30, 130.

Gumsley, A.P., Chamberlain, K.R., Bleeker, W., Söderlund, U., de Kock, M.O., Larsson, E.R., Bekker, A., 2017. Timing and tempo of the Great Oxidation Event. Proc. Natl. Acad. Sci. U. S. A. 114, 1811–1816. https://doi.org/10.1073/pnas.1608824114.

Hale, C.J., Lloyd, P., 1990. Paleomagnetic Analysis of Regional and Contact Strains. Ontario Geol. Surv. Misc. Paper. 150, 97-106.

Halls, H.C., 1978. The use of converging remagnetization circles in palaeomagnetism. Phys. Earth Planet. Inter. 16, 1–11. https://doi.org/10.1016/0031-9201(78)90095-X.

Halla, J., 2002. Origin and Paleoproterozoic reactivation of Neoarchean high-K granitoid rocks in eastern Finland. Finnish Academy of Science and Letters. Annales Academia e Scientiarum Fennicae, Geologica-Geographica 163, 105.

Halla, J., Whitehouse, M.J., Ahmad, T., Bagai, Z., 2017. Archaean granitoids: an overview and significance from a tectonic perspective. In: Halla, J., Whitehouse, M. J., Ahmad, T., Bagai, Z. (eds). Crust–Mantle Interactions and Granitoid Diversification: Insights from Archaean Cratons. Geological Society, London, Special Publications, 449, pp. 1–18. https://doi.org/10.1144/SP449.10.

Hawkesworth, C.J., Cawood, P.A., Dhuime, B., 2020. The Evolution of the Continental Crust and the Onset of Plate Tectonics. Frontiers in Earth Science, 8 (326). https://doi.org/10.3389/feart.2020.00326.

Holdsworth R.E. & Pinheiro R.V.L. 2000. The anatomy of shallow-crustal transpressional structures: insights from the Archean Carajás fault zone, Amazon, Brazil. Journal of Structural Geology, 22, 1105-1123. https://doi.org/10.1016/S0191-8141(00)00036-5.

Hrouda, F., 1994. A technique for the measurement of thermal changes of magnetic susceptibility of weakly magnetic rocks by the CS-2 Apparatus and KLY-2 Kappabridge. Geophys. 1. Int. 118, 604–612. https://doi.org/10.1111/j.1365-246X.1994.tb03987.x.

Kirschvink, J.L., 1980. The least-squares line and plane and the analysis of palaeomagnetic data. Geophys. J. Int. 62, 699–718. https://doi.org/10.1111/j.1365-246X.1980.tb02601.x.

Kirschvink, J.L., Kopp, R.E., Raub, T.D., Baumgartner, C.T., Holt, J.W., 2008. Rapid, precise, and high-sensitivity acquisition of paleomagnetic and rock-magnetic data: Development of a low-noise automatic sample changing system for superconducting rock magnetometers. Geochemistry Geophysics. Geosys. 9. https://doi.org/10.1029/2007GC001856.

Konhauser, K., Lalonde, S., Planavsky, N., Pecoits, E., Lyons, T., Mojzsis, S., Rouxel, O., Fralick, P., Barley, M., Kump, L., Bekker, A., 2011. Aerobic bacterial pyrite oxidation and acid rock drainage during the Great Oxidation Event. Nature 478, 369–373. https://doi.org/10.1038/nature10511.

Krymsky, R.S., Macambira, J.B., Macambira, M.J.B, 2002. Geocronologia U-Pb em zircão de rochas vulcânicas da Formação Carajás, Estado do Pará. In: Simpósio Sobre Vulcanismo e Ambientes Associados, 2, Belém, Anais. Belém, 41p. (in Portuguese).

Kumar, A., Parashuramulu, V., Shankar, R., Besse, J., 2017: Evidence for a Neoarchean LIP in the Singhbhum craton, eastern India: Implications to Vaalbara supercontinent. Precambrian Res. 292, 163-174. https://doi.org/10.1016/j.precamres.2017.01.018.

Liu Y, Mitchell RN, Li ZX, Kirscher U, Pisarevsky SA, Wang C. Archean geodynamics: Ephemeral supercontinents or long-lived supercratons. Archean geodynamics: Ephemeral supercontinents or long-lived supercratons. Geology, 49, G48575.1. https://doi.org/10.1130/G48575.1.

Lubnina, N.V., Slabunov, A.I., 2009. Paleomagnetism in the Neoarchean Polyphase Panozero Intrusion in the Fennoscandian Shield. Mosc. Univ. Geol. Bull. 64, 346–353. https://doi.org/10.3103/S0145875209060039.

Macambira, J.B., 2003. O ambiente deposicional da Formação Carajás e uma proposta de modelo evolutivo para a Bacia Grão Pará (Unpublish Ph.D. Thesis), Instituto de Geociências, Universidade Estadual de Campinas, pp. 217.

Machado, N., Lindenmayer, Z.G., Krogh, T.E., Lindenmayer, D., 1991. U-Pb geochronology of Archean magmatism and basement reactivation in the Carajás area, Amazon shield, Brazil. Precambrian Res. 49, 329–354. https://doi.org/10.1016/0301-9268(91)90040-H.

Martins, P.L.G., Toledo, C.L.B., Silva, A.M., Chemale Jr., F., Santos, J.O.S., Assis, L.M., 2017. Neoarchean magmatism in the southeastern Amazonian Craton, Brazil: petrography, geochemistry and tectonic significance of basalts from the Carajás Basin. Precambrian Res. 302, 340–357. https://doi.org/10.1016/j.precamres.2017.10.013.

Meert, J.G., Pivarunas, A. F., Evans, D.A.D., Pisarevsky, S.A., Pesonen, L.J., Li, Z., Elming, S., Miller, S.R., Zhang, S., Salminen, J.M., 2020. The magnificent seven: A proposal for modest revision of the Van der Voo (1990) quality index. Tectonophysics, 790, 228549. https://doi.org/10.1016/j.tecto.2020.228549.

Meirelles, M.R., Dardenne, M.A., 1991. Vulcanismo basáltico de afinidade shoshonítica e ambiente de arco arqueano, Grupo Grão-Pará, Serra dos Carajás, Pará. Revista Brasileira de Geociências 21, 41–50 (in Portuguese).

Mertanen, S., Korhonen, F., 2011. Paleomagnetic constraints on an Archean- Paleoproterozoic Superior-Karelia connection: New evidence for Archean Karelia. Precambrian Res. 186, 193–204. https://doi.org/10.1016/j.precamres.2011.01.018.

Moreto, C.P.N., Monteiro, L.V.S., Xavier, R.P., Creaser, R.A., DuFrane, S.A., Melo, G.H.C., Delinardo da Silva, M.A., Tassinari, C.C.G., Sato, K., 2015. Timing of multiple hydrothermal events in the iron oxide–copper–gold deposits of the Southern Copper Belt, Carajás Province, Brazil. Miner. Deposita 50, 517–546. https://doi.org/10.1007/s00126-014-0549-9.

Morrison, D.A., Davis, D.W., Wooden, J.L., Bogard, D.D., Maczuga, D.E., Phinney, W.C., Ashwal. L.D., 1985. Age of the Mulcahy Lake intrusion, northwest Ontario, and implications for the evolution of greenstone-granite terrains. Earth Planet. Sci. Lett, 73, 306-316. https://doi.org/10.1016/0012-821X(85)90079-2.

Müller, R.D., Cannon, J., Qin, X., Watson, R.J., Gurnis, M., Williams, S., Pfaffelmoser, T., Seton, M., Russel, S.H.J., Zahirovic, S., 2018. GPlates: Building a virtual Earth through deep time. Geochemistry, Geophysics, Geosystems, 19. https://doi.org/10.1029/2018GC007584.

Olsson, J.R., Söderlund, U., Klausen, M.B., Ernst, R.E., 2010. U-Pb baddeleyite ages linking major Archean dyke swarms to volcanic-rift forming events in the Kaapvaal craton (South Africa), and a precise age for the Bushveld Complex. Precambrian Res. 183, 490–500. https://doi.org/10.1016/j.precamres.2010.07.009.

Olszewski, W.J., Wirth, K.R., Gibbs, A.K., Gaudette, H.E., 1989. The age, origin, and tectonics of the Grão Pará Group and associated rocks, Serra dos Carajás, Brazil: Archean continental volcanism and rifting. Precambrian Res. 42, 229–254. https://doi.org/10.1016/0301-9268(89)90013-2.

Pesonen L.J., Elming S.Å., Mertanen S., Pisarevsky S., D'Agrella- Filho M.S., Meert J.G., Schmidt P.W., Abrahamsen N., Bylund G. 2003. Palaeomagnetic configuration of continents during the Proterozoic. Tectonophysics, 375:289-324. https://doi.org/10.1016/S0040-1951(03)00343-3.

Pivarunas, A.F., Meert, J.G., Miller, S.R., 2018. Assessing the intersection/ remagnetization puzzle with synthetic apparent polar wander paths. Geophys. J. Int. 214, 1164–1172. https://doi.org/10.1093/gji/ggy216.

Premo, W.R., Helz, R.T., Zientek, M.L., Langston, R.B., 2000. U-Pb and Sm-Nd ages for the Stillwater Complex and its associated sills and dikes, Beartooth Mountains, Montana: Identification of a parent magma? Geology 18, 1065–1068. https://doi.org/10.1130/0091-7613(1990)018<1065:UPASNA>2.3.CO;2.

Rapalini, A.E., Luppo, T., Llanos, M.P.I., Vásquez, C.A., Valencio, L.d.P.D.A., 2013. Successful paleomagnetic azimuthal orientation of drill cores from a hydrocarbon source rock reservoir: the case of the Vaca Muerta Formation, Neuquen Basin, Argentina. Latinmag Letters, 3, Special Issue, 1-5.

Reddy, S.M., Evans, D.A.D., 2009. Palaeoproterozoic supercontinents and global evolution: correlations from core to atmosphere. Geol. Soc. Spec. Pub. 323, 1–26. https://doi.org/10.1144/SP323.1.

Rolph, T.C., Shaw, J., Harper, T.R., Hagan, J.T., 1995. Viscous remanent magnetization: a tool for orientation of drill cores. Geological Society, London, Special Publications, 98, 239-243. https://doi.org/10.1144/GSL.SP.1995.098.01.14.

Rosière, C.A., Baars, F.J., Seoane, J.C.S., Lobato, L.M., Silva, L.L., Mendes, G.E., 2006. Structure and iron mineralization of the Caraj´as province. B. Appl. Earth Sci. 115 (4), 126–133. https://doi.org/10.1179/174327506X138986

Rossignol, C., Rego, E.S., Narduzzi, F., Teixeira, L., Ávila, J.N., Silva, M.A.L., Lana, C., Philippot, P., 2020. Stratigraphy and geochronological constraints of the Serra Sul Formation (Carajás Basin, Amazonian Craton, Brazil). Precambrian Res. 351, 105981. https://doi.org/10.1016/j.precamres.2020.105981.

Rossignol, C., Antonio, P.Y.J., Narduzzi, F., Rego, E.S., Teixeira, L., de Souza, R.A., Ávila, J.N., Silva, M.A.L., Lana, C., Trindade, R.I.F., Philippot, P., 2021. Unraveling one billion years of geological evolution of the southeastern Amazonia Craton from detrital zircon analyses. Geoscience Frontiers (in press), 101202. https://doi.org/10.1016/j.gsf.2021.101202.

Rudnick, R.L., Gao, S., 2003. Composition of the continental crust. In: Rudnick, R.L. (Ed.), The Crust. Elsevier-Pergamon, Oxford, pp. 1–64. https://doi.org/10.1016/B0-08-043751-6/03016-4.

Salminen, J., Oliveira, E. P., Piispa, E. J., Smirnov, A. V., Trindade, R. I. F., 2019. Revisiting the paleomagnetism of the Neoarchean Uauá mafic dyke swarm, Brazil: Implications for Archean supercratons. Precambrian Res. 329, 108-123, https://doi.org/10.1016/j.precamres.2018.12.001.

Schmidt, P.W., Embleton, B.J.J., 1985. Prefolding and overprint magnetic signatures in Precambrian (c.2.9-2.7 Ga) igneous rocks from the Pilbara craton and Hamersley Basin, NW Australia. J. Geophys. Res. 90, 2967–2984. https://doi.org/10.1029/JB090iB04p02967.

Selkin, P.A., Gee, J.S., Meurer, W.P., Hemming, S.R., 2008. Paleointensity record from the 2.7 Ga Stillwater Complex, Montana. Geochem. Geophys. Geosyst. 9, Q12023. https://doi.org/10.1029/2008GC001950.

Sergeyev, S.A., Lobach-Zhuchenko, S.B., Larionov, A.N., Berezhnaya, N.G., Guseva, N.S., 2007. Archaean age of miaskite lamproites from the Panozero complex, Karelia. Dokl. Earth Sci. 413, 420–423. https://doi.org/10.1134/S1028334X07030221.

Smirnov, A.V., Evans, D.A.D., Ernst, R.E., Söderlund, U., Li, Z.-X., 2013: Trading partners: Tectonic ancestry of southern Africa and western Australia, in Archean supercratons Vaalbara and Zimgarn. Precambrian Res. 224, 11-22. https://doi.org/10.1016/j.precamres.2012.09.020.

Strik, G., Blake, T.S., Zegers, T.E., White, S.H., Langereis, C.G., 2003. Palaeomagnetism of flood basalts in the Pilbara Craton, Western Australia: Late Archaean continental drift and the oldest known reversal of the geomagnetic field. Journal of Geophysical Research, Solid Earth 108, 1–21. https://doi.org/10.1029/2003JB002475.

Tallarico, F.H.B., Figueiredo, B.R., Groves, D.I., Kositcin, N., McNaughton, N.J., Fletcher, I.R., Rego, J.L., 2005. Geology and SHRIMP U-Pb geochronology of the Igarapé Bahia deposit, Carajás copper-gold belt, Brazil: an Archean (2.57 Ga) example of iron-oxide Cu-Au-(U-REE) mineralization. Econ. Geol. 100, 7–28. https://doi.org/10.2113/100.1.0007.

Tavares, F.M., Trouw, R.A.J., da Silva, C.M.G., Justo, A.P., Oliveira, J.K.M., 2018. The multistage tectonic evolution of the northeastern Carajás Province, Amazonian Craton, Brazil: Revealing complex structural patterns. J. S. Am. Earth Sci. 88, 238–252. https://doi.org/10.1016/j.jsames.2018.08.024.

Teixeira, J.B.G., Eggler, D.H., 1994. Petrology, geochemistry, and tectonic setting of Archaean basaltic and dioritic rocks from the N4 iron deposit, Serra dos Carajás, Pará, Brazil. Acta Geol. Leopoldensia 17, 71–114.

Teixeira, N. A., Campos, L. D., de Paula R. R., Lacasse, C., M., Ganade, C. E., Monteiro, C. F., Lopes, L. B. L., Oliveira, C. G., 2021. Carajás Mineral Province - Example of metallogeny of a rift above a cratonic lithospheric keel. J. S. Am. Earth Sci. 108, 103091. https://doi.org/10.1016/j.jsames.2020.103091.

Teixeira, W., Hamilton, M., Girardi, V.A.V., Faleiros, F.M., Ernst, R.E., 2019. U-Pb baddeleyite ages of key dyke swarms in the Amazonian Craton (Carajás/Rio Maria and Rio Apa areas): tectonic implications for events at 1880, 1110 Ma, 535 Ma and 200 Ma. Precambrian Res. 329, 138–155. https://doi.org/10.1016/j.precamres.2018.02.008.

Trendall, A.F., 1968. Three great basins of Precambrian iron formation deposition: asystematic comparison. Geol. Soc. Am. Bull. 79, 1527–1533. https://doi.org/10.1130/0016-7606(1968)79[1527:TGBOPB]2.0.CO;2.

Trendall, A.F., Basei, M.A.S., De Laeter, J.R., Nelson, D.R., 1998. SHRIMP zircon U-Pb constraints on the age of the Carajás Formation, Grão Pará Group, Amazon Craton. J. S. Am. Earth Sci. 11, 265– 277. https://doi.org/10.1016/S0895-9811(98)00015-7.

Vasquez, M.L., Carvalho, J.M.A., Sousa, C.S., Ricci, P.S.F., Macambira, E.M.B., Costa, L.T. R., 2008. Mapa Geológico do Pará em SIG. Brazilian Geological Survey – CPRM.

Williams, H., Hoffman, P.F., Lewry, J.F., Monger, J.W.H., Rivers, T., 1991. Anatomy of North America: thematic geologic portrayals of the continent. Tectonophysics 187, 117–134. https://doi.org/10.1016/0040-1951(91)90416-P.

Wingate, M.T.D., 1998: A palaeomagnetic test of the Kaapvaal-Pilbara (Vaalbara) connection at 2.78 Ga. South African J. Geol. 101, 257–274.

Wingate, M.T.D., 1999. Ion microprobe baddeleyite and zircon ages for late Archaean mafic dykes of the Pilbara Craton, Western Australia. Aust. J. Earth Sci. 46, 493–500. https://doi.org/10.1046/j.1440-0952.1999.00726.x.

Yoshihara, A., Hamano, Y., 2004. Paleomagnetic constraints on the Archean geomagnetic field intensity obtained from komatiites of the Barberton and Belingwe greenstone belts, South Africa and Zimbabwe. Precambrian Res. 131, 111–142. https://doi.org/10.1016/j.precamres.2004.01.003.

Zahirovic, S., Müller, R.D., Seton, M., Flament, N., 2015. Tectonic speed limits from plate kinematic reconstructions. Earth. Planet. Sci. Lett. 418, 40-52. https://doi.org/10.1016/j.epsl.2015.02.037.

Zhang, C.L., Ye, X.T., Ernst, R.E., Zhong, Y., Zhang, J., Li, H.K., Long, X.P., 2019. Revisiting the Precambrian evolution of the Southwestern Tarim Terrane: implication for its role in Precambrian supercontinents. Precambrian Res. 324, 18–31. https://doi.org/10.1016/j.precamres.2019.01.018.

Zijderveld, J., 1967. AC demagnetization of rocks: analysis of results. Methods Paleomagn. 3, 254.

Zucchetti, M., 2007, Rochas máficas do Supergrupo Grão Pará e sua relação com a mineralização de ferro dos depósitos N4 e N5, Carajás, PA: Unpublished Ph.D. thesis, Belo Horizonte, Brazil, Universidade Federal de Minas Gerais, 125 p (in Portuguese).

SUPLEMENTARY MATERIAL

This file contains:

Supplementary figures (Fig. S1 and S2)

Supplementary table (Table S1)

References

SUPPLEMENTARY FIGURES

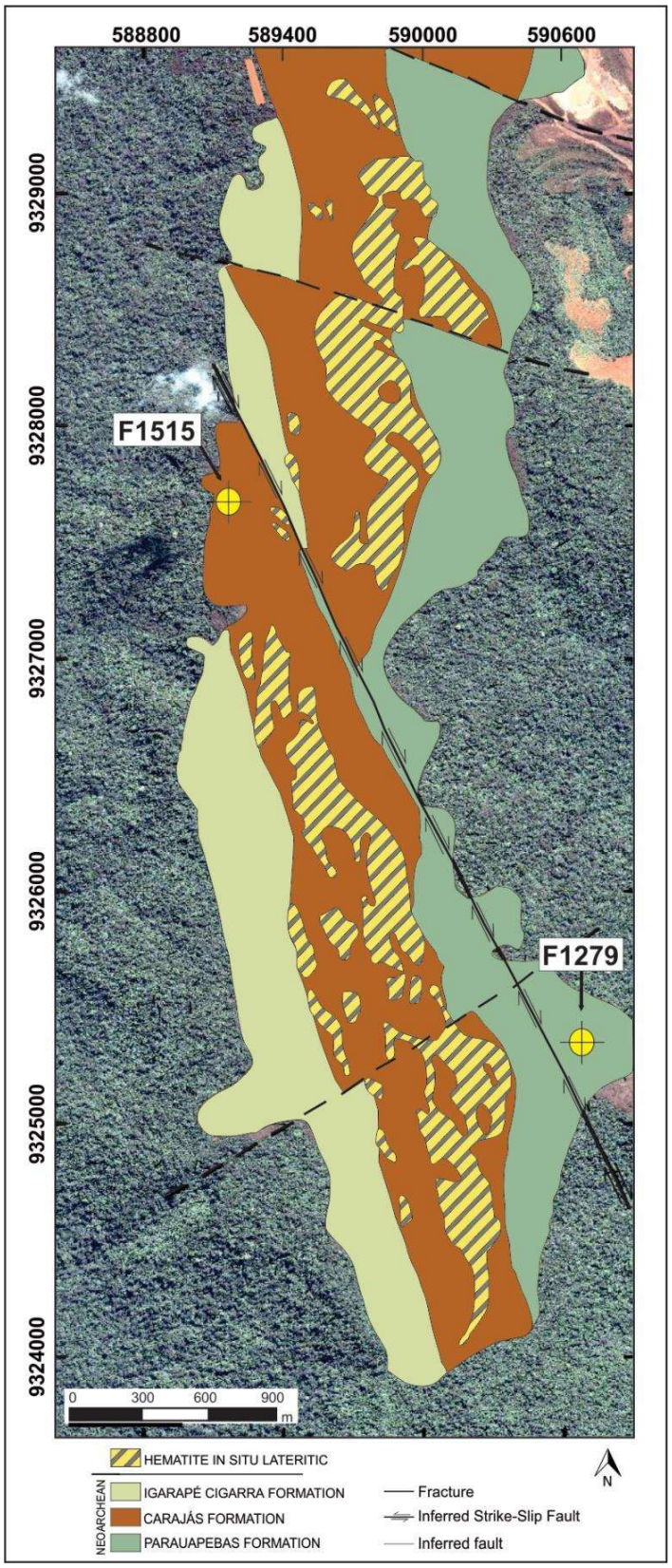

Fig. S1. *Geological map of the N4WS body, showing the position of each sampled drill hole (modified after Resende & Barbosa, 1972).*

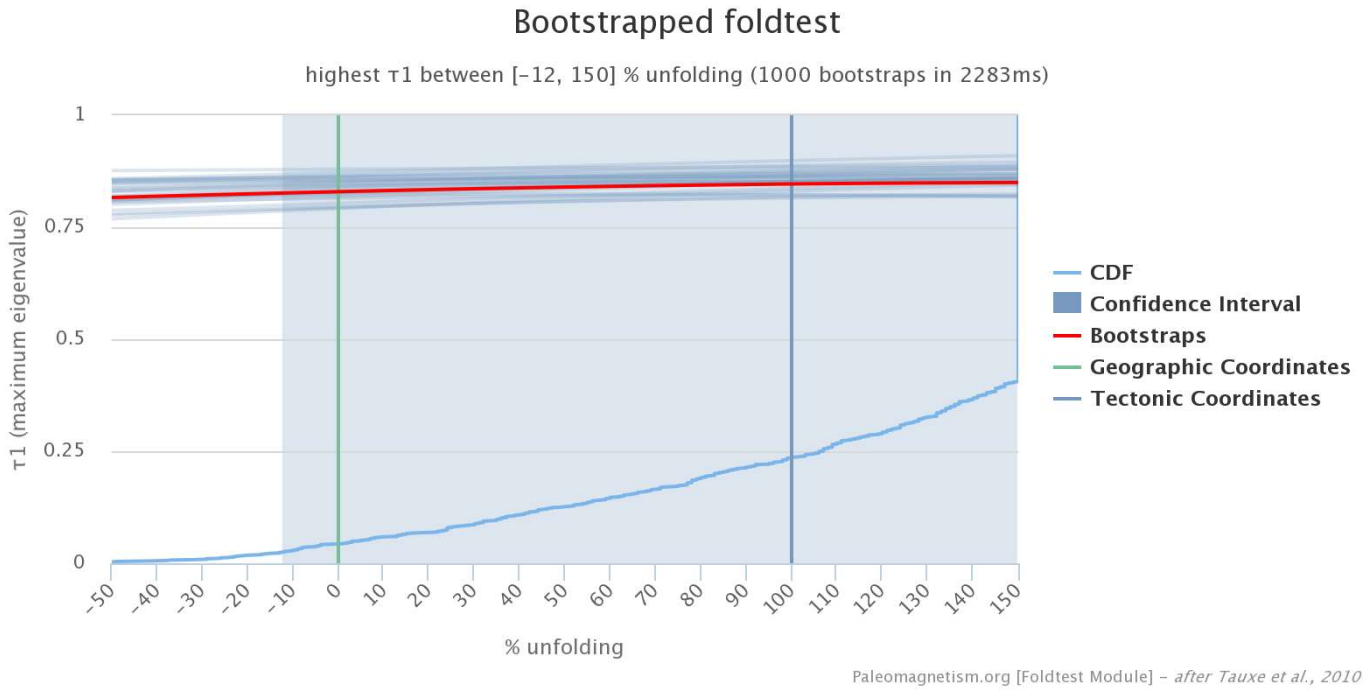

Fig S2. *Bootstrapped foldtest for Parauapebas Formation, Carajás Basin (C2 group samples). As the dip of the both side of the fold are really low, the fold test is inconclusive (Tauxe et al., 1994).*

SUPPLEMENTARY TABLE

Table S1. *Day plot (Day et al., 1977) database of the Parauapebas Formation's samples.*

Sample	Mass (Kg)	Mr (Am^2)	Ms (Am^2)	Hcr (T)	Hc (T)	Mr/Ms	Hcr/Hc
F1279-B	0.000124	2.60E-03	1.62E-02	4.78E-02	1.84E-02	0.16	2.60
F1279-C	0.000138	3.14E-03	2.28E-02	4.99E-02	1.55E-02	0.14	3.21
F1279-D	0.000152	1.33E-03	8.21E-03	4.23E-02	1.52E-02	0.16	2.78
F1279-G	0.000142	2.40E-03	1.48E-02	4.24E-02	1.58E-02	0.16	2.69
F1279-J	0.000132	4.56E-04	4.68E-03	3.96E-02	8.64E-03	0.10	4.59
F1279-M	0.000131	1.63E-03	8.31E-03	3.62E-02	1.49E-02	0.20	2.43
F1279-P	0.000141	1.61E-02	1.35E-01	3.60E-02	1.25E-02	0.12	2.89
F1279-R	0.000141	9.66E-02	7.35E-01	3.70E-02	1.40E-02	0.13	2.64
F1279-T	0.000147	2.58E-02	2.19E-01	3.53E-02	1.16E-02	0.12	3.04
F1279-X	0.000159	1.89E-04	2.87E-03	3.20E-02	8.04E-03	0.07	3.97
F1279-Y	0.000134	7.78E-04	8.45E-03	3.35E-02	9.31E-03	0.09	3.60
F1279-Z	0.000131	2.29E-03	2.03E-02	4.55E-02	1.21E-02	0.11	3.77
F1279-ZB	0.000134	5.29E-03	6.18E-02	4.08E-02	9.25E-03	0.09	4.41
F1279-ZD	0.000123	7.32E-04	8.83E-03	4.12E-02	9.81E-03	0.08	4.21
F1279-ZE	0.000174	1.61E-02	1.85E-01	3.68E-02	8.67E-03	0.09	4.25

Coercivity (Hc), Coercivity of remanence (Hcr), Saturation magnetization (Ms) and saturation remanence (Mr).

REFERENCES

Day, R., Fuller, M., Schmidt, V.A., 1977. Hysteresis properties of titanomagnetites: grainsize and compositional dependence. Phys. Earth Planet. Inter. 13 (4), 260–267.

Resende N.P., e Barbosa A.L.M., 1972, Relatório de Pesquisa de Minério de Ferro, Distrito Ferrífero da Serra dos Carajás, Estado do Pará. AMZA, Relatório Final de Pesquisa, v. 1, texto, 248 p, v. 2, mapas e seções geológicas, p. 119 (in Portuguese).

Tauxe, L. and G.S. Watson, The fold test: an eigen analysis approach. Earth and Planetary Science Letters, 1994. 122(3): p. 331-341.

CAPÍTULO 5 – ARTIGO II: *CHEMOSTRATIGRAPHY OF THE CARAJÁS BANDED IRON FORMATION, BRAZIL: A RECORD OF NEOARCHEAN OCEAN CHEMISTRY*

Observação

Este capítulo trará o artigo científico submetido ao periódico *Gondwana Research*, intitulado "*Chemostratigraphy of the Carajás banded iron formation, Brazil: A record of Neoarchean Ocean chemistry*". Os tópicos foram divididos e resumidos para se adequar a exigência da revista que o trabalho foi submetido. Os anexos citados no artigo foram acrescentados no final do capítulo.

CHEMOSTRATIGRAPHY OF THE CARAJÁS BANDED IRON FORMATION, BRAZIL: A RECORD OF NEOARCHEAN OCEAN CHEMISTRY

Pedro L.G. Martins[a,*]*; Catarina L.B. Toledo*[a]*; Adalene M. Silva*[a]*; Farid Chemale Jr.* [b]*; Corey Archer*[c]*; Luciano M. de Assis* [d]

[a] Universidade de Brasília, Instituto de Geociências, 70910-900 Brasília, DF, Brazil.

[b] Universidade do Vale do Rio dos Sinos, Departamento de Geologia, 93022-000 São Leopoldo, RS, Brazil.

[c] Institute of Geochemistry and Petrology, Department of Earth Sciences, ETH Zürich, Clausiusstrasse 25, 8092 Zürich, Switzerland.

[d] Exploração Mineral de Ferrosos, Vale S.A., CTF - Miguelão, Fazenda Rio de Peixe, s/nº, Nova Lima, MG, Brazil.

*Corresponding Author.

Tel: +55 61 993181098

E-mail address: plgmartins@gmail.com (P.L.G. Martins)

Abstract

One of the most important occurrences of banded iron formation (BIF) worldwide is situated in the Carajás Mineral Province, southeastern Amazonian Craton. The BIFs are jaspilites and are hosted in the Neoarchean (~2.74 Ga) volcano-sedimentary sequence of the Grão-Pará Group. They are mostly composed of cm-thick intercalations of hematite, jasper, and chert. Their primary textures and structures are still preserved, which make them an ideal archive to evaluate the paleomarine environment. Low abundance of Al_2O_3 (< 1.0 wt.%) and high field strength elements (< 1 ppm) for most BIF samples indicate an essentially detritus-free depositional environment. Overall, the rare earth elements and yttrium (REY) patterns show a

weak positive lanthanum (La) anomaly, and a pronounced positive europium (Eu) anomaly (Eu/Eu_{PAAS} = 1.86 – 5.05), although the presence of true cerium (Ce) anomaly is not evident. Stratigraphic variations in iron isotope compositions, up to 0.80 ‰ ($\delta^{56}Fe$ = +1.10 to +1.90 ‰) over tens to hundreds of meters of stratigraphic section, point to relative changes in the iron isotope composition of Carajás seawater over periods of a few million years. The jaspilites show heterogeneous distribution of Nd isotopic signature throughout the BIF sequence, and rocks from near the basaltic flows/jaspilite contact (type-II) have negative εNd (t) values (–4.97 to –0.90). In contrast, predominantly positive εNd(t) values (–0.84 to +5.40) are common in the remaining samples (type-I). The strongly positive δ56Fe values indicate a low degree of partial oxidation of Fe(II), which, combined with the pronounced positive Eu anomalies and the absence of Ce anomalies, hint towards that the deposition occurred mainly on a deep-sea environment with intense hydrothermal activity under anoxic and suboxic conditions, distal to continental landmasses. Locally, considerable oxygen was probably present in the ancient ocean's water masses, which led to the precipitation of BIFs.

Keywords: Carajás Province, Banded Iron Formation, Chemostratigraphy, Neoarchean Ocean chemistry, Fe isotopes.

1. Introduction

Banded Iron Formations (BIFs) are chemical sedimentary rocks composed of iron-rich (~30 wt.%) and siliceous-rich layers that were widely deposited in the Precambrian oceans (James, 1954; Cloud, 1973; Holland, 1973; Bekker et al., 2010; 2014; Konhauser et al., 2017). They have been studied widely in the last century to constrain the geochemical environment prevailing in the oceans at the time of their deposition (Bekker et al., 2014; Konhauser et al., 2017). Accordingly, the trace element signatures of BIFs have often been used to investigate

the chemical composition and oxidative conditions of ancient seawater. Nevertheless, in spite of its great interest, the mechanisms responsible for the deposition of Precambrian BIFs are not well understood.

The elemental composition of the rare earth element plus yttrium (REE+Y; simplified as REY throughout the text) of BIFs has been widely used as a geochemical proxy since 1960. These elements are considered as robust geochemical tracers to constrain the origins of BIFs, as they can provide information on the redox state of paleo-oceans in the early Precambrian (Bau et al., 1997; Alexander et al., 2008). Based on the composition of BIF, it is now generally accepted that deep-sea hydrothermal fluids are the most likely source of Fe (Bolhar et al., 2004; Konhauser et al., 2017). Because the Archaean crust was more mafic, a significant contribution of "continental" iron has been also suggested as possible source material for BIFs (Haugaard et al., 2013; Dhuime et al., 2015; Lee et al., 2016). Shale-normalized (SN) europium (Eu) anomalies have been central in the use of REY to trace the hydrothermal input. The enrichment of Eu in chemical sedimentary rocks precipitated from seawater (e.g., BIFs) indicates a strong influence of high-temperature hydrothermal fluids on the REE load dissolved in seawater (Klinkhammer et al., 1983; Michard & Albarède, 1986; Derry & Jacobsen, 1988, 1990). In addition to the characteristic REY patterns, samarium (Sm) and neodymium (Nd) isotopic abundances preserved in BIFs can be also used to unravel the REY sources of seawater. This is because the similar chemical affinities of Sm and Nd make the Sm/Nd ratio highly resistant to disturbances by metamorphism and continental weathering (Piepgras & Wasserburg, 1987; Elderfield et al., 1990; Andersson et al., 1992).

With the advancement in isotope mass spectrometry, the sources of iron and REY contents of seawater have been investigated based mostly on solution Fe isotope analyses coupled with the robust Sm–Nd isotope systematics (Konhauser et al., 2017; Peng et al., 2018;

Alfimova et al., 2019). Fe isotope geochemistry potentially provides a direct measurement of iron pathways involved in BIF genesis (e.g., Johnson et al., 2003, 2008; Dauphas et al., 2004, 2007; Rouxel et al., 2005; Frost et al., 2007; Whitehouse & Fedo, 2007; Hyslop et al., 2008; Planavsky et al., 2009; Heimann et al., 2010; Steinhoefel et al., 2010; Czaja et al., 2013, 2018; Li et al., 2015). In addition, the iron isotope is also an important tracer of oceanic redox process. Biotic or non-biotic oxidation of Fe(II) to Fe(III) in solution causes considerable Fe isotope fractionation, leading to Fe(III) to be enriched in heavy Fe, whereas Fe(II) is enriched in light Fe isotopes (Bullen et al., 2001; Johnson et al., 2002; Welch et al., 2003; Balci et al., 2006).

The Carajás Mineral Province (CMP), located in the southern Amazonian Craton of northern Brazil has one of the most important occurrences of BIFs worldwide (Fig. 1). The CMP (> 2.6 Ga) is the largest and best-preserved Archean segment of the craton. It is renowned for hosting several world-class mineral deposits, including several Cu-Au deposits, Ni deposits, and BIF-hosted giant iron deposits with an estimated inventory of approximately 18 billion ton of >65% Fe (DOCEGEO, 1988; Vasquez et al., 2008; Moreto et al., 2015). The province is comprised of two tectonic domains: (i) the Rio Maria Domain (3.0–2.85 Ga), and (ii) the Carajás Domain (Fig. 1B) (Souza et al., 2001; Vasquez et al., 2008). The geological characteristics of the CMP are summarized in the Supplementary Material. The iron deposits are mostly associated with BIFs (jaspilites) present in the volcano-sedimentary sequence of the Grão-Pará Group (Carajás Basin; Fig. 1C). Given their well-preserved BIF rock types, Carajás jaspilites provide an excellent opportunity for studying the genesis, depositional environment, and paleoenvironmental conditions during the formation of BIF at approximately 2.75 billion years ago (Trendall et al., 1998; Martins et al., 2017).

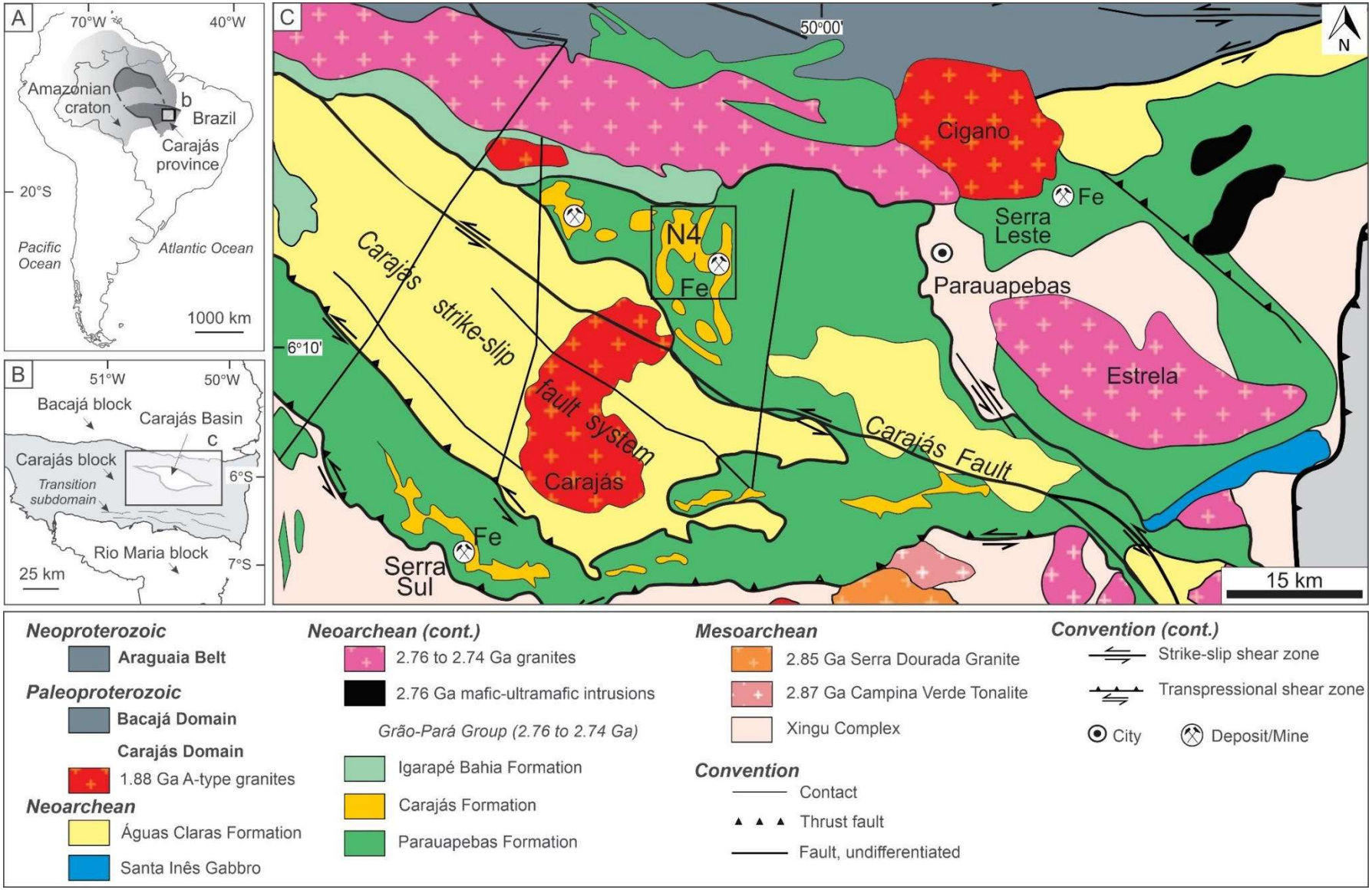
A
70°W
40°W
Amazonian craton
b
Brazil
Carajás province
20°S
Pacific Ocean
Atlantic Ocean
1000 km
B
51°W
50°W
Bacajá block
Carajás Basin
c
Carajás block
6°S
Transition subdomain
Rio Maria block
7°S
25 km
C
50°00'
N
Cigano
Fe
Serra Leste
N4
Fe
Parauapebas
Carajás strike-slip fault system
6°10'
Estrela
Carajás Fault
Carajás
Fe
Serra Sul
15 km
Neoproterozoic
Araguaia Belt
Paleoproterozoic
Bacajá Domain
Carajás Domain
1.88 Ga A-type granites
Neoarchean
Águas Claras Formation
Santa Inês Gabbro
Neoarchean (cont.)
2.76 to 2.74 Ga granites
2.76 Ga mafic-ultramafic intrusions
Grão-Pará Group (2.76 to 2.74 Ga)
Igarapé Bahia Formation
Carajás Formation
Parauapebas Formation
Mesoarchean
2.85 Ga Serra Dourada Granite
2.87 Ga Campina Verde Tonalite
Xingu Complex
Convention
Contact
Thrust fault
Fault, undifferentiated
Convention (cont.)
Strike-slip shear zone
Transpressional shear zone
City
Deposit/Mine

Fig. 1. A *Map showing the location of the Amazonian craton and the Carajás province in northern Brazil, South America;* ***B)*** *Carajás province map showing the location of the Carajás Basin in the Carajás block (from Araújo Filho et al., 2020);* ***C)*** *Simplified geologic map of the northeastern part of the Carajás Province, Carajás Basin (modified from Vasquez et al., 2008). The black rectangle indicates the approximate location of N4 deposit.*

The bulk-rock geochemical characteristics of BIFs in Carajás have attracted the interest of several researchers (Lindenmayer et al., 2001; Lobato et al., 2005; Figueiredo e Silva et al., 2008; Fabre et al., 2011; Justo et al., 2020). However, this key BIF has not been analyzed at high resolution, and a detailed comparison of its chemostratigraphy across a complete succession is yet to be attempted. In this study, we present petrography and a continuous chemostratigraphic dataset of major and trace element concentrations in an entire core section (~451 m) of the Carajás jaspilites across the N4 deposit (Serra Norte; Fig. 1C). We also provide Sm–Nd isotopic compositions and Fe isotope profiles at varying depths of the Carajás jaspilites to better identify the REY patterns and sources of Fe in seawater during their deposition. The data enable us to discuss the redox conditions of ancient seawater during the Neoarchean (~2.75 Ga), and thereby constrain the formation and depositional environment of the Carajás jaspilites.

2. Geological settings of Grão-Pará Group

The main geological assemblages of the Carajás Basin are Neoarchean to Paleoproterozoic. The basin is commonly divided into the lowermost metavolcanic–sedimentary Grão-Pará Group (2.76–2.74 Ga; Fig. 2) overlain by metasedimentary rocks of the 2.68–2.06 Ga Serra Sul and Águas Claras formations (Araújo & Nogueira, 2019; Araújo Filho et al., 2020; Rossignol et al., 2020). Because of the relatively low metamorphic grade (up to greenschist facies) of these sequences (Araújo & Maia, 1991; Vasquez et al., 2008), the prefix ‘meta’ has been omitted throughout this manuscript to simplify the rock description. The Grão-

Pará Group is the dominant volcano-sedimentary sequence of the Carajás Basin. It is approximately 260 km long and 70 km wide, and these rocks cover an area of approximately 18,000 km^2 (Macambira, 2003; Vasquez et al., 2008; Fig. 1C). The stratigraphic framework proposed by Araújo & Nogueira (2019) and Araújo Filho et al. (2020) suggests that the Grão-Pará Group can be divided, from base to top, into the Parauapebas, Carajás, and Igarapé Bahia formations (Fig. 2). The oldest unit is represented by the Parauapebas Formation, which encompasses extensive volcanism, and is dominated by mafic rocks dated at ~2.75 Ga (Olszewski et al., 1989; Trendall et al., 1998; Martins et al., 2017). It occurs concordantly beneath the Carajás Formation, which reflects contemporaneity among the two formations (Beisiegel et al., 1973; Macambira, 2003; Martins et al., 2017). This extensive volcanism is generally considered the result of an intraplate rifting of older continental crust (Gibbs et al., 1986; Olszewski et al., 1989; Martins et al., 2017; Tavares et al., 2018; Teixeira et al., 2021), although some authors (Meirelles & Dardenne, 1991; Teixeira & Eggler, 1994; Zucchetti, 2007; Figueiredo e Silva et al., 2020) have suggested the influence of a subduction-related environment.

The (intermediate) Carajás Formation (Fig. 2) comprises layers and discontinuous lenses of BIFs, as well as compact and soft (porous) iron ores, intruded by mafic sills and dikes (Macambira, 2003; Lobato et al., 2005). The BIFs are jaspilites, banded rocks consisting distinctive layering jasper (red chert) and hematite. The Carajás BIF has a thickness of ~250–400 m (Beisiegel et al., 1973; Macambira, 2003; Cabral et al., 2013), and host one of the largest high-grade (> 60 wt.% Fe) iron ore deposits in the world (Lobato et al., 2005; Figueiredo e Silva et al., 2008). They have cm-thick intercalations of iron oxide (mainly hematite), jasper, and chert, and are heavily weathered. However, the original textures and structures such as syn-sedimentary microfaults and soft-sediment deformation are still preserved (Macambira, 2003).

Previous studies on REY and isotopic compositions (e.g., Fe, C, and Nd isotopes) in these rock samples have concluded that the Carajás jaspilites were possibly deposited on deep and stable platforms, below the wave base level, and near hydrothermal vents (Lindenmayer et al., 2001; Fabre et al., 2011; Justo et al., 2020; Rego et al., 2021). The reported light REE (LREE) enrichment relative to heavy REE (HREE) and the positive Eu anomalies were mostly linked to the proximity of hydrothermal vents (Justo et al., 2020). Macambira (2003) and Ribeiro da Luz & Crowley (2012) observed clusters of microscopic spheroidal structures with a hematitic nucleus (spherulites) in chert bands of BIF samples from the Carajás region, which these researchers interpret as microfossils of dissimilatory iron-reducing bacteria (DIR). In contrast, by studying the δ^{56}Fe isotopes systematics combined with C isotope composition from two pristine drill cores intercepting the Carajás BIFs, Rego et al. (2021) advocated for the predominance of reducing conditions during the deposition of BIF, suggesting that anoxygenic photosynthesis was the most plausible mechanism responsible for Fe oxidation in the Carajás Basin.

The BIFs of the Carajás Formation are mainly exposed in the northern limb (Serra Norte) and in the southern limb (Serra Sul) of the Carajás fold. The exposures are located along the elongated flat ridges with little vegetation, and stand out at 100–200 m above the forest-covered lowlands (Cabral et al., 2013). U-Pb dating of zircon grains from a mafic sill that cuts the Carajás Formation carried out using SHRIMP suggests a minimum depositional age of 2740 ± 8 Ma for the Carajás jaspilites (Trendall et al., 1998). This age was further supported by SHIRIMP U-Pb zircon ages of two basaltic flows at 2749 ± 6.5 Ma and 2745 ± 5 Ma (Martins et al., 2017). The flows are intercalated in the Carajás Formation at the Serra Norte N4WS mine. On the other hand, the U-Pb zircon age obtained for a quartz-trachytic rock associated with the basal portions of the jaspilites established the maximum age for the Carajás Formation as 2751

± 3 Ma (Krymsky et al., 2002). If the maximum and minimum ages are correct and do not have a hiatus between the lower unit and the start of precipitation of BIF, the Carajás Formation could have been deposited in about 11 million years, which is coherent for the estimated current thickness of ~400 m. The BIF sequence is overlain by a set of volcanic and volcaniclastic rocks, in combination with subordinate deep-water marine turbidite strata belonging to the Igarapé Bahia Formation (Tallarico et al., 2005; Dreher et al., 2008; Galarza et al., 2008; Fig. 2). Existing U–Pb zircon data constrain the age of the volcanic rocks at 2744 ± 11 Ma (Galarza et al., 2008).

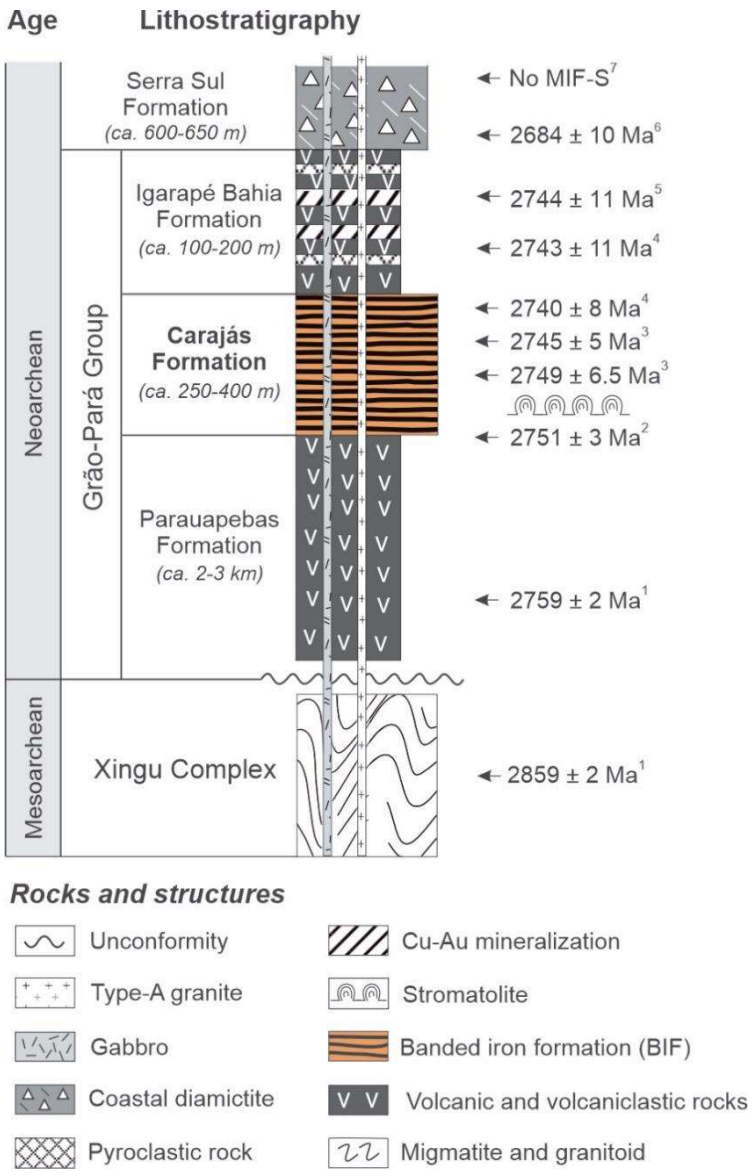

Fig. 2. *Stratigraphy of the basal part of the Carajás Basin, Amazonian craton, Brazil (modified from Araujo & Nogueira, 2019 and Araújo Filho et al., 2020). Geochronological data compiled from: 1—Machado et al. (1991); 2—Krymsky et al., 2002; 3—Martins et al. (2017); 4—Trendall et al. (1998); 5—Galarza et al. (2008); 6—Maximum depositional age from Rossignol et al. (2020). The data of mass-independent sulfur isotope fractionation (MIF-S) was compiled from 7—Cabral et al. (2013). The time column was adapted from Cohen et al. (2013).*

3. Sampling and analytical procedures

3.1. Sampling

Core samples were collected from five boreholes (Fig. S1; Supplementary Material) drilled over three E-W trending sections across the N4WS deposit. They were obtained from the Vale Core Library in Serra dos Carajás, Pará. Samples (~15 cm long) were collected at every 2 m from each drill core (~420 jaspilite samples in total). The core samples were split, and one half was stored for future reference. From bottom to top, the lithotypes observed in the core samples included mafic rocks (mainly basalt; Fig. 3D), jaspilite (Fig. 3B), and semi-decomposed mafic rocks. At least four basaltic flows or sills were intercalated in the BIF sequence (Fig. 3A; 3C). The samples were obtained from a core with total length of 451.8 m (70–521.8 m depth). This drill core was selected because it preserves the primary details due to lack of weathering, and seemingly lacked any post-depositional (hydrothermal and metamorphic) alteration that is ubiquitous in other drill cores containing iron ore bodies from the Carajás jaspilites. A total of 74 thin sections were processed and examined using reflected and transmitted light microscopy. Furthermore, the petrographic analysis was used to determine abundance of magnetite, hematite and goethite followed by selection for electron microprobe analysis. Procedures for electron microprobe analysis are provided in the Supplementary Material. For the chemostratigraphic study, after petrographic screening, a total of 49 jaspilite

samples from the N4WS-F1398 drill core (Fig. S1; 3) were selected for whole-rock major and trace element analyses, and 21 of these were further selected for Nd isotope analyses. In addition, milligram-sized samples (18) were separated from meso- or microbands for Fe isotope analysis (see Section 3.4 for details).

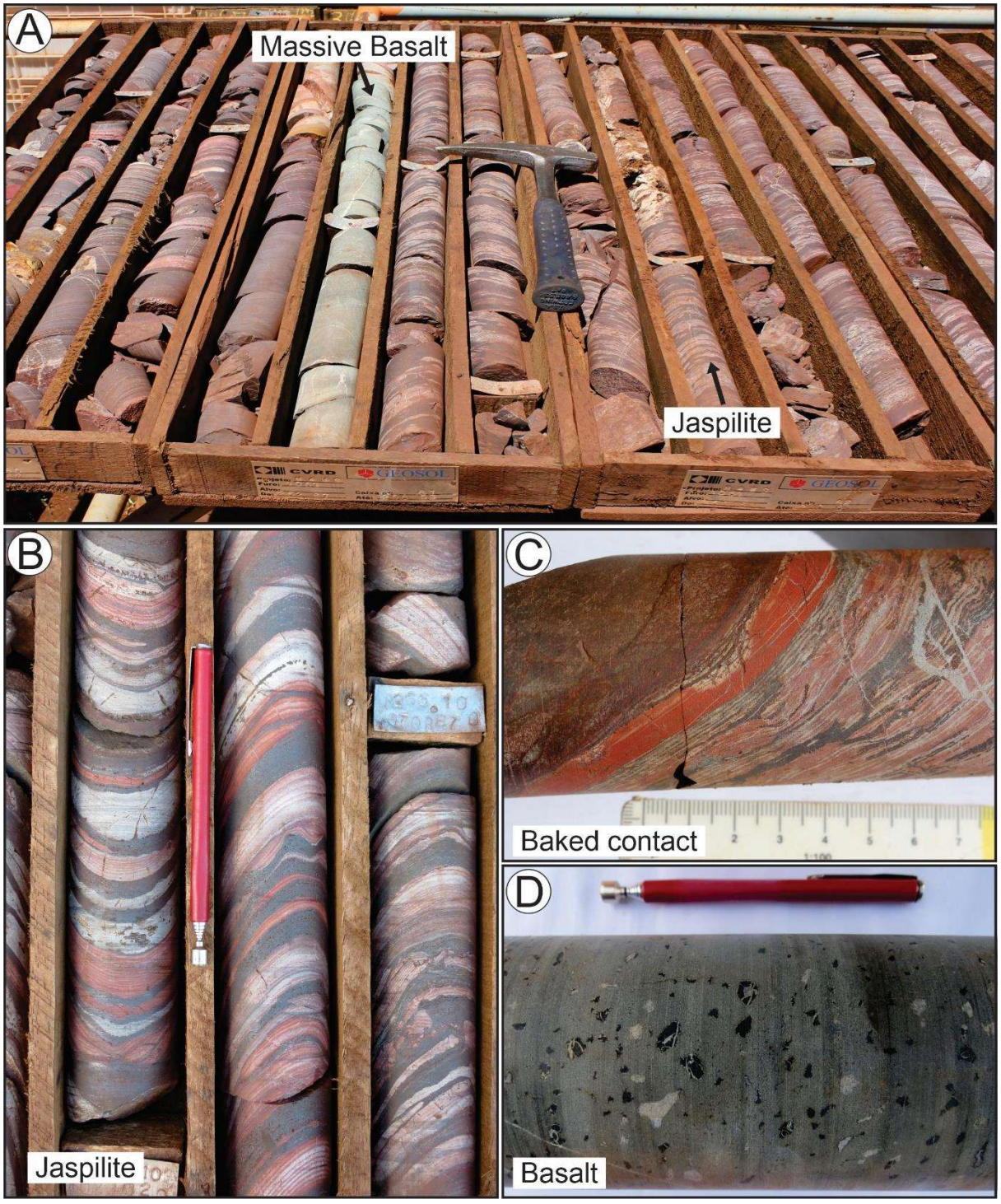

Fig. 3. *Representative core samples of the Carajás jaspilite and intercalated basalt:* ***A)*** *Overview of sampled drill cores showing basaltic rocks intercalated with jaspilites;* ***B)*** *Jaspilites with centimeter-thick intercalations of iron oxide (mainly hematite), jasper, and chert;* ***C)*** *Baked contact between metric lava flows and jaspilites;* ***D)*** *Amygdaloidal basalt with amygdules mainly filled by calcite and chlorite.*

3.2. Whole-rock geochemical analyses

Sample preparation and whole-rock chemical analyses were performed at ALS Chemex (Canada) following standard laboratory procedures. Major elements were determined by X-ray fluorescence, and the results have been reported as oxides in weight percentages. Ferrous iron (FeO) was acquired by H_2SO_4-HF acid digestion and titrimetric finish (Code: Fe-VOL05). The concentrations of REEs, high field strength elements (HFSE), and large ion lithophile elements were determined by Inductively Coupled Plasma - Mass Spectrometry (ICP-MS), and that of Ag, As, Cd, Co, Cu, Li, Mo, Ni, Pb, Sc, Tl, and Zn were determined by Inductively Coupled Plasma - Atomic Emission Spectrometry (ICP-AES). The loss on ignition has been provided using the differences in weight after heating. The ALS Chemex Home Page (www.alsglobal.com) provides a complete description of the analytical methods.

The Post-Archean Average Shale (PAAS, subscript SN) was used for shale normalization of REE (Taylor & McLennan, 1985). Because yttrium has similar chemical behavior to those of the REEs, it was inserted between Dy and Ho based on its ionic radius. Thus, Y and REEs were considered together for BIF samples (Henderson, 1984; Bau & Dulski, 1996). Normalized REY anomalies were calculated using the procedures proposed by Bau & Dulski (1996) and Bolhar et al. (2004), respectively. Normalized REY anomalies are defined as follows: $(Eu/Eu^*)_{SN} = [Eu/(0.5*Sm+0.5*Gd)]_{SN}$; $(Ce/Ce^*)_{SN} = [Ce/(0.5*La + 0.5*Pr)]_{SN}$; $(Pr/Pr^*)_{SN} = [Pr/(0.5*Ce + 0.5*Nd)]_{SN}$; $(La/La^*)_{SN} = [La/(0.5*Pr + 0.5*Nd)]_{SN}$; $(Y/Y^*)_{SN} = [Y/(0.5*Dy + 0.5*Ho)]_{SN}$.

3.3. Sm–Nd isotopic analyses

Whole-rock samples were pulverized, weighed (50 to 100 mg), spiked with a mixed ^{149}Sm-^{150}Nd spike solution, and subsequently dissolved using HF, HNO3, and HCl in Savillex vials. Chromatographic purification of Sm and Nd were carried out by two-stage ion-exchange resin following procedures described by Gioia & Pimentel (2000). Teflon columns filled with AG-50W-X8 100-200 mesh resin were used in the first stage, and LN-Spec 100-150 μm resin were used in the second stage. Sr extraction was carried out using Teflon columns filled with LN-Spec 50-100 μm resin, and Sr was eluted using HNO3. Nd isotope analyses were performed at the Laboratory of Geochronological, Geodynamic, and Environmental Studies at the Institute of Geosciences of the University of Brasília using a Thermo TRITON™ Plus Thermal Ionization Mass Spectrometer in static mode, equipped with nine Faraday cups and a central electron multiplier. Dry aliquots of Sm and Nd were loaded on a Re double filament prior to evaporation. Nd procedure blanks were found to be less than 100 pg. The analytical precision for ^{143}Nd/^{144}Nd isotope ratios was better than ± 0.0005% (2σ) based on repeated analyses of international rock standard BHVO-1 (Hawaiian basalt), with a measured 143Nd/144Nd value of 0.512989 ± 0.000014. The ^{143}Nd/^{144}Nd ratios were normalized to 146Nd/144Nd of 0.7219, and the decay constant used was $6.54\times10-12$ yr^{-1}. The isotope ratios obtained in this study were found to be in good agreement with published ^{143}Nd/^{144}Nd ratios of 0.512986 ± 0.000009 (Weis et al., 2005). Nd-model ages (TDM) were calculated following methods described by DePaolo (1981).

3.4. Fe isotope analysis

For Fe isotope analysis, 10 milligram aliquots of homogenized powders from the BIFs corresponding to 5-10 mg of iron (meso- or microbands) were sampled using a tungsten-carbide

drill bit (1 mm diameter) from a fresh rock surface, which was previously cleaned with distilled water. They were first digested in a mixture of ultrapure HF-HNO_3 on a hot plate for 12 hours, after which the solution was evaporated to dryness. The remaining residue was taken up in 2.0 mL of 6 mol L^{-1} HCl, and the sample was dried down. The remaining salt was dissolved in 5 mL of 7 mol L^{-1} HCl. Sample digestion described above were done in the clean laboratory at the Institute of Geosciences of the University of Brasília. After this point the solutions were sent to the Institute of Geochemistry and Petrology at ETH Zürich. From this solution, an aliquot containing approximately 1 μg of Fe was equilibrated with a ^{57}Fe–^{58}Fe double spike, and subsequently diluted to 1 mL of 7 mol L^{-1} HCl + H_2O_2. Fe was subsequently purified by an anion exchange column (AG MP-1M resin) using methods that were slightly modified after the established methods (Archer & Vance, 2004). The major modification involved eluting Fe with 1 mol L^{-1} HCl, which promoted a more efficient elution of Fe from the column. Typical blanks during column procedure were measured to be ~1 ng Fe, and were thus negligible.

The purified Fe fraction was analyzed for its isotopic composition using a Neptune Plus multi-collector ICP-MS (ThermoScientific) at ETH Zürich. Analyses were performed in high-resolution mode (M/ΔM>8000) to avoid spectral interferences on different masses of Fe. Samples were introduced in a 2% (v/v) (~0.3 mol L–1) HNO3 solution via a Savillex C-Flow PFA nebulizer (50 μl min−1) attached to a Teledyne-CETAC Aridus IITM desolvator. Approximately 300 ng of Fe was consumed in each analysis. Each analysis consists of 30 individual 4.2 second integrations at a single point on the resolved Fe shoulder (Weyer & Schwieters, 2003) for a total integration time of 2 minutes. ^{52}Cr was measured to monitor the potential interference from ^{54}Cr on ^{54}Fe. In all cases, the measured interferences were found to be negligible. Instrumental mass fractionation was corrected using the equilibrated Fe double spike, using methods analogous to those used for other metal isotope systems (e.g., Ni and Zn)

that are described elsewhere (Bermin et al., 2006; Cameron et al., 2009). The dissolved Fe concentrations were calculated by isotope dilution. The $^{56}Fe/^{54}Fe$ ratios have been reported using delta notation (in ‰) relative to IRMM-014 iron isotope reference material:

$$\delta^{56}\mathrm{Fe}\ (‰) = \left[\frac{(^{56}\mathrm{Fe}/^{54}\mathrm{Fe})_{\mathrm{sample}}}{(^{56}\mathrm{Fe}/^{54}\mathrm{Fe})_{\mathrm{IRMM\text{-}014}}} - 1\right] \times 1000$$

The long-term reproducibility of Fe isotopic analyses in the ETH Zürich lab, assessed over the course of this and parallel studies through repeated Fe isotope measurements of the primary IRMM-014 standard and a secondary standard (NIST SRM 3126a), was determined to be ±0.08‰ (2 standard deviation, 2σ). The value of NIST SRM 3126a was measured to be $\delta^{56}Fe$ = +0.35 ±0.08‰ (2σ, n = 236 over 6 years), which is close to the published values of 0.39 ± 0.13‰ (Rouxel & Auro, 2010) and 0.35 ± 0.06‰ (Stevenson et al., 2017), respectively. Internal errors, i.e., the reproducibility of 30 individual 4.2 second integrations that constituted a single analysis, induced during mass spectrometric analysis and during the propagation through double-spike algebra were found to be always substantially lower than the long-term reproducibility. The uncertainties shown in Figure 11 are the long-term reproducibility (±0.08), however, if the internal uncertainty was larger, the latter is shown. Two samples, F1398-049 and F1398-071, processed as duplicates through the ion exchange purification procedure, are in perfect agreement and serve to demonstrate the robustness of the analytical procedures.

4. Results

4.1. Petrography and mineralogy

Hand specimens of Carajás jaspilite display marked banded texture with fine banding down to millimeter scale (Fig. 3; 4). The bands are characterized by alternating quartz layers (in the form of chert or jasper) and iron oxides. The contacts between these two types of bands are mostly sharp, well-defined (Fig. 3A; 3B; 4A-D), and rarely diffused.

Hand specimens of Carajás jaspilite display marked banded texture with fine banding down to millimeter scale (Fig. 3; 4). The bands are characterized by alternating quartz layers (in the form of chert or jasper) and iron oxides. The contacts between these two types of bands are mostly sharp, well-defined (Fig. 3A; 3B; 4A-D), and rarely diffused.

Microcrystalline (~0.05 mm) chert appears as both mesobands (~1–5 cm) and microbands (0.25–1 mm), although, occasionally, chert forms lenses or nodules within oxide-rich bands. The color of chert ranges from white to grayish, and a redder variety (jasper) is observed when interstitial hematite grains are present (Fig. 3; 4A-C). The dominant parts of iron oxide bands are black and opaque, while its minor parts are blackish gray owing to interlayered chert microbands (Fig. 3B; 4). Iron-rich bands are characterized by hematite, and lesser amounts of magnetite. Hematite occurs primarily as fine (down to 0.03 mm; hematite^{1} in figure caption) and irregular grains in Fe-rich layers (Fig. 5A-D). Hematite occurs also as secondary crystals (martite) locally substituting magnetite (Fig. 5D; 5E), and as product of total pseudomorphic replacement of magnetite (hematite^{2}). The iron concentration (as FeO) of primary hematite (hematite^{1}), pseudomorphic hematite (hematite^{2}) and goethite are given in the Supplementary Material (Fig. S2; S3) (Table S2; S3). These minerals contain less total FeO than magnetite (with an average of 86.80, 85.56, and 75.12 wt.%, respectively), whereas the SiO_2, Al_2O_3, and TiO_2 abundance are higher than in magnetite.

The dimension of magnetite grains ranges from fine-grained to coarse-grained with a well-crystallized habit (Fig. 5C-E). A significant unidirectional variation in magnetite content with a well-crystallized habit was observed throughout the drill core; the concentration of magnetite was found to increase towards the deeper portions (below 350 m) of the Carajás jaspilite unit (Fig. 5C). These magnetite grains superimpose the original banding in different portions (Fig. 4A; 5C; 5D), and are associated with a post-depositional process, which was

probably of hydrothermal origin. Pseudomorphic replacement of magnetite by hematite (martitization; Fig. 5D; 5E) was observed in the middle to bottom parts of the core sections, particularly in samples where quartz veins were observed to crosscut the jaspilite banding. Iron-rich bands also have a brownish to yellowish color due to the higher concentration of goethite (Fig. 4B). The goethite pseudomorph was commonly observed in the top section of the Carajás BIF sequence, where the weathering of iron-rich minerals (mainly hematite pseudomorph) was intense.

Electron microprobe analyses of magnetite from the Carajás jaspilite show that magnetite has total iron concentration (expressed as FeO total) between 90.13 and 92.31 wt.% (Table S1; Fig. S2; S3). It has low Al_2O_3 (0.00 to 0.04 wt.%, average 0.02 wt.%) and TiO_2 contents (0.00 to 0.26 wt.%, average 0.08 wt.%), which is similar to the reported values for magnetite grains from typical BIFs from other regions across the world (Sun & Li, 2017). An increasing-downward pattern of FeO total contents was noticed in magnetite (Fig. S2). For example, in the upper part of the core, above 400 m, magnetite has lower FeO total contents (varying from 90.13 to 91.01 wt.%, n = 7), compared to those in the lower part of the core (91.23 and 92.31 wt.%, n = 13).

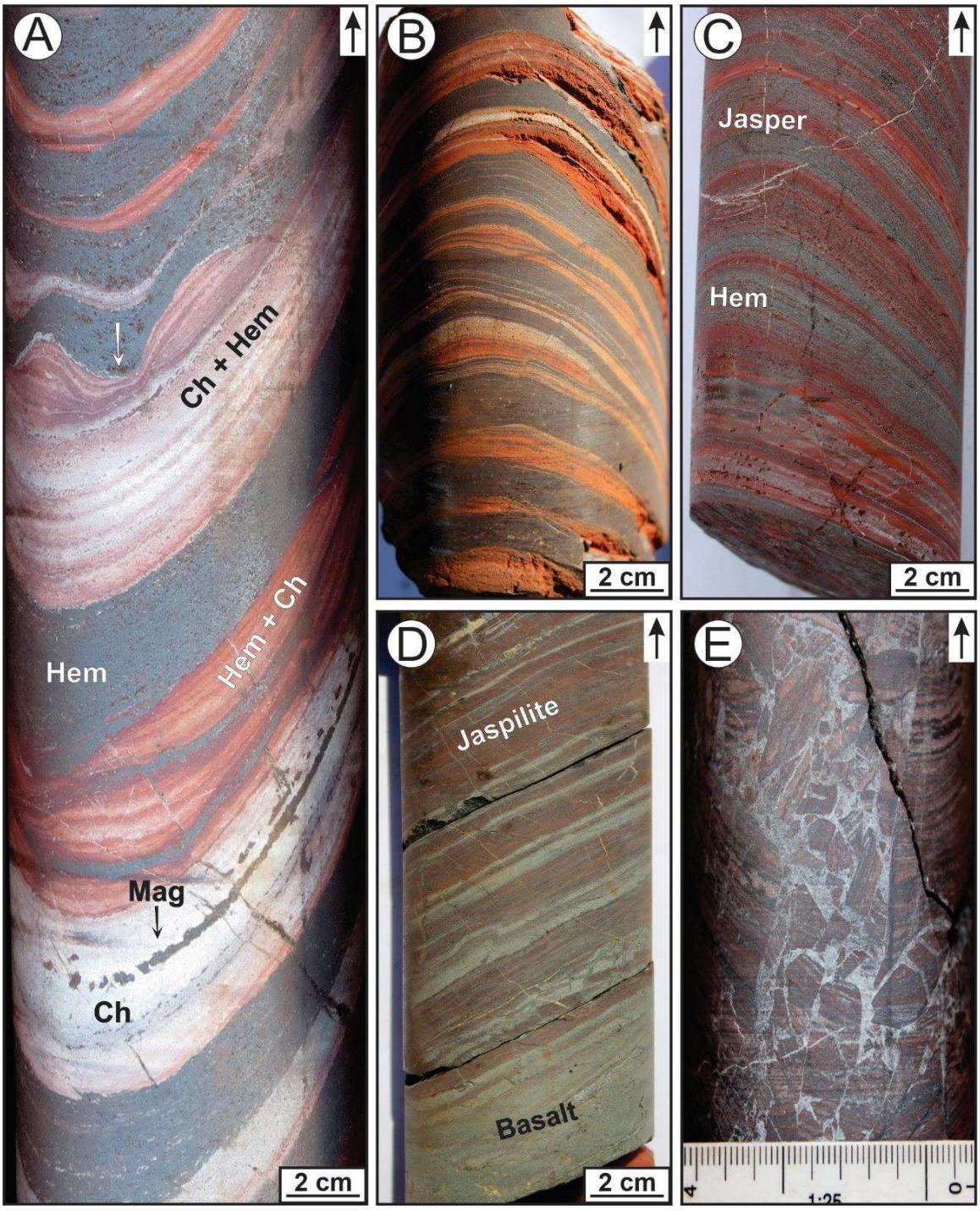

Fig. 4. *Macroscopic aspects of the jaspilites:* ***A)*** *Jaspilite (white arrow, sedimentary slumping can be seen in the upper half);* ***B)*** *Jaspilite from upper part of core section (orange color probably is associated with goethitic alteration);* ***C)*** *Well-preserved jaspilite showing alternating layers of jasper and iron oxides (mainly hematite);* ***D)*** *Jaspilite-basaltic gradational upper contact;* ***E)*** *Breccias with jasper*

fragments encompassed by a carbonate-rich matrix, mainly seen at lower parts of jaspilite unit. Ch = chert, Hem = hematite, Mag= magnetite. Arrows show upper direction of core.

Primary sedimentary structures were generally observed throughout BIF unit. In some parts of the core section, large numbers of colorless micro-spherules were observed (Fig. 5D; 5F). The micro-spherules have circular structures, and are of approximately 10–30 μm diameter with a hematitic nuclei surrounded by colorless chert and a thin layer of jasper. In a few locations, soft-sediment deformation was evident owing to the presence of sediment slumping between the bedding planes of jasper and iron oxide bands (indicated by white arrow in Fig. 4A). Other structures as microflames and pinch-and-swell were also observed throughout the jaspilite. The latter two structures are most likely of pre-diagenetic origin. The banding in the Carajás jaspilite is typically plane-to-wavy laminated, although, occasionally, banding was obliterated in certain places by veins, fractures, and microfaults (Fig. 4). The veins and fractures consist predominantly of medium to coarse grained quartz, secondary magnetite, carbonates, and minor microplaty hematite. The crosscutting veins with magnetite represent localized features (bottom part) and do not affect the general context. In fact, BIF are extremely well preserved in the Serra Norte de Carajás. (Martins et al., 2017; Justo et al., 2020; Figueiredo e Silva et al., 2020).

In addition, basaltic lava flows of Parauapebas Formation, which vary in thickness from 1.0 to 5.0 m (Martins et al., 2017), occur concordantly intercalated the jaspilites (Fig. S1; 3A; 3D; 4D), reflecting the contemporaneity of these two lithotypes. A baked contact was occasionally observed between jaspilite and basalt (Fig. 3C). Mafic sills and dikes were also observed crosscutting the jaspilite package. Brecciation was an important feature observed in some Carajás jaspilite samples, and the feature was particularly strong near the contact between basalts and jaspilites. Breccias comprised mostly of jaspilite fragments within a quartz-rich or

carbonate-rich matrix are commonly associated with quartz and/or carbonate veinlets (Fig. 4E). The relict clasts of jaspilite preserved the original banding of BIF.

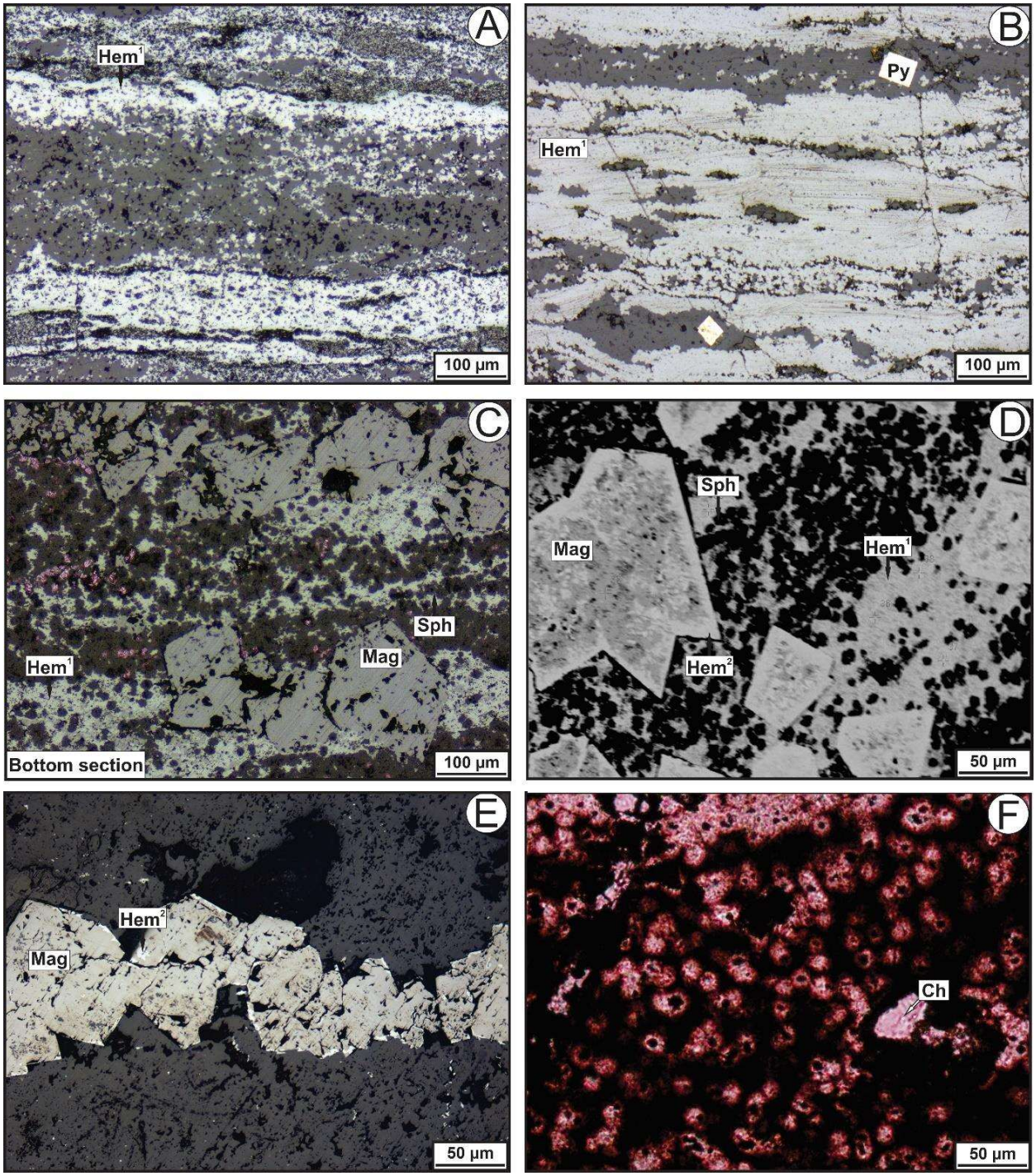

Fig. 5. *Photomicrographs illustrating the main petrographic characteristics of the Jaspilite, (H) taken with transmitted light:* ***A)*** *Hematite as primary fine irregular grains in Fe-layers;* ***B)*** *Alternating microbands of primary hematite and jasper with well-crystallized habit pyrite;* ***C)*** *Magnetite with well-*

crystallized habit crosscut primary hematite microbands (bottom section); ***D)*** *Backscatter image showing two types of hematite (middle to basal part of core section);* ***E)*** *Magnetite microbands with well-crystallized habit. Note also the secondary crystals (martite) in the corner of magnetite crystals;* ***F)*** *Microspherules structures with hematitic nuclei; Ch = chert, Hem^1 = primary hematite, Hem^2 = hematite as product of pseudomorphic replacement of magnetite, Mag= magnetite, Py = pyrite, Sph = spherules structures.*

4.2. Major and trace element geochemistry of whole-rock samples

The geochemical data for major and trace elements are presented in Table S4. Depth-wise variations in the abundance of selected major and trace elements are shown in Fig. 6. The Carajás jaspilites have markedly high contents of SiO_2 + Fe_2O_3 (t) (with an average of 97.90 wt.%) and significantly low Al_2O_3 content (<0.65 wt. %) (Fig. 6A-D; S4). Apart from the very low Al content, a constantly low concentration of TiO_2 (<0.08 wt. %) and HFSE such as Zr (average at 3.34 ppm) and Nb (<0.60 ppm) (Fig. 6I and 6J) could be attributed to minor additions of crustal materials during their deposition, which agrees with sample mineralogy as evinced by the lack of abundant clastic components. In contrast, the concentrations of CaO and MgO were found to be elevated in samples from the lowermost portion of the drill core (Fig. S4), which reflect the appearance of well-developed secondary carbonates in brecciated zones (Fig. 4E; 6F, 6G). Moreover, FeO and MnO contents were highly elevated in the bottom section (average of 1.11 to average of 7.33 wt. % and average of 0.021 to average of 0.117 wt. %, respectively) (Fig. 6C, 6E), whereas Fe_2O_3 show an increasing-upwards trend from an average of 45.26 wt. % to an average of 54.95 wt. % (Fig. 6B). This is consistent with the abundance of magnetite (Fig. 5C-E) in the bottom section. No apatite or other P-rich phases were detected by either X-ray diffraction or X-ray energy dispersive spectroscopy (data not shown). The abundance of other major oxides (Na_2O and K_2O) is lower than 0.04 wt.%. Redox-sensitive

trace elements such as U and Mo are present at very low concentrations. Transition metals (e.g., V, Cr, Mn, Co, Ni, Cu, and Zn) show a narrow range in their concentrations, and reach sub-ppm values in the majority of samples. Ten out of 49 samples, corresponding to type-II BIF, show a larger range in the concentration of HFSE (e.g., Zr, Th, Nb, and Hf) (Table S4; Fig. 10), with Al_2O_3 ranging from 0.11 to 0.64 wt.% (Fig. 6D). These samples were particularly found near the contact between the basaltic flows and jaspilites (Fig. S1). The remaining samples studied here (type-I BIF; n = 39) are characterized by extremely low concentrations of Al_2O_3 (<0.5 wt.%), TiO_2 (<0.02 wt.%) and HFSEs (e.g., Zr, Hf, and Th). Despite some being affected by adjacent volcanic activity, no mineralogical differences exist between the two types (I and II) of BIF. These types differ mainly in their REY, Sm-Nd, and $\delta^{56}Fe$ patterns.

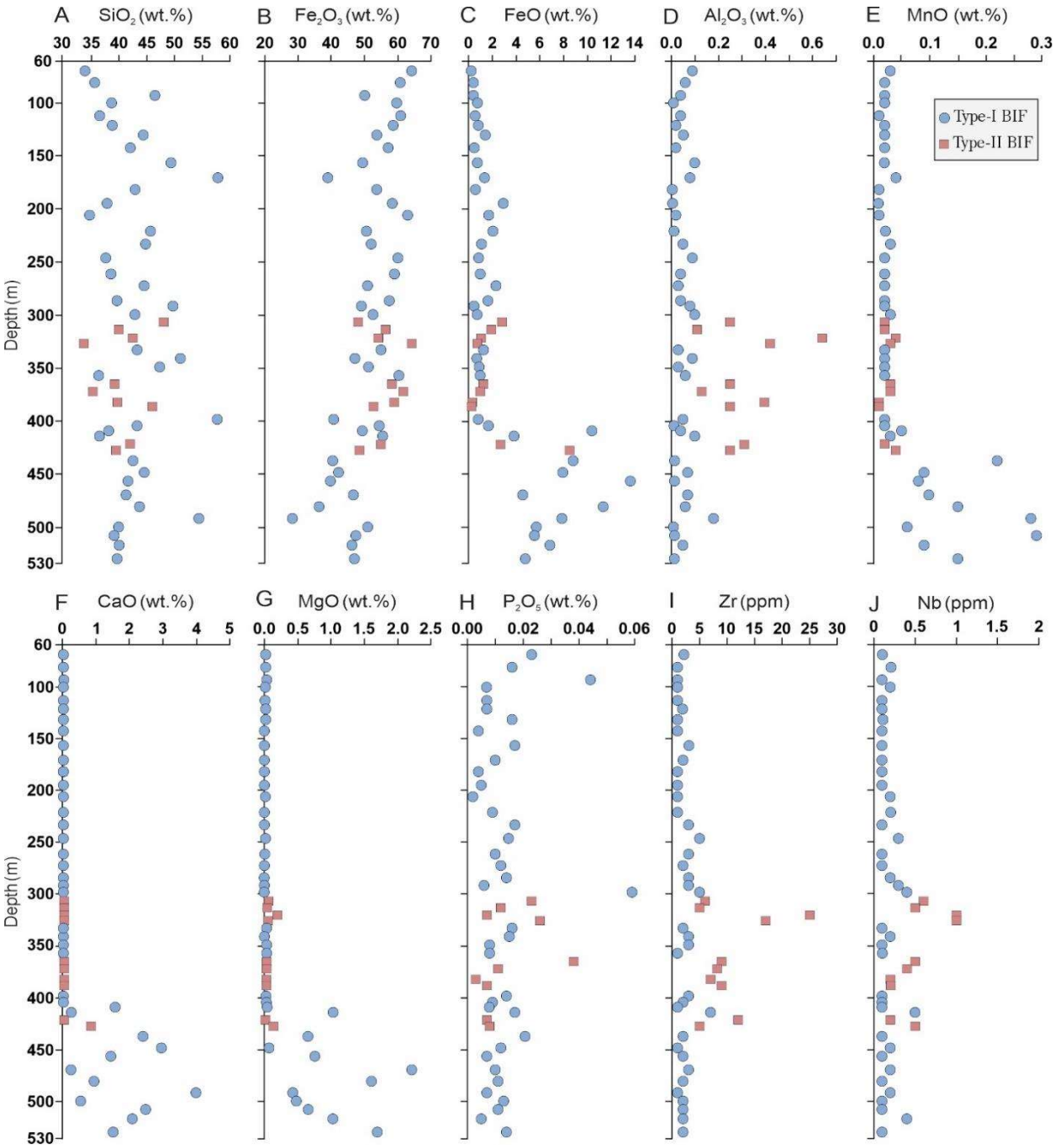

Fig 6. *Variation of selected major and trace elements with depth. Type-I and type-II BIFs are represented as blue dot and reddish-brown square, respectively. Type- II BIFs are samples influenced by volcanic adjacent activity, whereas, type-I BIFs are the remaining samples. See text for further explanation.*

The maximum, minimum and average shale-normalized REY patterns for the 49 Carajás jaspilites samples are illustrated in Fig. 7. The SN spectra for REY span a narrow range relative to the PAAS, which ranges between 0.01 and 0.1 (values from Taylor & McLennan, 1985) (Fig. 7). Total REE concentrations average 10.00 ppm (Fig. 8A; Table S5). Type-II BIFs display the highest REE concentration (5.40 to 52.03 ppm; average at 18.17 ppm), and REY patterns look like those of the intercalated basalts (Martins et al., 2017). REY patterns for both BIF types are highly diverse, with some samples showing LREE enrichment relative to HREE, whereas others show the reverse trend. La/Yb_{SN} and Sm/Yb_{SN} ratios range between 0.47–4.89 and 0.36–2.60 (Fig. 8B; 8C), respectively. Almost all type-I BIF show strongly superchondritic Y/Ho ratios, ranging from 40.0 to 75.0 with an average of 57.55 (Fig. 8G). These samples also displayed significantly positive La (La/La^*_{SN} = 0.88–7.54; Table S5) and Eu anomalies (Eu/Eu^*_{SN} = 1.86–5.05; Fig. 8D). In contrast, type-II BIF display slightly negative to weakly positive Eu (Eu/Eu^*_{SN} = 0.64–1.48) and La anomalies (La/La^*_{SN} = 0.8–1.64), with values of Y/Ho ratios (27.83–41.25) closer to that of the chondrites (Fig. 8G). Despite these differences, no systematic differences among samples from different stratigraphic horizons were identified with respect to their REY patterns. Another striking feature is Ce/Ce^*_{SN} ratios between 0.59 and 1.07 (Fig. 8E), which might be considered as negative Ce anomalies. However, the identification of Ce anomalies is complicated by the anomalous abundance of La. The existence or absence of true negative Ce anomalies is discussed in the subsequent sections.

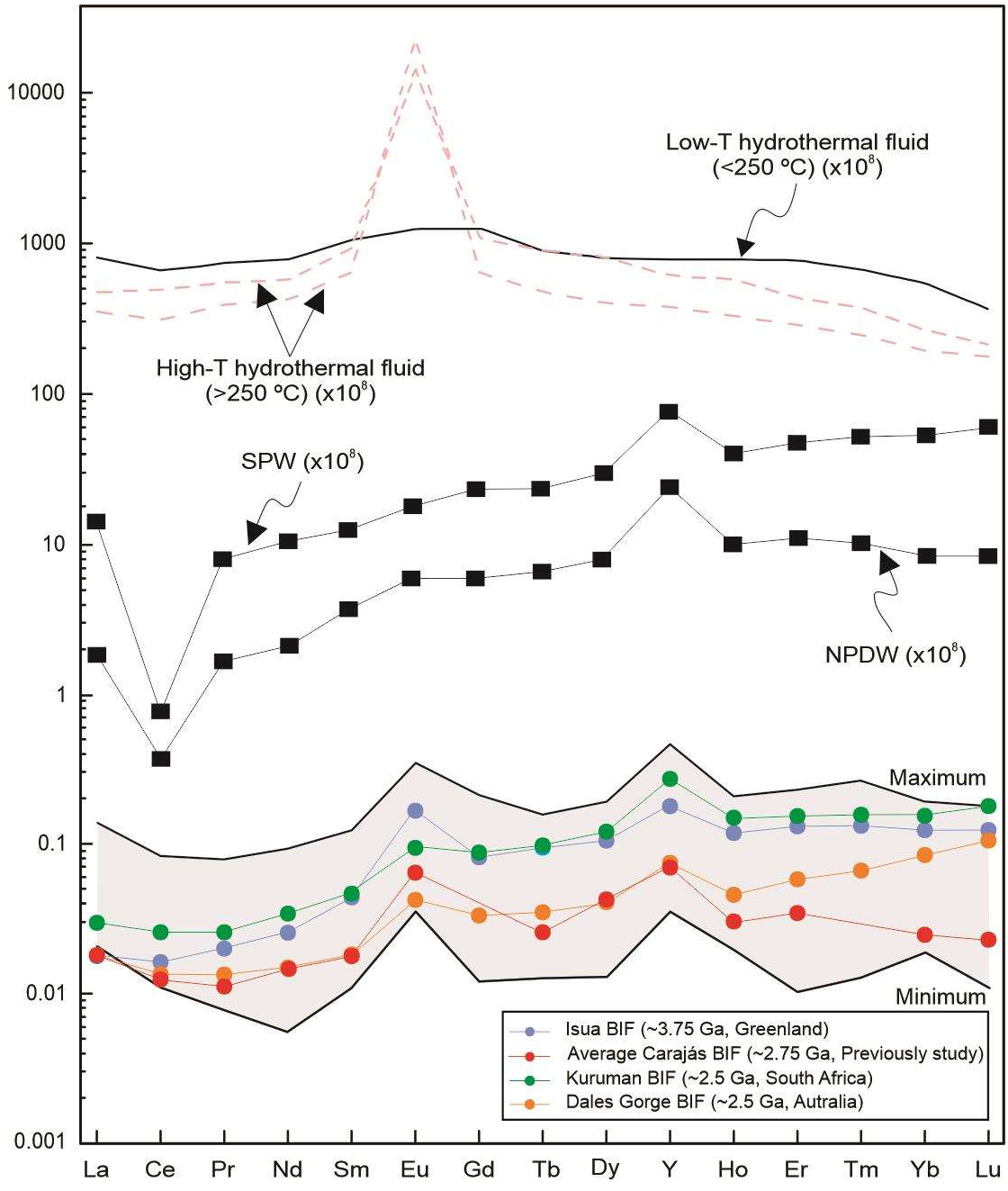

Fig 7. *PAAS-normalized REY distributions of the Carajás jaspilites (gray area represents 49 samples) showing flattened HREE to LREE pattern along with a pronounced Eu/Eu*$_{SN}$ anomaly compared with average data of Isua, Carajás, Kuruman and Dales Gorge IFs, as well as average high-T (> 250 °C) and low-T (< 250 °C) hydrothermal fluids, and average South Pacific and North Pacific Deep seawaters. Data from Bau & Dulski (1996, 1999); Bolhar et al. (2004); Bolhar & Van Kranendonk (2007); Fabre et al. (2011); and Pecoits et al. (2009).*

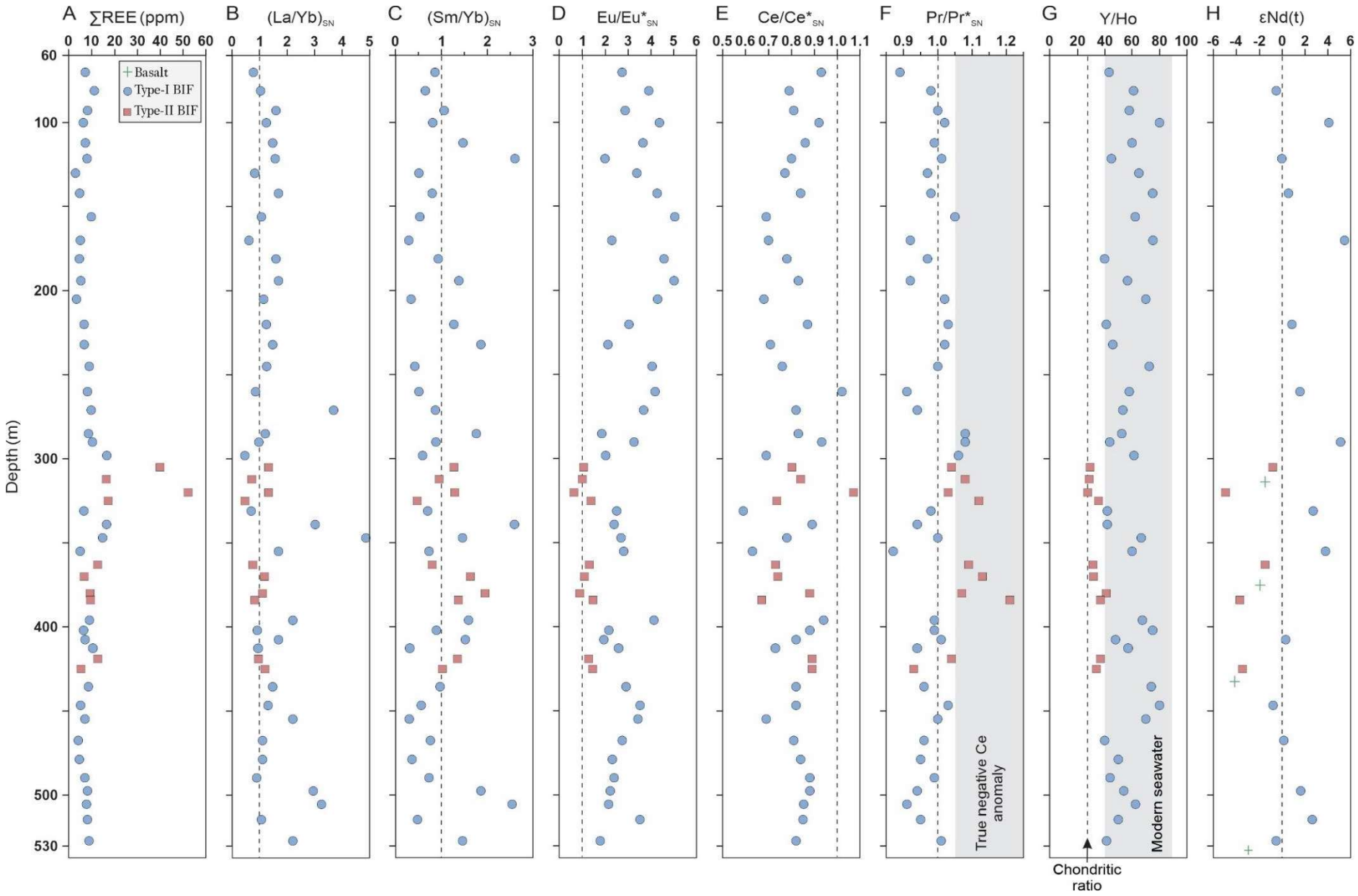
A ∑REE (ppm)
B (La/Yb)SN
C (Sm/Yb)SN
D Eu/Eu*SN
E Ce/Ce*SN
F Pr/Pr*SN
G Y/Ho
H εNd(t)
Depth (m)
Basalt
Type-I BIF
Type-II BIF
True negative Ce anomaly
Modern seawater
Chondritic ratio

Fig 8. *Evolution of selected geochemical parameters with depth. The green crosses indicate basaltic samples from Martins et al. (2017). Fields of true negative Ce anomaly and modern seawater from Bau & Dulski (1996) and Alibo & Nozaki (1999), respectively. εNd(t) was calculated for t = 2745 Ma (Martins et al., 2017)..*

4.3. Sm–Nd isotope systematics

Samarium and neodymium concentrations of the selected samples from Carajás BIF sequence displayed wide ranges (Table S6). Sm concentration varied from 0.038 to 0.671 ppm; Nd concentration vary from 0.257 to 3.089 ppm (Table S6). In addition, $^{143}Nd/^{144}Nd$ ratios range from 0.510579 to 0.511774, while $^{147}Sm/^{144}Nd$ ratios range from 0.0786 to 0.1588 (Table S6). Thus, the studied samples display a wide variation in εNd values (t = 2.75 Ga); the differences are particularly evident among samples collected near or far away from basaltic flows. For example, the samples near intercalated basaltic flows (type-II BIFs, n = 5) have consistently negative εNd(t) values (–4.97 to –0.90), whereas, the remaining samples (type-I BIF samples, n = 16) have predominantly positive εNd(t) values (–0.84 to +5.40) (Fig. 8H). Importantly, the T_{DM}(Nd) ages of these BIFs were found to vary between 2.49 and 3.60 Ga (Fig. 9), and a similar pattern was observed in variations of εNd(t) values. For instance, type-II BIFs display T_{DM}(Nd) ages ranging between 2.94 and 3.60 Ga, and thus older than their proposed depositional age (~2.75 Ga, Trendall et al., 1998; Martins et al., 2017). On the other hand, type-I BIFs show a limited range in their T_{DM}(Nd) ages, which are younger and reach values (2.49 – 2.96 Ga) closer to depositional ages for the Carajás jaspilites.

To further constrain the Nd isotopic sources of the Neoarchean seawater from where the Carajás jaspilites precipitated, we used published Nd isotopic data of the spatially associated volcanic and sedimentary rocks of Grão-Pará Group (Table S6; Fig. 9), which includes 4 basaltic samples from Martins et al. (2017), and 12 black-shale samples from Cabral et al.

(2013). These samples were chosen for being located at a stratigraphically lower position or at an equivalent position compared to that of Carajás jaspilites. They also occurred concordantly with the jaspilites, which reflects the contemporaneity of these rocks. Black-shale intervals were founded at bottom of the BIF unit, as well as within and on top of it (Cabral et al., 2017). In general, the volcanic rocks are characterized by negative initial Nd isotope values, with εNd(t) varying from –4.11 to –1.53 (Table S6; Fig. 9), reflecting enriched sources involved in the generation of these rocks. Except for one with negative εNd(t) of −0.8 and a slightly higher T_{DM}(Nd) age of 3.1 Ga, all black-shale samples have positive initial εNd values (+0.40 to +2.82), which correspond to depleted-mantle model ages of 2.8–3.0 Ga (Table S6; Fig.9). The εNd data indicate an age of 2.8–3.1-Ga for the source of the clastic components of the shales (Cabral et al., 2013).

Furthermore, Sm–Nd isotope data of all BIFs, in combination with previous data of Carajás jaspilites from Serra Norte (Justo, 2018) and associated basalts (4 samples) plot along a correlation line in the errorchron diagram (Fig. 10A) with an apparent age of 2707 ± 118 Ma (MSWD = 230) and an initial $^{143}Nd/^{144}Nd$ value of 0.5091310 ± 0.0000024. Nevertheless, this correlation line could represent a mixing line. A subset of these data (n = 20) with only type-I BIF samples also in combination with previous data (Justo, 2018), which displayed better alignment, yielded an errorchron. The observation suggests an older apparent age of 2795 ± 77 Ma (MSWD = 56, Fig. 10B) and an initial $^{143}Nd/^{144}Nd$ value of 0.5090862 ± 0.0000028. Both Sm–Nd isochron apparent ages are concordant with the proposed minimum formation age of the Carajás jaspilites at ~2745 Ma (Trendall et al., 1998; Martins et al., 2017).

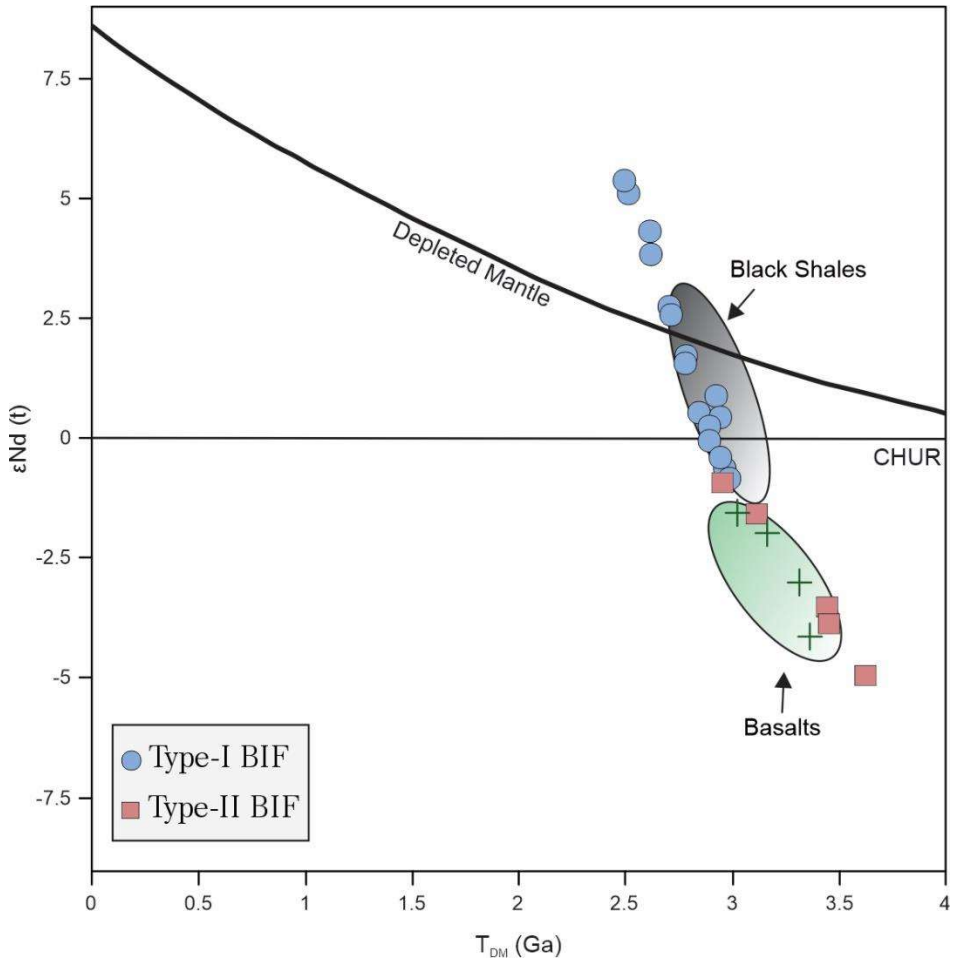

Fig 9. *εNd (t) vs T_{DM} of the Carajás jaspilites and associated rocks. Black and green fields represent black-shale samples from Cabral et al. (2013) and basaltic rocks samples from Martins et al. (2017). εNd(t) was calculated for t = 2745 Ma (Martins et al., 2017).*

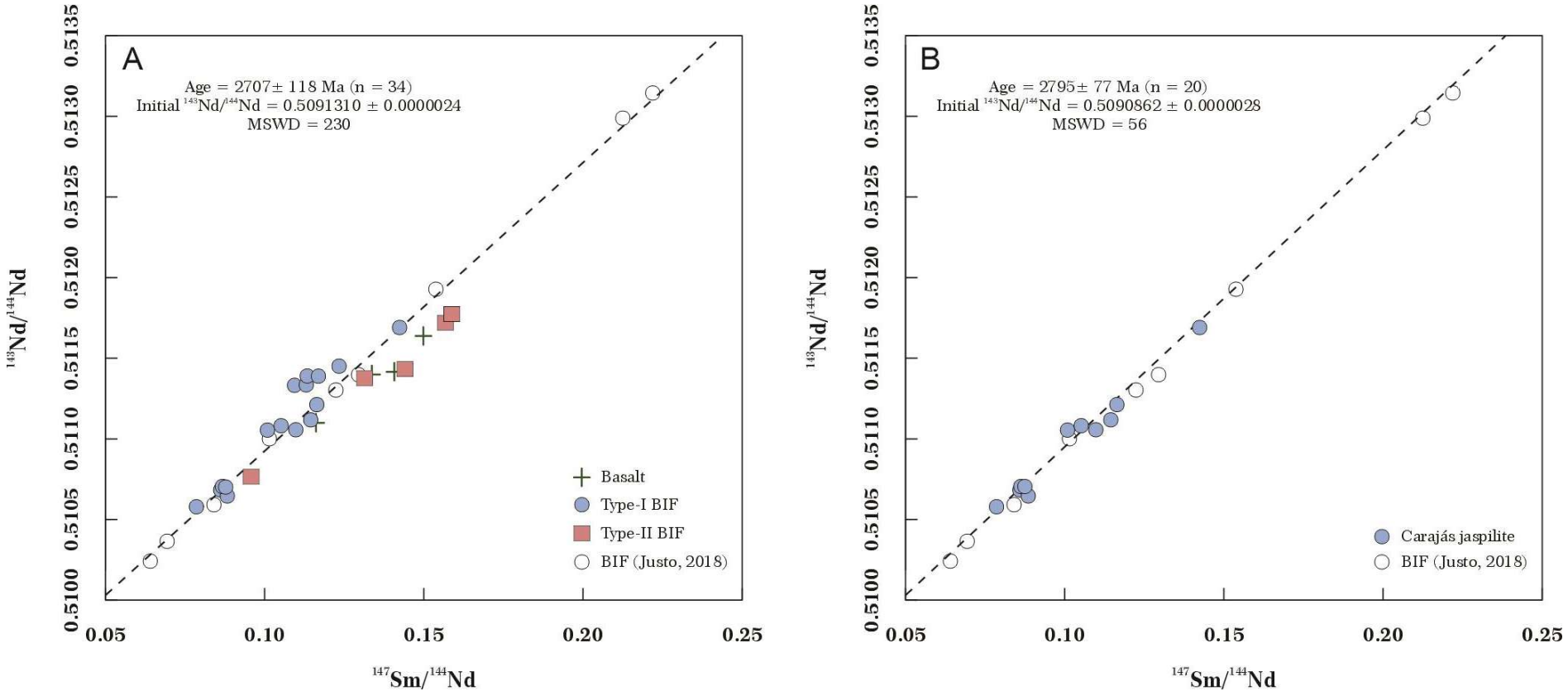

Fig 10. *Sm-Nd isotope composition of Carajás jaspilite analyzed in this study.* ***A)*** *Correlation line in a conventional isochron diagram for all BIF samples and associated basalts;* ***B)*** *Isochron diagram with only BIF samples and showing better alignment. Associated basaltic samples and previous Carajás BIFs data are from Martins et al. (2017) and Justo (2018).*

4.4. Fe isotope geochemistry

The Fe isotope values of the studied BIFs are presented in Table 1, and their stratigraphic depth-wise variations are plotted in Fig. 11. Despite we have shown some post-depositional features, such as formation of hematite after "original" magnetite, the samples that we used in isotopic analyses come from drill cores parts without these features. Overall, the $^{56}Fe/^{54}Fe$ isotope ratios (expressed as $\delta^{56}Fe$) values were remarkably positive ranging from +0.83 to +1.90 ‰ with an average of +1.34 ± 0.03 ‰ (n = 18), which is close to previously published average values of 1.38 ± 0.23 ‰ (Fabre et al., 2011) and 1.39 ± 0.22 ‰ (Rego et al., 2021), respectively. However, compared to published Fe isotope compositions of BIFs (Johnson et al., 2003, 2008; Rouxel et al., 2005; Konhauser et al., 2017), the respective values from Carajás are some of the most positive that have been ever measured, as noted by Fabre et al. (2011). Nevertheless, there are differences among the samples throughout the drill core. In the upper part of the core (Fig. 11), from 81 m to 355 m, nine samples have the highest $\delta^{56}Fe$ values averaging +1.57 ± 0.04 ‰ (+1.25 to +1.90 ‰). These samples were found in the hematite-rich (primary hematite, >90 %) and magnetite-poor (<10 %) sections of the core (Fig. 5A; 5B). Five samples collected from a lower part of the core at depths between 355 m and 515 m, have lower $\delta^{56}Fe$ values averaging +1.25 ± 0.03 ‰ (+1.10 to +1.38 ‰). These rocks tend to have a higher content of magnetite towards the deeper portions of the Carajás BIF unit (i.e., below 350 m; Fig. S2). In addition, type-II BIFs have the lowest positive $\delta^{56}Fe$ values, which average +0.95 ± 0.03 ‰ (+0.83 to +1.10 ‰). A significant positive correlation ($R^2 = 0.73$) exists between $\delta^{56}Fe$ and εNd(t) values (Fig. 16D).

Table 1. *Iron isotope compositions of Carajás jaspilite (expressed as δ56Fe in ‰), as a function of depth. The minerals shown are in order of decreasing abundance in the samples.*

Sample	Lithology	Main mineralogy	Depth (m)	δ^{56}Fe (‰)	± 2SE (int.)	± 2SD (ext.)
F1398-007	Type I-BIF	Ch (47%)-Hem (40%)-Gth (10%)-Mag	81.00	1.65	0.04	0.08
F1398-014	Type I-BIF	Ch (40%)-Hem (56%)-Mag (4%)	100.00	1.49	0.04	0.08
F1398-032	Type I-BIF	Ch (60%)-Hem (35%)-Mag (5%)	142.00	1.25	0.05	0.08
F1515-089	Type I-BIF	Ch (50%)-Hem (42%)-Mag (8%)	170.00	1.83	0.04	0.08
F1398-049	Type I-BIF	Ch (55%)-Hem (36%)-Mag (9%)	220.00	1.41	0.04	0.08
F1398-049*§	-	-	-	1.40	0.12	-
F1515-110	Type I-BIF	Ch (55%)-Hem (39%)-Mag (6%)	260.00	1.37	0.03	0.08
F1398/052	Type I-BIF	Ch (40%)-Hem (56%)-Mag (4%)	290.00	1.88	0.03	0.08
F1398/059	Type II-BIF	Ch (50%)-Hem (46%)-Mag (4%)	320.00	0.87	0.02	0.08
F1398-067	Type I-BIF	Ch (50%)-Hem (45%)-Mag (5%)	331.00	1.34	0.04	0.08
F1398-071	Type I-BIF	Ch (45%)-Hem (50%)-Mag (5%)	355.00	1.90	0.03	0.08
F1398-071*	-	-	-	1.88	0.04	-
F1051-126	Type II-BIF	Ch (55%)-Hem (39%)-Mag (6%)	363.00	1.10	0.02	0.08
F1398/081	Type II-BIF	Ch (50%)-Hem (47%)-Mag (3%)	384.00	0.83	0.03	0.08
F1398-083	Type I-BIF	Ch (50%)-Mag (30%)-Hem (20%)	408.00	1.10	0.03	0.08
F1398-094	Type II-BIF	Ch (48%)-Mag (27%)-Hem (25%)	425.00	1.00	0.04	0.08
F1398/110	Type I-BIF	Ch (55%)-Mag (25%)-Hem (20%)	447.00	1.21	0.04	0.08
F1515-259	Type I-BIF	Ch (60%)-Mag (20%)-Hem (20%)	468.00	1.28	0.03	0.08
F1051-143	Type I-BIF	Ch (60%)-Mag (20%)-Hem (20%)	498.00	1.38	0.03	0.08
F1398-134	Type I-BIF	Ch (57%)-Mag (23%)-Hem (20%)	515.00	1.29	0.04	0.08

Ch = chert, Gth = goethite, Hem = hematite, Mag = magnetite. * The samples F1398-049 and F1398-071 were measured as replicates. §Please note the high uncertainty on this replicate is a result of very low signal intensity (~5% of its replicate pair) due to sample loss during handling.

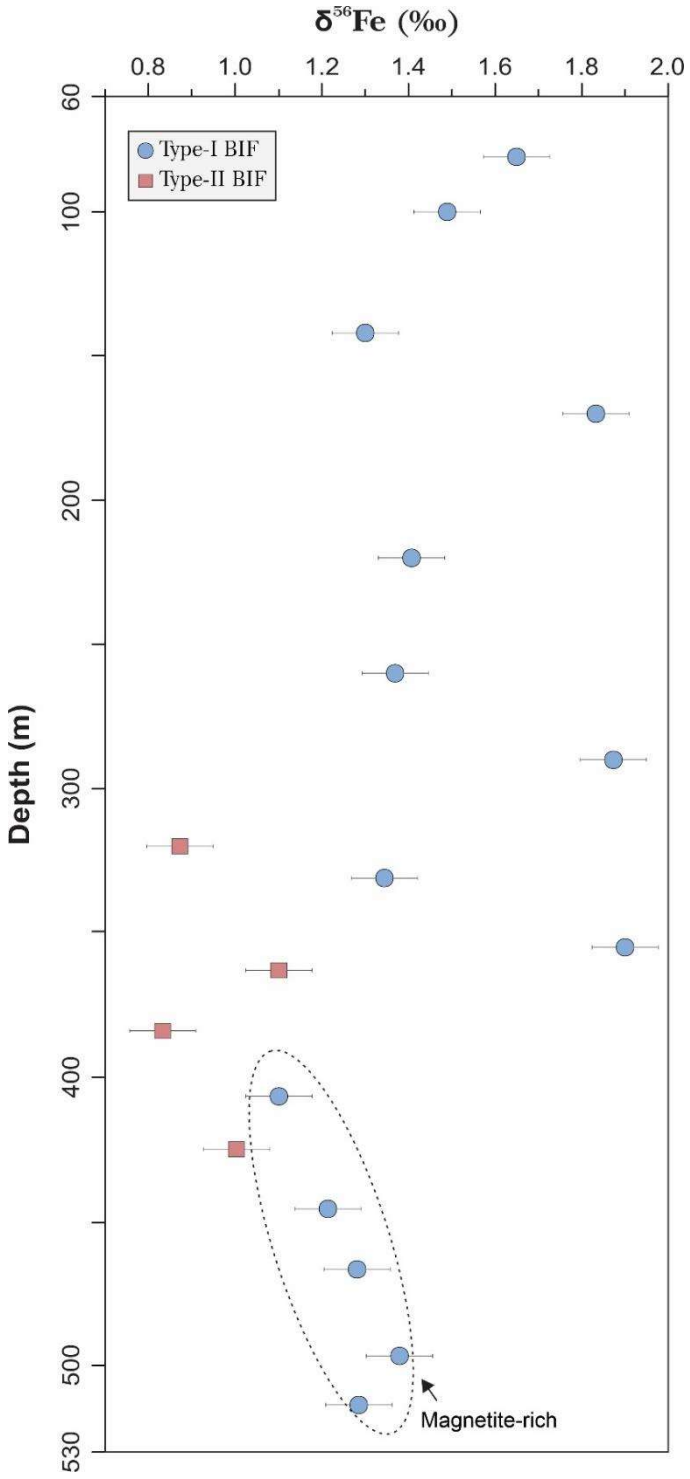

Fig 11. *Variation of Fe isotope values ($\delta^{56}Fe$) throughout the Carajás jaspilites. Fractionation by Fe oxidation is represented by more positive $\delta^{56}Fe$ values than the typical values for basaltic rocks. Magnetite-rich samples (bottom part) and type-II BIF samples have lower positive $\delta^{56}Fe$ values (+1.10*

to +1.38 ‰, and +0.83 to +1.10 ‰, respectively). For comparison, the average $\delta^{56}Fe$ values for basaltic rocks is generally unfractionated at 0 ± 0.15‰ (Sharma et al., 2001). See text for further details.

5. Discussion

5.1. Effects of post- and syn-depositional processes on REY patterns in Carajás jaspilites

Geochemical signatures of BIFs, particularly REY characteristics, are widely used to provide important information on the sources of solute that led to the precipitation of BIF, the chemical composition and redox conditions of Earth's early oceans, and also on the evolution of oxygenation in the contemporary atmosphere over time (Dymek & Klein, 1988; Derry & Jacobsen, 1990; Bau & Dulski, 1996; Bau et al., 1997; Bolhar et al., 2004; Kato et al., 2006; Alexander et al., 2008; Frei et al., 2008; Bekker et al., 2010). However, the geochemical characteristics of BIFs might be affected by several processes, including syn-depositional contamination (clastic or volcanic) and post-depositional processes (e.g., diagenesis and metamorphism). Hence, it is necessary to evaluate whether the REY primary signatures of the original protolith were modified or not before discussing the petrogenesis and paleoenvironmental implications of BIFs (Bau, 1993; Alexander et al., 2008; Albut et al., 2018, 2019; Bonnand et al., 2020).

In general, syn-depositional processes might affect the REY patterns of BIFs with respect to contemporaneous seawater owing to clastic contamination with crustal materials. The effect of clastic contamination can be assessed using trace elements that are practically immobile in aqueous solutions and enriched in clastic materials (such as Al, Ti, Th, Hf, Zr, and Sc) (Alexandre et al., 2008). Furthermore, because most crustal rocks (i.e., felsic and basaltic rocks) have a constant chondritic Y/Ho ratio of ~26, small admixtures of any of these contaminants could depress the seawater-like Y/Ho ratios of >43 (Bau & Dulski, 1996; Nozaki

et al., 1997; Bolhar et al., 2004). Most Carajás jaspilite (type-I) samples have very low concentrations of Al_2O_3 (< 0.10 wt.%; Fig. 6D) and TiO_2 (< 0.1 wt.%). They have significantly low abundances (< 1 ppm) of HFSEs (e.g., Zr, Hf, and Th) and elevated Y/Ho ratios (average of 57.55; Fig. 8G). These geochemical proxies demonstrate that Fe-rich sediments had a chemical origin with negligible clastic contamination (Bau & Dulski, 1996; Bolhar et al., 2004, 2005). In contrast, few samples (type-II BIF) displayed slightly higher concentrations of Al_2O_3 (0.11 wt.% to 0.64 wt.%) and incompatible elements (> 1 ppm), along with chondrite-like Y/Ho ratios (27.89 to 41.25; average of 33.46). The Y/Ho vs. Eu/Eu^*_{SN} (Fig. 16A) diagram also demonstrates that the composition of type-II BIFs was affected by minor detritus contamination. These features suggest that a minor (if any) concentration of detrital materials was involved in the deposition of type-II BIF (Bau, 1993; Bolhar et al., 2004), which were mostly restricted to their contact region with basaltic flows (Fig. S1). It is noteworthy to mention that the REY patterns of type-II BIF look like those of the intercalated basalts, indicating possible existence of additional REY sources (e.g., basaltic rocks).

Potential post-depositional mechanisms that could affected trace metals and REY distribution of Carajás jaspilites include diagenesis, hydrothermal alteration, and metamorphism. REY might get mobilized during the diagenesis of post-depositional sediments, which would tend to average out REY distributions in BIFs (Bau, 1993). However, it is widely accepted that REYs were not significantly changed, and therefore, they remained effectively immobile during diagenesis and lithification processes (Morris, 1993; Bau, 1993; Wang et al., 2017). During hydrothermal alteration, the redox-sensitive elements Ce and Eu are especially susceptible to mobilization relative to their neighboring REEs (Bolhar et al., 2015; Wang et al., 2017). Hence, it is essential to evaluate the effects of hydrothermal alteration on these elements. To test their mobility, we used Ce and Eu diagrams with respect to neighboring REEs (Fig. S5).

For example, the Ce contents of the Carajás jaspilites defined perfect linear relations with respect to Pr (R^2 of 0.97), indicating insignificant effects on Ce from hydrothermal alteration. Meanwhile, Eu contents displayed a better correlation without type-II BIF samples ($R^2 = 0.63$), which demonstrated a possible effect of basaltic input or hydrothermal alteration. Finally, the Carajás jaspilites do not exhibit Eu or LREE depletion, and tend to display consistent REY_{SN} patterns, thereby suggesting that they were not significantly altered by metamorphic processes (Grauch, 1989; Bau, 1993). In addition, the Carajás jaspilites display a marked banded texture and primary sedimentary structures. Metamorphic effects were weak or absent in the studied samples as they belong to sub-greenschist facies (Macambira, 2003; Martins et al., 2017; Figueiredo e Silva et al., 2020). Therefore, we can suggest that REY distributions of Carajás jaspilites were not significantly altered by post-depositional processes, and hence, they can be regarded as reliable proxies of the geochemical signature of seawater at the time of deposition of BIF. This is further supported by the close similarity between the seawater-like (except for redox sensitive Ce and Eu elements) REY_{SN} patterns of pure and pristine Carajás jaspilite that suggests that this BIF recorded the REY distribution in ambient seawater and are robust geological archives of marine biogeochemical proxies in spite of diagenesis and/or metamorphism (e.g., Bau et al., 1997; Alexander et al., 2008; Planavsky et., 2014).

5.2. Hydrothermal fluids influence in Carajás BIF

The Carajás jaspilites display patterns of pure marine chemical sediments (e.g., low Al_2O_3, TiO_2, and HFSE contents), which renders them suitable as archives of seawater from where they were precipitated. Modern seawater from the open ocean is characterized by positive La, Gd, and Y anomalies, as well as negative Ce anomalies and LREE depletion when normalized to shales (Taylor & McLennan, 1985; Bolhar et al., 2004; Planavsky et al., 2010). These patterns are typically mimicked in the REY patterns of post-Archaean BIFs such as the

Kuruman Iron Formation (Bau & Dulski, 1996) and the Dales Gorge Member of the Brockman Iron Formation (Ewers & Morris, 1981; Pecoits et al., 2009) (Fig. 7). Some of these characteristics REY patterns also occur in the classic Archean Isua BIF (Fig. 7; Bolhar et al., 2004) and the Carajás jaspilite samples analyzed in this study. The majority of Carajás jaspilites samples, with a minimum depositional age of ~2.74 Ga (Trendall et al., 1998), also display positive La, Gd, and Y anomalies (Fig. 7), even though, there is a lack in true negative Ce anomalies (Fig. 14). Instead, large positive Eu anomalies (Eu/Eu^*_{SN} = 1.86–5.05; Fig. 8D) were observed, which are typical features of iron formations older than 2.5 Ga (e.g., Alexander et al., 2008; Konhauser et al., 2017). Apart from redox-sensitive Ce and Eu anomalies, the general shape and details of the Carajás REY patterns were like those of the patterns for modern seawater, supporting the assertion that these sediments precipitated directly from the Archean seawater, and they possessed trace element characteristics of contemporaneous seawater.

Most of the Carajás jaspilite samples displayed intense positive Eu anomalies (Eu/Eu^*_{SN} = 1.86–5.05; Fig. 8D), hinting towards fluxes of high-temperature (>350 °C) hydrothermal fluids (Fig. 11). Fabre et al. (2011) measured a similar Eu/Eu^*_{SN} ratio ranging up to 7.16 in BIF samples from the N4 deposit. These unprecedented Eu anomalies from Carajás jaspilites have been also reported in other studies (Justo et al., 2020; Rego et al., 2021). Such elevated Eu/Eu^*_{SN} ratios indicate an unusually strong hydrothermal contribution to the Carajás Basin during the deposition of the BIF units. Similarly, the Al_2O_3 vs SiO_2 discrimination diagram (Wonder et al., 1988) shows that all BIF samples plot in the hydrothermal field (Fig. S6). This might also indicate that Si and Fe were likely derived from seawater and hydrothermal sources. Note that this does not imply that the Carajás jaspilite precipitated from a high-T hydrothermal fluid or a hydrothermal plume. Rather, it only reveals that the seawater had received significant REY input from hydrothermal vents, where the BIF was eventually formed (Bau & Alexander,

2009; Wang et al., 2017). In addition, the 10 samples of type-II BIFs displayed null or weakly negative Eu anomalies (Eu/Eu^*_{SN} = 0.64–1.48; Fig. 8D). Negative Eu anomalies, which is rarely seen in BIFs, suggest that the REY patterns of the Carajás jaspilites were also influenced by the heterogeneous input of volcanic materials within the depositional basin.

Secular changes in the magnitude of Eu anomalies in BIFs have been historically assumed to record diminishing hydrothermal flux with decreasing ages from Eoarchean to early Precambrian (Fig. 12). It is noteworthy that the large positive $(Eu/Eu^*)_{SN}$ anomalies of the Carajás Basin are comparable to or are significantly higher (1.86–5.05; Fig. 12) than those for ~2.7–2.5 Ga BIFs. For example, the value of $(Eu/Eu^*)_{SN}$ was 1.3 to 3.4 for the 2.62 Ga Slave Craton (Haugaard et al., 2017), 2.8 to 4.4 for the 2.6 Ga Krivoy Rog (Viehmann et al., 2015), 1.0 to 2.75 for the 2.5 Ga Kuruman Iron Formation (Bau & Dulski, 1996), and 1.2 to 2.1 for 2.46 Ga Joffre Member of the Brockman Iron Formation (1.2 to 2.1; Haugaard et al., 2016b). The origin of the highest $(Eu/Eu^*)_{SN}$ values in Carajás jaspilite is not yet clear, however, it could be associated with an extensive basaltic volcanism in the Parauapebas Formation with at least 11 lava flows (Martins et al., 2017). It is considered that volcanism in this region was generated in an extensional regime related to continental rift setting at approximately 2.75 Ga (Gibbs et al., 1986; Martins et al., 2017; Tavares et al., 2018; Teixeira et al., 2021). Therefore, we can suggest that the peak in the $(Eu/Eu^*)_{SN}$ values for these BIFs was probably due to the enhanced magmatism during this period.

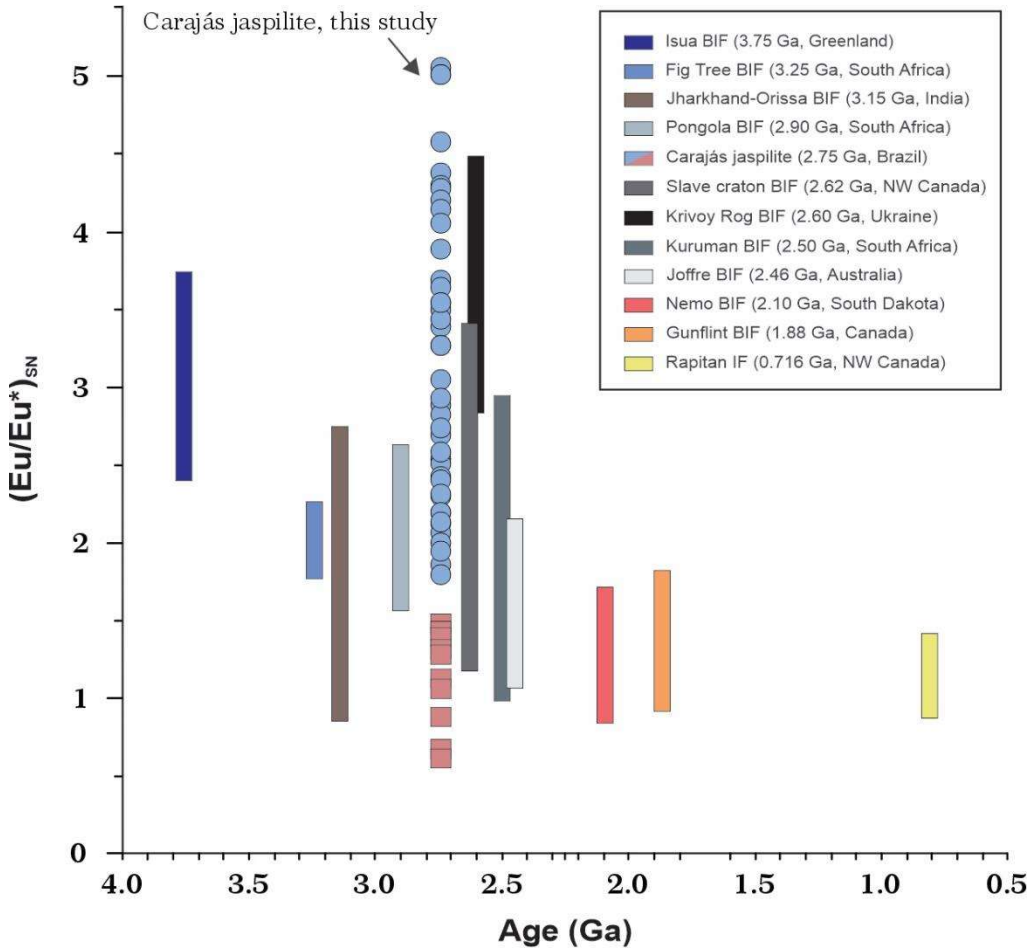

Fig 12. *PAAS-normalized (Taylor & McLennan, 1985) Eu anomaly $(Eu/Eu^*)_{SN}$ of Carajás jaspilite and some of the important worldwide BIFs through time; note that impure BIFs show divergent behavior with Eu anomaly varying from 0.64 to 1.48. Data for Isua from Frei & Polat (2007); Fig Tree from Derry & Jacobsen (1990) and Hofmann (2005); Jharkhand-Orissa from Bhattacharya et al. (2007); Pongola from Alexander et al. (2008); Slave Craton from Haugaard et al. (2016a, 2017); Krivoy Rog from Viehmann et al. (2015); Joffre from Haugaard et al. (2016b); Kuruman from Bau & Dulski (1996); Nemo from Frei et al. (2008); Gunflint from Danielson et al. (1992); Rapitan from Halverson et al. (2011).*

The presence of large positive Eu anomalies in the studied samples provides a clear evidence that the REY composition was derived from high-T hydrothermal fluids that influenced the seawater of the basin which hosted the Carajás jaspilite. However, the remaining

input of REY that affected the jaspilites was predominantly the Archean ambient seawater. Dymek & Klein (1988) and Alexander et al. (2008) introduced conservative two-component mixing models to assess the proportions of seawater and high-T hydrothermal fluids. This model uses trace element compositions of modern seawater and black smoker fluids, which offer the best analogs for high-T fluid compositions. For modeling, the Y/Ho, Sm/Yb, and Eu/Sm ratios were used as end-members to test the relative proportions of fluid that contributed to the observed REY distribution in Archean BIFs. The Eu/Sm variations in Carajás jaspilites can be modeled with the contribution from more than 0.1% and less than 1% hydrothermal fluid (Fig. 13A). Generally, this mixing ratio is in good agreement with a 1:100 or 1:1000 mixture of seawater and hydrothermal fluid to explain the REY patterns of other BIFs (Barrett et al., 1988; Dymek & Klein, 1988; Klein & Beukes, 1989). Nevertheless, such mixing could not produce consistent Sm/Yb and Y/Ho ratios. Mixing calculations indicate that a significantly higher contribution of hydrothermal fluid (1% to 5%) might account for the observed elemental ratios in the samples (Fig. 13C). Hence, this mixing ratio is inconsistent with the 0.1% to 1.0% contribution of the high-T fluids, which is necessary to account for the Eu/Sm variations (Fig. 13B). The poor fit of the mixing model in explaining the relatively high Sm/Yb ratios of the Carajás jaspilites indicate the possible existence of additional REY sources (e.g., basaltic rocks) in these BIF samples. It is noted that similar high Sm/Yb ratios were also observed in the 2.9 Ga Pongola BIF, which Alexander et al. (2008) explained by the input of continentally derived solutes. The Carajás samples exhibit such features (Fig. 13A; 13B), however, here we have considered that the high Sm/Yb ratios were associated with fluids derived from basaltic rocks (Fig. 13A; 13C). The influence of Fe-rich fluids derived from adjacent basalts could be also noticed based on the observed trend of type-II BIFs, which pointed to basaltic rocks in mixing diagrams (Fig. 13). This interpretation is further supported by the proximity of the Carajás

jaspilite to an intense submarine volcanic activity (Macambira, 2003; Martins et al., 2017; Justo et al., 2020). Hence, because of this basaltic input as an additional REY source, which would have resulted in a decrease of Y/Ho ratios and an increase of Sm/Yb ratios, the samples plot along and under the line of the high-T hydrothermal fluids and seawater mixing (Fig.13C). It can impart a higher mixing ratio and lead to the misidentification of the relative proportions of fluid that contributed to the REY distribution in Carajás BIFs. Taking it into consideration, the conservative two-end member mixing lines that best evaluate the proportions of seawater and high-T hydrothermal fluids are the Sm/Yb vs. Eu/Sm (Fig. 13A) and Y/Ho vs. Eu/Sm (Fig. 13B) diagrams. Therefore, the mixing models indicate that the jaspilites of the Carajás Basin could have been precipitated from more than 0.1% and less than 1% hydrothermal fluid mixed with seawater (Fig. 13).

In summary, we adopted a three-end-member mixing model involving seawater, high-temperature hydrothermal fluids, and fluids derived from basaltic rocks to match the observed REY characteristics of the Carajás jaspilites. The influence of flux derived from the mafic crust is observed mainly in the BIF samples close to the intercalated basaltic flows (type-II). However, negligible detrital components were present in Carajás jaspilites, which preclude the direct incorporation of mafic crustal detritus. Hence, we suggest that a small mafic crust-derived flux was derived from the mafic subjacent rocks represented by the Parauapebas basalts. The low Y/Ho ratios of ~26 and negative Eu anomalies (Martins et al., 2017) could have been incorporated into the ambient seawater and/or hydrothermal fluids through extensive high–temperature hydrothermal alteration and leaching of basalt-dominant crusts (Fig. 13). Minor incorporation of REY leached from basalts to the water masses from where the Carajás jaspilite was precipitated can significantly change the elemental ratios of seawater, as shown in the model (Fig. 13). The possible influence of basaltic crust-derived fluxes was also observed by

Huang et al. (2019) in samples from ~2.52 Ga Dengfeng BIFs, China. Such a process could also transfer enriched Nd isotopes from the crustal contaminated basaltic rocks to the ambient seawater and/or hydrothermal fluids (Alexander et al., 2009). The Sm–Nd isotopic constraints on ocean chemistry are further discussed in the subsequent paragraphs.

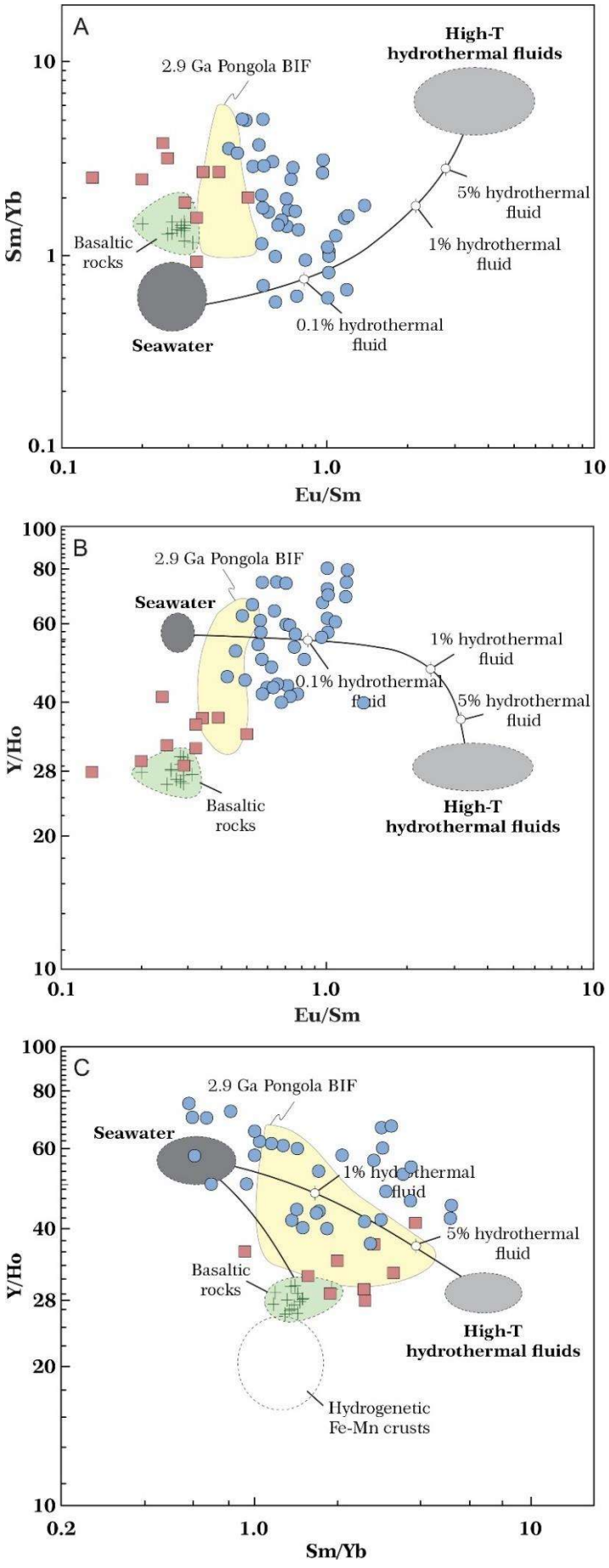
A
High-T
hydrothermal fluids
2.9 Ga Pongola BIF
5% hydrothermal
fluid
1% hydrothermal
fluid
Basaltic
rocks
0.1% hydrothermal
fluid
Seawater
Sm/Yb
Eu/Sm
B
2.9 Ga Pongola BIF
Seawater
1% hydrothermal
fluid
0.1% hydrothermal
fluid
5% hydrothermal
fluid
Basaltic
rocks
High-T
hydrothermal fluids
Y/Ho
Eu/Sm
C
2.9 Ga Pongola BIF
Seawater
1% hydrothermal
fluid
5% hydrothermal
fluid
Basaltic
rocks
High-T
hydrothermal fluids
Hydrogenetic
Fe-Mn crusts
Y/Ho
Sm/Yb

Fig 13. *Two-component mixing models in terms of;* ***A)*** *Sm/Yb versus Eu/Sm, showing that more than 0.1% and less than 1% (> 350 °C, Bau & Dulski, 1999) fluid contribution to waters with shallow (< 500 m) seawater REY distributions (Alibo & Nozaki, 1999) is sufficient to explain Eu/Sm ratios;* ***B)*** *Y/Ho as a function of Eu/Sm, demonstrating that relatively small (0.1%) contributions of black smoker fluid can model Y/Ho and Eu/Sm behavior in the Carajás jaspilite;* ***C)*** *Y/Ho versus Sm/Yb, indicating that a significantly higher contribution of hydrothermal fluid (1–5%) may account for these elemental ratios in the samples. The mixing diagrams are modified from Alexander et al. (2008). Data for the basaltic rocks and 2.9 Ga Pongola BIF are from Martins et al. (2017) and Alexander et al. (2008), respectively.*

5.3. Redox state of Neoarchean seawater in the Carajás Basin

Cerium concentrations in BIFs provide important information for constraining the paleo-redox conditions of ancient seawater. In general, oxygenated water display a strong negative Ce anomaly when normalized to shale composition (Ce/Ce^*_{SN}), whereas suboxic and anoxic marine settings lack negative Ce anomalies (German et al., 1991; Bau & Koschinsky, 2009). The oxidation of Ce^{3+} to Ce^{4+} significantly reduces Ce solubility, resulting in its preferential removal onto Mn-Fe oxyhydroxides, organic matter, and clay particles (Byrne & Sholkovitz, 1996). This process leaves the residual water column depleted in Ce, thereby creating a characteristic negative Ce anomaly. In contrast, suboxic and anoxic marine waters lack large Ce anomalies due to the reductive dissolution of Fe-Mn particles (German et al., 1991). However, it can be challenging to identify Ce anomalies because of the anomalous abundance of La. For this reason, Bau & Dulski (1996) established a Ce/Ce^*_{SN} versus Pr/Pr^*_{SN} discrimination diagram to distinguish “real” from “fake” Ce anomalies in seawater and marine chemical sediments. In this diagram (Fig. 14), most Carajás jaspilite samples displayed true positive La anomalies instead of negative Ce anomalies, and there were no deviation from trivalent Ce behavior, indicating that they were deposited under anoxic condition (Bau &

Dulski, 1996). Although the 10 type-II BIFs were initially interpreted to have true negative Ce anomalies, particularly owing to the significant influence of fluxes derived from mafic crust on their REY patterns, they were not considered further to avoid misidentification of paleo-redox conditions of Carajás ancient seawater. Fabre et al. (2011) and Justo et al. (2020) also reported an anoxic environment for the Carajás jaspilite samples in the Serra Norte district. However, in our dataset, three samples from the Carajás Formation exhibited true negative Ce anomalies (Fig. 14). These samples were restricted to a depth of 280 and 300 m (Fig. 8E; 8F) above a basaltic flow (Fig. S1). SHRIMP zircon U–Pb dating suggest that the samples have Early Neoarchean crystallization age of 2745 ± 5 Ma (Martins et al., 2017). This suggests that the Carajás jaspilites were deposited in an ocean with redox heterogeneity. Several studies have also reported negative Ce anomalies in Archaean BIF (Kato et al., 2006), however, it could be linked to post-depositional alteration (see Bonnand et al., 2020 for details). These studies highlight the need to carefully consider the potential of post-depositional alteration to modify elemental and isotopic redox proxies. Caution is warranted while inferring the ancient presence of O_2, especially if direct geochronological constraints on the age of the proxy signal is lacking (Bonnand et al., 2020). However, the Ce content of the Carajás jaspilites defines perfect linear relations with other relatively immobile elements (Pr) with R^2 of 0.97 (Fig. S5), which indicates insignificant effects of post-deposition alterations on Ce. Therefore, assuming that the observed Ce signature retains the original composition of the ancient seawater, we propose that considerable dissolved oxygen, although heterogeneously distributed, existed throughout the Carajás Basin, which permitted Fe(II) oxidation at a regional scale. However, such concentrations were high enough to convert Ce^{3+} to Ce^{+4} solely at a local scale (Bau & Dulski, 1996). This conclusion is consistent with the discontinuous redoxcline model proposed for conditions before the Great Oxidation Event (GOE) (Planavsky et al., 2012; Schier et al., 2020).

Moreover, the presence of oxygenated water for a short interval during BIF deposition was also suggested by a previous stable (Mo) isotope study that reported elevated $\delta^{98/95}$Mo compositions (up to 1.82‰) in Mo-rich black-shale samples from the bottom of the Carajás Formation, which the authors explained as a "oasis of oxygen" at the Neoarchean (Cabral et al., 2013). Mild oxidizing conditions were also suggested by Justo et al. (2020), who described the band-scale REY distribution in iron formations in Carajás. Our hypothesis agrees with earlier reports on the deduced oxic conditions based on Cr-isotope data from Archean BIF (Frei et al., 2009).

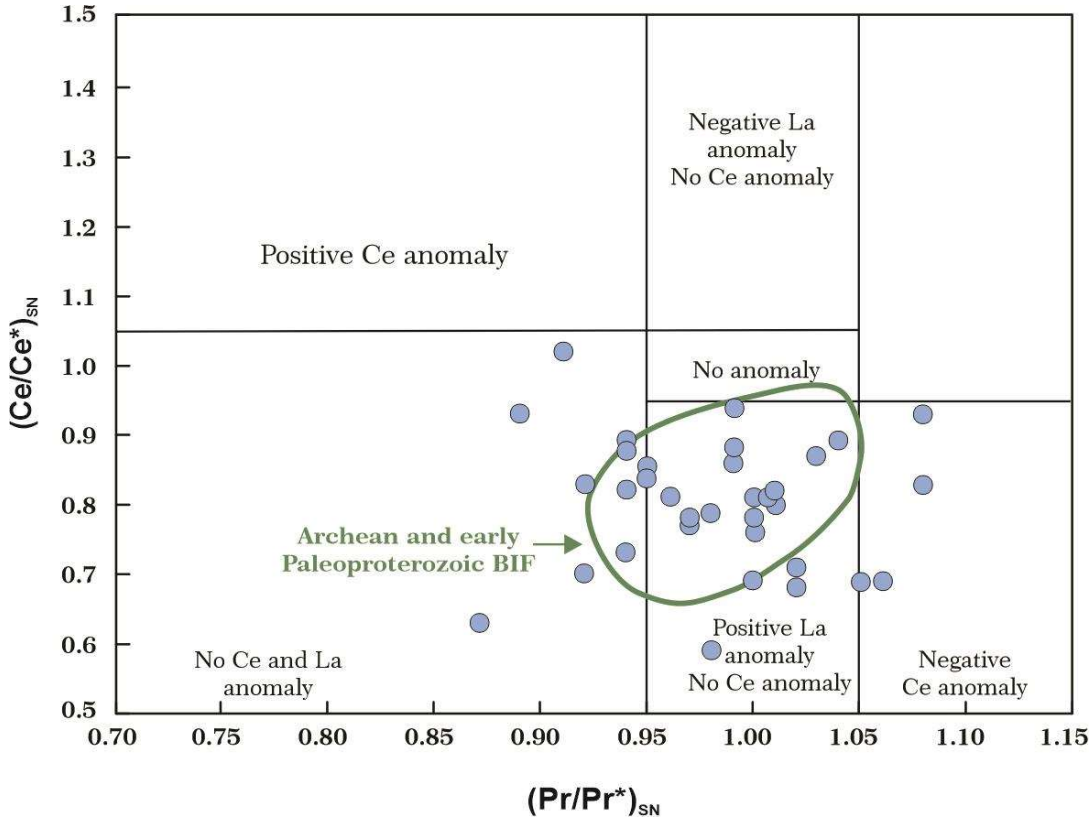

Fig 14. *Plot of Ce and Pr anomalies normalized to PAAS for the whole-rock data of the Carajás jaspilite to discriminate between positive La and true Ce anomalies (after Bau & Dulski, 1996). The type II BIF samples, which might initially be taken as the presence of true negative Ce anomalies, particularly, due to the significant influence on their REY patterns by flux derived from the mafic crust, will not be plotted to avoid misidentification of paleo-redox conditions of Carajás ancient seawater. The field for Archean and Early Paleoproterozoic (> 2.3 Ga) BIFs is modified after Planavsky et al. (2010).*

In conclusion, most of the geochemical data suggest that deposition of the Carajás jaspilite did not occur under a fully oxygenated environment (lack of Ce/Ce^*_{SN} anomalies). However, the presence of negative Ce anomalies in a few sections of the BIF sequence might suggest the occurrence of a very early oxygen whiff or localized oxygenated microenvironments at approximately 300 million years before the GOE (2.51–2.43 Ga; Konhauser et al., 2011; Gumsley et al., 2017; Warke et al., 2020).

5.4. Iron isotopic constraints

The positive $\delta^{56}Fe$ values obtained for the studied samples BIF (average of 1.34 ± 0.03 ‰, n = 18) are in agreement with the published data from solution-based ICP-MS analyses, which showed an enrichment of heavier isotopes (Fabre et al., 2011; Rego et al., 2021) (Fig. S7). Nevertheless, in the present study, we observe a heterogeneous distribution of positive $\delta^{56}Fe$ values in BIF samples with depth (Table 1; Fig. 11), in contrast to these previous results that showed a rather invariable iron isotope composition over the sedimentary package. This contrast is probably due the differences between the studied scale, as the present data extend over a wider thickness than it was previously investigated, spanning across a complete succession of the Carajás BIF. In the upper parts of the BIF sequence, mostly above the type-II BIFs, a large number of samples have significantly high $\delta^{56}Fe$ values (average $\delta^{56}Fe$ = +1.57 ‰, n = 9) compared to those in the lower part (average $\delta^{56}Fe$ = +1.25 ‰, n = 5). The lower $\delta^{56}Fe$ values in the lower part is likely due to the higher abundance of magnetite towards the deeper portions (below 350 m) of the Carajás BIF unit (Fig. S2). Although magnetite in many Archean BIFs is inferred to have formed after hematite (e.g., Bekker et al., 2010), the Fe isotope, petrographic, and geochemical data from the 2.75 Ga Carajás BIF presented here indicate the Carajás magnetite is a secondary feature formed after lithification of the primary jaspilitic chert and not via direct precipitation from seawater, as evidenced by the secondary magnetite

replacement (locally) of well-bedded jaspilitic layers at basal parts of the BIF sequence (Fig. 4A; 5C). Magnetite-rich bands formed during this secondary stage has lower average $\delta^{56}Fe$ values than those of the "primary" hematite-rich layers (Fig. 11). One interesting aspect is that the least positive $\delta^{56}Fe$ values of +0.83 to +1.10 ‰ (average +0.95 ‰, n = 4) were obtained in BIF samples influenced by adjacent volcanic activity (type-II BIF; Fig. S1; 11). Because igneous rocks generally have bulk rock $\delta^{56}Fe$ values of approximately 0 ± 0.15‰ (Sharma et al., 2001; Dauphas et al., 2017; Heard & Dauphas, 2020), the mixing of the lighter Fe isotope flux derived from the mafic subjacent rocks with ambient seawater and/or hydrothermal fluids might have resulted in the precipitation of hematite with less positive $\delta^{56}Fe$ values compared to the other jaspilites. This flux, enrichened in lighter isotopes, probably was leached through convection of seawater along the fractures in the basalts. Fe isotopes in the Carajás jaspilite could have been affected by Fe derived from clastic materials or secondary minerals present in the rocks, not solely reflecting chemically precipitated Fe oxides. However, the samples used for the Fe isotope study to interpret the paleoenvironment conditions responsible for BIF deposition in the Carajás Basin (Table 1) came from the most preserved intervals that lack any evidence of weathering and post-depositional (hydrothermal and metamorphic) alteration. In addition, negligible clastic materials present in Carajás jaspilite preclude the direct modification of Fe isotope compositions of the chemical precipitates. Therefore, the high Fe isotope values in the studied samples were likely originated from the chemical precipitation during sedimentation.

Overall, Fe isotope are remarkably positive ($\delta^{56}Fe$ = +1.34 ± 0.03 ‰). Considering the average $\delta^{56}Fe$ values of sedimentary Fe oxides from various time periods in the Archean, some authors suggested an apparent overall Fe isotope trend from high positive $\delta^{56}Fe$ values in the Paleoarchean to less positive $\delta^{56}Fe$ values in the Early Neoarchean (Johnson et al., 2003; Rouxel

et al., 2005; Planavsky et al., 2012; Czaja et al., 2018). This overall trend suggests a general increase in the oxidative power on the Earth's surface with decreasing age over the course of the Archean (Satkoski et al., 2015; Czaja et al., 2018). The average δ^{56}Fe value of the precursor Fe-oxide precipitate in the Fe-Si precipitate that produced the hematite-rich Carajás jaspilite is +1.57 ‰ based on the preservation of a primary seawater signature from which these rocks were formed. This value is lower than the average δ^{56}Fe value of ~2.0‰ for hematite grains from the 3.46 Ga Marble Bar Chert (Li et al., 2013), but higher than the estimated average δ^{56}Fe values of 1.2 ‰ in the 3.8 Ga Isua BIF (Czaja et al., 2013) and that of ~0.4 ‰ in the 3.25 Ga Manzimnyama BIF (Satkoski et al., 2015). In a δ^{56}Fe versus age diagram (Fig. 15), the Fe isotope values measured for the Carajás jaspilite plot close to the most positive ones ever measured in Archean BIFs (Johnson et al., 2003; Rouxel et al., 2005; Johnson et al., 2008; Konhauser et al., 2017). Hence, the highly positive Fe isotopic signatures recorded in the Carajás jaspilite require the existence of a complementary isotopically light Fe isotope reservoir (Fabre et al., 2011) such as surface seawater containing dissolved Fe(II) and/or a high input of heavy Fe isotope-rich material. The conspicuous positive Fe isotope peak corresponding to the ~2.74 Ga Carajás jaspilite (Fig. 15) is associated with the noteworthy large positive Eu anomalies (Fig. 12). Although the origin of these two characteristics is not yet clear, it likely corresponds to an intense input of hydrothermally derived fluids at that time (Viehmann et al., 2015; Konhauser et al., 2017), possibly triggered by major magmatic activity (Viehmann et al., 2015). This hypothesis is further supported by the proximity (adjacent) of an extensive rift-related volcanism (Martins et al., 2017), which could have provided an increased flux of mantle-derived fluids during this period, intensifying the hydrothermal activity (high δ^{56}Fe). A combination of factors, such as BIF deposition in an environment where significant hydrothermal activity took place has been also proposed (Rego et al., 2021).

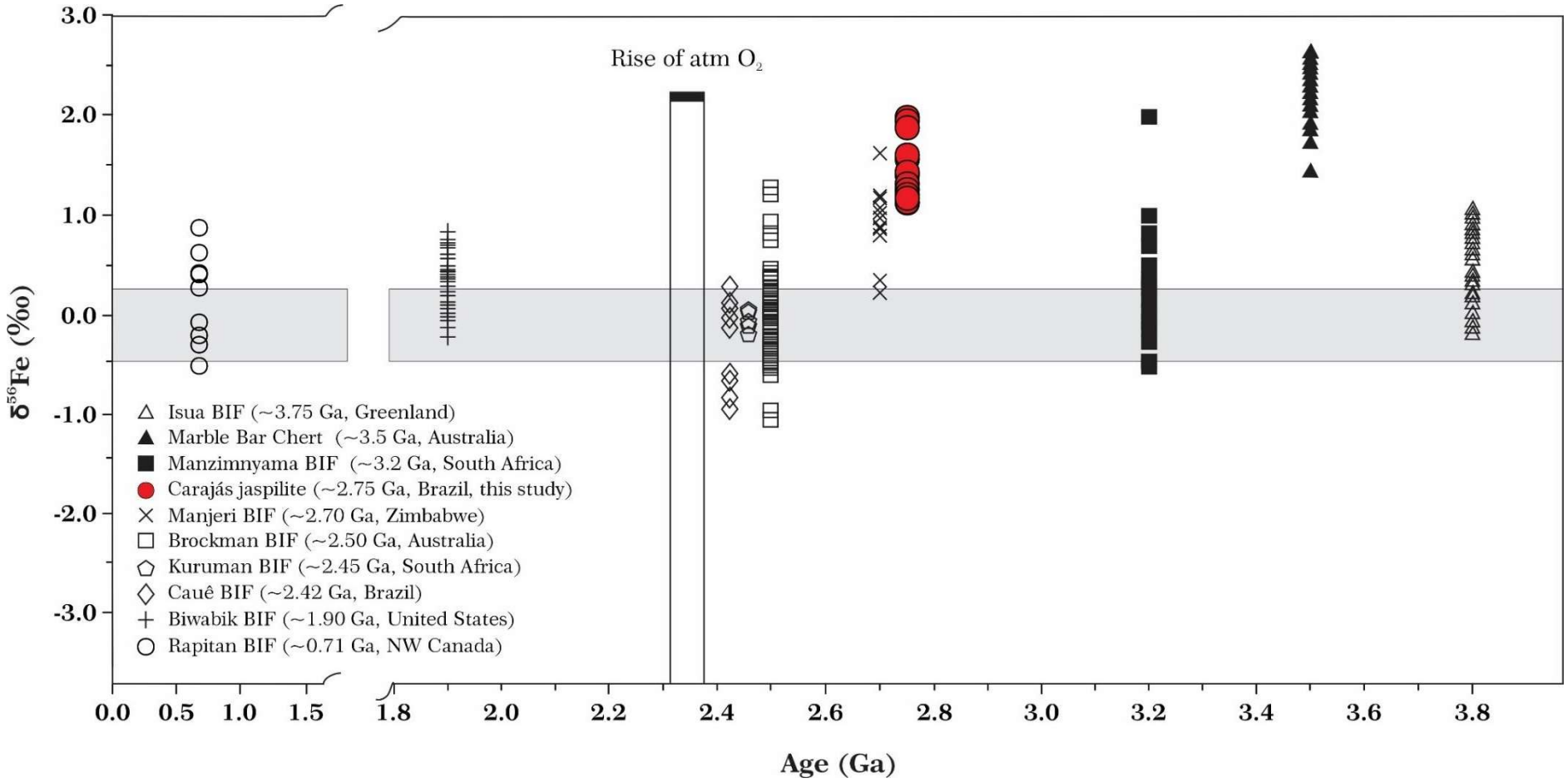
Rise of atm O_2
δ^{56}Fe (‰)
Age (Ga)
Isua BIF (~3.75 Ga, Greenland)
Marble Bar Chert (~3.5 Ga, Australia)
Manzimnyama BIF (~3.2 Ga, South Africa)
Carajás jaspilite (~2.75 Ga, Brazil, this study)
Manjeri BIF (~2.70 Ga, Zimbabwe)
Brockman BIF (~2.50 Ga, Australia)
Kuruman BIF (~2.45 Ga, South Africa)
Cauê BIF (~2.42 Ga, Brazil)
Biwabik BIF (~1.90 Ga, United States)
Rapitan BIF (~0.71 Ga, NW Canada)

Fig 15. *Plot of whole-rock $\delta^{56}Fe$ values for iron oxides (magnetite, hematite, or mixed) versus age for worldwide BIFs and other iron rich deposits (after Rouxel et al., 2005). The gray area corresponds to $\delta^{56}Fe$ values of Fe derived from igneous rocks (at 0.1‰) and hydrothermal sources (about -0.5‰) (Sharma et al., 2001; Severmann et al., 2004; Rouxel et al., 2008). Data for Isua from Czaja et al. (2013); Marble Bar Chert from Li et al. (2013); Manzimnyama BIF from Satkoski et al. (2015); Manjeri from Planavsky et al. (2012); Brockman from Johnson et al. (2008); Kuruman from Steinhoefel et al. (2010); Cauê from Mendes et al. (2017); Biwabik from Frost et al. (2007), Hyslop et al. (2008); and Rapitan from Halverson et al. (2011). The rise of atmospheric oxygen (atm O_2) is defined by multiple sulfur isotope analyses of (Bekker et al., 2004).*

The primary sedimentary structures occurring throughout the BIF unit (Fig. 3; 4) indicate that these rocks are in excellent degree of preservation and that these structures could be used to provide additional information on the mechanisms that led to the precipitation of BIF. Spherulitic microstructures in some parts of the BIF section (Fig. 5D; 5F) were previously interpreted as microfossils (Lindenmayer et al., 2001, Macambira, 2003; Ribeiro da Luz & Crowley, 2012) based on morphology and stable carbon isotope analysis. Because a deep-water setting (beyond ~200 m) in an open ocean has been attributed as a depositional environment for the Carajás BIF (Fabre et al., 2011; Justo et al., 2020), the micro-spherules were interpreted to represent microfossils of dissimilatory iron-reducing bacteria (DIR) (Ribeiro da Luz & Crowley 2012). The positive correlation between εNd(t) and $\delta^{56}Fe$ for the studied samples (Fig. 16D), and the lowest positive $\delta^{56}Fe$ values of the magnetite-rich samples (Fig. 11) could potentially be attributed to DIR that released isotopically light dissolved Fe(II) fluids (Beard et al., 2003; Johnson et al., 2008; Heimann et al., 2010; Czaja et al., 2013), eventually transported to the deep basin (Li et al., 2015; Konhauser et al., 2017). However, partial oxidation of magnetite to secondary hematite would also produce more positive $\delta^{56}Fe$ values. This is probably why the $\delta^{56}Fe$ values of BIF decrease systematically with increasing percentage of magnetite in the

samples (Fig. S10), whereas the δ^{56}Fe values of hematite-rich BIF do not display such changes. Moreover, the strongly positive Fe isotope compositions measured here for all samples indicate a minimal role of DIR bacteria during the formation of the analyzed jaspilite. The most likely formation mechanism of the Carajás jaspilites could be the direct transformation of Fe-oxyhydroxide seawater precipitates into hematite (Hem^1; Fig. 5A-D; S2; S3). The positive δ^{56}Fe values of hematite-rich type-I BIF are here interpreted to reflect the partial oxidation of hydrothermally derived Fe(II). Based on Fe isotope analyses, Fabre et al. (2011) also suggested that after the deposition of Carajás jaspilite, only a minor amount (if any) of hematite was partially reduced to magnetite, for instance by DIR. Hence, it is likely that this mechanism might had little impact on the bulk BIF Fe isotope composition (Fig. 16D) because their magnetite content was low (< 10% in each sample; see Section 4.1).

Based on our data, we suggest that during the deposition of Carajás jaspilite, submarine hydrothermal fluids injected throughout the basin, together with Fe-flux derived from leaching of the mafic crust, played a significant role in influencing the seawater chemistry. This is expected given that the entire Carajás Formation has been linked to an extensive magmatic event, which is generally considered a result of rifting that probably opened an restricted ocean (Gibbs et al., 1986; Olszewski et al., 1989; Martins et al., 2017; Tavares et al., 2018). A breakout event (rifting) could cause shallower mid-ocean ridges (Ernst et al., 2004), which, in turn, might have led to transgressive events that submerged the shallow shelf under waters directly owing to the influence of submarine mantle degassing and leaching of the oceanic crust (Haugaard et al., 2016b). The Carajás jaspilite samples enriched in heavy Fe isotopes indicate that only part of the Fe within the paleo-seawater was oxidized to Fe(III), and then precipitated. The mixing of Fe(II)-rich fluids, abundant reduced gases from the mantle (e.g., CH_4, H_2, H_2S), and alteration of new oceanic crust would have acted as O_2 sinks, which likely promoted marine

anoxia in the Carajás Basin (Haugaard et al., 2016b). The intense hydrothermal activity might have provided substantial Fe(II), and maintained general anoxic conditions in the Carajás Basin (Rego et al., 2020) reflected in strong Eu anomalies in REE patterns.

In the hematite-rich samples from upper part of the drill core of Carajás jaspilite, $\delta^{56}Fe$ values were found to vary by 0.80 ‰ ($\delta^{56}Fe$ = +1.10 to +1.90 ‰) over tens to hundreds of meters of section (Fig. 11). This suggests that the Fe isotope composition of seawater had changed over periods on the order of a few million years (<20 million years). One could argue that the relative abundance (%) of magnetite and hematite in these rocks can afford the heterogeneous-like signature. However, each hematite-rich samples have very low average magnetite content (presented as percent magnetite by area in Table 1). In addition, the average $\delta^{56}Fe$ values for each of this sample do not vary systematically with the percentage of hematite (Fe_2O_3) in the sample (Fig. S9). Only magnetite-rich $\delta^{56}Fe$ values vary systematically with the percentage of magnetite in the sample (Fig. S10). Therefore, the stratigraphic variation observed in $\delta^{56}Fe$ values in the studied Carajás jaspilite suggest that the Fe cycle in the late Archean seawater was affected by fractionation mechanisms (Steinhoefel et al., 2010; Haugaard et al., 2016b). This implies a non-steady state of the Archean Fe cycle with variable Fe concentrations caused by the competitive effect of partial oxidation of Fe and subsequent precipitation, and Fe supply from hydrothermal sources (Rouxel et al., 2005). Again, it is important to stress that the hematite-rich bands sampled for this study had primary bedding textures (Fig. 5A; 5B) suggesting they also preserved primary Fe-isotope compositions. Rapid changes in Fe concentration are consistent with the idea that Fe oxide deposition in BIFs resulted from the episodic upwelling of Fe-rich deep waters, accompanied by partial biological and/or abiological oxidation in shallow waters (Rouxel et al., 2005). The jaspilites lack a true negative Ce anomaly, which might reflect the absence of free oxygen in some localities of

Carajás Basin. Based on the absence of true negative Ce anomalies, Planavsky et al. (2010) proposed that microbially mediated (anaerobic) iron oxidation was dominating during the deposition of Archean and Paleoproterozoic iron formations. We suggest that anaerobic microbial Fe(II) oxidation, distinct from DIR, might have also played a role in the Carajás ambient seawater. This suggests that the Carajás jaspilites were formed under anoxic conditions, and anoxygenic photosynthesis could be the most plausible mechanism responsible for Fe oxidation in the Carajás Basin, which has been also suggested by previous studies in the basin (Rego et al., 2021). Nevertheless, the giant deposits of Carajás jaspilites might have formed through a combination of biological and abiotic oxidation, with the latter occurring in oxygen oases of the surface ocean preceding the GOE (Anbar et al., 2007; Frei et al., 2009; Cabral et al., 2013; Mendes et al., 2017). Mild oxidizing conditions were also suggested by Justo et al. (2020) due to the presence of negative Ce anomalies in a few sections of the BIF sequence, which would imply that the Neoarchean seawater environment was more oxidizing than that is commonly accepted (Canfield, 2005; Holland, 2005, 2006) at ~300 Ma before the GOE (2.51–2.43 Ga; Konhauser et al., 2011; Gumsley et al., 2017; Warke et al., 2020). This is supported by the emerging evidence for free oxygen in the Meso- to Neoarchean shallow oceans (Satkoski et al., 2015; Ossa Ossa et al., 2016; Eickmann et al., 2018). However, this Fe isotope reference frame cannot be uniformly expanded to the entire ocean because of the distinct changes in the redox state of the ocean–atmosphere system that could have occurred during this period and the complexity of Fe cycling in the Archean, in combination with its natural setting (Czaja et al., 2018).

5.5. Constraints from Sm-Nd isotopic composition of Carajás jaspilites

Carajás jaspilite samples were mostly formed during chemical precipitation from the ocean. Therefore, their REY composition can be used to determine the geochemistry of

seawater during the formation of BIFs. Thus, their Nd isotopic compositions can be utilized as ideal proxies for the ocean at ~2.74 Ga ago. However, it is necessary to examine whether the Nd isotopic contents recorded in the Carajás jaspilite samples were modified by post-depositional processes. Previous studies have shown that the Sm–Nd isotopic age determinations can also be used to identify post-depositional alteration (Shimizu et al., 1990; Alibert & McCulloch, 1993; Bonnand et al., 2020). The Sm–Nd isotope data of the Carajás jaspilite measured in this study define an isochron indicating that they were formed at 2707 ± 118 Ma (n = 34), whereas a subset of these data (n = 20) generated an isochron that suggests an older apparent age of 2795 ± 77 Ma (Fig. 10B). Both Sm–Nd isochrone apparent ages are concordant with the proposed minimum formation age of the Carajás jaspilites of ~2745 Ma (Trendall et al., 1998; Martins et al., 2017). If post-depositional events such as the ~2.00 Ga metamorphism recognized in the Trans-Amazonian cycle (Cordani et al., 1984; Macambira et al., 2009) or the multiple IOCG-type hydrothermal episodes (see Trunfull et al., 2020 and Schutesky & Oliveira et al., 2020) had altered the Sm–Nd isotope values, it would have reset and the isochron calculations would have yielded a younger metamorphic/hydrothermal age (Viehmann et al., 2014). Because the negative εNd(0) values and *f*Sm/Nd ratios were different from those of samples whose Sm–Nd isotopic system were obviously altered during post-depositional processes (Wang et al., 2014; Peng et al., 2018), the Carajás jaspilites appear to have preserved primary Nd isotopic signatures, and any possible metamorphic overprinting were excluded from these samples (Section 5.1). Therefore, we can conclude that all the studied samples have remained isotopically closed shortly after deposition/formation.

Overall, it is likely that the Archaean and Proterozoic oceans were strongly heterogeneous in their Nd isotopic composition, with εNd(t) values estimated to range from +1 to +5 in deep-water dominated by depleted mantle-like hydrothermal sources. On the other

hand, εNd(t) values down to −4 would have been typical of shallow waters dominated by terrestrial sources (Miller & O'Nions, 1985; Jacobsen & Pimentel-Klose, 1988; Alexander et al., 2008). The studied Carajás jaspilite samples display a wide range of εNd (t = 2.75 Ga) values between −4.97 and +5.40 (Fig. 12H; 13), and have heterogeneous Nd isotopic signatures throughout the drill core (Table S6; Fig. 8H). The studied rocks have negative εNd (t) values, when close to the basaltic flows/jaspilite contact (type-II, Fig. S1), and predominantly positive εNd(t) values in the remaining samples. The predominantly positive, depleted mantle-like initial εNd (t) values (–0.84 to +5.40, n = 15) for most of the samples of Carajás jaspilite unit (Table S6; Fig. 17) are coupled with pronounced positive Eu anomalies (Eu/Eu^*_{SN} = 1.86 to 5.05) and strongly super-chondritic Y/Ho ratios (average of 57.55) (Fig. 16A-C). This information supports the interpretation that submarine high-T hydrothermal input was a significant (if not dominant) source for the Nd isotopic signatures of seawater from where the BIF samples precipitated. However, the relatively wide range of εNd (t = 2.75 Ga) values observed in the Carajás jaspilite samples (Fig. 9 and 17), and their REY similarity with that of seawater further indicated that the coeval ambient (i.e., surface) seawater, which contributed materials to the studied BIFs, probably had lower initial εNd values compared to those inferred for the hydrothermal end-member (Peng et al., 2018).

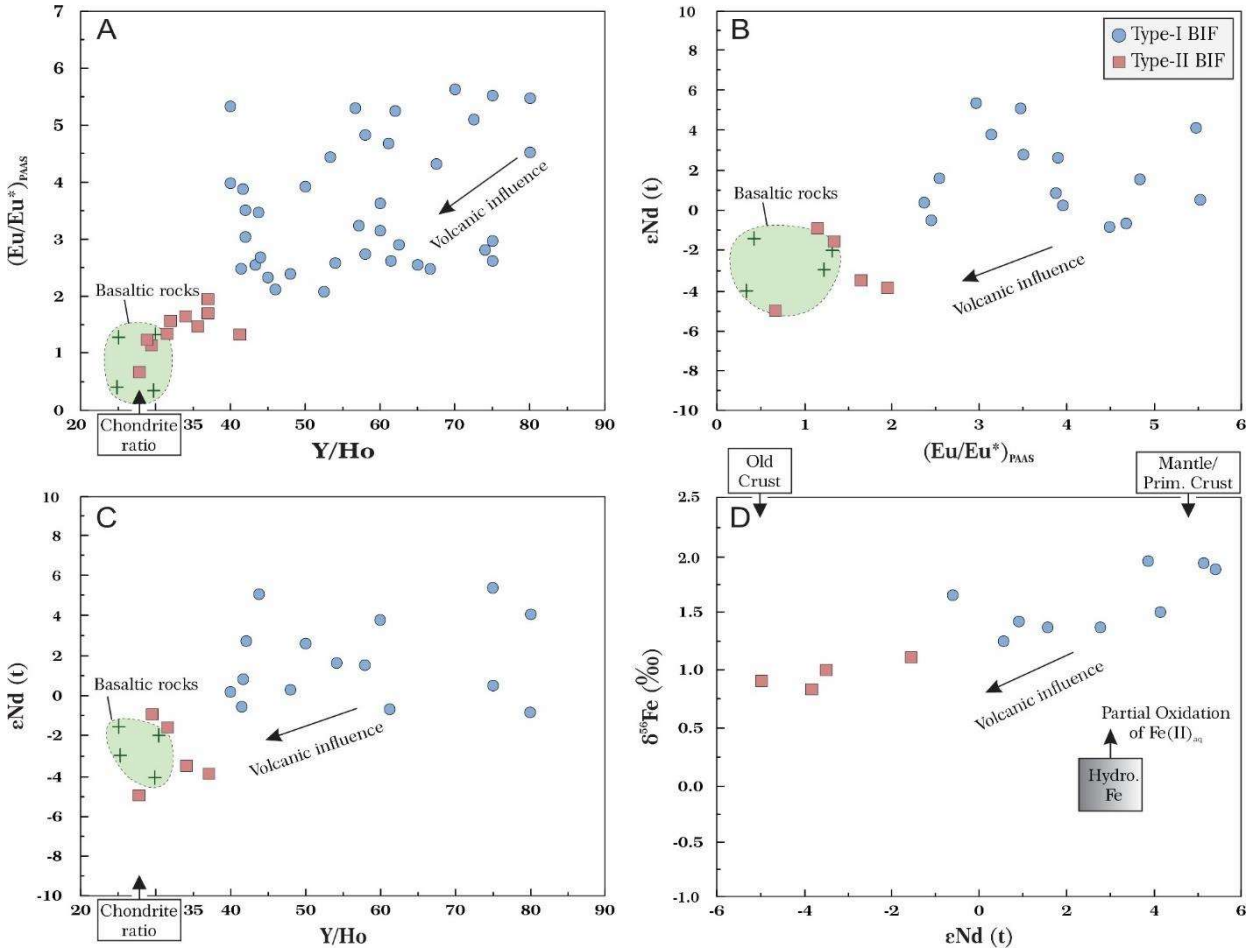

Fig 16. *Correlation diagrams using geochemical paleoenvironment proxies for Carajás jaspilites:* ***A)*** *Eu/Eu*$_{SN}$ and Y/Ho;* ***B)*** *εNd (t) and Eu/Eu*$_{SN}$;* ***C)*** *εNd (t) and Y/Ho;* ***D)*** *δ^{56}Fe and εNd (t) for hematite-rich samples. The positive correlation between εNd(t) and δ^{56}Fe seen in BIF samples is interpreted to reflect mixing between a hydrothermal (high-εNd(t), high-δ^{56}Fe) iron source and a minor iron mobilized by leaching of the mafic crust (low-εNd(t), low-δ^{56}Fe). Type-II BIF overlap basaltic rocks field demonstrating the volcanic influence in the geochemical signature of the Carajás jaspilite. Data of for the basaltic rocks are from Martins et al. (2017). εNd(t) was calculated for t = 2745 Ma (Martins et al., 2017).*

Hence, the deviation towards negative εNd(t) values (–4.97 to –0.90, n = 6) in samples near the basaltic flows/jaspilite contact (type-II BIFs) might suggest that the seawater during their formation was influenced by the weathering of older and isotopically evolved continental

flux (Alexander et al., 2008). This feature is also reflected in the T_{DM} (Nd) ages (2.94 to 3.60 Ga), which are predominantly older than the BIF depositional age (ca. 2.75 Ga) (Table S6; Fig. S8). Nevertheless, the lack of detrital materials in these samples indicates a deep-water depositional environment (i.e., distal to continental landmasses). Thus, it argues against a continentally derived solute source that might have contributed to Nd evolution. Two additional explanations for the enriched εNd(t) values of type-II BIFs may be advanced. Seafloor-vented hydrothermal fluids from enriched mantle or interactions with an enriched mantle source can produce enriched Nd isotopic compositions (Døssing et al., 2009; Grasse et al., 2012). Alternatively, the interaction of high-T hydrothermal fluids with the underlying older terrigenous clastic sediments or enriched crust can generate aqueous fluids with enriched Nd isotopic compositions (Piepgras & Wasserburg, 1987; Alexander et al., 2009). Given that the seafloor-vented hydrothermal fluids derived their isotopic compositions mostly by alteration of the subjacent crust (Kamber & Webb, 2001; Frei & Polat, 2007; Døssing et al., 2009; Wang et al., 2017), the initial εNd value of this end-member could be well constrained by that of the coeval mafic volcanic rock. The enriched εNd(t) values (–4.11 to –1.53; Table S6; Fig. 9; 16; 17) of the associated basaltic rocks in the Carajás Basin favor the presence of either an enriched mantle, or interaction with the underlying older terrigenous clastic sediments, or and enriched continental crust. Therefore, the Nd isotopic composition in seawater that were precipitated by type-II BIF samples were probably controlled by direct hydrothermal input rather than by terrigenous sources. It is important to note that these significant changes in εNd and T_{DM} (Nd) values occur near lava flows intercalated with Carajás jaspilite (Fig. 8H) supporting the hypothesis of intense high-T hydrothermal input throughout the BIF sequence. This information supports the above hypothesis for isotopically enriched or less depleted Nd reservoirs in the Carajás area. Furthermore, with the advancement in isotope mass spectrometry, some

investigations on the sources of iron and silica contents of seawater have been carried out by analyzing solution Fe isotopic data coupled with robust Sm–Nd isotope systematics (e.g., Li et al., 2015). The subtle positive correlation between εNd(t) values, Eu anomalies, Y/Ho ratios, and δ^{56}Fe values (Fig. 16) in the Carajás jaspilite data might imply that both iron and REY were derived from a similar source (i.e., the hydrothermal fluids and ambient/surface seawater, together with flux derived from mafic crust). Also, the Fe/Nd ratios of the end-members did not change significantly in the Neoarchean Ocean (Planavsky et al., 2020). Cabral et al. (2013) reported Nd isotopic data from black-shale samples associated with Carajás jaspilites. These samples had depleted εNd values from 0.4 to 2.8, corresponding to depleted-mantle model ages of 2.8–3.0 Ga (Table S6; Fig. 9; 16). Differences in εNd values between the black shales and jaspilite could have aroused because of their differential nature, as the former is a clastic sedimentary rock, whereas the latter is chemical sediment. A recent study by Rousseau et al. (2015) on REE concentrations and Nd isotopic compositions for both dissolved and particulate materials in the Amazon estuary highlight that the dissolved and suspended end-member components might have decoupled and/or had different εNd values. In this respect, we consider that it is highly possible that particles that formed the black shales were sourced mainly from the nearby depleted rocks. In contrast, seawater dissolved materials derived their composition by mixing isotopically different Nd sources (more enriched or less depleted source).

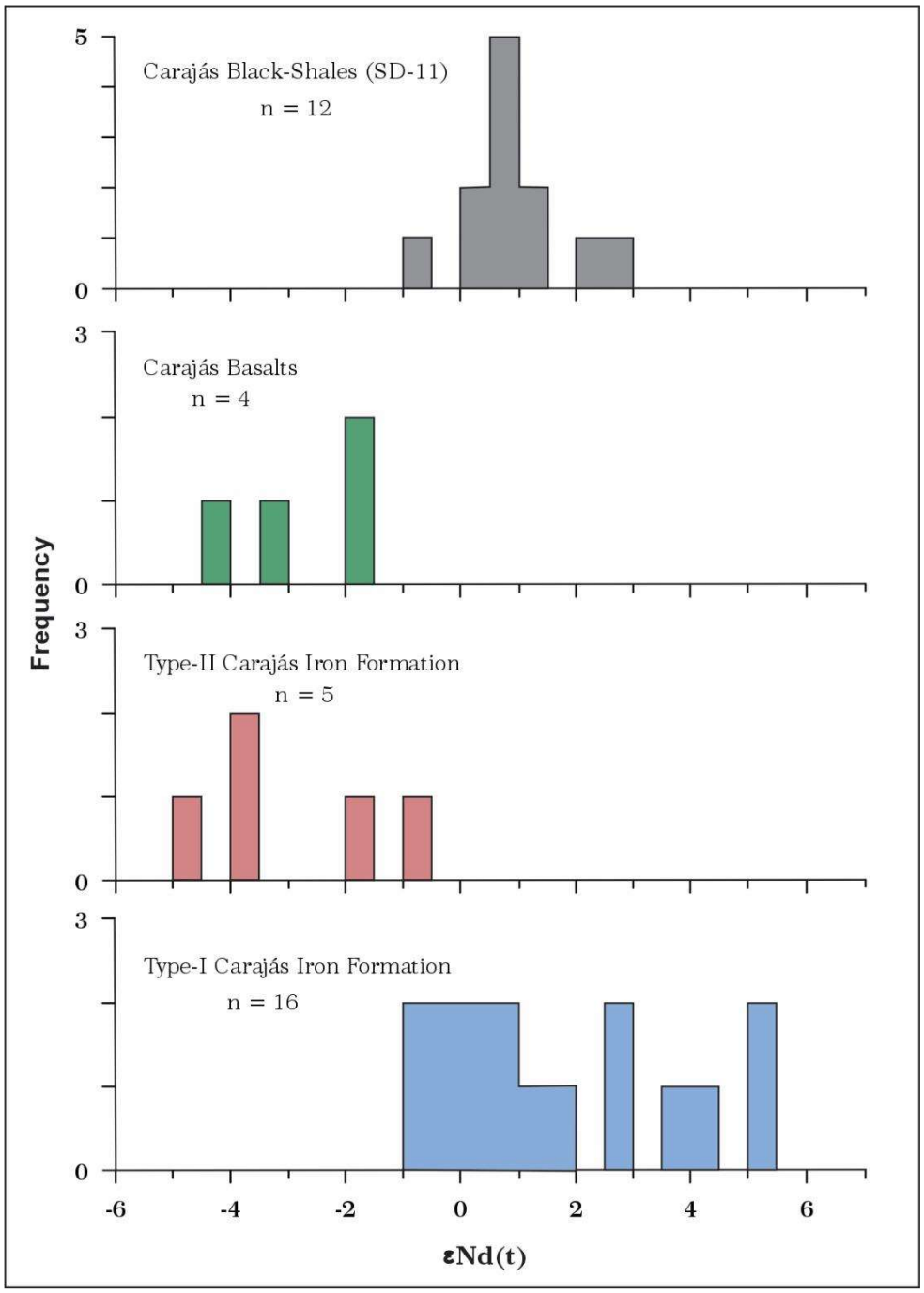

Fig 17. *Histograms of* εNd (t) *values for Carajás jaspilite samples, as well as associated rocks. Data for black shales and basalts from Cabral et al. (2013) and Martins et al. (2017), respectively.*

5.6. Depositional environment and tectonic settings

The Carajás jaspilites are grouped into the Carajás Formation that conformably overlie or are occasionally interlayered with the basalts and basaltic andesites of the Parauapebas Formation (Klein & Ladeira, 2002; Martins et al., 2017). These rocks belong to the Neoarchean Grão-Pará Group, the main volcano-sedimentary sequence of the Carajás Basin (~2.75 Ga; Gibbs et al., 1986; Wirth et al., 1986; Olszewski et al., 1989; Machado et al., 1991; Trendall et al., 1998; Martins et al., 2017). Although several models have suggested a subduction-related environment (Meirelles & Dardenne, 1991; Teixeira & Eggler, 1994; Zucchetti, 2007; Figueiredo e Silva et al., 2020), the formation of the Carajás Basin is usually considered the result of a rift-related event., which caused extensive bimodal magmatism with significant contamination of upper crustal rocks (Gibbs et al., 1986; Martins et al., 2017; Tavares et al., 2018; Teixeira et al., 2021). Considering the geochemical features from basaltic rocks, Martins et al. (2017) suggested that these basalts most likely formed during continental rifting before 2.76 Ga, and not in an arc-like environment. The basalts from N4W deposit display predominant negative εHf(t) values, suggesting that the source material had evolved from the Paleoarchean crust. Recently, detailed sedimentological investigations and U-Pb dating of detrital zircon (Rossignol et al., 2020) from the newly defined Serra Sul Formation suggested that this formation and the underlying Grão-Pará Group were deposited during successive extensional tectonic phases that affected the Amazonian Craton during late Neoarchean to early Paleoproterozoic. Following this and the new data presented here, we consider that Carajás jaspilites were formed in an extensional setting. The large positive Eu anomalies indicate BIF deposition near a hydrothermal vent, probably in a rift-basin environment, like other Archean to Paleoproterozoic BIFs worldwide, such as those from the Hamersley Group in Australia. The strongly positive Fe isotope compositions measured in this study interpreted to reflect partial

oxidation of hydrothermally derived Fe(II), further indicate that its deposition occurred mainly on deep-water in conditions with very low to no free O_2. Moreover, the lack of detrital materials, such as clay, and the lack of any syn-sedimentological features besides fine banding (i.e., absence of current-, tide-, or wave-generated sedimentary structures) in the studied samples also indicates a deep-water depositional environment, probably with distal to continental landmasses. Fe-rich fluids derived from leaching/alteration of subjacent mafic rocks (volcanic activity) could have been also incorporated into the water masses from where the Carajás jaspilite precipitated. Thus, it can be concluded that insignificant terrigenous input, high-T hydrothermal fluids, ambient seawater, and potential Fe flux derived from the submarine mafic rocks controlled the material sources of Carajás jaspilites. The deposition took place at ~2.75 to 2.73 Ga (Gibbs et al., 1986; Wirth et al., 1986; Olszewski et al., 1989; Trendall et al., 1998; Martins et al., 2017) mainly in deep-water, distal to continental landmasses, in a hydrothermal region overprinted by submarine environment of an rift-related basin.

BIFs are broadly classified as either Algoma-type or Superior-type based on the depositional environment (Gross, 1980, 1983). The large Eu anomalies observed in the Carajás jaspilite (average of 2.71; Fig. 12) are consistent with those of Algoma-type BIFs (Huston & Logan, 2004), mainly those of Archean and late Paleoproterozoic (Planavsky et al., 2010). In addition, abundant (mostly basalt) volcanic rocks interlayered with BIF bands (Fig. S1; 3) (Beisiegel et al., 1973; Macambira, 2003; Martins et al., 2017) suggests an Algoma-type BIF affinity. Nevertheless, the Carajás jaspilites are laterally very extensive and thick, with the original estimated thickness being more than 400 m in some cases (Macambira, 2003; Fig. 2), in contrast to most Algoma-type BIFs, which rarely extend for >10 km along strike and are typically <50 m thick (Bekker et al., 2010). Additionally, the studied BIF samples are poor in transition metals such as V (mean of 4.61 ppm), Co (2.79 ppm), and Ni (<1 ppm), which are

characteristic features of Superior-type BIFs (Gross & McLeod, 1980). Therefore, we suggest that neither Algoma-type nor Lake Superior-type BIFs can completely describe the Carajás jaspilite. We agree with the idea that it is more practical to consider these classifications as end-members, with a spectrum of intermediate varieties (Bekker et al., 2012; 2014; Konhauser et al., 2017).

It is now widely accepted that the deposition ages of the large, and economically important BIF deposits (Bekker et al., 2010) are consistent with mantle plume breakout events, which are recorded by the secular distribution of large igneous provinces (LIPs), dike swarms, and submarine-emplaced mafic volcanic rocks (Isley, 2005; Isley & Abbott, 1999; Rasmussen et al., 2012). One of these periods was associated with a mafic superplume event between 2.75 and 2.70 Ga (Isley & Abbott, 1999), corresponding to the accepted minimum age of ~2.74 Ga for the deposition of the Carajás BIFs (Trendall et al., 1998; Martins et al., 2017). Mantle plume activity provides the source of iron and enhances the precipitation of the BIF (Isley & Abbott, 1999). Although the data presented here suggest that the depositional setting of jaspilites from the Carajás Formation resulted from the rifting of older continental crust, it is unclear whether the attributed rift-related setting was linked to a mantle plume event or if it reflects a transition process from a collisional to a post-collisional environment, followed by rifting (Martins et al., 2017; Tavares et al., 2018). The absence of plume signature (e.g., enrichment in potassium and light rare earth elements) on the geochemical data from the Parauapebas formation basalts indicate that this rift-related setting was a result of post-collisional environment in the period 15–8 Ma (Tavares et al., 2018), and therefore, it was not directly associated with a mantle plume breakout event. Nevertheless, the hypothesis that Parauapebas volcanism originated from mantle plume activity cannot be entirely ruled out. Owing to post-eruption tectonic fragmentation and erosion, the preserved volume of the Parauapebas basalts is less than the

minimum required size for a LIP (100,000 km^3) (e.g., Ernst, 2014). However, precise geochronological data revealed that the thick volcanic lava sequences from Parauapebas were formed over a short period between ~2770 Ma and ~2750 (Machado et al., 1991; Olszewski et al., 1989; Martins et al., 2017; Toledo et al., 2019). A short-lived magmatic event (with duration as short as ~ 1 Ma) was also suggested based on the abundance of zircon from volcaniclastic rocks interbedded in the Carajás jaspilite (Rossignol et al., 2021). In addition, the large thickness of the basalts (2–3 km; Cabral et al., 2013; Fig. 2) is comparable to that of Siberia and Emeishan LIPs (Zhang et al., 2019). If correct, the ~2760 Ma igneous activity in the Carajás Basin meets at least the following three characteristics of a LIP: short duration, large thickness, and typical rift-like geochemical signatures. The emplacement of this LIP was probably immediately preceded by a continental extensional phase that formed a rift basin filled with Carajás iron formations (Rossignol et al., 2021). Because this hypothesis is not well constrained, it opens an opportunity for further research.

5.7. Genetic model

A genetic model is proposed for the Carajás jaspilites, whereby the crustal spreading in the extensional rift-related basin led to upwelling of asthenospheric mantle and, consequently, provided heat leading to partial melting of the lithospheric mantle (Fig. 18). Along the spreading center, abundant hydrothermal fluid dissolved Fe(II) and Si, and the alteration of new oceanic crust acted as O_2 sinks, which probably made the seawater anoxic (Fig. 18A). The hydrothermally generated Fe(II) and Si might have originated from deeper parts of the basin, where subaqueous volcanism was significant (Fig. 18B). According to Bekker et al. (2010), when the hydrothermal flux overwhelms the oceanic oxidation state, reduced Fe from hydrothermal vents gets transported to the upper water column. In the regions where the hydrothermal flux is insufficient to overwhelm the seawater redox state, Fe becomes rapidly

oxidized, and becomes proximally precipitated as Fe(III) oxyhydroxides. Hence, it is likely that the dissolved Fe(II) and Si were not deposited near the spreading center. Rather, Fe(II) and Si were brought in as an "iron shuttle" (Silverman & Lundgren, 1959) to the shallow-water environment at the rift basin margins following cold and heated water convection, where it encountered a chemocline that separated the bottom anoxic water from the surficial mildly oxidized layer (Fig. 18A). Owing to the higher influx of Fe(II) caused by the higher degree of hydrothermal activity in the deeper basin (recorded by higher Eu/Eu^*_{SN} and positive εNd(t) values), a larger quantity of reduced iron reached the chemocline, which was subsequently oxidized and precipitated as ferric iron oxyhydroxides at the contact with the shallow oxidized water layer. Iron-rich particles are subsequently transported and settled to the bottom of the basin, reaching the soft-sediment layer (Fig. 18). Additionally, only a minor amount of Fe(III) was consumed by microbes in sedimentary pile, perhaps through partial DIR, thereby producing magnetite. Anoxygenic photosynthesis was probably the most plausible mechanism responsible for Fe oxidation in the Carajás Basin (Rego et al., 2021). Locally, an oxygen whiff or, alternatively, oxygenated microenvironments were probably present in water masses of the Carajás Basin, which led to the precipitation of jaspilites of the Carajás Formation, thereby indicating that emerging oxidizing conditions had influenced certain areas of the Carajás Basin before the onset of the GOE.

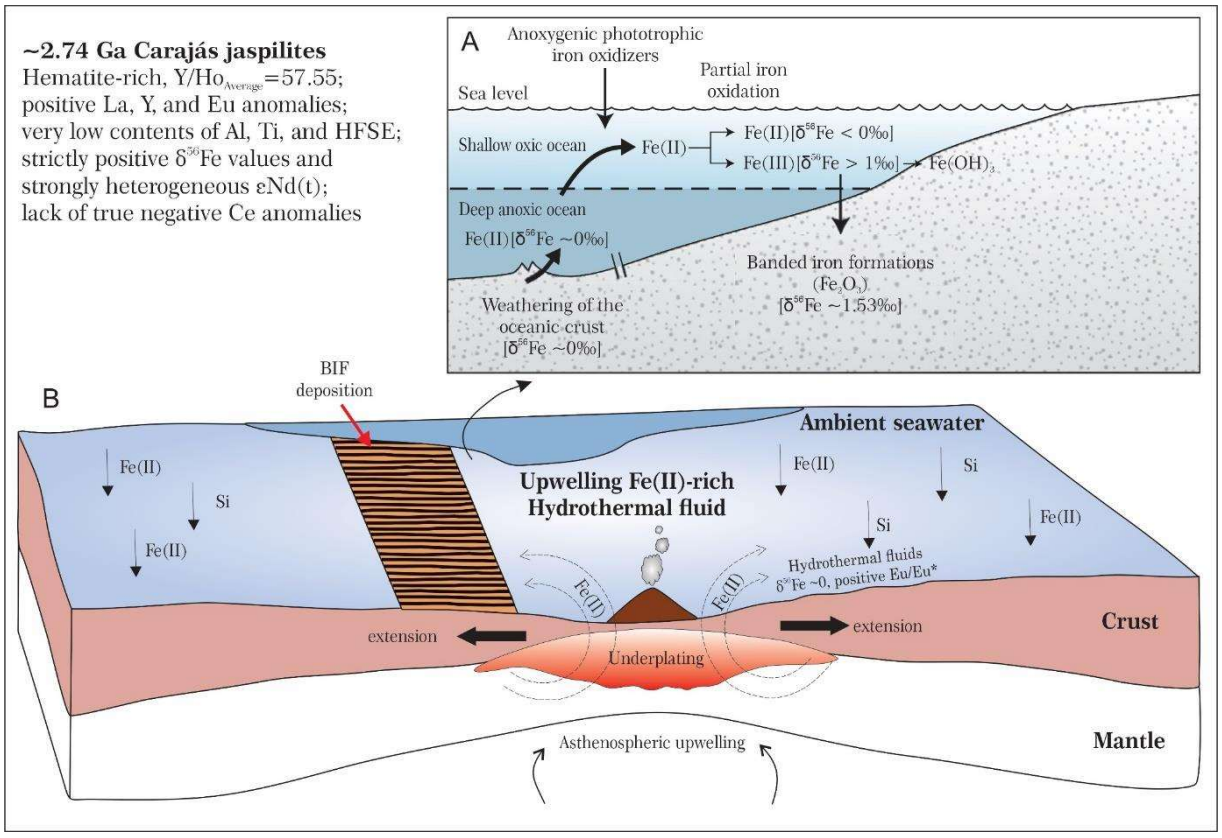

Fig 18. *Model for the deposition of the Carajás jaspilites in the Serra Norte region.* ***A)*** *Schematic view of Fe isotope exchange reactions between the different oceanic reservoirs and BIF deposits (after Fabre et al., 2011);* ***B)*** *Deposition model involving the ocean redox structure based on REY patterns and Fe and Nd isotopic results. See text for discussion.*

6. Conclusion

The following conclusions are drawn based on geological, petrological, and geochemical analyses of the Carajás jaspilite in the ~2.75 Ga volcano-sedimentary sequence of the Grão-Pará Group:

(1) Major and trace elements and REY concentrations indicate that the Carajás jaspilites are neither of Algoma-type nor Superior-type BIFs. Mixing models pointed to that more than 0.1% and less than 1% of high-temperature hydrothermal fluids (> 250 °C) mixed in with ambient seawater, together with flux derived from the mafic crust, were involved in the

formation of the jaspilites. Submarine hydrothermal fluids associated with mafic volcanic activity produced BIF-forming materials, particularly silicon and iron. Overall, low Al_2O_3, TiO_2, and HFSE abundance indicate that the formation of the Carajás jaspilite had minor (if any) contributions from detrital input.

(2) Variations in $\delta^{56}Fe$ values up to 0.80‰ for hematite-rich samples over tens to hundreds of meters of the stratigraphic section hint towards relatively sharp changes in iron isotope composition of seawater over large periods (i.e., on the order of the deposition time of Carajás jaspilite unit; a few million years). Hypothetically, the variation implies a non-steady state of the iron cycle during the late Neoarchean, with variable iron concentrations being caused by the competitive effect of iron oxide precipitation and iron supply from hydrothermal sources. It is likely that redox variations had induced isotopic variations. The strongly positive $\delta^{56}Fe$ values indicate that the deposition of Carajás jaspilite occurred mainly in deep-water at extremely low or no free O_2. However, this Fe isotope reference frame cannot be uniformly expanded to the entire ocean because of the distinct changes in the redox state of the ocean-atmosphere system, which might have occurred during this period, the complexity of Fe cycling in the Archean, and the natural setting in general (Czaja et al., 2018).

(3) The origin of both conspicuous positive Fe isotopic anomalies over time and the unprecedented large positive Eu anomalies of the Carajás jaspilites is not clear, but likely corresponds to an extremely high input of hydrothermal-derived fluids at that time. The enhanced flux of mantle-derived materials during this period was probably associated with extensive rift-related volcanism (~2.75 Ga magmatism). The breakout event (rifting) generated shallower mid-ocean ridges, which, in turn, might have led to transgressive events

that submerged the shallow shelf under water influenced by submarine mantle degassing and hydrothermal alteration of the oceanic crust (Haugaard et al., 2016b).

(4) Sm–Nd isotope data of the Carajás jaspilite plot along a correlation line in a conventional isochron diagram yielding an age of 2707 ± 118 Ma. A subset of these data provided an older isochron age of 2795 ± 77 Ma. Both Sm–Nd isochron apparent ages are concordant with the proposed minimum formation age of the Carajás jaspilites of ~2745 Ma (Trendall et al., 1998; Martins et al., 2017). In addition, the samples had a heterogeneous Nd isotopic signature throughout the drill core, where rocks with negative εNd (t) values (–4.97 to –0.90, n = 6) were found near the basaltic flows/jaspilite contact. Meanwhile, predominantly positive εNd(t) values (–0.84 to +5.40, n = 15) were widespread in the remaining samples.

(5) The redox state reconstructed from Carajás jaspilites argues against widespread elevated oxygen levels in the late Neoarchean seawater. A depositional model for Neoarchean Carajás jaspilite was constructed, whereby dissolved Fe(II) in the upwelling hydrothermal fluids was oxidized to Fe(III) through anoxygenic photosynthesis and subsequently precipitated as oxyhydroxides in the upper water column before being deposited on the seafloor. Locally, considerable oxygen was probably present in the water masses of the Carajás Basin, which led to the precipitation of jaspilites, thereby suggesting that the emerging oxidizing conditions could have influenced the Carajás Basin before the GOE.

(6) Jaspilites in the Carajás Basin were precipitated in a deep-sea environment (i.e., distal to continental landmasses) near volcanic centers with intense hydrothermal activity. The Fe deposits were mainly derived from ferrosilicon materials generated by the venting of hydrothermal fluids under anoxic and suboxic conditions.

Acknowledgements

The authors wish to extend their special thanks to Vale S.A. mining company for permitting the use of geological data and access to the N4 deposit, as well as providing research funding. This study was financed in part by the Coordenação de Aperfeiçoamento de Pessoal de Nível Superior - Brasil (CAPES) - Finance Code 001. We also would like to thank the Fundação de Apoio à Pesquisa do Distrito Federal (FAP-DF) (23411.93.27701.29052018) for supporting this research. Catarina L.B. Toledo, Adalene M. Silva and Farid Chemale Jr. thank Conselho Nacional de Desenvolvimento Científico e Tecnológico (CNPq) for providing research grants. Pedro L. G. Martins held a scholarship from CNPq and this study is part of his PhD thesis developed at the Instituto de Geociências (Universidade de Brasília).

References

Albut, G., Babechuk, M.G., Kleinhanns, I.C., Benger, M., Beukes, N.J., Steinhilber, B., Smith, A.J.B., Kruger, S.J., Schoenberg, R., 2018. Modern rather than Mesoarchaean oxidative weathering responsible for the heavy stable Cr isotopic signatures of the 2.95 Ga old Ijzermijn iron formation (South Africa). Geochim. Cosmochim. Acta 228, 157–189. https://doi.org/10.1016/j.gca.2018.02.034.

Albut, G., Kamber, B.S., Brüske, A., Beukes, N.J., Smith, A.J.B., Schoenberg, R., 2019. Modern weathering in outcrop samples versus ancient paleoredox information in drill core samples from a Mesoarchaean marine oxygen oasis in Pongola Supergroup, South Africa. Geochim. Cosmochim. Acta 265, 330–353. https://doi.org/10.1016/j.gca.2019.09.001.

Alexander, B.W., Bau, M., Andersson, P., Dulski, P., 2008. Continentally-derived solutes in shallow Archean seawater: rare earth element and Nd isotope evidence in iron formation

from the 2.9 Ga Pongola Supergroup, South Africa. Geochim. Cosmochim. Acta 72, 378–394. https://doi.org/10.1016/j.gca.2007.10.028.

Alexander, B.W., Bau, M., Andersson, P., 2009. Neodymium isotopes in Archean seawater and implications for the marine Nd cycle in Earth's early oceans. Earth Planet. Sci. Lett. 283, 144–155. https://doi.org/10.1016/j.epsl.2009.04.004.

Alibert, C., McCulloch, M.T., 1993. Rare element and neodymium isotopic compositions of the banded iron-formations and associated shales from Hamersley, Western Australia. Geochim. Cosmochim. Acta 57, 187–204. https://doi.org/10.1016/0016-7037(93)90478-F.

Alibo, D.S., Nozaki, Y., 1999. Rare earth elements in seawater: particle association, shale-normalization, and Ce oxidation. Geochim. Cosmochim. Acta 63, 363–372. https://doi.org/10.1016/S0016-7037(98)00279-8.

Anbar, A.D., Duan, Y., Lyons, T.W., Arnold, G.L., Kendall, B., Creaser, R.A., Kaufman, A.J., Gordon, G.W., Scott, C., Garvin, J., Buick, R., 2007. A whiff of oxygen before the Great Oxidation Event? Science 317, 1903–1906. https://doi.org/10.1126/science.1140325.

Andersson, P.S., Wasserburg, G.J., Ingri, J., 1992. The sources and transport of Sr and Nd isotopes in the Baltic Sea. Earth Planet. Sci. Lett. 113, 459–472. https://doi.org/10.1016/0012-821X(92)90124-E.

Araújo, O.J.B., Maia, R.G.N., 1991. Programa de levantamentos geológicos básicos do Brasil. Programa grande Carajás. Serra dos Carajás folha SB. 22-Z-A. Estado do Pará. Texto. DNPM/CPRM, Brasília, 164p (in Portuguese).

Araújo, R., Nogueira, A., 2019. Serra sul diamictite of the Carajás Basin (Brazil): a paleoproterozoic glaciation on the amazonian craton. Geology 47, 1166–1170. https://doi.org/10.1130/G46923.1.

Araújo Filho, R., Nogueira, A.C.R., Araújo, R.N., 2020. New stratigraphic proposal of a Paleoproterozoic siliciclastic succession: implications for the evolution of the Carajás Basin, Amazonian craton, Brazil. J. S. Am. Earth Sci. 102, 102665. https://doi.org/10.1016/j.jsames.2020.102665.

Archer, C., Vance, D., 2004, Mass discrimination correction in multiple-collector plasma source mass spectrometry: An example using Cu and Zn isotopes: Journal of Analytical Atomic Spectrometry, 19, 656–665. https://doi.org/10.1039/b315853e.

Bhattacharya, H., Chakraborty, I., Ghosh, K., 2007. Geochemistry of some banded ironformations of the Archean supracrustals, Jharkhand-Orissa region, India. J. Earth Syst. Sci. 116, 245–259. https://doi.org/10.1007/s12040-007-0024-4.

Barrett, T.J., Wares, R.P., Fox, J.S., 1988. Two-stage hydrothermal formation of a Lower Proterozoic sediment-hosted massive sulfide deposit, northern Labrador Trough, Quebec. Can. Mineral. 26, 871–888.

Bau, M., 1993. Effects of syn-depositional and post-depositional processes on the rare-earth element distribution in Precambrian iron-formations. Eur. J. Mineral. 5, 257–267. https://doi.org/10.1127/ejm/5/2/0257.

Bau, M., Alexander, B.W., 2009. Distribution of high field strength elements (Y, Zr, REE, Hf, Ta, Th, U) in adjacent magnetite and chert bands and in reference standards FeR-3 and FeR-4 from the Temagami iron-formation, Canada, and the redox level of the Neoarchean ocean. Precambrian Res. 174, 337–346. https://doi.org/10.1016/j.precamres.2009.08.007.

Bau, M., Dulski, P., 1996. Distribution of yttrium and rare-earth elements in the Penge and Kuruman iron formations, Transvaal Supergroup, South Africa. Precambrian Res. 79, 37–55. https://doi.org/10.1016/0301-9268(95)00087-9.

Bau, M., Dulski, P., 1999. Comparing yttrium and rare earths in hydrothermal fluids from the Mid-Atlantic Ridge: implications for Y and REE behavior during near-vent mixing and for the Y/Ho ratio of Proterozoic seawater. Chem. Geol. 155, 77–90. https://doi.org/10.1016/S0009-2541(98)00142-9.

Bau, M., Koschinsky, A., 2009. Oxidative scavenging of cerium on hydrous Fe oxide: evidence from the distribution of rare earth elements and yttrium between Fe oxides and Mn oxides in hydrogenetic ferromanganese crusts. Geochem. J. 43, 37–47.

Bau, M., Hohndorf, A., Dulski, P., Beukes, N.J., 1997. Sources of rare-earth elements and iron in Paleoproterozoic iron-formations from the Transvaal Supergroup, South Africa: evidence from neodymium isotopes. J. Geol. 105, 121–129. https://doi.org/10.1086/606152.

Beard, B.L., Johnson, C.M., Skulan, J.L., Nealson, K.H., Cox, L., Sun, H., 2003. Application of Fe isotopes to tracing the geochemical and biological cycling of Fe. Chem. Geol. 195, 87-117. https://doi.org/10.1016/S0009-2541(02)00390-X.

Beisiegel, V.R., Bernardelli, A.L., Drummond, N.F., Ruff, A.W., Tremaine, J.W., 1973. Geologia e Recursos Minerais da Serra dos Carajás. Revista Brasileira de Geociências 3, 215-242 (in Portuguese).

Bekker, A., Holland, H.D., Wang, P.L., Rumble III, D., Stein, H.J., Hannah, J.L., Coetzee, L.L., Beukes, N.J., 2004. Dating the rise of atmospheric oxygen. Nature 427, 117–120. https://doi.org/10.1038/nature02260.

Bekker, A., Slack, J.F., Planavsky, N., Krapež, B., Hofmann, A., Konhauser, K.O., Rouxel, O.J., 2010. Iron formation: the sedimentary product of a complex interplay among mantle, tectonic, oceanic, and biospheric processes. Econ. Geol. 105, 467–508. https://doi.org/10.2113/gsecongeo.105.3.467.

Bekker, A., Krapež, B., Slack, J., Planavsky, N., Hofmann, A., Konhauser, K.O., Rouxel, O.J., 2012. Iron formation: the sedimentary product of a complex interplay among mantle, tectonic, oceanic, and biospheric processes – a reply. Econ. Geol. 107, 379–380. https://doi.org/10.2113/econgeo.107.2.379.

Bekker, A., Planavsky, N., Krapež, B., Rasmussen, B., Hofmann, A., Slack, J.F., Rouxel, O.J., Konhauser, K.O., 2014. Iron formations: their origins and implications for ancient seawater chemistry. In: Holland, H.D., Turekian, K.K. (Eds.), Treatise of Geochemistry, second ed. v. 9. Elsevier, pp. 561–628.

Bermin, J., Vance, D., Archer, C., Statham, P.J., 2006. The determination of the isotopic composition of Cu and Zn in seawater. Chem. Geol. 226, 280–297. https://doi.org/10.1016/j.chemgeo.2005.09.025.

Bolhar, R., Van Kranendonk, M.J., 2007. A non-marine depositional setting for the northern Fortescue Group, Pilbara Craton, inferred from trace element geochemistry of stromatolitic carbonates. Precambrian Res. 155, 229–250. https://doi.org/10.1016/j.precamres.2007.02.002.

Bolhar, R., Kamber, B.S., Moorbath, S., Fedo, C.M., Whitehouse, M.J., 2004. Characterization of early Archaean chemical sediments by trace element signatures. Earth Planet. Sci. Lett. 222, 43–60. https://doi.org/10.1016/j.epsl.2004.02.016.

Bolhar, R., Van Kranendonk, M.J., Kamber, B.S., 2005. Trace element study of siderite jasper banded iron formation in the 3.45 Ga Warrawoona Group, Pilbara Craton formation from hydrothermal fluids and shallow seawater. Precambrian Res. 137, 93–114. https://doi.org/10.1016/j.precamres.2005.02.001.

Bolhar, R., Hofmann, A., Siahi, M., Feng, Y.X., Delvigne, C., 2015. A trace element and Pb isotopic investigation into the provenance and deposition of stromatolitic carbonates, ironstones and associated shales of the ~3.0 Ga Pongola Supergroup, Kaapvaal Craton. Geochim. Cosmochim. Acta 158, 57–78. https://doi.org/10.1016/j.gca.2015.02.026.

Bonnand, P., Lalonde, S.V., Boyet, M., Heubeck, C., Homann, M., Nonnotte, P., Foster, I., Konhauser, K.O., Köhler, I., 2020. Post-depositional REE mobility in a Paleoarchean banded iron formation revealed by La-Ce geochronology: A cautionary tale for signals of ancient oxygenation. Earth Planet. Sci. Lett. 547, 116452. https://doi.org/10.1016/j.epsl.2020.116452.

Byrne, R., Sholkovitz, E., 1996. Marine Chemistry and Geochemistry of the Lanthanides. In: Gschneider, K.A., Eyring, L. (Eds.), Handbook on the Physics and Chemistry of the Rare Earths. Elsevier, Amsterdam, pp. 497–593.

Cabral, A.R., Creaser, R.A., Nagler, T., Lehmann, B. Voegelin, A.R., Beltasky, B., Pasava, J., Gomes, A.A.S., Galbiatti, H., Bottcher, M.E., Escher, P., 2013. Trace-element and multi-isotope geochemistry of Late-Archean black shales in the Carajás iron-ore district, Brazil. Chem. Geol. 362, 91 – 104. https://doi.org/10.1016/j.chemgeo.2013.08.041.

Cameron V., Vance D., Archer C., House C.H., 2009. A biomarker based on the stable isotopes of nickel. Proc. Natl. Acad. Sci. 106, 10944–10948. https://doi.org/10.1073/pnas.0900726106.

Canfield, D.E., 2005. The early history of atmospheric oxygen: homage to Robert M. Garrels. Ann. Rev. Earth Planet Sci. 33, 1–36. https://doi.org/10.1146/annurev.earth.33.092203.122711.

Cloud, P., 1973. Paleoecological significance of banded iron-formation. Econ. Geol. 68, 1135–1143.

Czaja, A. D., Johnson, C. M., Beard, B. L., Roden, E. E., Li, W., & Moorbath, S., 2013. Biological Fe oxidation controlled deposition of banded iron formation in the ca. 3770 Ma Isua Supracrustal Belt (West Greenland). Earth Planet. Sci. Lett. 363, 192–203. https://doi.org/10.1016/j.epsl.2012.12.025.

Czaja, A. D., Van, K. M. J., Beard, B. L., Johnson, C. M., 2018. A multistage origin for Neoarchean layered hematite-magnetite iron formation from the Weld Range, Yilgarn Craton, Western Australia. Chem. Geol. 488, 125–137. https://doi.org/10.1016/j.chemgeo.2018.04.019.

Cohen, K.M., Finney, S.C., Gibbard, P.L., Fan, J.-X., 2013. The ICS international chronostratigraphic chart (updated). Episodes 36, 199–204.

Cordani, U.G., Tassinari, C.C.G., Kawashita, K.A., 1984. A Serra dos Carajás como região limítrofe entre províncias tectônicas. Cien. Terra 9, 6–11.

Danielson, A., Möller, P., Dulski, P., 1992. The europium anomalies in banded iron formations and the thermal history of the oceanic crust. Chem. Geol. 97, 89–100. https://doi.org/10.1016/0009-2541(92)90137-T.

Dauphas, N., John, S.G., Rouxel, O., 2017. Iron isotope systematics. In Non-traditional Stable Isotopes (eds. F.-.-Z. Teng, J. M. Watkins and N. Dauphas). Mineralogical Society of America, Chantilly, VA, pp. 415–510. https://doi.org/10.1515/9783110545630-012.

DePaolo, D.J., 1981. Neodymium isotopes in the Colorado Front Range and implications for crust formation and mantle evolution in the Proterozoic. Nature 291, 193–197. https://doi.org/10.1038/291193a0.

Derry, L.A., Jacobsen, S.B., 1988. The Nd and Sr isotopic evolution of Proterozoic seawater. Geophys. Res. Lett. 15, 397–400. https://doi.org/10.1029/GL015i004p00397.

Derry, L.A., Jacobsen, S.B., 1990. The chemical evolution of Precambrian seawater: evidence from REEs in banded iron formations. Geochim. Cosmochim. Acta 54, 2965–2977. https://doi.org/10.1021/cen-v026n044.p3274.

Dhuime, B., Wuestefeld, A., Hawkesworth, C., 2015. Emergence of modern continental crust about 3 billion years ago. Nature Geosci. 8, 552–555. https://doi.org/10.1038/ngeo2466.

DOCEGEO – Rio Doce Geologia e Mineração, 1988. Revisão Litoestratigráfica da Província Mineral de Carajás. 35 Congresso Brasileiro de Geologia, Belém, Brasil, Anais, Sociedade Brasileira de Geologia, pp. 11–59 (in Portuguese).

Døssing, L.N., Frei, R., Stendal, H., Mapeo, R.B.M., 2009. Characterization of enriched lithospheric mantle components in ~2.7 Ga Banded Iron Formations: an example from the Tati Greenstone Belt, Northeastern Botswana. Precambrian Res. 172, 334–356. https://doi.org/10.1016/j.precamres.2009.06.004.

Dreher, A.M., Xavier, R.P., Taylor, B.E., Martini, S.L., 2008. New geologic, fluid inclusion and stable isotope studies on the controversial Igarapé Bahia Cu-Au deposit, Carajás Province, Brazil. Miner. Deposita 43, 161–184. https://doi.org/10.1007/s00126-007-0150-6.

Dymek, R., Klein, C., 1988. Chemistry, petrology and origin of banded iron-formation lithologies from the 3800 Ma Isua Supracrustal Belt, West Greenland. Precambrian Res. 39, 247–302. https://doi.org/10.1016/0301-9268(88)90022-8.

Elderfield, H., Upstill-Goddard, R., Sholkovitz, E.R., 1990. The rare earth elements in rivers, estuaries, and coastal seas and their significance to the composition of ocean waters. Geochim. Cosmochim. Acta 54, 971–991. https://doi.org/10.1016/0016-7037(90)90432-K.

Eickmann, B., Hofmann, A., Wille, M., Bui, T.H., Wing, B.A., Schoenberg, R., 2018. Isotopic evidence for oxygenated Mesoarchean shallow oceans. Nat. Geosci. 11, 133–138. http://dx.doi.org/10.1038/s41561-017-0036-x.

Ernst, R.E., 2014. Large Igneous Provinces, 1–653. Cambridge University Press, Cambridge.

Ernst, R.E., Buchan, K.L., Prokoph, A., 2004. Large igneous province record through time. In: Eriksson, P.G., Altermann, W., Nelson, D.R., Mueller, W.U., Catuneanu, O. (Eds.), The Precam- brian Earth: Tempos and Events. Developments in Precambrian Geology, vol. 12. Elsevier, Amsterdam, pp. 173–180.

Ewers, W., Morris, R., 1981, Studies of the Dales Gorge Member of the Brockman iron formation, Western Australia. Econ. Geol. 76, 1929–1953. https://doi.org/10.2113/gsecongeo.76.7.1929.

Fabre, S., A., Nédélec, F., Poitrasson, H., Strauss, C., Thomazo, and A., Nogueira, 2011. Iron and sulphur isotopes from the Carajás Mining Province (Pará, Brazil): Implications for the

oxidation of the ocean and the atmosphere across the Archaean–Proterozoic transition. Chem. Geol. 289, 124–39. https://doi.org/10.1016/j.chemgeo.2011.07.019.

Figueiredo e Silva, R.C., Lobato, L.M., Rosière, C.A., Zucchetti, M., Hagemann, S., Morais, R., Andrade, I., 2008. A hydrothermal origin for the jaspilite-hosted, giant Serra Norte iron ore deposits in the Carajás Mineral Province, Pará State, Brazil. Econ. Geol. 15, 255–290. https://doi.org/10.5382/Rev.15.10.

Figueiredo e Silva, R.C., Lobato, L.M., Zucchetti, M., Hagemann, S., Vennemann, T., 2020. Geotectonic signature and hydrothermal alteration of metabasalts under-and overlying the giant Serra Norte iron deposits, Carajás mineral Province. Ore Geol. Rev. 120, 103407. https://doi.org/10.1016/j.oregeorev.2020.103407.

Frei, R., Polat, A., 2007. Source heterogeneity for the major components of ~3.7 Ga banded iron formations (Isua Greenstone Belt, western Greenland): tracing the nature of interacting water masses in BIF formation. Earth Planet. Sci. Lett. 253, 266–281. https://doi.org/10.1016/j.epsl.2006.10.033.

Frei, R., Dahl, P.S., Duke, E.F., Frei, K.M., Hansen, T.R., Frandsson, M.M., Jensen, L.A., 2008. Trace element and isotopic characterization of Neoarchean and Paleoproterozoic iron formations in the Black Hills (South Dakota, USA): assessment of chemical change during 2.9-1.9 Ga deposition bracketing the 2.4-2.2 Ga first rise of atmospheric oxygen. Precambrian Res. 162, 441–474. https://doi.org/10.1016/j.precamres.2007.10.005.

Frei R., Gaucher C., Poulton S.W., Canfield D.E., 2009. Fluctuations in Precambrian atmospheric oxygenation recorded by chromium isotopes. Nature, 461, 250-254. https://doi.org/10.1038/nature08266.

Frost, C.D., von Blanckenburg, F., Schoenberg, R., Frost, B.R., Swapp, S.M., 2007. Preservation of Fe isotope heterogeneities during diagenesis and metamorphism on banded iron formation. Contrib. Mineral. Petrol. 153, 211–235. https://doi.org/10.1007/s00410-006-0141-0.

Galarza, M.A., Macambira, M.J.B., Villas, R.N.N., 2008. Dating and isotopic characteristics (Pb and S) of the Fe oxide-Cu-Au-U-REE Igarapé Bahia ore deposit, Carajás mineral province, Pará state, Brazil. J. S. Am. Earth Sci. 25, 377–397. https://doi.org/10.1016/j.jsames.2007.07.006.

German, C.R., Holliday, B.P., Elderfield, H., 1991. Redox cycling of rare earth elements in the suboxic zone of the Black Sea. Geochim. Cosmochim. Acta 55, 3553–3558. https://doi.org/10.1016/0016-7037(91)90055-A.

Gioia, S.M.C.L., Pimentel, M.M., 2000. The Sm-Nd isotopic method in the geochronology laboratory of University of Brasilia. An. Acad. Bras. Ciênc. 72, 219–245.

Gibbs, A.K., Wirth, K.R., Hirata, W.K., Olszewski Jr., W.J., 1986. Age and composition of the Grão Pará Group volcanics, Serra dos Carajás. Revista Brasileira de Geociências 16, 201–211.

Grasse, P., Stichel, T., Stumpf, R., Stramma, L., Frank, M., 2012. The distribution of neodymium isotopes and concentrations in the Eastern Equatorial Pacific: Water mass advection versus particle exchange. Earth Planet. Sci. Lett. 353–354, 198–207. https://doi.org/10.1016/j.epsl.2012.07.044.

Grauch, R.I., 1989. Rare earth elements in metamorphic rocks. Rev. Mineral. Geochem. 21, 147–167. https://doi.org/10.1515/9781501509032-009.

Gross, G.A., 1980. A classification of iron-formation based on depositional environments. Can. Mineral. 18, 215–222.

Gross, G.A., 1983. Tectonic systems and the deposition of iron-formation. Precambrian Res. 7, 63–79. https://doi.org/10.1016/S0166-2635(08)70242-1.

Gross, G.A., Mcleod, C.R., 1980. A preliminary assessment of the chemical composition of iron formations in Canada. Can. Mineral. 18, 223–229.

Gumsley, A.P., Chamberlain, K.R., Bleeker, W., Söderlund, U., de Kock, M.O., Larsson, E.R., Bekker, A., 2017. Timing and tempo of the Great Oxidation Event. Proc. Natl. Acad. Sci. U. S. A. 114, 1811–1816. https://doi.org/10.1073/pnas.1608824114.

Halder, S., 2017. Genesis of BIF-hosted iron ore deposits in the Carajás mineral province, Brazil: constraints from in-situ Fe isotope analysis and whole-rock geochemistry. Doctoral Thesis. Faculty of Energy and Management Science, Clausthal University of Technology, Lindenberg, Germany, 131p.

Halverson, P., Poitrasson, F., Hoffman, P.F., Nédélec, A., Montel, J.M., Kirby, J., 2011. Fe isotope and trace element geochemistry of the Neoproterozoic syn-glacial Rapitan Iron Formation. Earth Planet. Sci. Lett. 309, 100–112. https://doi.org/10.1016/j.epsl.2011.06.021.

Haugaard, R., Frei, R., Stendal, H., Konhauser, K., 2013. Petrology and geochemistry of the ~2.9 Ga Itilliarsuk banded iron formation and associated supracrustal rocks, West Greenland: source characteristics and depositional environment. Precambrian Res. 229, 150–176. https://doi.org/10.1016/j.precamres.2012.04.013.

Haugaard, R., Ootes, L., Creaser, R.A., Konhauser, K.O., 2016a. The nature of Mesoarchaean seawater and continental weathering in 2.85 Ga banded iron formation, Slave Craton, NW Canada. Geochim. Cosmochim. Acta 194, 34–56. https://doi.org/10.1016/j.gca.2016.08.020.

Haugaard, R., Pecoits, E., Lalonde, S., Rouxel, O., Konhauser, K.O., 2016b. The Joffre Banded Iron Formation, Hamersley Group, Western Australia: assessing the paleoenvironment through detailed petrology and chemostratigraphy. Precambrian Res. 273, 12–37. https://doi.org/10.1016/j.precamres.2015.10.024.

Haugaard, R., Ootes, L., Creaser, R.A., Konhauser, K.O., 2017. Neoarchean banded iron formation within a 2620 Ma turbidite-dominated deep-water basin, Slave craton, NW Canada. Precambrian Res. 292, 130–151. https://doi.org/10.1016/j.precamres.2017.01.025.

Heard, A.W., Dauphas, N., 2020. Constraints on the coevolution of oxic and sulfidic ocean iron sinks from Archean-Paleoproterozoic iron isotope records. Geology 48, 358–362. https://doi.org/10.1130/G46951.1.

Heimann, A., Johnson, C.M., Beard, B.L., Valley, J.W., Roden, E.E., Spicuzza, M.J., Beukes, N.J., 2010. Fe, C, and O isotope compositions of banded iron formation carbonates demonstrate a major role for dissimilatory iron reduction in ~2.5 Ga marine environments. Earth Planet. Sci. Lett. 294, 8-18. https://doi.org/10.1016/j.epsl.2010.02.015.

Henderson, P., 1984. General Geochemical Properties and Abundances of the Rare Earth Elements. Elsevier, Amsterdam, v.2, pp. 1–32. ISSN 0921-3198. https://doi.org/10.1016/B978-0-444-42148-7.50006-X.

Hofmann, A., 2005. The geochemistry of sedimentary rocks from the Fig Tree Group, Barberton Greenstone Belt: Implications for tectonic, hydrothermal and surface processes

during mid-Archaean times. Precambrian Res. 143, 23–49. https://doi.org/10.1016/j.precamres.2005.09.005.

Holland, H.D., 1973. Oceans - possible source of iron in iron-formations. Econ. Geol. 68, 1169–1172.

Holland, H.D., 2005. Sedimentary mineral deposits and the evolution of Earth's near-surface environments. Econ. Geol. 100, 1489–1509. https://doi.org/10.2113/gsecongeo.100.8.1489.

Holland, H.D., 2006. The oxygenation of the atmosphere and oceans. Philos. Trans. R. Soc. B. 361, 903–915. https://doi.org/10.1098/rstb.2006.1838.

Hou, K., Li, Y., Gao, J., Liu, F., Qin, Y., 2014. Geochemistry and Si–O–Fe isotope constraints on the origin of banded iron formations of the Yuanjiacun Formation, Lvliang Group, Shanxi, China. Ore Geol. Rev. 57, 288-298. https://doi.org/10.1016/j.oregeorev.2013.09.018.

Huang, B., Kusky, T.M., Wang, L., Deng, H., Wang, J., Fu, D., Peng, H., Ning, W., 2019. Age and genesis of the Neoarchean Algoma-type banded iron formations from the Dengfeng greenstone belt, southern North China Craton: Geochronological, geochemical and Sm–Nd isotopic constraints. Precambrian Res. 333, 105437. https://doi.org/10.1016/j.precamres.2019.105437.

Huston, D.L., Logan, G.A., 2004. Barite, BIFs and bugs: Evidence for the evolution of the Earth's early hydrosphere. Earth Planet. Sci. Lett. 220, 41–55. https://doi.org/10.1016/S0012-821X(04)00034-2.

Hyslop, E.V., Valley, J.W., Johnson, C.M., Beard, B.L., 2008. The effects of metamorphism on O and Fe isotope compositions in the Biwabik Iron Formation, northern Minnesota. Contrib. Mineral. Petrol. 155, 313–328. https://doi.org/10.1007/s00410-007-0244-2.

Isley, A.E., 1995. Hydrothermal plumes and the delivery of iron to banded iron formation. J. Geol. 103, 169–185.

Isley, A.E., Abbott, D.H., 1999. Plume-related mafic volcanism and the deposition of banded iron formation. J. Geophys. Res. 104, 15461–15477. https://doi.org/10.1029/1999JB900066.

Jacobsen, S.B., Pimentel-Klose, M.R., 1988. A Nd isotopic study of the Hamersley and Michipicoten banded iron formations: the source of REE and Fe in Archean oceans. Earth Planet. Sci. Lett. 87, 29–44. https://doi.org/10.1016/0012-821X(88)90062-3.

James, H.L., 1954. Sedimentary facies of iron-formation. Econ. Geol. 49, 235–293. https://doi.org/10.2113/gsecongeo.49.3.235.

Johnson, C.M., Beard, B.L., Beukes, N.J., Klein, O'Leary, J.M., 2003. Ancient geochemical cycling in the earth as inferred from Fe isotope studies of banded iron formation from the Transvaal craton. Contrib. Mineral. Petrol. 144, 523–547. https://doi.org/10.1007/s00410-002-0418-x.

Johnson, C.M., Roden, E.E., Welch, S.A., Beard, B.L., 2005. Experimental constraints on Fe isotope fractionation during magnetite and Fe carbonate formation coupled to dissimilatory hydrous ferric oxide reduction. Geochim. Cosmochim. Acta 69, 963–993. https://doi.org/10.1016/j.gca.2004.06.043.

Johnson, C.M., Beard, B.L., Klein, C., Beukes, N.J., Roden, E.E., 2008. Iron isotopes constrain biologic and abiologic processes in banded iron formation genesis. Geochim. Cosmochim. Acta 72, 151–169. https://doi.org/10.1016/j.gca.2007.10.013.

Justo, A.P., 2018. As formações ferríferas bandadas (BIFs) e a evolução paleoambiental e geodinâmica da Bacia de Carajás: Unpublished Ph.D. thesis, Brasília, Brazil, Universidade de Brasília, 149 p.

Justo, A. P., Dantas, E.L., Bau, M., Freitas-Silva, F.H., Santos, R.V., Schorscher, J.H.D., 2020. Paleobasinal to band-scale REE+Y distribution in Iron Formations from Carajás, Amazon Craton, Brazil, Ore Geol. Rev. 127, 103750. https://doi.org/10.1016/j.oregeorev.2020.103750.

Kamber, B.S., Webb, G.E., 2001. The geochemistry of late Archaean microbial carbonate: implications for ocean chemistry and continental erosion history. Geochim. Cosmochim. Acta 65, 2509–2525. https://doi.org/10.1016/S0016-7037(01)00613-5.

Kato, Y., Yamaguchi, K.E., Ohmoto, H., 2006. Rare earth elements in Precambrian banded iron formations: secular changes of Ce and Eu anomalies and evolution of atmospheric oxygen. In: Ohmoto, H., Kessler, S.K. (Eds.), Chemical and Biological Evolution of Early Earth: Constraints from Banded Iron-formations. Geological Society of America Memoirs, v. 198, 269–289. https://doi.org/10.1130/2006.1198(16).

Klein, C., Beukes, N.J., 1989. Geochemistry and sedimentology of a facies transition from limestone to iron-formation deposition in the early Proterozoic Transvaal Supergroup, South Africa. Econ. Geol. 84, 1733–1774. https://doi.org/10.2113/gsecongeo.84.7.1733.

Klinkhammer, G., Elderfield, H., Hudson, A., 1983. Rare-earth elements in seawater near hydrothermal vents. Nature 305, 185–188. https://doi.org/10.1038/305185a0.

Konhauser, K., Lalonde, S., Planavsky, N., Pecoits, E., Lyons, T., Mojzsis, S., Rouxel, O., Fralick, P., Barley, M., Kump, L., Bekker, A., 2011. Aerobic bacterial pyrite oxidation and acid rock drainage during the Great Oxidation Event. Nature 478, 369–373. https://doi.org/10.1038/nature10511.

Konhauser, K.O., Planavsky, N.J., Hardisty, D.S., Robbins, L.J., Warchola, T.J., Haugaard, R., Lalonde, S.V., Partin, C.A., Oonk, P.B.H., Tsikos, H., Lyons, T.W., Bekker, A., Johnson, C.M., 2017. Iron formations: a global record of Neoarchaean to Palaeoproterozoic environmental history. Earth Sci. Rev. 172, 140–177. https://doi.org/10.1016/j.earscirev.2017.06.012.

Krymsky, R.S., Macambira, J.B., Macambira, M.J.B, 2002. Geocronologia U-Pb em zircão de rochas vulcânicas da Formação Carajás, Estado do Pará. In: Simpósio Sobre Vulcanismo e Ambientes Associados, 2, Belém, Anais. Belém, 41p. (in Portuguese).

Lee, CT., Yeung, L.Y., McKenzie, N.R., Yokoyama, Y., Ozaki, K., Lenardic, A., 2016. Two-step rise of atmospheric oxygen linked to the growth of continents. Nature Geosci. 9, 417–424. https://doi.org/10.1038/ngeo2707.

Li, C., Planavsky, N.J., Love, G.D., Reinhard, C.T., Hardisty, D., Feng, L., Bates, S.M., Huang, J., Zhang, Q., Chu, X., Lyons, T.W., 2015. Marine redox conditions in the middle Proterozoic ocean and isotopic constraints on authigenic carbonate formation: insights from the Chuanlinggou Formation, Yanshan Basin, North China. Geochim. Cosmochim. Acta 150, 90–105. https://doi.org/10.1016/j.gca.2014.12.005.

Li, W., Czaja, A.D., Van Kranendonk, M.J., Beard, B.L., Roden, E.E., Johnson, C.M., 2013. An anoxic, Fe(II)-rich, U-poor ocean 3.46 billion years ago. Geochim. Cosmochim. Acta 120, 65–79. https://doi.org/10.1016/j.gca.2013.06.033.

Li, W., Beard, B.L., Johnson, C.M., 2015. Biologically-recycled continental iron: a major component in banded iron formations. Proc. Natl. Acad. Sci. 112, 8193–8198. https://doi.org/10.1073/pnas.1505515112.

Lindenmayer, Z.G., Laux, J.H., Teixeira, J.B.G. 2001. Considerações sobre a origem das Formações Ferríferas da Formação Carajás, Serra dos Carajás. Revista Brasileira de Geociências, 31, 21-28 (in Portuguese).

Lobato L.M., Figueiredo e Silva R.C., Rosière C.A., Zucchetti M., Baars F.J., Seoane J. C.S., Rios F.J., Monteiro A.M., 2005. Hydrothermal origin for the iron mineralization, Carajás Province, Pará State, Brazil. In: Proceedings Iron Ore 2005, The Australasian Institute of Mining and Metallurgy, Publication Series No. 8, 99-110.

Macambira, J.B., 2003. O ambiente deposicional da Formação Carajás e uma proposta de modelo evolutivo para a Bacia Grão Pará. Unpublish, Ph.D. Thesis, Instituto de Geociências, Universidade Estadual de Campinas, 217p. (in Portuguese).

Macambira, M.J.B., Vasquez, M.L., Silva, D.C.C., Galarza, M.A., Barros, C.E.M., Camelo, J.F., 2009. Crustal growth of the central-eastern Paleoproterozoic domain, SW Amazonian craton: juvenile accretion vs. reworking. J. S. Am. Earth Sci. 27, 235–246. https://doi.org/10.1016/j.jsames.2009.02.001.

Machado, N., Lindenmayer, Z.G., Krogh, T.E., Lindenmayer, D., 1991. U–Pb geochronology of Archean magmatism and basement reactivation in the Carajás area, Amazon shield, Brazil. Precambrian Res. 49, 329–354. https://doi.org/10.1016/0301-9268(91)90040-H.

Markl, G., von Blanckenburg, F., Wagner, T., 2006. Iron isotope fractionation during hydrothermal ore deposition and alteration. Geochim Cosmochim Acta 70, 3011–3030. https://doi.org/10.1016/j.gca.2006.02.028.

Martins, P.L.G., Toledo, C.L.B., Silva, A.M., Chemale Jr, F., Santos, J.O.S., Assis, L.M., 2017. Neoarchean magmatism in the southeastern Amazonian Craton, Brazil: petrography, geochemistry and tectonic significance of basalts from the Carajás Basin. Precambrian Res. 302, 340–357. https://doi.org/10.1016/j.precamres.2017.10.013.

Mendes, M., Lobato, L.M., Kunzmann, M. Halverson, G.P., Rosière, C.A., 2017. Iron isotope and REE+Y composition of the Cauê banded iron formation and related iron ores of the Quadrilátero Ferrífero, Brazil. Mineral. Deposita 52, 159–180. https://doi.org/10.1007/s00126-016-0649-9.

Meirelles, M.R., Dardenne, M.A., 1991. Vulcanismo basáltico de afinidade shoshonítica e ambiente de arco arqueano, Grupo Grão-Pará, Serra dos Carajás, Pará. Revista Brasileira de Geociências 21, 41–50 (in Portuguese).

Michard, A., Albarède, F., 1986. The REE content of some hydrothermal fluids. Chem. Geol. 55, 51–60. https://doi.org/10.1016/0009-2541(86)90127-0.

Miller, R.G., O'Nions, R.K., 1985. Sources of Precambrian chemical and clastic sediments. Nature 314, 325–330. https://doi.org/10.1038/314325a0.

Moreto, C.P.N., Monteiro, L.V.S., Xavier, R.P., Creaser, R.A., DuFrane, S.A., Melo, G.H.C., Delinardo da Silva, M.A., Tassinari, C.C.G., Sato, K., 2015. Timing of multiple hydrothermal events in the iron oxide–copper–gold deposits of the Southern Copper Belt, Carajás Province, Brazil. Mineral. Deposita 50, 517–546. https://doi.org/10.1007/s00126-014-0549-9.

Morris, R.C., 1993. Genetic modelling for banded iron-formations of the Hamersley Group, Pilbara Craton, Western Australia. Precambrian Res. 60, 243–286. https://doi.org/10.1016/0301-9268(93)90051-3.

Nozaki, Y., Zhang, J., Amakawa, H., 1997. The fractionation between Y and Ho in the marine environment. Earth Planet. Sci. Lett. 148, 329–340. https://doi.org/10.1016/S0012-821X(97)00034-4.

Olszewski, W.J., Wirth, K.R., Gibbs, A.K., Gaudette, H.E., 1989. The age, origin, and tectonics of the Grão Pará Group and associated rocks, Serra dos Carajás, Brazil: Archean continental volcanism and rifting. Precambrian Res. 42, 229–254. https://doi.org/10.1016/0301-9268(89)90013-2.

Ossa Ossa, F., Hofmann, A., Vidal, O., Kramers, J.D., Belyanin, G., Cavalazzi, B., 2016. Unusual manganese enrichment in the Mesoarchean Mozaan Group, Pongola Supergroup, South Africa. Precambrian Res. 281, 414–433. https://doi.org/10.1016/j.precamres.2016.06.009.

Pecoits, E., Gingras, M.K., Barley, M.E., Kappler, A., Posth, N.R., Konhauser, K.O., 2009. Petrography and geochemistry of the Dales Gorge banded iron formation: paragenetic sequence, source and implications for palaeo-ocean chemistry. Precambrian Res. 172, 163–187. https://doi.org/10.1016/j.precamres.2009.03.014.

Peng, Z., Wang, C., Tong, X., Zhang, L., Zhang B., 2018. Element geochemistry and neodymium isotope systematics of the Neoarchean Banded Iron Formations in the Qingyuan Greenstone Belt, North China Craton. Ore Geol. Rev. 102, 562–584. https://doi.org/10.1016/j.oregeorev.2018.09.008.

Piepgras, D.J., Wasserburg, G.J., 1987. Rare earth element transport in the western North Atlantic inferred from Nd isotopic observations. Geochim. Cosmochim. Acta 51, 1257–1271. https://doi.org/10.1016/0016-7037(87)90217-1.

Planavsky, N., Bekker, A., Rouxel, O., Knudsen, A., Lyons, T.W., 2010. Rare earth element and yttrium compositions of Archean and Paleoproterozoic iron formations revisited: new perspectives on the significance and mechanisms of deposition. Geochim. Cosmochim. Acta 74, 6387–6405. https://doi.org/10.1016/j.gca.2010.07.021.

Planavsky, N., Rouxel, O., Bekker, A., Hofmann, A., Little, C.T.S., Lyons, T.W., 2012. Iron isotope composition of some Archean and Proterozoic iron formation. Geochim. Cosmochim. Acta 80, 158–169. https://doi.org/10.1016/j.gca.2011.12.001.

Rasmussen, B., Fletcher, I.R., Bekker, A., Muhling, J.R., Gregory, C.J., Thorne, A.M., 2012. Deposition of 1.88-billion-year-old iron formations as a consequence of rapid crustal growth. Nature 484, 498–501. https://doi.org/10.1038/nature11021.

Rego, E.S., Busigny, V., Lalonde, S.V., Philippot, P., Bouyon, A., Rossignol, C., Babinski, M., Zapparoli, A.C., 2021. Anoxygenic photosynthesis linked to Neoarchean iron formations in Carajás (Brazil). Geobiology 00, 1–16. https://doi.org/10.1111/gbi.12438.

Ribeiro da Luz, B., Crowley, J.K., 2012. Morphological and chemical evidence of stromatolitic deposits in the 2.75 Ga Carajás banded iron formation, Brazil. Earth Planet. Sci. Lett. 355, 60–72. https://doi.org/10.1016/j.epsl.2012.08.028.

Rossignol, C., Rego, E.S., Narduzzi, F., Teixeira, L., Ávila, J.N., Silva, M.A.L., Lana, C., Philippot, P., 2020. Stratigraphy and geochronological constraints of the Serra Sul Formation (Carajás Basin, Amazonian Craton, Brazil). Precambrian Res. 351, 105981. https://doi.org/10.1016/j.precamres.2020.105981.

Rossignol, C., Antonio, P.Y.J., Narduzzi, F., Rego, E.S., Teixeira, L., de Souza, R.A., Ávila, J.N., Silva, M.A.L., Lana, C., Trindade, R.I.F., Philippot, P., 2021. Unraveling one billion years of geological evolution of the southeastern Amazonia Craton from detrital zircon

analyses. Geoscience Frontiers (in press), 101202. https://doi.org/10.1016/j.gsf.2021.101202.

Rousseau, T.C.C., Sonke, J.E., Chmeleff, J., van Beek, P., Souhaut, M., Boaventura, G., Seyler, P., Jeandel, C., 2015. Rapid neodymium release to marine waters from lithogenic sediments in the Amazon estuary. Nat. Commun. 6, 1–8. https://doi.org/10.1038/ncomms8592.

Rouxel O. J., Auro M., 2010. Iron isotope variations in coastal seawater determined by multicollector ICP-MS. Geostand. Geoanal. Res. 34, 135–144. https://doi.org/10.1111/j.1751-908X.2010.00063.x.

Rouxel, O.J., Bekker, A., Edwards, K.J., 2005. Iron isotope constraints on the Archaean and Paleoproterozoic ocean redox state. Science 307, 1088–1090. https://doi.org/10.1126/science.1105692.

Rouxel, O., Shanks, W.C., Bach, W., Edwards, K.J., 2008. Integrated Fe- and S-isotope study of seafloor hydrothermal vents at East Pacific Rise 9–10ºN. Chem. Geol. 252, 214–227. https://doi.org/10.1016/j.chemgeo.2008.03.009.

Rudnick, R.L., Gao, S., 2003. Composition of the continental crust. In: Rudnick, R.L. (Ed.), The Crust. Elsevier-Pergamon, Oxford, pp. 1–64. https://doi.org/10.1016/B0-08-043751-6/03016-4.

Satkoski, A.M., Beukes, N.J., Li, W., Beard, B.L., Johnson, C.M., 2015. A redox-stratified ocean 3.2 billion years ago. Earth Planet. Sci. Lett. 430, 43–53. https://doi.org/10.1016/j.epsl.2015.08.007.

Schier, K., Bau, M., Smith, A.J.B., Beukes, N.J., Coetzee, L.L., Viehmann, S., 2020. Chemical evolution of seawater in the Transvaal Ocean between 2426 Ma (Ongeluk Large Igneous

Province) and 2413 Ma ago (Kalahari Manganese Field). Gondwana Res. 88, 373–388. https://doi.org/10.1016/j.gr.2020.09.001.

Schutesky, M.E., Oliveira, C.G., 2020. From the roots to the roof: An integrated model for the Neoarchean Carajás IOCG System, Brazil. Ore Geol. Rev. 127, 103833. https://doi.org/10.1016/j.oregeorev.2020.103833.

Severmann, S., Johnson, C.M., Beard, B.L., German, C.R., Edmonds, H.N., Chiba, H., Green, D.R.H., 2004. The effect of plume processes on the Fe isotope composition of hydrothermally derived Fe in the deep ocean as inferred from the Rainbow vent site, Mid-Atlantic Ridge, 36º14′N. Earth. Planet. Sci. Lett. 225, 63–76. https://doi.org/10.1016/j.epsl.2004.06.001.

Severmann, S., Lyons, T.W., Anbar, A., McManus, J., Gordon, G., 2008. Modern iron isotope perspective on the benthic iron shuttle and the redox evolution of ancient oceans. Geology 36, 487–490. https://doi.org/10.1130/G24670A.1.

Sharma, M., Polizzotto, M., Anbar, A.D., 2001. Iron isotopes in hot springs along the Juan de Fuca Ridge. Earth Planet. Sci. Lett. 194, 39–51. https://doi.org/10.1016/S0012-821X(01)00538-6.

Shimizu, H., Umemoto, N., Masuda, A., Appel, P.W.U., 1990. Sources of iron formations in the Archean Isua and Malene supracrustals, West Greenland: evidence from La-Ce and Sm-Nd isotopic data and REE abundances. Geochim. Cosmochim. Acta 54, 1147–1154. https://doi.org/10.1016/0016-7037(90)90445-Q.

Souza, Z.S., Potrel, H., Lafon, J.M., Althoff, F.J., Pimentel, M.M., Dall'Agnol, R., Oliveira, C.G., 2001. Nd, Pb and Sr isotopes of the Identidade Belt, an Archaean greenstone belt of the Rio Maria region (Carajás Province, Brazil): implications for the Archaean geodynamic

evolution of the Amazonian Craton. Precambrian Res. 109, 293–315. https://doi.org/10.1016/S0301-9268(01)00164-4.

Steinhoefel, G., von Blanckenburg, F., Horn, I., Konhause, K.O., Beukes, N.J., Gutzmer, J., 2010. Deciphering formation processes of banded iron formations from the Transvaal and the Hamersley successions by combined Si and Fe isotope analysis using UV femtosecond laser ablation. Geochim. Cosmochim. Acta 74, 2677–2696. https://doi.org/10.1016/j.gca.2010.01.028.

Stevenson E.I., Fantle M.S., Das S.B., Williams H.M., Aciego S.M., 2017. The iron isotopic composition of subglacial streams draining the Greenland ice sheet. Geochim. Cosmochim. Acta 213, 237–254. https://doi.org/10.1016/j.gca.2017.06.002.

Sun, Si, Li, Yi-Liang, 2017. Microstructures, crystallography and geochemistry of Magnetite in 2500 to 2200 million-year-old banded iron formations from South Africa, Western Australia and North China. Precambrian Res. 298, 292–305. https://doi.org/10.1016/j.precamres.2017.06.015.

Tallarico, F.H.B., Figueiredo, B.R., Groves, D.I., Kositcin, N., McNaughton, N.J., Fletcher, I.R., Rego, J.L., 2005. Geology and SHRIMP U-Pb geochronology of the Igarapé Bahia deposit, Carajás copper-gold belt, Brazil: an Archean (2.57 Ga) example of iron-oxide Cu-Au-(U-REE) mineralization. Econ. Geol. 100, 7–28. https://doi.org/10.2113/100.1.0007.

Tavares, F.M., Trouw, R.A.J., da Silva, C.M.G., Justo, A.P., Oliveira, J.K.M., 2018. The multistage tectonic evolution of the northeastern Carajás Province, Amazonian Craton, Brazil: Revealing complex structural patterns. J. S. Am. Earth Sci. 88, 238–252. https://doi.org/10.1016/j.jsames.2018.08.024.

Taylor, S.R., McLennan, S.M., 1985. The Continental Crust; Its composition and evolution; an examination of the geochemical record preserved in sedimentary rocks. Blackwell, Oxford. 312.

Teixeira, J.B.G., Eggler, D.H., 1994. Petrology, geochemistry, and tectonic setting of Archaean basaltic and dioritic rocks from the N4 iron deposit, Serra dos Carajás, Pará, Brazil. Acta Geol. Leopoldensia 17, 71–114.

Teixeira, N. A., Campos, L. D., de Paula R. R., Lacasse, C., M., Ganade, C. E., Monteiro, C. F., Lopes, L. B. L., Oliveira, C. G., 2021. Carajás Mineral Province - Example of metallogeny of a rift above a cratonic lithospheric keel. J. S. Am. Earth Sci. 108, 103091. https://doi.org/10.1016/j.jsames.2020.103091.

Toledo, P.I.F., Moreto, C.P.N., Xavier, R.P., Gao, J.F., de Matos, J.H.S.N., de Melo, G.H.C., 2019. Multistage evolution of the Neoarchean (ca. 2.7 Ga) Igarapé cinzento (GT-46) iron oxide copper-gold deposit, Cinzento shear zone, Carajás Province, Brazil. Econ. Geol. 114, 1–34. https://doi.org/10.5382/econgeo.2019.4617.

Trendall, A.F., Basei, M.A.S., De Laeter, J.R., Nelson, D.R., 1998. SHRIMP zircon U-Pb constraints on the age of the Carajás Formation, Grão Pará Group, Amazon Craton. J. S. Am. Earth Sci. 11, 265– 277. https://doi.org/10.1016/S0895-9811(98)00015-7.

Trunfull, E.F., Hagemann, S.G., Xavier, R.P., Moreto, C.P.N., 2020. Critical assessment of geochronological data from the Carajás Mineral Province, Brazil: Implications for metallogeny and tectonic evolution. Ore Geol. Rev. 121, 103556. https://doi.org/10.1016/j.oregeorev.2020.103556.

Vasquez, M.L., Carvalho, J.M.A., Sousa, C.S., Ricci, P.S.F., Macambira, E.M.B., Costa, L.T. R., 2008. Mapa Geológico do Pará em SIG. Brazilian Geological Survey – CPRM.

Viehmann, S., Hoffmann, J.E., Münker, C., Bau, M., 2014. Decoupled Hf-Nd isotopes in Neoarchean seawater reveal weathering of emerged continents. Geology 42, 115–118. https://doi.org/10.1130/G35014.1.

Viehmann, S., Bau, M., Hoffmann, J.E., Muenker, C., 2015. Geochemistry of the Krivoy Rog Banded Iron Formation, Ukraine, and the impact of peak episodes of increased global magmatic activity on the trace element composition of Precambrian seawater. Precambrian Res. 270, 165–180. https://doi.org/10.1016/j.precamres.2015.09.015.

Wang, C.L., Zhang, L.C., Dai, Y.P., Li, W.J., 2014. Source characteristics of the ~2.5 Ga Wangjiazhuang banded iron formation from the Wutai greenstone belt in the North China Craton: evidence from neodymium isotopes. J. Asian Earth Sci. 93, 288–300. https://doi.org/10.1016/j.jseaes.2014.07.038.

Wang, C.L., Wu, H.Y., Li, W.J., Peng, Z.D., Zhang, L.C., Zhai, M.G., 2017. Changes of Ge/Si, REE+Y and Sm–Nd isotopes in alternating Fe- and Si-rich mesobands reveal source heterogeneity of the ~2.54 Ga Sijiaying banded iron formation in Eastern Hebei, China. Ore Geol. Rev. 80, 363–376. https://doi.org/10.1016/j.oregeorev.2016.06.036.

Warke, M.R., Rocco, T.D., Zerkle, A.L., Lepland, A., Prave, A.R., Martin, A.P., Ueno, Y., Condon, D.J., and Claire, M.W., 2020, The Great Oxidation Event preceded a Paleoproterozoic "snowball Earth". Proc. Natl. Acad. Sci. 117, 13.314–13.320. https://doi.org/10.1073/pnas.2003090117.

Weis, D., Kieffer, B., Pretorius, W., Barling, J., 2005. High-precision Pb-Sr-Nd-Hf isotopic characterization of USGS BHVO-1 and BHVO-2 reference materials. Geochem. Geophys. Geosyst., 6. http://dx.doi.org/10.14288/1.0041627.

Weyer S., Schwieters J. B., 2003. High precision Fe isotope measurements with high mass resolution MC-ICPMS. Int. J. Mass Spectrom. 226, 355–368. https://doi.org/10.1016/S1387-3806(03)00078-2.

Wirth, K.R., Gibbs, A.K., Olszewski, W., 1986. U-Pb zircon ages of the Grão Pará Group and Serra dos Carajás Granite. Revista Brasileira de Geociências, 16, 195-200.

Wonder, J., Spry, P., Windom, K., 1988. Geochemistry and origin of manganese-rich rocks related to iron-formation and sulfide deposits, western Georgia. Econ. Geol. 83, 1070–1081. https://doi.org/10.2113/gsecongeo.83.5.1070.

Zhang, L., Ren, Z.-Y., Handler, M.R., Wu, Y.-D., Zhang, L., Qian, S.-P., Xia, X.-P., Yang, Q., Xu, Y.-G., 2019. The origins of high-Ti and low-Ti magmas in large igneous provinces, insights from melt inclusion trace elements and Sr-Pb isotopes in the Emeishan large Igneous Province. Lithos 344-345, 122–133. https://doi.org/10.1016/j.lithos.2019.06.014.

Zucchetti, M., 2007, Rochas máficas do Supergrupo Grão Pará e sua relação com a mineralização de ferro dos depósitos N4 e N5, Carajás, PA: Unpublished Ph.D. thesis, Belo Horizonte, Brazil, Universidade Federal de Minas Gerais, 125p (in Portuguese).

SUPLEMENTARY MATERIAL

This file contains:

Supplementary information

Supplementary figures (Fig. S1, S2, S3, S4, S5, S6, S7, and S8)

Supplementary tables (Table S1, S2, S3, S4, S5, and S6)

References

SUPPLEMENTARY INFORMATION

S1. Carajás Mineral Province (Geological Background)

The Carajás Mineral Province is an Archean nucleus located in the southeastern portion of the Amazonian Craton, Brazil (Fig. 1A). It contains world-class deposits of Fe and Cu, as well as Mn an Ni mines (Beisiegel et al., 1973; DOCEGEO, 1988; Monteiro et al., 2014; Moreto et al., 2015). The province is divided in two domains, the northern Carajás Domain and the southern Rio Maria Domain (Fig. 1B). A broad E-W striking shear zone (known as "Transition" subdomain), mostly within the Carajás Domain, occurs between the metavolcano-sedimentary Carajás Basin sequence and rocks of the Rio Maria Domain (Fig. 1B).

The Rio Maria Domain is a typical granite-greenstone terrane, mainly composed of tonalite–-trondhjemite–granodiorite (TTG) associations, surrounded by greenstone belts, with formation ages between ca. 3.0–2.8 Ga (Althoff et al., 2000; Souza et al., 2001; Dall'Agnol et al., 2006; Almeida et al., 2011, 2013; Oliveira et al., 2011). Diverse Archean plutonic rocks are intrusive in the TTG–greenstone basement rocks including a sanukitoid suite of 2.87–2.86 Ga,

high Ba–Sr leucogranodiorite–granites and associated K–rich granites (Oliveira et al., 2009; Almeida et al., 2010, 2011; 2013).

Apart from the strongly deformed granitoids and gneissic rocks of the Transition subdomain, Carajás domain is composed essentially of the Carajás Basin (Vasquez et al., 2008; Fig. 1C), also known as the central sigmoid of Carajás (Araújo et al., 1988; Araújo & Maia, 1991; Pinheiro & Holdsworth, 1997; Holdsworth & Pinheiro, 2000). The basement of the Carajás Basin comprises ca. 2.85 Ga Mesoarchean igneous and metamorphic rocks, which include granite and gneiss of TTG-type, belonging to the Xingu Complex (Machado et al., 1991). Many authors considered the ca. 3.0 Ga Pium Diopside-Norite Complex (Pidgeon et al., 2000) and the Chicrim-Cateté orthogranulite unit (Araújo & Maia, 1991; Vasquez et al., 2008) as part of the basement assembly of this basin as well. The main assemblages of the Carajás Basin are of Neoarchean to Paleoproterozoic age and it is commonly segmented into the lowermost metavolcanic–sedimentary Grão-Pará Group (2.76–2.73 Ga; Fig. 2) overlain by metasedimentary rocks of the ca. 2.68–2.06 Ga Serra Sul and Águas Claras formations (Araújo & Nogueira, 2019; Araújo Filho et al., 2020; Rossignol et al., 2020) (Fig. 1C). The Paleoproterozoic Serra Sul Formation is composed of subglacial and marine diamictite interbedded with mudstone and black shale strata (Araújo & Nogueira, 2019), while the Águas Claras Formation consists mainly of fluvial siliciclastic rocks (Araújo Filho et al., 2020). Both units overlie in unconformity the Grão-Pará Group (Araújo Filho et al., 2020).

Several ca. 2.76 Ga mafic-ultramafic layered complexes are exposed near the borders of the Carajás Basin (Machado et al., 1991; Vasquez et al., 2008; Fig. 1C), including the PGE-mineralized Luanga layered complexes, and large Ni-laterite mineralized layered intrusions of the Cateté Suite (Lafon et al., 2000; Ferreira Filho et al., 2007). Paleoproterozoic (~1.88 Ga) intrusions including several anorogenic granitic plutons (e.g., Carajás granite), and dike swarms

(Machado et al., 1991; Teixeira et al., 2018; Giovanardi et al., 2019) cross-cut the Carajás Basin, post-dating the deposition within the basin.

The most conspicuous structural feature of the Carajás Basin is an S-shaped syncline-anticline pair (Rosière et al., 2006), the Carajás fold, and partially disrupted by the Carajás strike-slip system (Fig. 1C). The latter divides the Serra dos Carajás in two main blocks, named Serra Norte and Serra Sul.

S2. Electron microprobe analytical methods

Mineral analyses were performed on polished thin section using a JEOL JXA-8230 SuperProbe with 5 wavelengths dispersive (WDS) spectrometers at the Electron Microprobe Laboratory of the University of Brasília, Brazil. Systematic WDS analyses were obtained for magnetite, hematite, and goethite. Operating conditions for all minerals were 15 kV accelerating voltage, a beam current of 10 nA and probe diameters of 1 μm. Count times on peak and on background were 10 and 5 s, respectively. Both synthetic and natural mineral standards were used for the analyses and the same standards and procedure were retained throughout the analytical work. 10s. In additional, X-ray energy dispersive spectroscopy (EDS) was also performed on several minerals to support petrographic studies. The results are provided in Supplementary Tables.

SUPPLEMENTARY FIGURES

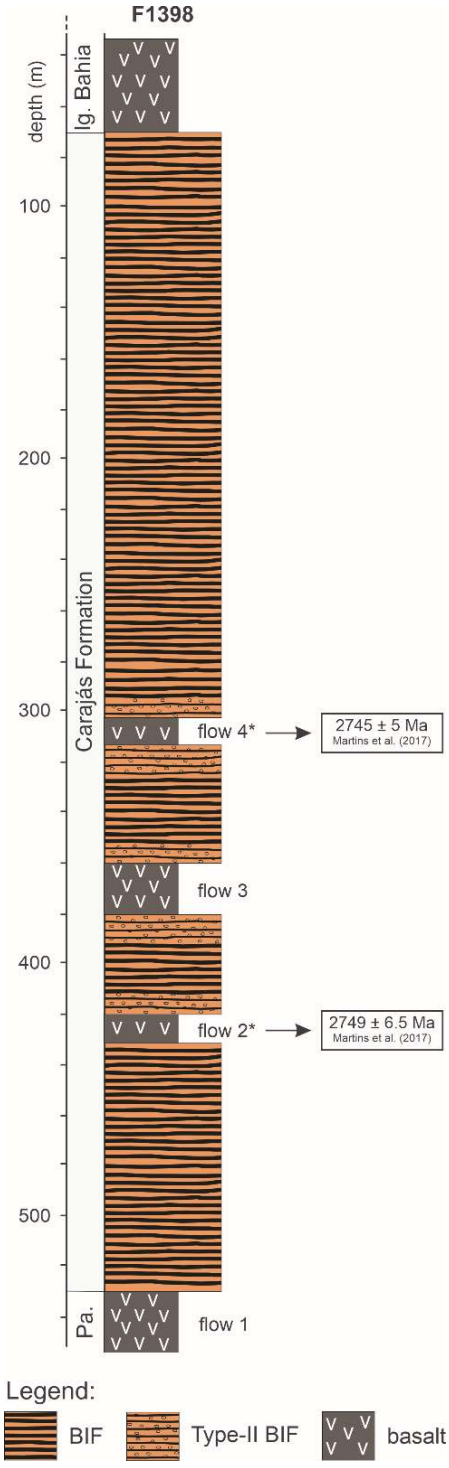

Fig. S1. *Litholog for N4WS-F1398, displaying the stratigraphic position and relationship between different lithologies within the core. Note the important SHRIMP U–Pb zircon ages (Martins et al., 2017) from individual basaltic flows.*

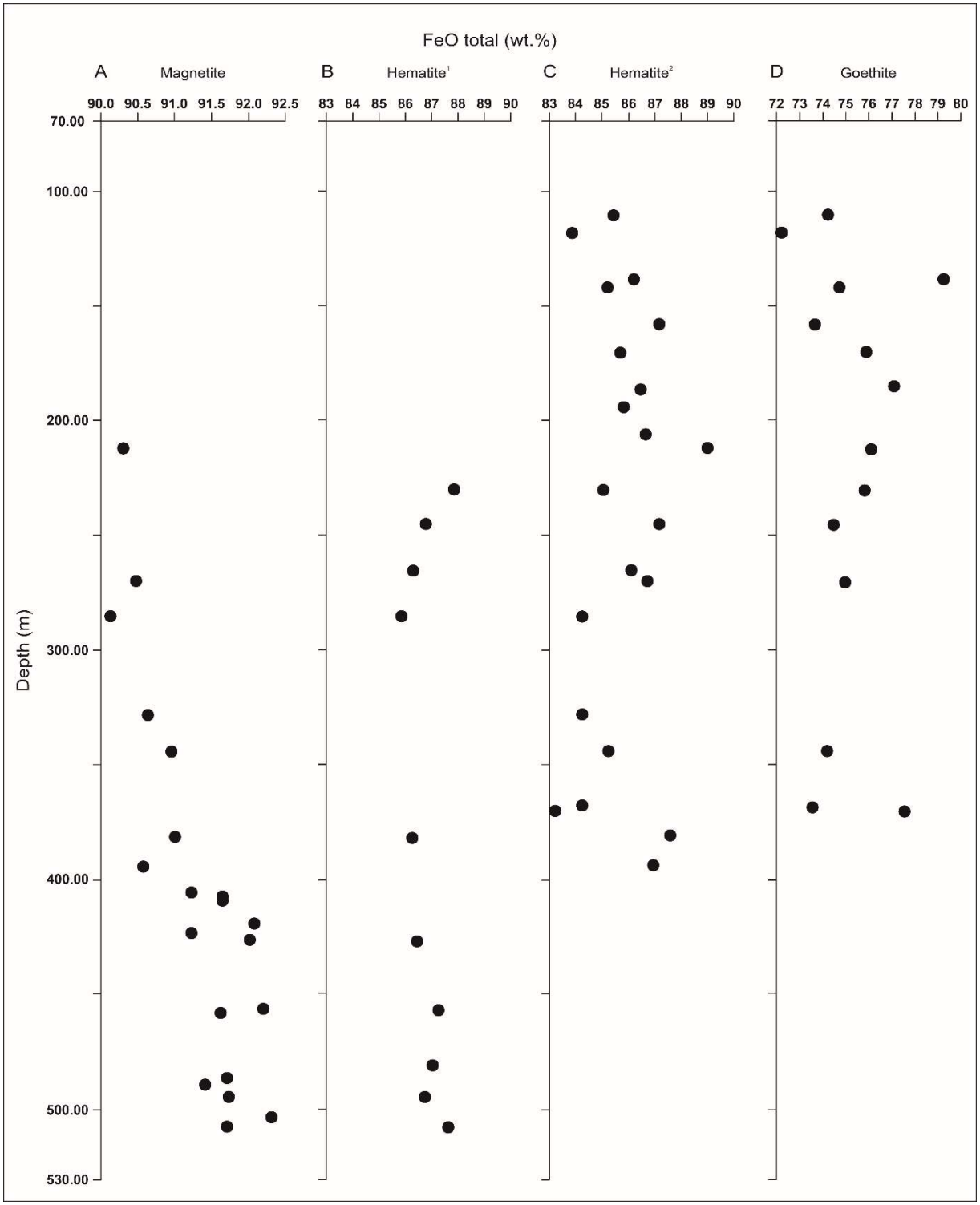

Fig. S2. *Distribution of total iron content expressed as FeO total with depth for electron microprobe analyses of magnetite (A), hematite[1] (B), hematite[2] (C), and goethite (D) from the Carajás jaspilite.*

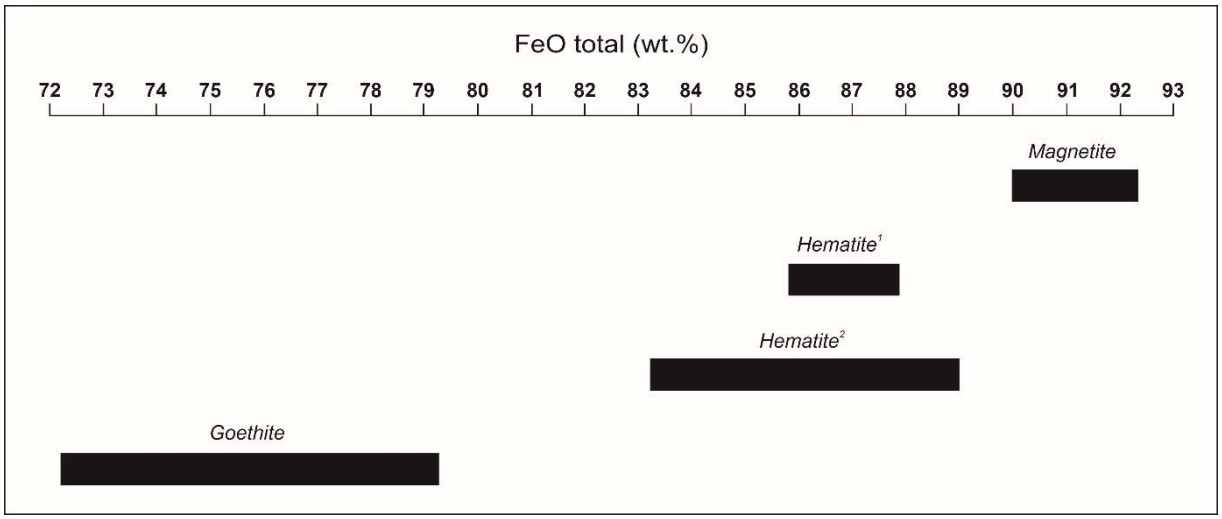

Fig S3. *Variation of total iron content expressed as FeO total for electron microprobe analyses of magnetite, primary hematite (Hematite[1]), pseudomorphic hematite (Hematite[2]), and goethite.*

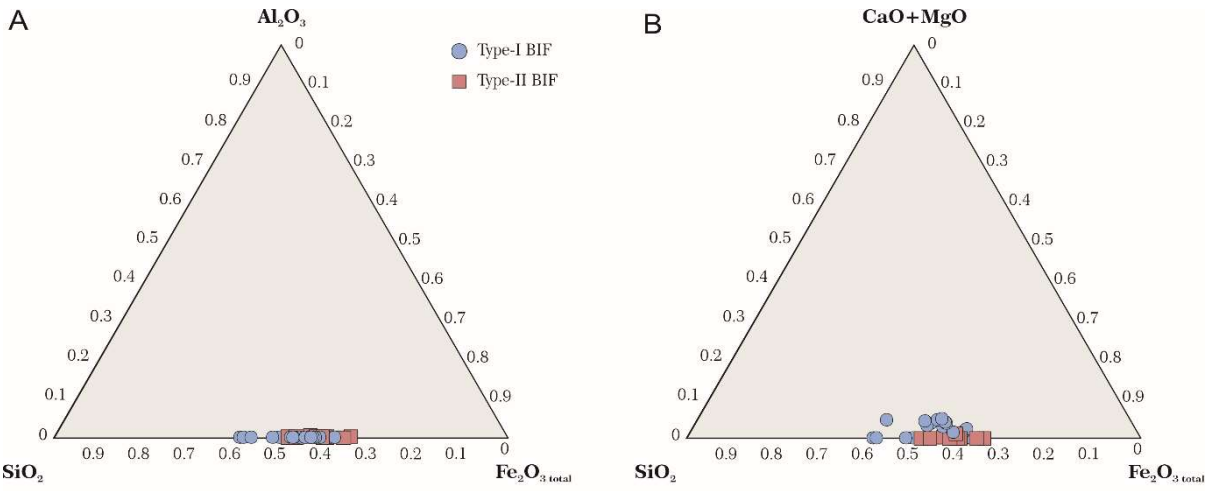

Fig S4. *Major bulk element data from the Carajás BIF plotted in ternary diagrams. (A) SiO_2–Fe_2O_3(t)–Al_2O_3 and (B) SiO_2–Fe_2O_3(t)–CaO + MgO. Type-II BIF are samples influenced by volcanic adjacent activity, meanwhile, Type-I BIF is the remaining samples. See text for further explanation.*

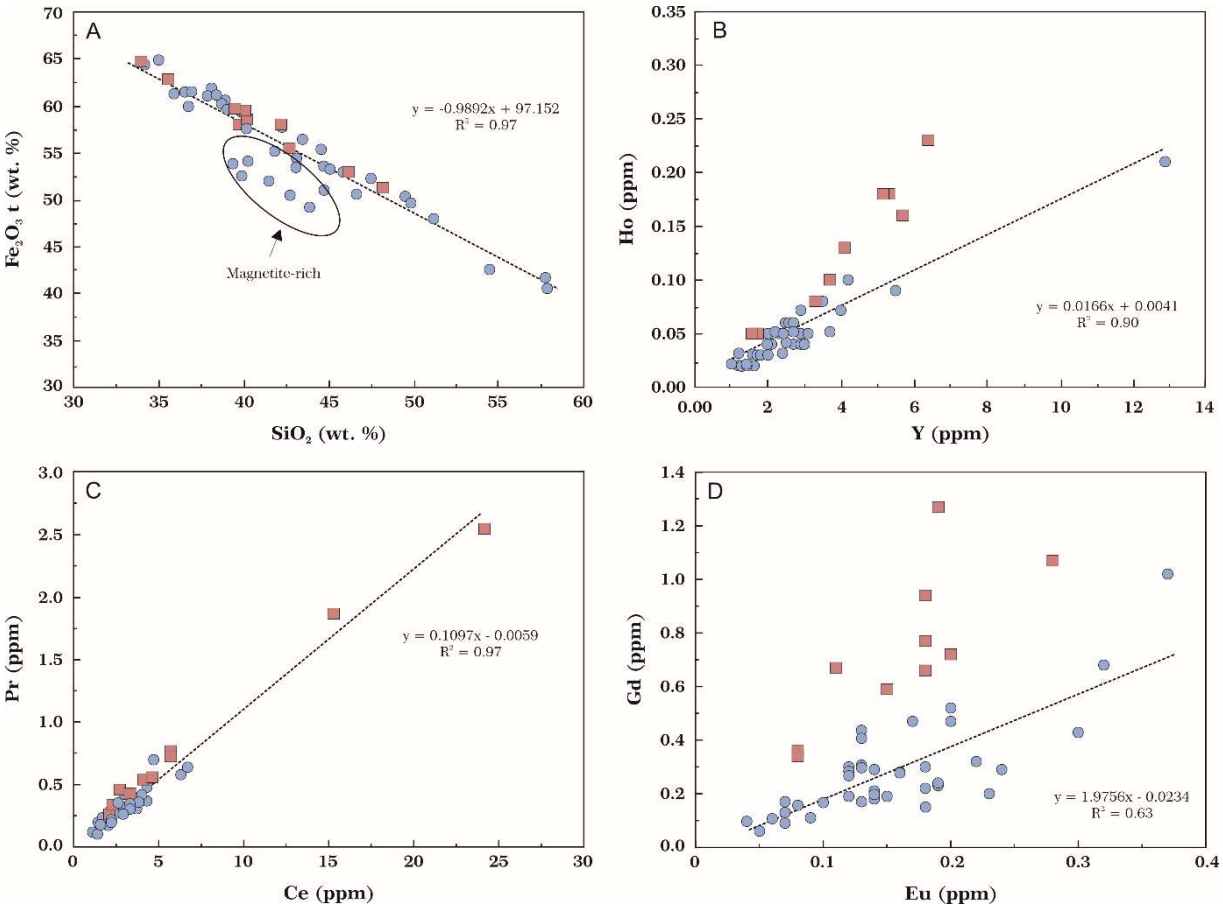

Fig S5. *Correlation diagrams between major elements and trace elements of the Carajás jaspilite:* ***A)*** *SiO_2 and Fe_2O_3(total); the better alignment (without magnetite-rich samples) gives an R^2 = 0.97;* ***B)*** *Y and Ho;* ***C)*** *Ce and Pr;* ***D)*** *Eu and Gd. R^2 from (B) and (D) taken without Type-II BIF samples.*

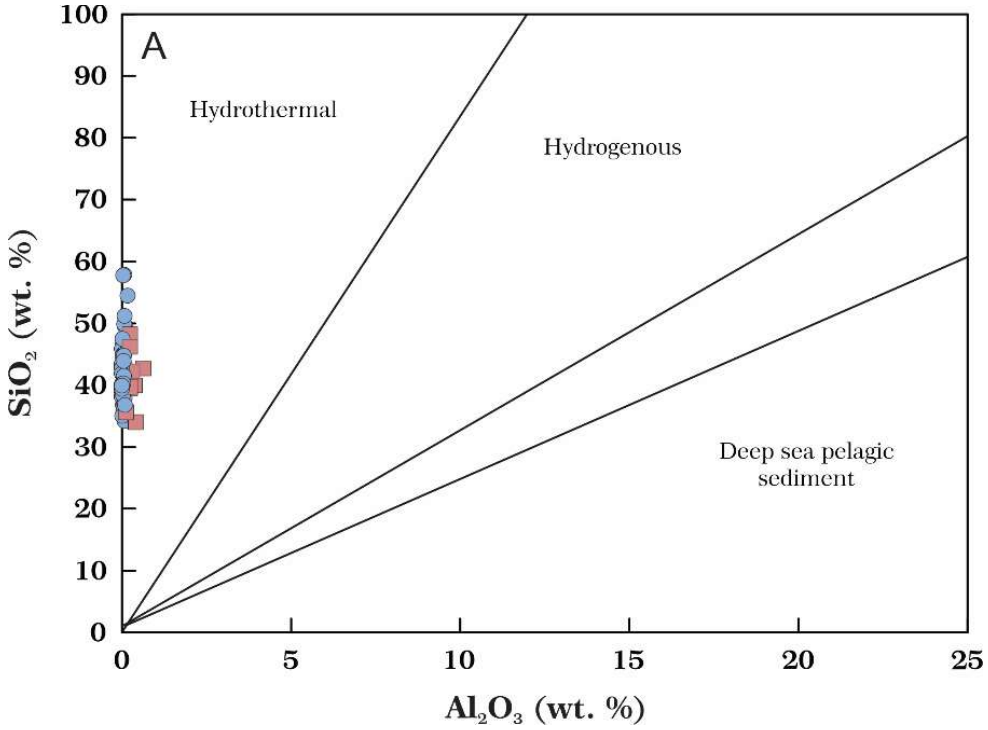

Fig S6. *SiO_2 vs. Al_2O_3 discrimination diagram indicating the hydrothermal affinity of the studied BIF.*

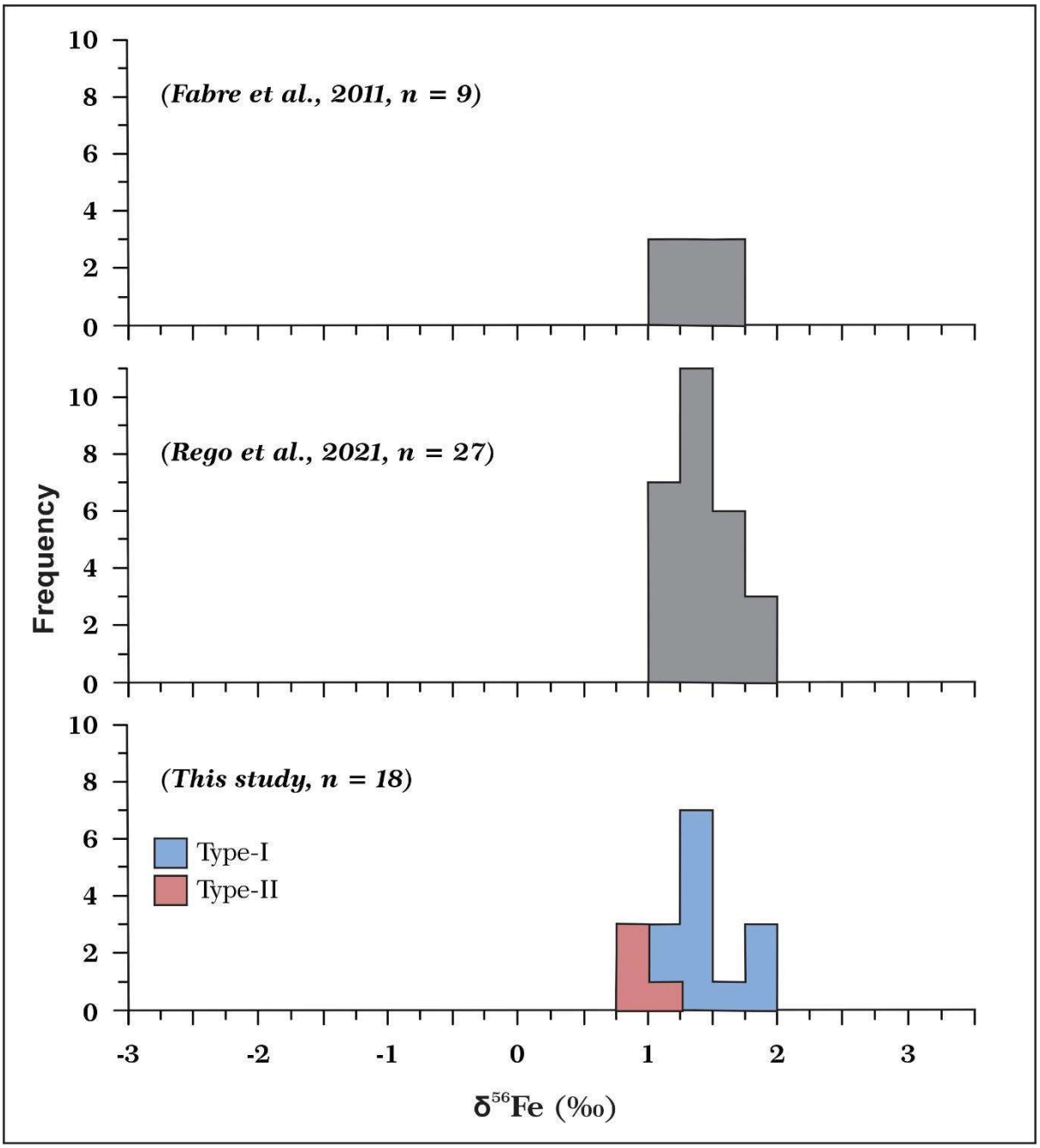

Fig S7. *Histograms of $\delta^{56}Fe$ values for Carajás BIF samples, as well as previous results from Fabre et al., 2011 and Rego et al., 2021.*

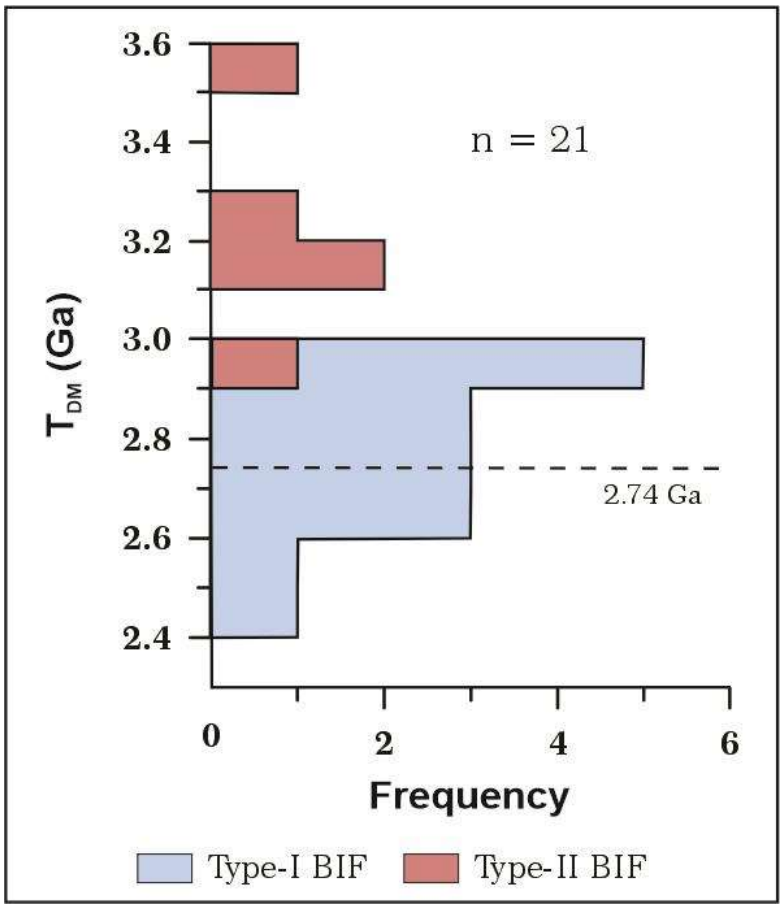

Fig S8. *Histograms of T_{DM} values for Carajás jaspilite samples. Dotted line is approximately the minimum depositional age of the jaspilites (Galarza et al., 2008).*

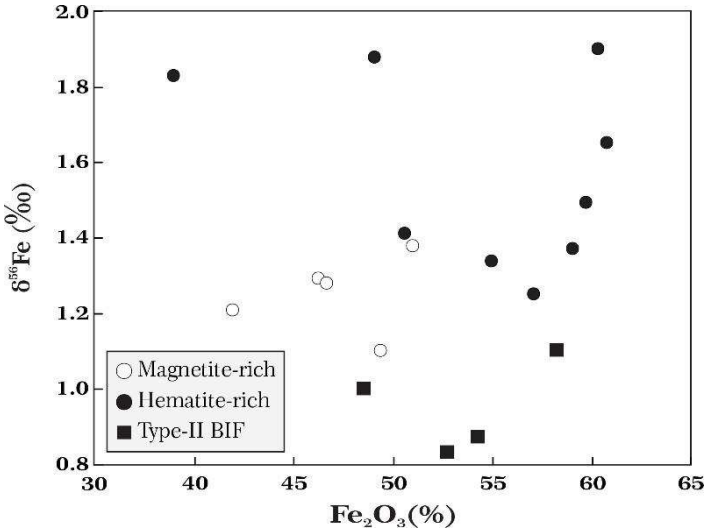

Fig S9. *Average differences in hematite and magnetite $\delta^{56}Fe$ values plotted against the Fe_2O_3 content of each core sample. The average $\delta^{56}Fe$ values for each of this sample do not vary systematically with the percentage of hematite (Fe_2O_3) in the sample.*

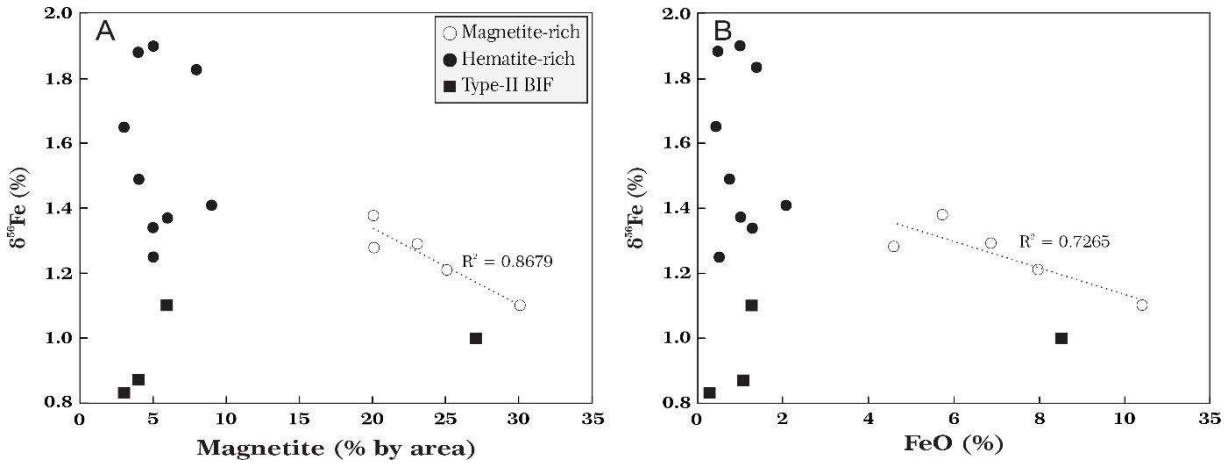

Fig S10. A) *Average differences in hematite and magnetite $\delta^{56}Fe$ values plotted against the average magnetite content of each core sample. Magnetite contents are presented as percent magnetite by area.* ***B)*** *Average $\delta^{56}Fe$ values plotted against the FeO content of each core sample. Average total magnetite in each core section as determined by image analysis (see Table 1 for data).*

SUPPLEMENTARY TABLES

Table S1

Microprobe analyses of magnetite with core depth from the Carajás BIF.

No.	Depth (m)	Sample	SiO_2 (wt.%)	Al_2O_3	TiO_2	FeO total*	MnO	MgO	CaO	K_2O	Cr_2O_3	V_2O_3	NiO	Total
1	212.00	F1398-034	0.89	0.01	0.03	90.31	0.00	0.02	0.01	0.02	0.00	0.00	0.00	91.30
2	270.00	F1398-048	0.81	0.02	0.00	90.48	0.03	0.05	0.03	0.01	0.00	0.03	0.00	91.46
3	285.00	F1398-054	1.41	0.00	0.00	90.13	0.14	0.10	0.01	0.00	0.04	0.05	0.00	91.88
4	328.00	F1398-066	1.18	0.04	0.00	90.64	0.00	0.11	0.03	0.00	0.00	0.03	0.06	92.10
5	344.00	F1398-070	0.78	0.00	0.17	90.96	0.07	0.03	0.02	0.00	0.03	0.00	0.00	92.06
6	381.00	F1398-082	0.29	0.00	0.06	91.01	0.00	0.01	0.01	0.02	0.06	0.00	0.00	91.45
7	394.00	F1398-085	1.12	0.01	0.06	90.58	0.07	0.08	0.02	0.00	0.02	0.03	0.02	92.01
8	405.00	F1398-088	0.62	0.02	0.04	91.23	0.01	0.03	0.02	0.01	0.03	0.02	0.02	92.06
9	407.00	F1398-089	0.67	0.01	0.01	91.65	0.01	0.04	0.13	0.03	0.00	0.00	0.00	92.55
10	409.00	F1398-090	0.85	0.02	0.02	91.65	0.02	0.04	0.03	0.01	0.01	0.02	0.00	92.66
11	419.00	F1398-097	0.29	0.01	0.05	92.08	0.01	0.01	0.02	0.00	0.01	0.02	0.02	92.52
12	423.00	F1398-104	1.18	0.03	0.01	91.23	0.02	0.14	0.10	0.02	0.01	0.04	0.00	92.79
13	426.00	F1398-105	0.82	0.01	0.00	92.02	0.03	0.12	0.01	0.00	0.02	0.02	0.00	93.05
14	456.00	F1398-113	1.26	0.02	0.00	92.20	0.01	0.37	0.04	0.01	0.01	0.04	0.00	93.96
15	458.00	F1398-114	0.66	0.01	0.16	91.62	0.03	0.06	0.03	0.02	0.03	0.00	0.01	92.62
16	486.00	F1398-123	0.61	0.01	0.26	91.71	0.03	0.06	0.01	0.00	0.03	0.03	0.02	92.77
17	489.00	F1398-125	0.89	0.01	0.26	91.41	0.03	0.11	0.01	0.01	0.02	0.01	0.01	92.77
18	494.00	F1398-127	0.66	0.02	0.10	91.74	0.03	0.08	0.02	0.01	0.01	0.00	0.01	92.69
19	503.00	F1398-130	0.86	0.01	0.02	92.31	0.05	0.06	0.02	0.02	0.02	0.01	0.02	93.39
20	507.00	F1398-132	1.03	0.02	0.12	91.71	0.04	0.13	0.01	0.01	0.02	0.02	0.01	93.11

*Total iron content expressed as FeO total

Table S2

Electron microprobe analyses of hematite with core depth from the Carajás BIF.

No.	Depth (m)	Sample	SiO_2 (wt.%)	Al_2O_3	TiO_2	FeO total*	MnO	MgO	CaO	K_2O	Cr_2O_3	V_2O_3	NiO	Total
Pseudomorphic hematite (secondary)														
1	110.00	F1398-009	0.98	0.03	0.05	85.43	0.04	0.04	0.08	0.07	0.02	0.02	0.00	86.77
2	118.00	F1398-011	1.15	0.07	0.10	83.86	0.03	0.04	0.10	0.00	0.04	0.05	0.01	85.45
3	138.00	F1398-016	0.49	0.01	0.03	86.19	0.08	0.02	0.09	0.04	0.07	0.02	0.00	87.04
4	142.00	F1398-017	0.47	0.00	0.05	85.21	0.05	0.01	0.07	0.08	0.02	0.02	0.01	85.97
5	158.00	F1398-21	0.96	0.00	0.00	87.16	0.07	0.00	0.10	0.02	0.00	0.03	0.02	88.36
6	170.00	F1398-024	1.02	0.02	0.00	85.70	0.00	0.02	0.02	0.00	0.00	0.00	0.00	86.79
7	186.00	F1398-027	1.30	0.09	0.08	86.47	0.04	0.01	0.07	0.01	0.05	0.04	0.00	88.15
8	194.00	F1398-029	1.56	0.08	0.00	85.81	0.08	0.05	0.05	0.02	0.03	0.02	0.00	87.70
9	206.00	F1398-032	0.59	0.05	0.09	86.67	0.02	0.02	0.09	0.02	0.02	0.00	0.03	87.59
10	212.00	F1398-032	1.32	0.00	0.18	88.99	0.04	0.11	0.09	0.00	0.00	0.00	0.00	90.72
11	230.00	F1398-038	0.86	0.00	0.02	85.05	0.04	0.02	0.03	0.04	0.00	0.03	0.01	86.11
12	245.00	F1398-042	0.63	0.02	0.07	87.16	0.00	0.03	0.02	0.00	0.04	0.02	0.04	88.03
13	265.00	F1398-046	1.36	0.06	0.03	86.12	0.04	0.04	0.03	0.02	0.03	0.00	0.01	87.74
14	270.00	F1398-048	1.12	0.00	0.12	86.73	0.01	0.03	0.03	0.02	0.00	0.01	0.00	88.05
15	285.00	F1398-052	1.23	0.24	0.05	84.23	0.02	0.02	0.02	0.00	0.06	0.02	0.00	85.89
16	328.00	F1398-066	1.13	0.09	0.00	84.23	0.03	0.04	0.07	0.01	0.03	0.00	0.02	85.66
17	344.00	F1398-070	0.64	0.00	0.06	85.23	0.07	0.01	0.09	0.05	0.04	0.05	0.03	86.27
18	368.00	F1398-076	1.79	0.11	0.06	84.26	0.04	0.12	0.02	0.01	0.00	0.03	0.02	86.45
19	370.00	F1398-077	2.53	0.38	0.13	83.22	0.01	0.03	0.07	0.05	0.05	0.02	0.01	86.51
20	381.00	F1398-082	1.04	0.00	0.00	87.60	0.05	0.02	0.02	0.02	0.05	0.01	0.03	88.84
21	394.00	F1398-085	0.21	0.03	0.14	86.93	0.03	0.01	0.03	0.02	0.02	0.01	0.01	87.44
Fine irregular hematite (primary)														
1	230.00	F1398-038	0.24	0.05	0.13	87.86	0.03	0.00	0.10	0.00	0.00	0.04	0.00	88.44
2	245.00	F1398-042	0.34	0.08	0.08	86.76	0.06	0.01	0.07	0.05	0.01	0.02	0.02	87.49
3	265.00	F1398-046	0.77	0.13	0.14	86.29	0.06	0.01	0.05	0.03	0.02	0.02	0.01	87.52
4	285.00	F1398-052	0.41	0.14	0.04	85.84	0.03	0.03	0.04	0.01	0.26	0.01	0.01	86.82
5	381.00	F1398-082	0.33	0.07	0.07	86.25	0.03	0.02	0.03	0.02	0.02	0.01	0.00	86.86
6	426.00	F1398-105	1.10	0.04	0.00	86.45	0.06	0.05	0.07	0.05	0.01	0.01	0.06	87.90
7	456.00	F1398-113	0.77	0.04	0.03	87.26	0.00	0.06	0.09	0.04	0.07	0.02	0.00	88.37

8	480.00	F1398-125	0.38	0.09	0.18	87.03	0.03	0.02	0.13	0.07	0.07	0.02	0.00	88.02
9	494.00	F1398-127	0.40	0.06	0.05	86.75	0.01	0.04	0.07	0.02	0.03	0.01	0.00	87.44
10	507.00	F1398-132	0.31	0.04	0.03	87.62	0.02	0.02	0.06	0.02	0.03	0.01	0.01	88.16

*Total iron content expressed as FeO total

Table S3

Electron microprobe analyses of goethite with core depth from the Carajás BIF.

No.	Depth (m)	Sample	SiO_2 (wt.%)	Al_2O_3	TiO_2	FeO total*	MnO	MgO	CaO	K_2O	Cr_2O_3	V_2O_3	NiO	Total
1	110.00	F1398-009	0.95	0.14	0.06	74.22	0.06	0.03	0.09	0.00	0.02	0.00	0.02	75.58
2	118.00	F1398-011	1.18	0.03	0.02	72.22	0.03	0.02	0.07	0.05	0.01	0.00	0.02	73.63
3	138.00	F1398-016	1.00	0.06	0.00	79.26	0.12	0.01	0.02	0.00	0.00	0.02	0.01	80.49
4	142.00	F1398-017	0.97	0.00	0.02	74.73	0.04	0.04	0.07	0.01	0.05	0.02	0.00	75.93
5	158.00	F1398-021	0.65	0.21	0.00	73.64	0.14	0.03	0.05	0.02	0.07	0.00	0.00	74.79
6	170.00	F1398-024	1.14	0.01	0.00	75.87	0.00	0.00	0.03	0.03	0.02	0.02	0.05	77.17
7	185.00	F1398-027	1.44	0.46	0.00	77.08	0.08	0.08	0.09	0.05	0.00	0.00	0.02	79.30
8	212.00	F1398-034	1.17	0.00	0.04	76.11	0.02	0.01	0.02	0.01	0.00	0.02	0.00	77.40
9	230.00	F1398-038	1.01	0.00	0.02	75.83	0.00	0.05	0.03	0.01	0.00	0.00	0.00	76.96
10	245.00	F1398-042	0.96	0.03	0.01	74.48	0.02	0.01	0.04	0.02	0.04	0.02	0.01	75.65
11	270.00	F1398-048	0.88	0.01	0.03	74.96	0.01	0.00	0.05	0.03	0.00	0.02	0.02	76.01
12	344.00	F1398-070	2.22	0.74	0.05	74.19	0.02	0.17	0.04	0.01	0.07	0.01	0.07	77.59
13	368.00	F1398-076	2.70	0.35	0.03	73.54	0.04	0.08	0.04	0.02	0.06	0.00	0.01	76.85
14	370.00	F1398-077	1.91	0.14	0.00	77.56	0.00	0.05	0.03	0.02	0.02	0.01	0.00	79.73

*Total iron content expressed as FeO total

Table S4

The major elements as oxides with core depth in the Carajás BIF.

Depth (m)	Element oxide	SiO_2 (wt.%)	Al_2O_3	Fe_2O_3	FeO	MnO	MgO	CaO	Na_2O	K_2O	TiO_2	P_2O_5	LOI	Total
	Detection limit	0.01	0.01	0.01	0.01	0.01	0.01	0.01	0.01	0.01	0.01	0.001	0.01	-
74.00	F1398-003	34.17	0.09	64.24	0.10	0.03	0.04	0.03	0.02	<0.01	<0.01	0.023	2.08	100.82
81.00	F1398-007	35.90	0.06	60.76	0.44	0.02	0.04	0.03	0.02	0.01	<0.01	0.016	3.01	100.31
93.00	F1398-011	46.64	0.04	50.06	0.44	0.02	0.04	0.05	0.02	0.01	<0.01	0.044	1.83	99.19
100.00	F1398-014	38.91	0.01	59.69	0.78	0.02	0.03	<0.01	<0.01	0.01	<0.01	0.007	1.03	100.49
112.00	F1398-018	36.79	0.04	60.88	0.58	0.01	0.02	0.05	0.01	<0.01	<0.01	0.007	1.61	100.00
121.00	F1495-281	39.04	0.02	58.64	0.85	0.02	0.04	0.01	<0.01	<0.01	<0.01	0.007	1.47	100.09
130.00	F1398-025	44.56	0.05	53.73	1.44	0.02	0.04	0.03	0.01	<0.01	<0.01	0.016	0.46	100.36
142.00	F1398-032	42.25	0.02	57.12	0.51	0.02	0.03	0.02	0.01	<0.01	<0.01	0.004	0.51	100.49
156.00	F1515-087	49.50	0.10	49.46	0.77	0.02	0.03	0.02	0.01	<0.01	<0.01	0.017	0.59	100.52
170.00	F1515-089	57.86	0.08	38.98	1.38	0.04	0.03	0.02	0.01	<0.01	<0.01	0.010	1.65	100.06
181.00	F1398-036	43.11	<0.01	53.69	0.61	0.01	0.03	0.02	0.01	<0.01	<0.01	0.004	2.90	100.38
194.00	F1398-040	38.11	<0.01	58.37	3.13	0.01	0.03	0.02	0.01	<0.01	<0.01	0.005	1.45	101.14
205.00	F1398-043	34.99	0.02	62.88	1.73	0.01	0.03	0.03	0.02	<0.01	<0.01	0.002	0.79	100.50
220.00	F1398-049	45.85	0.01	50.61	2.08	0.02	0.03	0.02	0.03	<0.01	<0.01	0.009	0.85	99.51
232.00	F1515-102	44.97	0.05	52.03	1.12	0.03	0.02	0.02	<0.01	<0.01	<0.01	0.017	1.37	99.62
245.00	F1515-107	37.87	0.09	60.05	0.88	0.02	0.04	0.03	0.01	<0.01	0.01	0.015	1.05	100.07
260.00	F1515-110	38.79	0.04	59.02	1.01	0.02	0.03	0.02	<0.01	<0.01	<0.01	0.010	1.79	100.73
271.00	F1515-121	44.71	0.03	50.94	2.34	0.02	0.03	0.02	0.01	<0.01	<0.01	0.012	1.78	99.89
285.00	F1495-282	39.86	0.04	57.47	1.66	0.02	0.03	0.01	0.01	<0.01	<0.01	0.014	1.40	100.51
290.00	F1398-052	49.85	0.08	49.07	0.49	0.02	0.03	0.03	0.02	<0.01	<0.01	0.006	0.46	100.06
298.00	F1515-123	43.07	0.10	52.57	0.75	0.03	0.03	0.05	<0.01	0.01	0.02	0.058	2.68	99.36
305.00	F1051-123	48.19	0.25	48.08	2.84	0.02	0.13	0.02	0.01	0.01	0.01	0.023	0.36	99.95
312.00	F1398-058	40.19	0.11	56.34	1.95	0.02	0.07	0.02	0.01	0.01	0.01	0.012	1.20	99.94

320.00	F1398-059	42.69	0.64	54.24	1.09	0.04	0.39	0.01	<0.01	0.01	0.02	0.007	0.77	99.91
325.00	F1051-125	33.97	0.42	64.22	0.77	0.03	0.11	0.03	0.01	0.03	0.07	0.026	0.96	100.65
332.00	F1398-067	43.46	0.03	54.96	1.29	0.02	0.08	0.07	<0.01	0.01	<0.01	0.016	1.25	101.18
339.00	F1515-158	51.18	0.09	47.14	0.72	0.02	0.03	0.04	<0.01	0.01	0.01	0.015	0.78	100.03
347.00	F1515-140	47.49	0.03	51.21	0.92	0.02	0.04	0.02	<0.01	<0.01	<0.01	0.008	0.97	100.71
355.00	F1398-071	36.62	0.06	60.35	1.01	0.02	0.06	0.02	0.01	0.01	<0.01	0.008	1.91	100.08
363.00	F1051-126	39.48	0.25	58.24	1.28	0.03	0.05	0.02	<0.01	0.01	0.01	0.038	0.48	99.89
370.00	F1398-074	35.56	0.13	61.68	1.01	0.03	0.04	0.02	0.01	0.01	<0.01	0.011	1.18	99.68
380.00	F1398-080	39.93	0.02	58.95	0.34	0.01	0.03	0.02	0.01	<0.01	<0.01	0.003	0.54	99.86
384.00	F1398-081	46.18	0.03	52.74	0.28	0.01	0.03	0.02	<0.01	0.01	<0.01	0.007	0.53	99.84
396.00	F1515-159	57.75	0.05	40.73	0.84	0.02	0.03	0.04	<0.01	0.01	<0.01	0.014	0.46	99.94
402.00	F1051-131	43.45	0.01	54.45	1.70	0.02	0.05	0.02	0.01	0.01	<0.01	0.009	0.39	100.12
408.00	F1398-083	38.39	0.04	49.36	10.40	0.05	0.12	1.58	0.01	0.01	<0.01	0.008	0.37	100.34
413.00	F1515-218	36.75	0.10	55.43	3.85	0.03	2.07	0.27	<0.01	0.01	0.02	0.017	0.87	99.42
419.00	F1398-090	42.19	0.31	54.97	2.72	0.02	0.07	0.04	0.01	0.01	<0.01	0.007	0.11	100.46
425.00	F1398-094	39.71	0.25	48.50	8.52	0.04	0.27	0.86	0.01	0.03	0.01	0.008	0.29	98.50
436.00	F1051-144	42.73	0.01	40.45	8.82	0.22	1.31	2.41	<0.01	0.01	<0.01	0.021	3.14	99.12
446.00	F1398-110	44.73	0.07	41.95	7.95	0.09	0.14	2.96	0.02	<0.01	<0.01	0.012	1.58	99.50
455.00	F1515-243	41.83	0.01	39.77	13.65	0.08	1.52	1.45	<0.01	<0.01	<0.01	0.007	1.03	99.35
468.00	F1515-259	41.48	0.07	46.67	4.59	0.10	4.41	0.26	0.01	<0.01	<0.01	0.010	2.65	100.25
479.00	F1515-261	43.88	0.06	36.36	11.35	0.15	3.20	0.95	0.01	<0.01	<0.01	0.011	2.96	98.93
490.00	F1398-126	54.47	0.18	28.58	7.88	0.28	0.83	3.99	<0.01	0.01	<0.01	0.007	3.53	99.76
498.00	F1051-143	40.16	0.01	50.98	5.73	0.06	0.96	0.55	<0.01	0.01	<0.01	0.013	0.52	99.00
506.00	F1051-154	39.36	0.01	47.42	5.57	0.29	1.32	2.49	<0.01	<0.01	<0.01	0.011	3.45	99.92
515.00	F1398-134	40.25	0.05	46.25	6.87	0.09	2.06	2.09	0.01	0.01	<0.01	0.005	1.64	99.33
528.00	F1051-157	39.89	0.01	46.98	4.80	0.15	3.40	1.52	<0.01	0.01	<0.01	0.014	2.62	99.39

Table S5

Selected trace elements and relevant REY anomalies with core depth in the Carajás BIF.

Depth (m)	Element oxide	Rb (ppm)	Ba	Cr	V	Sc	Co	Th	U	Nb	Hf	Zr	Sr	Zn	Pb	Y	(Y/Ho)
	Detection limit	0.20	0.50	1.00	1.00	1.00	0.50	0.05	0.05	0.20	0.20	2.00	0.10	2.00	2.00	0.50	
70.00	F1398-003	0.50	9.30	2.00	3.00	1.00	7.50	0.07	0.26	<0.2	<0.2	2.00	0.10	21.0	7.00	2.60	43.33
81.00	F1398-007	0.20	3.90	5.00	8.00	1.00	2.00	0.42	0.28	0.20	<0.2	<2	<0.1	15.00	3.00	5.50	61.11
93.00	F1398-011	0.50	8.60	3.00	1.00	1.00	2.20	0.08	0.24	<0.2	<0.2	<2	2.70	32.0	5.00	2.90	58.00
100.00	F1398-014	0.40	9.70	4.00	2.00	1.00	1.50	0.08	0.20	0.20	<0.2	<2	1.10	3.00	5.00	1.60	80.00
112.00	F1398-018	0.40	9.90	4.00	3.00	1.00	1.70	0.08	0.39	<0.2	<0.2	<2	1.00	8.00	8.00	1.80	60.00
121.00	F1495-281	<0.2	3.30	9.00	1.00	<1	2.20	0.05	0.19	<0.2	<0.2	2.00	0.60	15.00	<2	2.70	45.00
174.00	F1398-025	0.40	4.10	2.00	4.00	1.00	1.40	0.11	0.18	<0.2	<0.2	<2	1.30	7.00	12.0	1.30	65.00
142.00	F1398-032	0.40	8.20	2.00	1.00	<1	3.60	0.22	0.16	<0.2	<0.2	<2	1.20	3.00	5.00	1.50	75.00
156.00	F1515-087	0.20	5.60	14.00	5.00	<1	0.60	<0.05	0.05	<0.2	<0.2	3.00	0.80	25.00	7.00	3.10	62.00
170.00	F1515-089	<0.2	8.40	14.00	2.00	<1	0.80	<0.05	0.06	<0.2	<0.2	2.00	0.70	58.00	<2	3.00	75.00
181.00	F1398-036	0.60	4.50	5.00	<1	<1	2.30	<0.05	0.17	<0.2	<0.2	<2	1.10	4.00	5.00	2.00	40.00
194.00	F1398-040	0.50	5.90	2.00	<1	<1	2.50	0.12	0.12	<0.2	<0.2	<2	0.50	4.00	6.00	1.70	56.67
205.00	F1398-043	0.60	9.20	4.00	1.00	<1	1.30	0.26	0.12	0.20	<0.2	<2	1.00	<2	8.00	1.40	70.00
220.00	F1398-049	0.50	7.20	7.00	9.00	<1	1.60	0.17	0.24	0.20	<0.2	<2	0.80	8.00	7.00	2.50	41.67
232.00	F1515-102	0.50	7.20	7.00	9.00	<1	1.60	0.17	0.24	0.20	<0.2	<2	0.80	8.00	7.00	2.50	46.00
245.00	F1515-107	0.30	3.80	15.00	9.00	<1	1.50	0.13	<0.05	<0.2	<0.2	3.00	0.70	34.00	4.00	2.30	72.50
260.00	F1515-110	0.40	4.40	11.00	7.00	<1	1.20	0.34	0.10	0.30	<0.2	5.00	0.70	10.00	6.00	2.90	58.00
271.00	F1515-121	0.30	4.60	8.00	6.00	<1	1.30	0.06	<0.05	<0.2	<0.2	3.00	0.60	38.00	7.00	2.90	53.33
285.00	F1495-282	0.30	3.50	12.00	3.00	<1	1.30	0.08	0.05	<0.2	<0.2	2.00	0.60	20.00	6.00	1.60	52.50
290.00	F1398-052	0.60	10.2	3.00	1.00	<1	1.30	0.27	0.24	0.30	<0.2	3.00	1.60	4.00	5.00	3.50	43.75
298.00	F1515-123	0.40	5.10	27.00	33.00	1.00	2.90	0.23	0.15	0.40	<0.2	5.00	0.80	82.00	7.00	12.90	61.43
305.00	F1051-123	1.00	8.80	21.00	7.00	1.00	3.00	0.27	0.37	0.60	<0.2	6.00	1.90	22.00	7.00	5.30	29.44

312.00	F1398-058	0.40	6.20	4.00	1.00	<1	3.20	0.31	0.19	0.50	<0.2	5.00	0.70	5.00	8.00	5.20	28.89
320.00	F1398-059	0.60	5.80	3.00	12.00	<1	4.30	1.41	0.48	1.00	0.60	25.00	0.80	22.00	6.00	6.40	27.83
325.00	F1051-125	2.10	18.10	3.00	11.00	1.00	1.60	0.44	0.12	1.00	0.40	17.00	3.90	20.00	12.00	5.70	35.63
331.00	F1398-067	0.40	5.70	1.00	9.00	<1	2.20	0.11	0.16	<0.2	<0.2	2.00	1.00	5.00	6.00	4.20	42.00
339.00	F1515-158	0.70	9.60	19.00	3.00	<1	1.20	0.27	0.09	0.20	<0.2	3.00	0.80	40.00	6.00	4.20	42.00
347.00	F1515-140	0.30	2.90	12.00	1.00	<1	1.10	<0.05	0.05	<0.2	<0.2	3.00	0.50	16.00	4.00	2.00	66.67
355.00	F1398-071	0.30	3.10	11.00	1.00	<1	4.20	0.08	0.18	<0.2	<0.2	<2	0.50	6.00	6.00	1.20	60.00
363.00	F1051-126	1.20	9.90	16.00	4.00	<1	1.80	0.44	0.13	0.50	0.20	9.00	1.80	19.00	<2	4.10	31.54
370.00	F1398-074	0.70	5.10	<1	5.00	<1	7.90	0.18	0.27	0.40	<0.2	<2	2.00	5.00	8.00	1.60	32.00
380.00	F1398-080	0.40	5.00	2.00	6.00	<1	5.00	0.09	0.24	0.20	<0.2	<2	1.60	10.00	5.00	3.30	41.25
384.00	F1398-081	0.50	4.70	4.00	2.00	<1	5.30	0.09	0.19	0.20	<0.2	<2	1.80	12.0	10.0	3.70	37.00
396.00	F1515-159	0.50	7.20	18.00	2.00	<1	1.40	0.09	0.06	<0.2	<0.2	3.00	0.90	35.00	7.00	2.70	67.50
402.00	F1051-131	0.50	6.60	17.00	4.00	<1	1.70	<0.05	<0.05	<0.2	<0.2	2.00	1.50	18.00	6.00	3.00	75.00
408.00	F1398-083	0.60	6.30	2.00	4.00	<1	4.70	0.05	0.23	<0.2	<0.2	<2	9.40	6.00	10.00	2.40	48.00
413.00	F1515-218	1.10	8.10	3.00	4.00	<1	1.80	0.42	0.20	0.50	0.20	7.00	1.90	23.00	5.00	4.00	57.14
419.00	F1398-090	0.60	6.20	4.00	3.00	<1	3.80	0.12	0.22	0.20	<0.2	12.00	2.40	9.00	6.00	3.70	37.00
425.00	F1398-094	2.50	9.00	3.00	5.00	<1	3.30	0.51	0.23	0.50	<0.2	5.00	7.20	7.00	10.00	1.70	34.00
436.00	F1051-144	0.30	6.20	13.00	3.00	<1	2.60	<0.05	<0.05	<0.2	<0.2	2.00	3.60	12.00	3.00	3.70	74.00
447.00	F1398-110	0.70	10.4	4.00	2.00	1.00	6.40	0.10	0.32	0.20	<0.2	<2	18.3	5.00	11.0	2.40	80.00
455.00	F1515-243	0.30	3.00	13.00	2.00	<1	1.70	<0.05	0.06	<0.2	<0.2	2.00	3.20	14.00	2.00	1.40	70.00
468.00	F1515-259	0.50	4.90	4.00	<1	<1	1.90	0.41	0.06	0.20	<0.2	3.00	1.50	11.00	4.00	1.20	40.00
479.00	F1515-261	0.40	4.00	4.00	1.00	<1	2.60	0.17	<0.05	<0.2	<0.2	2.00	2.90	8.00	<2	1.00	50.00
490.00	F1398-126	0.40	6.80	3.00	6.00	1.00	5.10	0.11	0.19	0.20	<0.2	<2	20.2	11.0	5.00	2.20	44.00
498.00	F1051-143	0.60	9.70	9.00	4.00	<1	3.20	<0.05	<0.05	<0.2	<0.2	2.00	2.10	20.00	7.00	2.70	54.00
506.00	F1051-154	0.40	4.90	16.00	3.00	<1	3.60	<0.05	<0.05	<0.2	<0.2	2.00	4.00	19.00	5.00	2.50	62.50
515.00	F1398-134	0.60	9.40	1.00	3.00	1.00	3.40	0.34	0.36	0.40	<0.2	2.00	12.0	5.00	8.00	2.00	50.00

528.00	F1051-157	0.50	6.40	3.00	3.00	<1	5.20	0.61	<0.05	<0.2	<0.2	2.00	2.70	17.00	5.00	2.90	41.43				

***Table S5** (Continued)*

Depth (m)	Element	La	Ce	Pr	Nd	Sm	Eu	Gd	Tb	Dy	Ho	Er	Tm	Yb	Lu	∑REE	$(La/La^*)_{SN}$	$(La/Yb)_{SN}$	$(Sm/Yb)_{SN}$	$(Ce/Ce^*)_{SN}$	$(Pr/Pr^*)_{SN}$	$(Eu/Eu^*)_{SN}$
	Detection limit	0.50	0.50	0.03	0.10	0.03	0.03	0.05	0.01	0.05	0.01	0.03	0.01	0.03	0.01	-	-	-	-	-	-	-
70.00	F1398-003	1.70	2.70	0.25	1.00	0.27	0.16	0.28	0.06	0.38	0.06	0.20	0.03	0.16	0.03	7.28	1.72	0.78	0.86	0.93	0.89	2.72
81.00	F1398-007	3.10	4.00	0.41	1.50	0.28	0.30	0.43	0.06	0.42	0.09	0.32	0.04	0.22	0.04	11.21	1.60	1.04	0.65	0.79	0.98	3.89
93.00	F1398-011	2.60	3.30	0.30	0.90	0.25	0.14	0.21	0.04	0.19	0.05	0.13	0.03	0.12	0.02	8.28	1.39	1.60	1.06	0.81	1.00	2.88
100.00	F1398-014	1.70	2.70	0.26	0.80	0.16	0.19	0.24	0.03	0.16	0.02	0.08	0.01	0.10	<0,01	6.45	1.08	1.25	0.81	0.92	1.02	4.38
112.00	F1398-018	1.80	2.80	0.31	1.20	0.26	0.19	0.23	0.04	0.23	0.03	0.11	0.02	0.09	0.01	7.32	1.36	1.48	1.47	0.86	0.99	3.66
121.00	F1495-281	1.70	2.60	0.33	1.40	0.41	0.20	0.52	0.07	0.46	0.06	0.18	0.03	0.08	0.01	8.05	1.51	1.57	2.60	0.80	1.01	2.00
130.00	F1398-025	0.90	1.10	0.11	0.40	0.08	0.05	0.06	0.02	0.09	0.02	0.06	0.02	0.08	0.01	3.00	1.71	0.83	0.51	0.77	0.97	3.39
142.00	F1398-032	1.60	2.00	0.16	0.40	0.11	0.13	0.17	0.02	0.06	0.02	0.06	0.01	0.07	0.01	4.82	1.36	1.69	0.80	0.84	0.98	4.28
156.00	F1515-087	3.20	3.50	0.38	1.30	0.23	0.23	0.20	0.03	0.32	0.05	0.21	0.02	0.22	0.02	9.91	1.60	1.07	0.53	0.69	1.05	5.05
170.00	F1515-089	1.60	1.70	0.17	0.70	0.11	0.07	0.17	0.02	0.20	0.04	0.11	0.03	0.19	0.03	5.14	2.54	0.62	0.29	0.70	0.92	2.30
181.00	F1398-036	1.30	1.70	0.18	0.70	0.11	0.15	0.19	0.03	0.09	0.05	0.12	<0,01	0.06	0.02	4.70	1.71	1.60	0.93	0.78	0.97	4.58
194.00	F1398-040	1.60	2.10	0.19	0.70	0.19	0.18	0.15	0.02	0.10	0.03	0.11	<0,01	0.07	0.01	5.45	1.80	1.69	1.38	0.83	0.92	5.02
205.00	F1398-043	1.40	1.30	0.10	0.20	0.06	0.07	0.09	0.01	0.06	0.02	0.04	<0,01	0.09	0.01	3.45	1.65	1.15	0.34	0.68	1.02	4.30
220.00	F1398-049	1.70	2.60	0.27	0.90	0.25	0.18	0.30	0.03	0.19	0.06	0.17	0.02	0.10	0.01	6.78	1.15	1.25	1.27	0.87	1.03	3.05
232.00	F1515-102	1.80	2.20	0.27	1.10	0.33	0.14	0.29	0.05	0.32	0.05	0.18	0.01	0.09	0.01	6.84	1.76	1.48	1.86	0.71	1.02	2.13
245.00	F1515-107	2.90	3.50	0.35	1.20	0.14	0.14	0.18	0.02	0.18	0.04	0.14	0.03	0.17	0.03	9.02	1.58	1.26	0.42	0.76	1.00	4.06
260.00	F1515-110	2.10	3.60	0.30	1.00	0.18	0.18	0.22	0.03	0.16	0.05	0.19	0.02	0.18	0.03	8.24	1.28	0.86	0.51	1.02	0.91	4.19
271.00	F1515-121	3.50	4.30	0.36	1.10	0.12	0.09	0.11	0.01	0.07	0.03	0.07	0.01	0.07	0.01	9.85	1.60	3.69	0.87	0.82	0.94	3.69
285.00	F1495-282	1.80	3.10	0.41	1.60	0.38	0.17	0.47	0.07	0.35	0.04	0.16	0.01	0.11	0.01	8.68	1.05	1.21	1.76	0.83	1.08	1.86
290.00	F1398-052	2.40	4.30	0.47	1.50	0.31	0.22	0.32	0.05	0.30	0.08	0.24	0.02	0.18	0.02	10.41	0.88	0.98	0.88	0.93	1.08	3.27
298.00	F1515-123	3.60	4.70	0.69	3.00	0.66	0.37	1.02	0.12	0.88	0.21	0.64	0.11	0.57	0.08	16.65	1.64	0.47	0.59	0.69	1.06	2.03

305.00	F1051-123	10.30	15.30	1.86	7.20	1.42	0.28	1.07	0.13	0.81	0.18	0.53	0.12	0.57	0.07	39.84	1.30	1.33	1.27	0.80	1.04	1.07
312.00	F1398-058	3.20	5.70	0.76	3.00	0.62	0.18	0.94	0.14	0.87	0.18	0.46	0.04	0.33	0.03	16.45	1.03	0.72	0.95	0.84	1.08	1.06
320.00	F1398-059	10.80	24.20	2.54	8.70	1.52	0.19	1.27	0.19	1.02	0.23	0.60	0.09	0.60	0.08	52.03	0.81	1.33	1.29	1.07	1.03	0.64
325.00	F1051-125	4.40	5.70	0.72	2.50	0.62	0.20	0.72	0.12	0.69	0.16	0.56	0.10	0.67	0.08	17.24	1.19	0.48	0.47	0.73	1.12	1.39
331.00	F1398-067	1.80	1.70	0.22	1.00	0.26	0.20	0.47	0.05	0.33	0.10	0.29	0.02	0.19	0.03	6.66	2.99	0.70	0.70	0.59	0.98	2.51
339.00	F1515-158	4.50	6.70	0.63	2.30	0.56	0.32	0.68	0.07	0.36	0.10	0.18	0.05	0.11	0.02	16.58	1.50	3.02	2.59	0.89	0.94	2.40
347.00	F1515-140	5.30	6.30	0.57	1.70	0.23	0.12	0.19	0.04	0.18	0.03	0.05	0.03	0.08	0.03	14.85	1.49	4.89	1.46	0.78	1.00	2.70
355.00	F1398-071	1.60	1.60	0.19	1.00	0.10	0.07	0.13	0.02	0.16	0.02	0.11	<0,01	0.07	<0,01	5.07	7.54	1.69	0.73	0.63	0.87	2.82
363.00	F1051-126	3.10	4.10	0.53	2.00	0.47	0.15	0.59	0.11	0.66	0.13	0.41	0.06	0.30	0.04	12.65	1.31	0.76	0.80	0.73	1.09	1.31
370.00	F1398-074	1.60	2.30	0.32	1.20	0.32	0.08	0.36	0.02	0.28	0.05	0.15	0.01	0.10	0.01	6.80	1.10	1.18	1.63	0.74	1.13	1.10
380.00	F1398-080	1.80	3.30	0.42	1.60	0.46	0.11	0.67	0.05	0.43	0.08	0.28	0.01	0.12	0.01	9.34	0.98	1.11	1.95	0.88	1.07	0.90
384.00	F1398-081	1.90	2.70	0.45	1.70	0.46	0.18	0.66	0.07	0.59	0.10	0.29	0.02	0.17	0.02	9.31	0.95	0.83	1.37	0.67	1.21	1.48
396.00	F1515-159	2.40	3.90	0.37	1.20	0.25	0.24	0.29	0.05	0.16	0.04	0.09	0.03	0.08	0.01	9.11	1.14	2.21	1.59	0.94	0.99	4.14
402.00	F1051-131	1.50	2.40	0.26	1.00	0.21	0.12	0.30	0.04	0.35	0.04	0.15	0.04	0.12	0.01	6.54	1.34	0.92	0.89	0.88	0.99	2.17
408.00	F1398-083b	1.60	2.60	0.33	1.40	0.21	0.13	0.40	0.06	0.23	0.05	0.12	0.01	0.07	0.01	7.22	1.42	1.69	1.52	0.82	1.01	1.95
413.00	F1515-218	3.60	3.90	0.35	1.20	0.17	0.13	0.29	0.04	0.29	0.07	0.22	0.01	0.28	0.04	10.59	1.96	0.95	0.31	0.73	0.94	2.59
419.00	F1398-090b	2.60	4.60	0.55	2.10	0.53	0.18	0.77	0.08	0.57	0.10	0.38	0.01	0.20	0.01	12.68	1.08	0.96	1.35	0.89	1.04	1.28
425.00	F1398-094	1.30	2.00	0.20	0.80	0.16	0.08	0.34	0.06	0.13	0.05	0.14	0.03	0.08	0.03	5.40	1.64	1.20	1.02	0.89	0.93	1.46
436.00	F1051-144	2.40	3.30	0.34	1.30	0.23	0.16	0.28	0.06	0.20	0.05	0.13	0.05	0.12	0.04	8.66	1.62	1.48	0.97	0.82	0.96	2.92
447.00	F1398-110	1.60	2.10	0.20	0.60	0.10	0.10	0.16	0.02	0.13	0.03	0.09	0.02	0.09	0.01	5.25	1.29	1.31	0.56	0.82	1.03	3.54
455.00	F1515-243	3.00	2.90	0.24	0.60	0.06	0.06	0.10	<0.01	<0.05	0.02	0.03	0.01	0.10	0.02	7.14	1.70	2.21	0.30	0.69	1.00	3.44
468.00	F1515-259	1.20	1.60	0.16	0.60	0.12	0.08	0.15	0.01	0.08	0.03	0.10	0.03	0.08	<0.01	4.24	1.66	1.11	0.76	0.81	0.96	2.75
479.00	F1515-261	1.50	2.00	0.18	0.60	0.07	0.04	0.09	<0.01	<0.05	0.02	0.05	0.03	0.10	0.01	4.69	1.52	1.11	0.36	0.84	0.95	2.32
490.00	F1398-126	1.70	2.70	0.29	1.10	0.20	0.13	0.30	0.05	0.27	0.05	0.13	0.03	0.14	0.01	7.10	1.32	0.90	0.73	0.88	0.99	2.40
498.00	F1051-143	2.40	3.40	0.30	1.00	0.22	0.12	0.28	0.04	0.19	0.05	0.11	0.05	0.06	0.04	8.26	1.46	2.95	1.86	0.88	0.94	2.23
506.00	F1051-154	2.20	3.10	0.30	1.20	0.25	0.12	0.27	0.02	0.15	0.04	0.09	0.03	0.05	0.01	7.83	1.85	3.25	2.54	0.85	0.91	2.16

515.00	F1398-134	2.60	3.40	0.29	0.90	0.17	0.14	0.20	0.03	0.17	0.04	0.08	0.03	0.18	0.01	8.24	1.50	1.07	0.48	0.85	0.95	3.52
528.00	F1051-157	2.40	3.40	0.36	1.30	0.23	0.13	0.43	0.05	0.27	0.07	0.13	0.04	0.08	0.02	8.91	1.38	2.21	1.46	0.82	1.01	1.80

Table S6

Sm-Nd isotopic of the Carajás jaspilites and associated rocks.

Sample	Lithology	Depth (m)	Sm (ppm)	Nd (ppm)	$^{147}Sm/^{144}Nd$	$^{143}Nd/^{144}Nd \pm 2E$	Age (Ma)	$\varepsilon_{Nd}(0)$	$\varepsilon_{Nd}(t)$	fSm/Nd	T_{DM} (Ga)	Sources
F1398 drill hole BIF												
F1398-007	Type I BIF	81.00	0.192	1.015	0.1145	0.511118 ± 8	2745	-29.65	-0.60	-0.42	2.96	This study
F1398-014	Type I BIF	100.00	0.184	0.985	0.1131	0.511335 ± 7	2745	-25.42	4.14	-0.42	2.60	This study
F1495-251	Type I BIF	121.00	0.070	0.473	0.0898	0.510698 ± 17	2745	-37.83	-0.07	-0.54	2.91	This study
F1398-032	Type I BIF	142.00	0.092	0.637	0.0875	0.510688 ± 15	2745	-38.03	0.56	-0.55	2.84	This study
F1515-089	Type I BIF	170.00	0.127	0.703	0.1094	0.511332 ± 19	2745	-25.48	5.40	-0.44	2.49	This study
F1398-049	Type I BIF	220.00	0.179	1.256	0.0862	0.510683 ± 14	2745	-38.14	0.91	-0.56	2.82	This study
F1515-110	Type I BIF	260.00	0.158	1.213	0.0786	0.510579 ± 11	2745	-40.16	1.59	-0.60	2.77	This study
F1398/052	Type I BIF	290.00	0.352	1.878	0.1134	0.51139 ± 39	2745	-24.3	5.13	-0.42	2.53	This study
F1051-123	Type II BIF	305.00	0.313	1.996	0.0948	0.510746 ± 11	2745	-36.90	-0.90	-0.52	2.95	This study
F1398/059	Type II BIF	320.00	0.231	0.971	0.1441	0.511433 ± 9	2745	-23.51	-4.97	-0.27	3.60	This study
F1398-067	Type I BIF	331.00	0.221	1.085	0.1234	0.511451 ± 3	2745	-23.15	2.77	-0.37	2.70	This study
F1398-071	Type I BIF	355.00	0.327	1.690	0.1169	0.511389 ± 6	2745	-24.4	3.86	-0.41	2.62	This study
F1051-126	Type II BIF	363.00	0.671	3.089	0.1314	0.511376 ± 14	2745	-24.62	-1.55	-0.33	3.11	This study
F1398/081	Type II BIF	384.00	0.363	1.398	0.1568	0.51172 ± 9	2745	-17.9	-3.84	-0.20	3.48	This study
F1398-083	Type I BIF	408.00	0.258	1.095	0.1424	0.511674 ± 12	2745	-18.80	0.39	-0.28	2.94	This study
F1398-094	Type II BIF	425.00	0.243	0.923	0.1588	0.511774 ± 5	2745	-16.85	-3.49	-0.19	3.46	This study

F1398/110	Type I BIF	447.00	0.038	0.257	0.0886	0.510637 ± 21	2745	-39.0	-0.84	-0.55	2.92	This study
F1515-259	Type I BIF	468.00	0.053	0.274	0.1164	0.511196 ± 24	2745	-28.13	0.25	-0.41	2.89	This study
F1051-143	Type I BIF	498.00	0.155	0.889	0.1052	0.511065 ± 12	2745	-30.69	1.67	-0.47	2.78	This study
F1398-134	Type I BIF	515.00	0.067	0.399	0.1009	0.511038 ± 15	2745	-31.20	2.65	-0.49	2.71	This study
F1051-157	Type I BIF	528.00	0.088	0.485	0.1098	0.511040 ± 10	2745	-31.17	-0.45	-0.44	2.94	This study
Associated rocks												
AM-02	Black-shale	-	0.744	3.926	0.11453	0.511309 ± 5	2710	-	2.82	-	2.82	Cabral et al. 2013
AM-03	Black-shale	-	1.480	7.373	0.12135	0.511247 ± 5	2710	-	−0.80	-	3.12	Cabral et al. 2013
AM-04A	Black-shale	-	3.518	20.17	0.10546	0.511015 ± 5	2710	-	0.24	-	2.99	Cabral et al. 2013
AM-09	Black-shale	-	1.643	9.400	0.10565	0.511060 ± 5	2710	-	1.06	-	2.93	Cabral et al. 2013
AM-11	Black-shale	-	2.642	15.33	0.10418	0.511034 ± 3	2710	-	1.06	-	2.93	Cabral et al. 2013
AM-21-2	Black-shale	-	4.975	26.94	0.11163	0.511157 ± 4	2710	-	0.86	-	2.96	Cabral et al. 2013
AM-21-3	Black-shale	-	2.952	16.03	0.11134	0.511152 ± 3	2710	-	0.86	-	2.96	Cabral et al. 2013
AM-21-5	Black-shale	-	2.391	13.13	0.11008	0.511122 ± 4	2710	-	0.71	-	2.97	Cabral et al. 2013
AM-21-6	Black-shale	-	2.335	12.96	0.10891	0.511093 ± 5	2710	-	0.56	-	2.98	Cabral et al. 2013
AM-21-7	Black-shale	-	1.748	9.872	0.10701	0.511140 ± 5	2710	-	2.15	-	2.85	Cabral et al. 2013
AM-21-8	Black-shale	-	2.866	16.11	0.10755	0.511085 ± 3	2710	-	0.88	-	2.95	Cabral et al. 2013
AM 21-9	Black-shale	-	2.928	16.11	0.10988	0.511103 ± 3	2710	-	0.41	-	2.99	Cabral et al. 2013
F1398/057	Basalt	295.00	6.961	36.252	0.1161	0.511100 ± 6	2749	-30.0	-1.53	-0.41	3.02	Martins et al. 2017
F1398/101	Basalt	420.80	5.365	23.04	0.1408	0.511416 ± 27	2749	-23.8	-4.11	-0.28	3.36	Martins et al. 2017
F1398/151	Basalt	557.00	3.602	14.525	0.1499	0.511638 ± 14	2749	-19.5	-2.99	-0.24	3.31	Martins et al. 2017
F1279/Z	Basalt	70.00	3.670	16.601	0.1337	0.511396 ± 23	2749	−24.22	−1.95	-0.32	3.16	Martins et al. 2017

REFERENCES

Almeida, J.A.C., Dall'Agnol, R., Dias, S.B., Althoff, F.J., 2010. Origin of the archean leucogranodiorite-granite suites: evidence from the Rio Maria. Lithos 120, 235–257.

Almeida, J.A.C., Dall'Agnol, R., Oliveira, M.A., Macambira, M.J.B., Pimentel, M.M., Rämö, O.T., Guimarães, F.V., Leite, A.A.S., 2011. Zircon geochronology and geochemistry of the TTG suites of the Rio Maria granite-greenstone terrane: implications for the growth of the Archean crust of Carajás Province, Brazil. Precambr. Res. 187, 201–221.

Almeida, J.A.C., Dall'Agnol, R., Leite, A.A.S., 2013. Geochemistry and zircon geochronology of the Archean granite suites of the Rio Maria granite-greenstone terrane, Carajás Province, Brazil. J. S. Am. Earth Sci. 42, 103–126.

Althoff, F.J., Barbey, P., Boullier, A.M., 2000. 2.8-3.0 Ga plutonism and deformation in the SE Amazonian craton: the Archean granitoids of Marajoara (Carajás Mineral province, Brazil). Precambr. Res. 104, 187–206.

Araújo, O.J.B., Maia, R.G.N., 1991, Programa levantamentos geológicos básicos do Brasil. Projeto especial mapas de recursos minerais, de solos e de vegetação para a área do Programa Grande Carajás: Subprojeto Recursos Minerais, Serra dos Carajás, Folha SB. 22-Z-A: Brasília, DNPM/CPRM, 152 p.

Araújo, R., Nogueira, A., 2019. Serra sul diamictite of the Carajás Basin (Brazil): a paleoproterozoic glaciation on the amazonian craton. Geology 47 (12), 1166–1170.

Araújo, O.J.B., Maia, R.G.N., João, X.S.J., and Costa, J.B.S., 1988, A megaestruturação arqueana da folha Serra dos Carajás: Congresso Latino-Americano de Geologia, 7th, Belém, Anais, vol. 1, p. 324–328.

Araújo Filho, R., Nogueira, A.C.R., Araújo, R.N., 2020. New stratigraphic proposal of a Paleoproterozoic siliciclastic succession: implications for the evolution of the Carajás Basin, Amazonian craton, Brazil. J. S. Am. Earth Sci. 102, 102665.

Beisiegel, V.R., Bernardelli, A.L., Drummond, N.F., Ruff, A.W., Tremaine, J.W. 1973. Geologia e Recursos Minerais da Serra dos Carajás. Revista Brasileira de Geociências, 3: 215-242 (in Portuguese).

Dall'Agnol, R., Oliveira, M.A., Almeida, J.A.C., Althoff, F.J., Leite, A.A.S., Oliveira, D.C., Barros, C.E.M., 2006. Archean and Paleoproterozoic granitoids of the Carajás Metallogenic Province, eastern Amazonian craton. Symposium on Magmatism, Crustal Evolution, and Metallogenesis of the Amazonian Craton, Abstracts Volume and Field Trips Guide (150 pp.).

DOCEGEO – Rio Doce Geologia e Mineração, 1988. Revisão Litoestratigráfica da Província Mineral de Carajás. 35 Congresso Brasileiro de Geologia, Belém, Brasil, Anais, Sociedade Brasileira de Geologia, pp. 11–59 (in Portuguese).

Ferreira Filho, C.F., Cançado, F., Correa, C., Macambira, E.M.B., Siepierski, L., Brod, T.C.J., 2007. Mineralizações estratiformes de EGP-Ni associadas a complexos acamadados em Carajás: os exemplos de Luanga e Serra da Onça. Publitec Gráfica & Editora, Contribuições à Geologia da Amazônia 5, 01–14 (in Portuguese).

Holdsworth, R.E., Pinheiro, R.V.L., 2000. The anatomy of shallow crustal transpressional structures: insights from the Archean Carajás fault zone, Amazon, Brazil. J. Struct. Geol. 22, 1105–1123.

Lafon, J.M., Macambira, M.J.B., Pidgeon, R.T., 2000. Zircon U-Pb SHRIMP dating of Neoarchean magmatism in the southwestern part of the Carajás Province (eastern Amazonian Craton, Brazil). In: 30th International Geological Congress, Abstract Volume, CD-ROM.

Machado, N., Lindenmayer, Z.G., Krogh, T.E., Lindenmayer, D., 1991. U–Pb geochronology of Archean magmatism and basement reactivation in the Carajás area, Amazon shield, Brazil. Precambrian Research 49, 329–354.

Monteiro, L.V.S., Xavier, R.P., Souza Filho, C.R., Moreto, C.P.N., 2014. Metalogenia da Província Carajás. In: -Metalogenia das Províncias Tectônicas Brasileiras‖. Serviço geológico do Brasil- CPRM. 1 ed, 50p (in Portuguese).

Moreto, C.P.N., Monteiro, L.V.S., Xavier, R.P., Creaser, R.A., DuFrane, S.A., Melo, G.H.C., Delinardo da Silva, M.A., Tassinari, C.C.G., Sato, K., 2015. Timing of multiple hydrothermal events in the iron oxide–copper–gold deposits of the Southern Copper Belt, Carajás Province, Brazil. Miner. Deposita 50, 517–546.

Oliveira, M.A., Dall'Agnol, R., Althoff, F.J., Leite, A.A.S., 2009. Mesoarchean sanukitoid rocks of the Rio Maria granite–greenstone terrane, Amazonian craton, Brazil. J. S. Am. Earth Sci. 27, 146–160.

Oliveira, M.A., Dall'Agnol, R., Almeida, J.A.C., 2011. Petrology of the Mesoarchean Rio Maria suit and the discrimination of sanukitoid series. Lithos 137, 192–209.

Pidgeon, R., Macambira, M.J.B., Lafon, J.M., 2000. Th-U-Pb isotopic systems and internal structures from an enderbite from the Pium Complex, Carajás Province, Brazil: evidence for the ages of granulite facies metamorphism and the protolith of the enderbite. Chem. Geol. 166, 159–171.

Pinheiro, R.V.L., Holdsworth, R.E., 1997. Reactivation of Archean strike-slip fault systems, Amazon region, Brazil. J. Geol. Soc. 154, 99–103.

Rosière, C.A., Baars, F.J., Seoane, J.C.S., Lobato, L.M., da Silva, L.L., de Souza, S.R.C., Mendes, G.E., 2006. Structure and iron mineralization of the Carajás Province. Appl. Earth Sci. 115, 126–133.

Rossignol, C., Rego, E.S., Narduzzi, F., Teixeira, L., Ávila, J.N., Silva, M.A.L., Lana, C., Philippot, P., 2020. Stratigraphy and geochronological constraints of the Serra Sul Formation (Carajás Basin, Amazonian Craton, Brazil). Precambr. Res. 351, 105981. https://doi.org/10.1016/j.precamres.2020.105981.

Souza, Z.S., Potrel, H., Lafon, J.M., Althoff, F.J., Pimentel, M.M., Dall'Agnol, R., Oliveira, C.G., 2001. Nd, Pb and Sr isotopes of the Identidade Belt, an Archaean greenstone belt of the Rio Maria region (Carajás Province, Brazil): implications for the Archaean geodynamic evolution of the Amazonian Craton. Precambr. Res. 109, 293–315.

Teixeira, W., Hamilton, M.A., Girardi, V.A.V., Faleiros, F.M., Ernst, R.E., 2018. U-Pb baddeleyite ages of key dyke swarms in the Amazonian Craton (Carajás/Rio Maria and Rio Apa areas): tectonic implications for events at 1880, 1110 Ma, 535 Ma and 200 Ma. Precambrian Res, 329, 138-155. https://doi.org/10.1016/j.precamres.2018.02.008.

Vasquez, M.L., Carvalho, J.M.A., Sousa, C.S., Ricci, P.S.F., Macambira, E.M.B., Costa, L.T. R., 2008. Mapa Geológico do Pará em SIG. Brazilian Geological Survey – CPRM.

CAPÍTULO 6 – CONSIDERAÇÕES FINAIS

6. CONSIDERAÇÕES FINAIS

A sequência vulcanossedimentar do Grupo Grão-Pará, localizada na porção norte da Província Mineral de Carajás, é a principal sequência da Bacia Carajás. A bacia é preenchida inicialmente por uma espessa camada de rochas vulcânicas, associada ao vulcanismo Parauapebas, seguida pelas formações ferríferas bandadas de Carajás. Tais rochas possibilitam o acesso às condições ambientais e geográficas vigentes durante o Neoarqueano (~2.75 Ga) e aos processos tectônicos associados à formação da bacia. Neste estudo, ambos os aspectos foram investigados a partir de análises de dados petrográficos e geoquímicos de elementos maiores e traços, bem como a composição isotópica de Nd e Fe nas amostras das FFBs de Carajás. Além disso, estudos paleomagnéticos foram realizados nas rochas vulcânicas máficas da Formação Parauapebas no intuito de reconstruir as condições paleogeográficas durante a formação da bacia. Os dados obtidos permitiram as seguintes observações:

I. As FFBs de Carajás são formadas por bandas alternadas, milimétricas a centimétricas, de quartzo cripto- a microcristalino (chert e/ou jaspe) e óxidos de ferro (geralmente hematita). O jaspe é uma variedade de chert contendo inclusões microscópicas de hematita que lhe conferem a cor vermelha. Estruturas primárias são comumente observadas em todo pacote sedimentar, por exemplo: bandamento, *microflames, scour-and-fill*, *pinch-and-swell* e esferulitos.

II. De maneira geral, as FFBs estudadas destacam-se pela pureza, sendo formadas quase que exclusivamente por SiO_2 + Fe_2O_3 total (96,40 a 99,90 %). Além disso, os baixos conteúdos de Al_2O_3 (<1,00 %), TiO_2 (<0,01 %) e HFSE (p.ex., Zr, Hf e Th) (<1 ppm) em boa parte das amostras estudadas também indica um ambiente deposicional livre de detritos. Possuem, relativo aos valores do PAAS, leve fracionamento nos elementos terras raras mais ítrio (ETR + Y) com algumas amostras apresentando enriquecimento nos pesados em relação aos leves, enquanto outras mostraram a tendência inversa (La/Yb_{PAAS} = 0,47–4,89 e Sm/Yb_{PAAS} = 0,36–2,60). Os padrões de ETR + Y para a maioria das amostras também mostram anomalia

positiva leve de La, ausência de anomalia negativa verdadeira de Ce e anomalia positiva acentuada de Eu (Eu/Eu $_{PAAS}$ = 1,86–5,05) (Fig. 13). Tais características indicam a entrada significativa de fluidos hidrotermais de alta temperatura (> 250 °C) e um estado não oxidado da água do mar durante a deposição dos jaspilitos. No entanto, a presença de anomalias negativas verdadeiras de Ce em parte do pacote de jaspilitos pode sugerir a ocorrência precoce de oxigênio ou, alternativamente, microambientes oxigenados ~250 milhões de anos antes do Grande Evento de Oxidação. Os resultados ainda indicam que fluidos hidrotermais quentes a partir de ventes submarinas misturados com a água do mar, juntamente com o fluxo derivado da crosta máfica subjacente, estiveram envolvidos na precipitação dos jaspilitos.

III. Os valores de $\delta^{56}Fe$ (razão $^{56}Fe/^{54}Fe$) para as FFBs de Carajás são estritamente positivos com uma média de +1,34 ± 0,08 ‰ (Fig. 13), sendo um dos valores mais altos já medidos em FFBs arqueanas (Johnson et al., 2003, 2008; Rouxel et al., 2005; Konhauser et al., 2017). Tais valores indicam a entrada significativa de material rico no componente pesado dos isótopos de Fe (^{56}Fe) na água do mar contemporânea a precipitação das FFBs. Neste contexto, os fluidos hidrotermais quentes gerados a partir de ventes submarinas seriam a fonte mais provável desse material. Além disso, os valores de $\delta^{56}Fe$ para as amostras ricas em hematitas primárias variam ao longo do pacote de jaspilitos (+1,10 a +1,90 ‰), o que indica que a composição isotópica de Fe variou durante o período de deposição das FFBs de Carajás (< 20 Ma). Esta variação corrobora com a hipótese de um estado não estacionário do ciclo do Fe durante o arqueano com concentrações variáveis de Fe causadas pelo efeito competitivo da precipitação do óxido de Fe e fornecimento de Fe oriundo de fontes hidrotermais (Rouxel et al., 2005).

IV. Dados isotópicos fornecidos pela sistemática Sm–Nd nos jaspilitos de Carajás identificaram uma assinatura heterogênea, onde as rochas com valores negativos de εNd (t = 2745 Ma) (–

4,97 a –0,90, n = 6) foram encontradas próximas ao contato jaspilito/basalto (tipo-II), enquanto as demais amostras apresentaram valores predominantemente positivos de εNd (t = 2745 Ma) (-0,84 a +5,40, n = 15). Os valores negativos de εNd (t) indicam a presença de manto enriquecido ou alguma interação com rochas "enriquecidas" (p.ex., basaltos adjacentes). Além disso, as isócronas (Sm–Nd) fornecidas resultaram em idades deposicionais de 2707 ± 118 Ma (MSWD = 230, n = 34) e de 2795 ± 77 Ma (MSWD = 56, n = 20) concordantes com a idade mínima difundida na literatura para a deposição das FFBs de Carajás de ~ 2745 Ma (p.ex., Trendall et al., 1998; Martins et al., 2017).

V. As FFB de Carajás apresentam uma assinatura ETR + Y semelhante à água do mar; no entanto, as anomalias pronunciadas positivas de Eu, valores positivos de εNd (t) e razões Y/Ho menores quando comparados à água do mar indicam uma possível mistura com fluidos hidrotermais de alta temperatura (> 1,0%).

VI. O estudo quimioestratigráfico e o contexto geológico regional indicam que os jaspilitos de Carajás não se enquadram dentro da classificação convencional entre tipo Algoma ou tipo Superior (Gross, 1980). As anomalias positivas e acentuadas de Európio (Eu/Eu_{PAAS} = 1.86 – 5.05) observadas nas amostras e a existência de atividade vulcânica contemporânea a deposição dos jaspilitos são consistentes com os FFBs do tipo Algoma (Gross, 1980; Huston & Logan, 2004). Entretanto, os jaspilitos possuem teores negligíveis de metais de transição como V (média de 4,61 ppm), Co (2,79 ppm) e Ni (<1 ppm), comumente observados em FFBs do tipo Superior (Gross & McLeod, 1980). Além disso, os jaspilitos de Carajás são muito extensos e espessos, possuindo espessura original estimada de 200 a 400 m (Macambira, 2003; Cabral et al., 2013), diferente do observado na maioria das FFBs do tipo Algoma, as quais raramente se estendem por mais de 10 km e tipicamente possuem espessura menor que 50 m (Bekker et al., 2010). Portanto, a ideia de que é mais prático considerar os tipos Algoma e Superior como membros de classificação finais seja a mais adequada, com

um espectro de variedades intermediárias entre elas (Bekker et al., 2012; 2014; Konhauser et al., 2017).

VII. Dados paleomagnéticos obtidos para os derrames basálticos da Formação Parauapebas, porção basal do grupo Grão-Pará, forneceram duas componentes características de magnetização primárias denominada C1 e C2. Tais componentes foram posteriormente usadas para calcular o pólo paleomagnético médio para cada um: C1 (~ 2759 Ma; 40,5ºE, -44,6ºS A95 = 6,5º, K = 18,5) e C2 (~ 2745 Ma; 342,4ºE, -54,3ºS, A95 = 14,8º, K = 27,8). Os dados paleomagnéticos obtidos na região da Província Carajás foram os primeiros coletados para um fragmento Arqueano do Cráton Amazônico, o que aumenta o registro paleomagnético do Cráton. Estes dados, integrados com evidências geológicas revelam que o Bloco Carajás ocupava baixas latitudes na época de deposição da bacia (Fig. 14), e poderia ter feito parte da configuração do supercráton conhecido como "Supervaalbara" (Gumsley, 2017; Salminen et al., 2019) durante o Neoarqueano (~ 2,75 Ga). Além disso, uma sequência de três eventos de reversão magnética é identificada nos derrames basálticos estudados; o que indicaria a existência de um geodínamo dinâmico anterior a 2,7 Ga.

VIII. A Bacia Carajás provavelmente foi formada em regime divergente relacionada a um ambiente do tipo rifte por volta de 2,75 Ga (Gibbs et al., 1986; Martins et al., 2017; Tavares et al., 2018), onde a bacia foi preenchida inicialmente por uma espessa camada de rochas vulcânicas, associada ao vulcanismo Parauapebas, seguida de ampla deposição de formação ferrífera bandada (Formação Carajás) ainda no Neoarqueano (2,76-2,74 Ga) (Fig. 15). A deposição da FFB de Carajás ocorreu em mar profundo, distal às massas continentais, em uma região intensamente influenciada por fluidos hidrotermais de alta temperatura e com baixa disponibilidade de oxigênio (Fig. 13). Além disso, a reconstrução paleogeográfica fornecida pelos dados paleomagnéticos corrobora com a hipótese de rifte, a qual indica que após 2,75 Ga, as paleolatitudes do bloco Carajás e dos demais crátons arqueanos divergem

consideravelmente, o que seria indicativo do início da separação desses blocos (Fig. 14). Tal fato poderia registrar a ruptura de um dos primeiros supercontinentes documentados (Gumsley et al., 2017; Salminen et al., 2019; Rossignol et al., 2020; 2021).

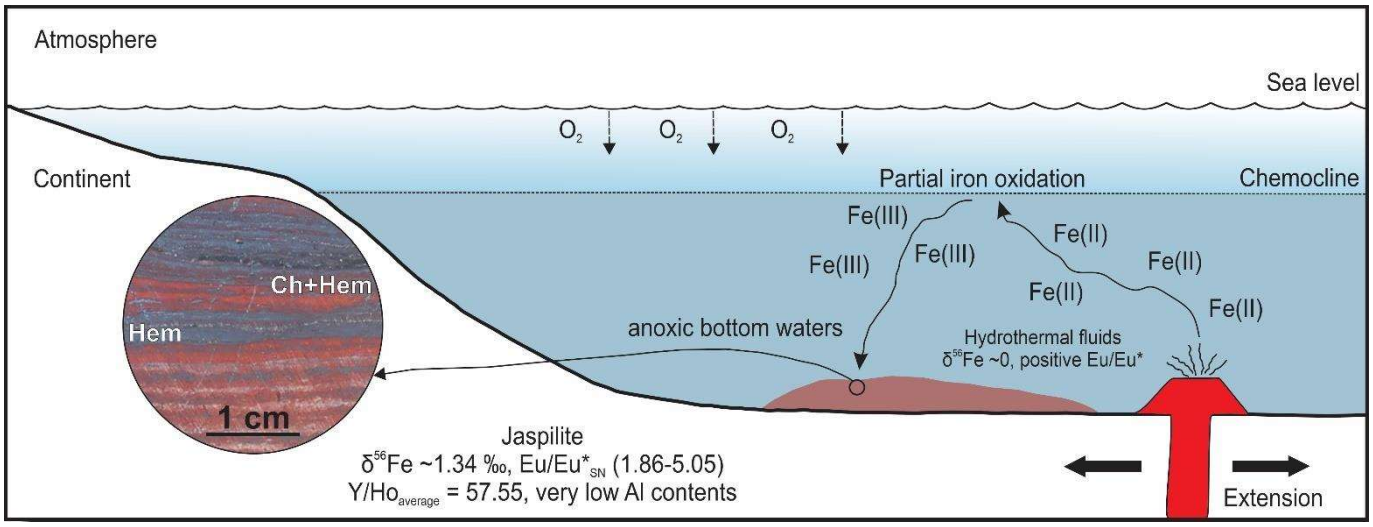

Figura 13. *Principais características das formações ferríferas bandadas de Carajás e modelo genético simplificado. A deposição ocorreu em mar profundo, distal às massas continentais, em uma região intensamente influenciada por fluidos hidrotermais de alta temperatura e com baixa disponibilidade de oxigênio O Fe(II), proveniente de sistemas hidrotermais de água profundas, sobe até regiões mais rasas se transformando em Fe(III) na zona fótica e precipitado como hidrato de ferro, Fe(OH)3. Por fim, o hidrato de ferro é depositado no assoalho oceânico como precursor das formações ferríferas.*

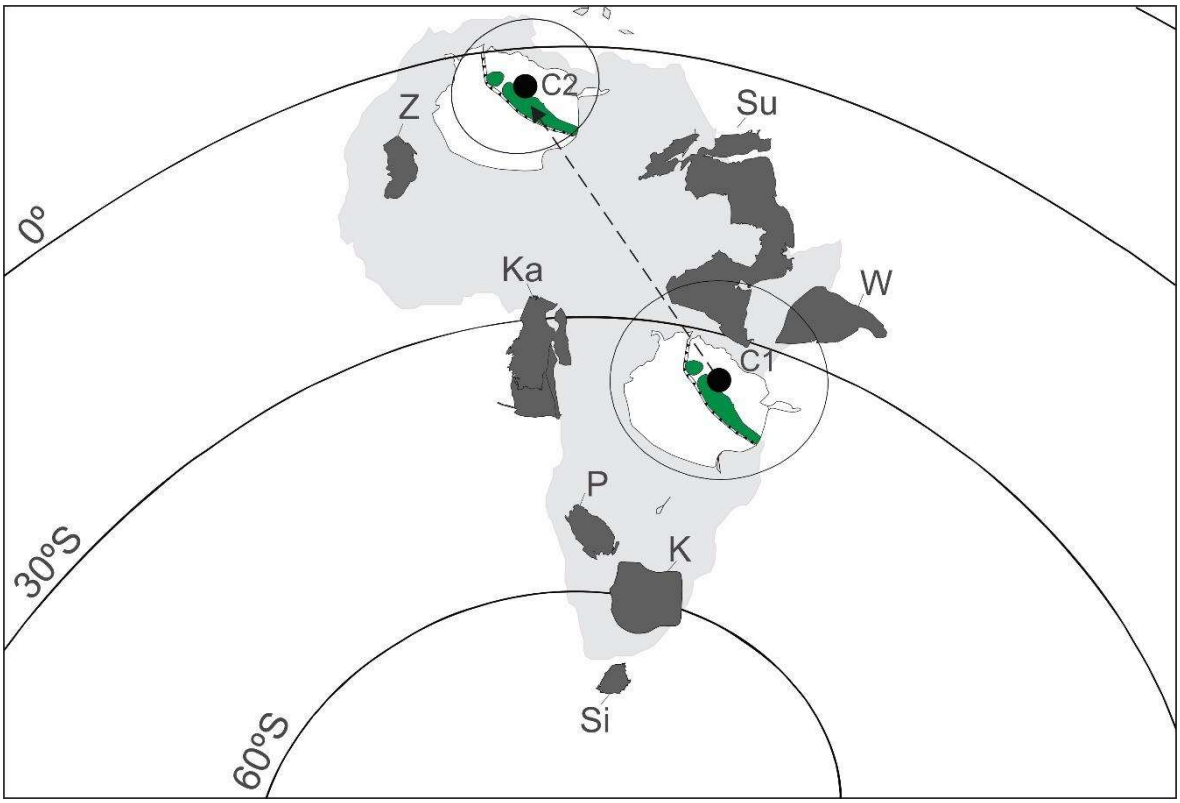

Figura 14. *Projeção de Mollweide demonstrando de forma simplificada as paleoposições de alguns crátons arqueanos durante o Neoarqueano (~2760 Ma). Os pontos pretos representam os polos obtidos para a Província Carajás (C1 e C2) e em verde a região arqueana do Cráton Amazónico. A reconstrução foi feita utilizando o software "PaleoMac" (Cogne, 2003) e tendo como referência o Cráton de Kaapvaal. A seta pontilhada indica a possível movimentação do bloco Carajás entre ~2760-2745 Ma. K = Kaapvaal; Ka = Karelia; P = Pilbara; Si = Singhbhum; Su; Superior; W = Wyoming; Z = Zimbabwe.*

Por fim, algumas questões levantadas nesta tese carecem de maior esclarecimento, e serão objetos de estudos posteriores:

I. As anomalias negativas de Ce observadas em algumas porções da sequência de jaspilitos seriam evidência da produção de O_2 em 2,75 Ga na Província de Carajás, e consequentemente, a existência de micro-organismos capazes de produzir o O_2? Até o momento, existem os relatos de microfósseis associado aos esferulitos encontrados nas FFBs de Carajás (Macambira, 2003; Ribeiro da Luiz & Crowley, 2012; Justo et al., 2020), os quais poderiam ser responsáveis por esta leve oxigenação. No entanto, trabalhos recentes (p.ex.,

Justo et al., 2020; Rego et al., 2020) defendem que as condições de redução eram predominantes e que a fotossíntese anaeróbica era o mecanismo mais plausível responsável pela oxidação do Fe na Bacia de Carajás. Outra questão a se destacar é se as anomalias observadas seriam produto ou não de alterações pós deposicionais? Bonnand et al. (2020) demonstraram que mesmo proxies redox considerados mais imóveis como o cério podem ser mais sensíveis à alteração pós-deposicional do que se pensava anteriormente; o que indica a necessidade de buscar estudar tais proxies paleoredox acoplados a geocronologia (p.ex., sistema La-Ce) para permitir a datação direta desses sinais antigos de oxigenação presente na superfície terrestre (pré-GOE);

II. Apesar de haver um consenso a respeito da idade de deposição das FFBs de Carajás (~2,75 Ga; Trendall et al., 1998; Krymsky et al., 2002; Martins et al., 2017), ainda não foi possível avaliar sua taxa de deposição. Dados geocronológicos de U-Pb em zircão em rochas vulcânicas intercaladas com a FFB estabelecem um limite mínimo para sua idade de deposição por volta de ~2745 Ma (Galarza & Macambira, 2002; Galarza et al., 2008; Martins et al., 2017). Por outro lado, a idade da Formação Parauapebas, unidade subjacente a FFB de Carajás, varia entre 2759 ± 2 Ma (Machado et al. 1991) e 2751 ± 2 Ma (Krymsky et al., 2002), o que estabelece sua idade máxima para a deposição. Estes dados geocronológicos indicariam que a FFB de Carajás se depositou entre um período de 10 a 20 Ma, o que é razoável para uma espessura máxima aproximada de 400 m (Macambira 2003; Cabral et al., 2013). No entanto, estes dados são apenas superficiais havendo a necessidade de se fazer um estudo mais robusto e completo, buscando quantificar de forma mais detalhada a taxa de sedimentação da FFB de Carajás. A taxa de sedimentação/deposição seria um dado importante para se reconstruir com mais precisão as condições paleoambientais e geodinâmicas existentes durante sua precipitação. Datações U-Pb em andamento no âmbito do grupo de pesquisa serão cruciais para elucidação dessa questão;

III. As evidências encontradas corroboram a ideia de que a bacia de Carajás se formou a partir do rifteamento de uma crosta continental (Gibbs et al., 1986; Olszewski et al., 1989; Martins et al., 2017; Tavares et al., 2018; Teixeira et al., 2021), no entanto, não está claro se esta abertura poderia estar relacionada a presença de uma pluma mantélica (Rossignol et al., 2021; Teixeira et al., 2021) ou provocada por um relaxamento da crosta ocasionado após um evento orogênico, ou seja, durante a transição de um ambiente colisional para um pós-colisional (Martins et al., 2017; Tavares et al., 2018). Considerando os dados geoquímicos estudados para FFB de Carajás (p.ex., intensa atividade hidrotermal e vulcânica), paleomagnéticos e geológicos obtidos nas rochas vulcânicas da Formação Parauapebas (*magmatic barcodes*), a possibilidade da existência de uma pluma mantélica se faz válida, necessitando de um aprofundamento maior nessa questão.

IV. A reconstrução paleogeográfica observada para o Bloco Carajás revelou uma mudança significativa da paleolatitude (média de 31,2 °) entre o limite dos derrames 3 e 4 (~ 55m, C1 para C2 (Fig. 14). Tal deslocamento poderia indicar a atuação de tectônica semelhante a moderna durante este período? Caso sim, a velocidade atuante neste bloco seria semelhante ou mais rápida que a observada atualmente ~ 4 cm/ano (Zahirovic et al., 2015)? Se as idades de SHRIMP U-Pb adotadas estiverem corretas (2759 ± 1 para C1; Machado et al., 1991 e 2749 ± 6.5 Ma para C2; Martins et al., 2017), a diferença entre essas duas paleolatitudes encontradas seria em média de 10 ± 8,5 Ma. Assim, assumindo a Terra com o raio atual, o deslocamento médio seria de ~ 3466 km, o que daria uma velocidade média de ~ 34,6 cm/ano (3,12º/Ma) para o Bloco Carajás durante este período. Entretanto, esta hipótese seria apenas especulativa, tendo em vista que a discrepância na paleolatitude observada poderia ser explicada por outras variáveis como TPW (*true polar wander*) e campo magnético não dipolar (Brenner et al., 2020). Além disso, estudar mais detalhadamente a mudança observada na paleolatitude com novos dados paleomagnéticos em regiões diferentes da

Bacia Carajás acoplada com geocronologia de alta resolução seria necessário para o melhor entendimento dessas variações e, consequentemente, da tectônica atuante durante o período de formação da bacia.

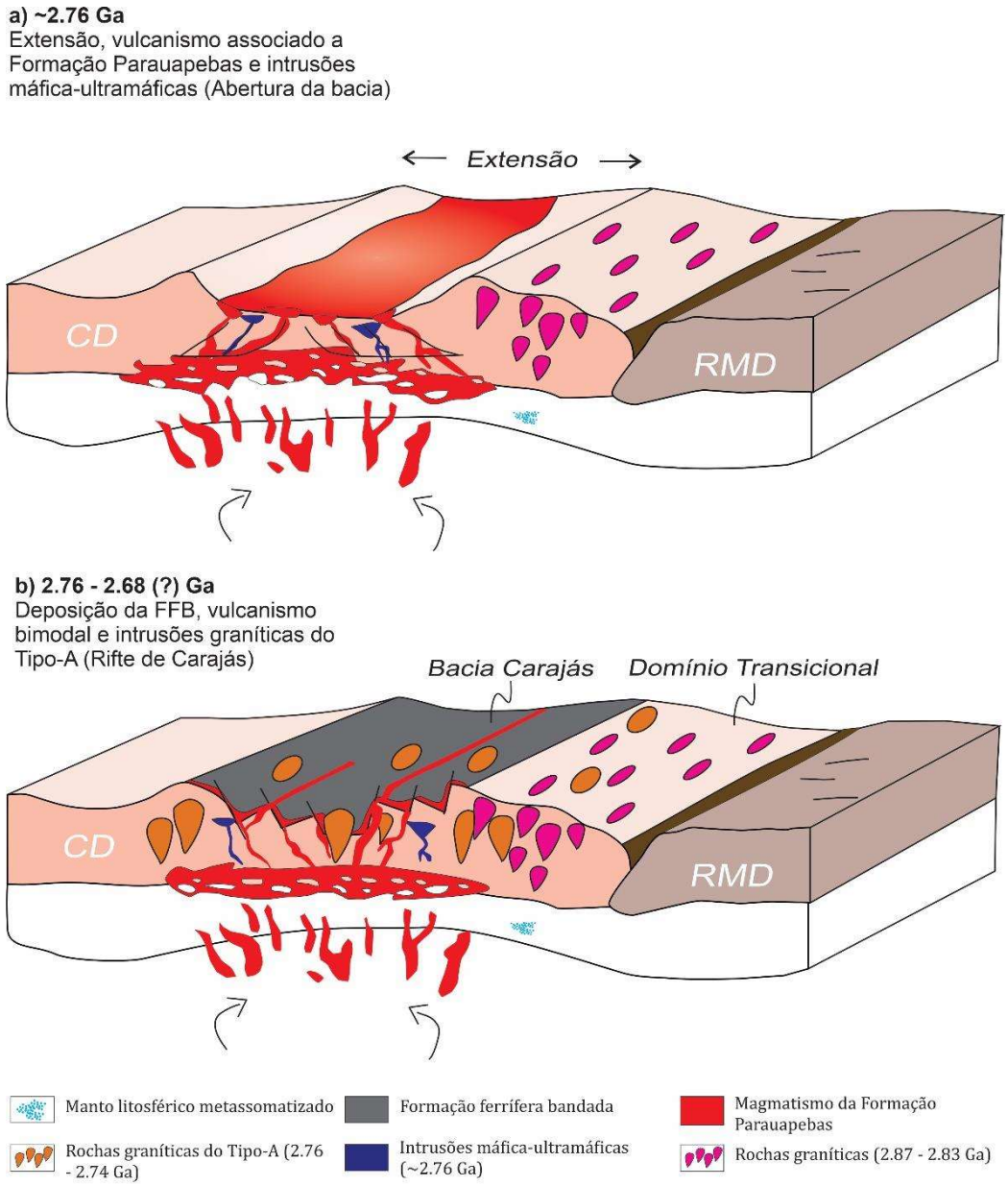

Figura 15. *Modelo tectônico para a geração dos espessos derrames de rochas vulcânicas associados ao vulcanismo Parauapebas em cerca. 2,75 Ga (modificado de Martins et al., 2017). As camadas das FFBs de Camadas se depositaram imediatamente acima dos estratos vulcânicos.*

7. REFERÊNCIAS BIBLIOGRÁFICAS

Alexander, B.W., Bau, M., Andersson, P., Dulski, P., 2008. Continentally-derived solutes in shallow Archean seawater: rare earth element and Nd isotope evidence in iron formation from the 2.9 Ga Pongola Supergroup, South Africa. Geochim. Cosmochim. Acta 72, 378–394. https://doi.org/10.1016/j.gca.2007.10.028.

Althoff, F.J., Barbey, P., Boullier, A.M., 2000. 2.8-3.0 Ga plutonism and deformation in the SE Amazonian craton: the Archean granitoids of Marajoara (Carajás Mineral province, Brazil). Precambrian Res. 104, 187–206. https://doi.org/10.1016/S0301-9268(00)00103-0.

Araújo, R.N., 2020. Estratigrafia e eventos da transição Neoarqueano-Paleoproterozoico da Bacia de Carajás, sudeste do Cráton Amazônico. Universidade Federal do Pará, Instituto de Geociências, Tese de Doutorado Nº 149, Província de Carajás (187 p).

Araújo, O.J.B., Maia, R.G.N., 1991. Programa de levantamentos geológicos básicos do Brasil. Programa grande Carajás. Serra dos Carajás folha SB. 22-Z-A. Estado do Pará. Texto. DNPM/CPRM, Brasília, 164p (in Portuguese).

Araújo, O.J.B., Maia, R.G.N., João, X.S.J., Costa, J.B.S., 1988. A megaestruturação arqueana da Folha Serra dos Carajás. Congresso Latino Americano de Geologia, Belém- Brazil, Anais, pp. 324–338.

Araújo, R., Nogueira, A., 2019. Serra sul diamictite of the Carajás Basin (Brazil): a Paleoproterozoic glaciation on the Amazonian craton. Geology 47, 1166–1170. https://doi.org/10.1130/G46923.1.

Araújo Filho, R., Nogueira, A.C.R., Araújo, R.N., 2020. New stratigraphic proposal of a Paleoproterozoic siliciclastic succession: implications for the evolution of the Carajás Basin, Amazonian craton, Brazil. J. S. Am. Earth Sci. 102, 102665. https://doi.org/10.1016/j.jsames.2020.102665.

Bhattacharya, H., Chakraborty, I., Ghosh, K., 2007. Geochemistry of some banded iron formations of the Archean supracrustals, Jharkhand-Orissa region, India. J. Earth Syst. Sci. 116, 245–259. https://doi.org/10.1007/s12040-007-0024-4.

Bau, M., Dulski, P., 1996. Distribution of yttrium and rare-earth elements in the Penge and Kuruman Iron-Formations, Transvaal Supergroup, South Africa. Precambrian Res. 79, 37–55. https://doi.org/10.1016/0301-9268(95)00087-9.

Beisiegel, V.R., Bernardelli, A.L., Drummond, N.F., Ruff, A.W., Tremaine, J.W. 1973. Geologia e Recursos Minerais da Serra dos Carajás. Revista Brasileira de Geociências, 3: 215-242.

Bekker A., Holland H.D., Wang P-L., Rumble D.I.I.I, Stein H.J., Hannah J.L., Coetzee L.L., Beukes N.J., 2004. Dating the rise of atmospheric oxygen. Nature 427, 117–120. https://doi.org/10.1038/nature02260.

Bekker, A., Slack, J., Planavsky, N., Krapež, B., Hofmann, A., Konhauser, K.O., Rouxel, O.J., 2010. Iron formation: the sedimentary product of a complex interplay among mantle, tectonic, oceanic, and biospheric processes. Econ. Geol. 105, 467–508. https://doi.org/10.2113/gsecongeo.105.3.467.

Bekker, A., Krapež, B., Slack, J., Planavsky, N., Hofmann, A., Konhauser, K.O., Rouxel, O.J., 2012. Iron formation: the sedimentary product of a complex interplay among mantle, tectonic, oceanic, and biospheric processes – a reply. Econ. Geol. 107, 379–380. https://doi.org/10.2113/econgeo.107.2.379.

Bekker, A., Planavsky, N., Krapež, B., Rasmussen, B., Hofmann, A., Slack, J.F., Rouxel, O.J., Konhauser, K.O., 2014. Iron formations: their origins and implications for ancient seawater chemistry. In: Holland, H.D., Turekian, K.K. (Eds.), Treatise of Geochemistry, second ed. v. 9. Elsevier, pp. 561–628.

Biggin, A.J., de Wit, M.J., Langereis, C.G., Zegers, T.E., Voûte, S., Dekkers, M.J., Drost, K., 2011. Palaeomagnetism of Archean rocks of the Onverwacht Group, Barberton Greenstone Belt (southern Africa): Evidence for a stable and potentially reversing geomagnetic field at ca. 3.5 Ga. Earth Planet. Sci. Lett. 302, 314-328. https://doi.org/10.1016/j.epsl.2010.12.024.

Bleeker, W., 2003. The late Archean record: a puzzle in ca. 35 pieces. Lithos 71, 99–134. https://doi.org/10.1016/j.lithos.2003.07.003.

Bonnand, P., Lalonde, S.V., Boyet, M., Heubeck, C., Homann, M., Nonnotte, P., Foster, I., Konhauser, K.O., Köhler, I., 2020. Post-depositional REE mobility in a Paleoarchean banded iron formation revealed by La-Ce geochronology: A cautionary tale for signals of ancient oxygenation. Earth Planet. Sci. Lett. 547, 116452. https://doi.org/10.1016/j.epsl.2020.116452.

Brenner, A. R., Fu, R. R., Evans, D.A.D., Smirnov, A.V., Trubko, R., Rose, I.R., 2020. Paleomagnetic evidence for modern-like plate motion velocities at 3.2 Ga. Sci. Adv. 6, eaaz8670. https://doi.org/10.1126/sciadv.aaz8670.

Buchan, K. L., Mertanen, S., Park, R. G. Pesonen, L. J., Elming, S. A., Abrahamsen, N., Bylund, G., 2000. Comparing the drift of Laurentia and Baltica in the Proterozoic: the importance of key palaeomagnetic poles. Tectonophysics, vol. 319, n. 3, pg. 167-198. https://doi.org/10.1016/S0040-1951(00)00032-9.

Butler, R.F., 1992. Paleomagnetism: Magnetic Domains to Geologic Terranes. Blackwell Scientific Publications.

de Kock, M.O., Evans, D.A., Beukes, N.J., 2009. Validating the existence of Vaalbara in the Neoarchean. Precambrian Res. 174, 145–154. https://doi.org/10.1016/j.precamres.2009.07.002.

Cabral, A.R., Creaser, R.A., Nagler, T., Lehmann, B. Voegelin, A.R., Beltasky, B., Pasava, J., Gomes, A.A.S., Galbiatti, H., Bottcher, M.E., Escher, P., 2013. Trace-element and multi-isotope geochemistry of Late-Archean black shales in the Carajás iron-ore district, Brazil. Chem. Geol. 362, 91 – 104. https://doi.org/10.1016/j.chemgeo.2013.08.041.

Cloud, P., 1973. Paleoecological significance of banded iron-formation. Econ. Geol. 68, 1135–1143.

Cogne, J.P., 2003. Paleo Mac: a MacintoshTM application for treating paleomagnetic data and making plate reconstructions. Geochem. Geophys. Geosyst. 4, 1007. http://dx.doi.org/10.1029/2001GC000227.

Dall'Agnol, R., Oliveira, M.A., Almeida, J.A.C., Althoff, F.J., Leite, A.A.S., Oliveira, D.C., Barros, C.E.M., 2006. Archean and Paleoproterozoic granitoids of the Carajás Metallogenic Province, eastern Amazonian craton. Symposium on Magmatism, Crustal Evolution, and Metallogenesis of the Amazonian Craton, Abstracts Volume and Field Trips Guide (150 pp.).

Danielson, A., Möller, P., Dulski, P., 1992. The europium anomalies in banded iron formations and the thermal history of the oceanic crust. Chem. Geol. 97, 89–100. https://doi.org/10.1016/0009-2541(92)90137-T.

Denyszyn, S.W., Feinberg, J.M., Renne, P.R., Scott, G.R., 2013. Revisiting the age and paleomagnetism of the Modipe Gabbro of South Africa. Precambrian Res. 238, 176–185. https://doi.org/10.1016/j.precamres.2013.10.002.

Derry, L.A., Jacobsen, S.B., 1990. The chemical evolution of Precambrian seawater: evidence from REEs in banded iron formations. Geochim. Cosmochim. Acta 54, 2965–2977. https://doi.org/10.1021/cen-v026n044.p3274.

DOCEGEO - Rio Doce Geologia e Mineração, 1988. Revisão Litoestratigráfica da Província Mineral de Carajás. 35° Congresso Brasileiro de Geologia, Belém, Brasil, Anais, Sociedade Brasileira de Geologia, pp. 11–59.

Dreher, A.M., Xavier, R.P., Taylor, B.E., Martini, S.L., 2008. New geologic, fluid inclusion and stable isotope studies on the controversial Igarapé Bahia Cu-Au deposit, Carajás Province, Brazil. Miner. Deposita 43, 161–184. https://doi.org/10.1007/s00126-007-0150-6.

Evans, D.A.D., Li, Z.-X., Murphy, J.B., 2016. Four-dimensional context of Earth's supercontinents. Geological Society, London, Special Publications 424.

Feio, G.R.L., Dall'Agnol, R., Dantas, E.L., Macambira, M.J.B., Gomes, A.C.B., Sardinha, A. S., Oliveira, D.C., Santos, R.D., e Santos, P.A., 2012. Geochemistry, geochronology, and origin of the Neoarchean Planalto Granite suite, Carajás, Amazonian craton: A-type or hydrated charnockitic granites?. Lithos, 151, 57-73. https://doi.org/10.1016/j.lithos.2012.02.020.

Feio, G.R.L., Dall'Agnol, R., Dantas, E.L., Macambira, M.J.B., Santos, J.O.S., Althoff, F.J., Soares, J.E.B., 2013. Archean granitoid magmatism in the Canaã dos Carajás area: implications for crustal evolution of the Carajás province, Amazonian craton, Brazil. Precambrian Res. 227, 157–185. https://doi.org/10.1016/j.precamres.2012.04.007.

Figueiredo e Silva, R.C., Lobato, L.M., Zucchetti, M., Hagemann, S., Vennemann, T., 2020. Geotectonic signature and hydrothermal alteration of metabasalts under-and overlying the giant Serra Norte iron deposits, Carajás mineral Province. Ore Geol. Rev. 120, 103407. https://doi.org/10.1016/j.oregeorev.2020.103407.

Ferreira Filho, C.F., Cançado, F., Correa, C., Macambira, E.M.B., Siepierski, L., Brod, T.C.J., 2007. Mineralizações estratiformes de EGP-Ni associadas a complexos acamadados em Carajás: os exemplos de Luanga e Serra da Onça. Publitec Gráfica & Editora, Contribuições à Geologia da Amazônia 5, 01–14.

Frei, R., Polat, A., 2007. Source heterogeneity for the major components of ~3.7 Ga Banded Iron Formations (Isua Greenstone Belt, Western Greenland): tracing the nature of interacting water masses in BIF formation. Earth Planet. Sci. Lett. 253, 266–281. https://doi.org/10.1016/j.epsl.2006.10.033.

Frei, R., Dahl, P.S., Duke, E.F., Frei, K.M., Hansen, T.R., Frandsson, M.M., Jensen, L.A., 2008. Trace element and isotopic characterization of Neoarchean and Paleoproterozoic iron formations in the Black Hills (South Dakota, USA): assessment of chemical change during 2.9-1.9 Ga deposition bracketing the 2.4-2.2 Ga first rise of atmospheric oxygen. Precambrian Res. 162, 441–474. https://doi.org/10.1016/j.precamres.2007.10.005.

Galarza, M.A.; Macambira, M.J.B., 2002. Geocronologia e evolução crustal da área do depósito de Cu-Au Gameleira, Província Mineral de Carajás (Pará), Brasil. Revista do Instituto de Geociências da USP, 2:143-159.

Galarza, M.A., Macambira, M.J.B., Villas, R.N.N., 2008. Dating and isotopic characteristics (Pb and S) of the Fe oxide-Cu-Au-U-REE Igarapé Bahia ore deposit, Carajás mineral province, Pará state, Brazil. J. S. Am. Earth Sci. 25, 377–397. https://doi.org/10.1016/j.jsames.2007.07.006.

Gibbs, A.K., Wirth, K.R., Hirata, W.K., Olszewski Jr., W.J., 1986. Age and composition of the Grão Pará Group volcanics, Serra dos Carajás. Rev. Bras. Geoc. 16, 201-211.

Gross, G.A., 1980. A classification of iron-formation based on depositional environments. Can. Mineral. 18, 215–222.

Gross, G.A., Mcleod, C.R., 1980. A preliminary assessment of the chemical composition of iron formations in Canada. Can. Mineral. 18, 223–229.

Gruner, J.W., 1922. The origin of sedimentary iron-formations: the Biwabik Formation of the Mesabi Range. Econ. Geol. 22, 407–460.

Gumsley, A.P., 2017. Validating the existence of the supercraton Vaalbara in the Mesoarchaean to Palaeoproterozoic. Doctoral dissertation, Lithosphere and Biosphere Science, Department of Geology, Lund University. Litholund theses 30, 130.

Gumsley, A.P., Chamberlain, K.R., Bleeker, W., Söderlund, U., de Kock, M.O., Larsson, E.R., Bekker, A., 2017. Timing and tempo of the Great Oxidation Event. Proc. Natl. Acad. Sci. U. S. A. 114, 1811–1816. https://doi.org/10.1073/pnas.1608824114.

Halverson, P., Poitrasson, F., Hoffman, P.F., Nédélec, A., Montel, J.M., Kirby, J., 2011. Fe isotope and trace element geochemistry of the Neoproterozoic syn-glacial Rapitan Iron Formation. Earth Planet. Sci. Lett. 309, 100–112. https://doi.org/10.1016/j.epsl.2011.06.021.

Haugaard, R., Frei, R., Stendald, H., Konhauser, K.O., 2013. Petrology and geochemistry of the ~2.9 Ga Itilliarsuk banded iron formation and associated supracrustal rocks, West Greenland: source characteristics and depositional environment. Precambrian Res. 229, 150–176. https://doi.org/10.1016/j.precamres.2012.04.013.

Haugaard, R., Ootes, L., Creaser, R.A., Konhauser, K.O., 2016a. The nature of Mesoarchean seawater and continental weathering in 2.85 Ga banded iron formation, Slave Craton, NW Canada. Geochim. Cosmochim. Acta 194, 34–56. https://doi.org/10.1016/j.gca.2016.08.020.

Haugaard, R., Pecoits, E., Lalonde, S., Rouxel, O., Konhauser, K.O., 2016b. The Joffre Banded Iron Formation, Hamersley Group, Western Australia: assessing the paleoenvironment through detailed petrology and chemostratigraphy. Precambrian Res. 273, 12–37. https://doi.org/10.1016/j.precamres.2015.10.024.

Haugaard, R., Ootes, L., Creaser, R.A., Konhauser, K.O., 2017. Neoarchean banded iron formation within a 2620 Ma turbidite-dominated deep-water basin, Slave craton, NW Canada. Precambrian Res. 292, 130–151. https://doi.org/10.1016/j.precamres.2017.01.025.

Hoffman, P.F., Kaufman, A.J., Halverson, G.P., Schrag, D.P., 1998. A Neoproterozoic Snowball Earth. Science 281 (5381), 1342–1346. https://doi.org/10.1126/science.281.5381.1342.

Hofmann, A., 2005. The geochemistry of sedimentary rocks from the Fig Tree Group, Barberton Greenstone Belt: Implications for tectonic, hydrothermal and surface processes during mid-Archaean times. Precambrian Res. 143, 23–49. https://doi.org/10.1016/j.precamres.2005.09.005.

Huston, D.L., Logan, G.A., 2004. Barite, BIFs and bugs: Evidence for the evolution of the Earth's early hydrosphere. Earth Planet. Sci. Lett. 220, 41–55. https://doi.org/10.1016/S0012-821X(04)00034-2.

Huston D.L, Pehrsson, S., Eglington, B.M., & Zaw, K., 2010. The geology and metallogeny of volcanic hosted massive sulfide deposits: Variations through geologic time and with tectonic setting. Econ. Geol. 105, 571−591. https://doi.org/10.2113/gsecongeo.105.3.571.

Isley, A.E., Abbott, D.H., 1999. Plume-related mafic volcanism and the deposition of banded iron formation. J. Geophys. Res. 104, 461–477. https://doi.org/10.1029/1999JB900066.

Johnson, C.M., Roden, E.E., Welch, S.A., Beard, B.L., 2005. Experimental constraints on Fe isotope fractionation during magnetite and Fe carbonate formation coupled to dissimilatory hydrous ferric oxide reduction. Geochim. Cosmochim. Acta 69, 963–993. https://doi.org/10.1016/j.gca.2004.06.043.

Johnson, C.M., Beard, B.L., Klein, C., Beukes, N.J., Roden, E.E., 2008. Iron isotopes constrain biologic and abiologic processes in banded iron formation genesis. Geochim. Cosmochim. Acta 72, 151–169. https://doi.org/10.1016/j.gca.2007.10.013.

Justo, A. P., Dantas, E.L., Bau, M., Freitas-Silva, F.H., Santos, R.V., Schorscher, J.H.D., 2020. Paleobasinal to band-scale REE+Y distribution in Iron Formations from Carajás, Amazon Craton, Brazil, Ore Geol. Rev. 127, 103750. https://doi.org/10.1016/j.oregeorev.2020.103750.

Klein, C., 2005. Some Precambrian banded iron-formations (BIFs) from around the world: Their age, geologic setting, mineralogy, metamorphism, geochemistry, and origins. Am. Mineral. 90 (10), 1473–1499. https://doi.org/10.2138/am.2005.1871.

Klein, C., Beukes, N.J., 1993. Sedimentology and geochemistry of the glaciogenic late Proterozoicn Rapitan iron-formation in Canada. Econ. Geol. 88 (3), 542–565. https://doi.org/10.2113/gsecongeo.88.3.542.

Konhauser, K., Lalonde, S., Planavsky, N., Pecoits, E., Lyons, T., Mojzsis, S., Rouxel, O., Fralick, P., Barley, M., Kump, L., Bekker, A., 2011. Aerobic bacterial pyrite oxidation and acid rock drainage during the Great Oxidation Event. Nature 478, 369–373. https://doi.org/10.1038/nature10511.

Konhauser, K.O., Planavsky, N.J., Hardisty, D.S., Robbins, L.J., Warchola, T.J., Haugaard, R., Lalonde, S.V., Partin, C.A., Oonk, P.B.H., Tsikos, H., Lyons, T.W., Bekker, A., Johnson, C.M., 2017. Iron

formations: a global record of Neoarchaean to Palaeoproterozoic environmental history. Earth Sci. Rev. 172, 140–177. https://doi.org/10.1016/j.earscirev.2017.06.012.

Krymsky, R.S., Macambira, J.B., Macambira, M.J.B, 2002. Geocronologia U-Pb em zircão de rochas vulcânicas da Formação Carajás, Estado do Pará. In: Simpósio Sobre Vulcanismo e Ambientes Associados, 2, Belém, Anais. Belém, 41p. (in Portuguese).

Kumar, A., Parashuramulu, V., Shankar, R., Besse, J., 2012. Evidence for a Neoarchean LIP in the Singhbhum craton, eastern India: Implications to Vaalbara supercontinent. Precambrian Res. 292, 163–174. https://doi.org/10.1016/j.precamres.2018.12.001.

Lafon, J.M., Macambira, M.J.B., Pidgeon, R.T., 2000. Zircon U-Pb SHRIMP dating of Neoarchean magmatism in the southwestern part of the Carajás Province (eastern Amazonian Craton, Brazil). In: 30th International Geological Congress, Abstract Volume, CD-ROM.

Leith, C.K., 1903. The Mesabi iron-bearing district of Minnesota. In: Monographs. 43. U.S. Geological Survey, pp. 1–324.

Lindenmayer, Z.G., Laux, J.H., Teixeira, J.B.G. 2001. Considerações sobre a origem das Formações Ferríferas da Formação Carajás, Serra dos Carajás. Revista Brasileira de Geociências, 31: 21-28.

Lobato, L.M., Rosière, C.A., Silva, R.C.F., Zucchetti, M., Baars, F.J., Seoane, J.C.S., Rios, F.J., Pimentel, M., Mendes, G.E. e Monteiro, A.M., 2005, A mineralização hidrotermal de ferro da Província Mineral de Carajás - controle estrutural e contexto na evolução metalogenética da Província. In: Marini, J.O.; Queiróz, E.T.; Ramos, W.B. (eds.), Caracterização de distritos mineiros da Amazônia. DNPM-CT-Mineral-ADIMB, 25–92.

Lottermoser, B.G., Ashley, P.M., 2000. Geochemistry, petrology and origin of Neoproterozoic ironstones in the eastern part of the Adelaide Geosyncline, South Australia. Precambrian Res. 101, 49–67. https://doi.org/10.1016/S0301-9268(99)00098-4.

Macambira, J. B. 2003. O ambiente deposicional da Formação Carajás e uma proposta de modelo evolutivo para a Bacia Grão-Pará. Tese de Doutorado. Campinas, Unicamp, 214p.

Machado, N., Lindenmayer, Z.G., Krogh, T.E., Lindenmayer, D., 1991. U–Pb geochronology of Archean magmatism and basement reactivation in the Carajás area, Amazon shield, Brazil. Precambrian Research 49, 329–354. https://doi.org/10.1016/0301-9268(91)90040-H.

Martins, P.L.G., Toledo, C.L.B., Silva, A.M., Assis, L.M., 2016. Petrografia e geoquímica dos corpos de gabro do Corpo N5S, Carajás-PA. 48º Congresso Brasileiro de Geologia, Porto Alegre, Brasil, Anais, Sociedade Brasileira de Geologia, pp. 883.

Martins, P.L.G., 2017. Petrologia e Geoquímica dos Basaltos da Formação Parauapebas: Implicações para o Ambiente Tectônico da Bacia Grão Pará. Universidade de Brasília, Instituto de Geociências, Dissertação de Mestrado, Província de Carajás (93 p).

Martins, P.L.G., Toledo, C.L.B., Silva, A.M., Chemale Jr, F., Santos, J.O.S., Assis, L.M., 2017. Neoarchean magmatism in the southeastern Amazonian Craton, Brazil: Petrography, geochemistry and tectonic significance of basalts from the Carajás Basin. Precambrian Res. 302, 340–357. https://doi.org/10.1016/j.precamres.2017.10.013.

Meert, J.G., 2014. Strange attractors, spiritual interlopers and lonely wanderers: The search for pre-Pangean supercontinents. Geoscience Frontiers 5, 155-166. https://doi.org/10.1016/j.gsf.2013.12.001.

Meirelles, M.R., Dardenne, M.A., 1991. Vulcanismo basáltico de afinidade shoshonítica e ambiente de arco arqueano, Grupo Grão-Pará, Serra dos Carajás, Pará. Revista Brasileira de Geociências 21, 41–50 (in Portuguese).

Mloszewska, A., Pecoits, E., Cates, N., Mojzsis, S.J., O'Neil, J., Robbins, L.J., Konhauser, K.O., 2012. The composition of Earth's oldest iron formations: the Nuvvuagittuq Supracrustal Belt (Québec, Canada). Earth Planet. Sci. Lett. 317-318, 331–342. https://doi.org/10.1016/j.epsl.2011.11.020.

Mloszewska, A.M., Mojzsis, S.J., Pecoits, E., Papineau, D., Dauphas, N., Konhauser, K.O., 2013. Chemical sedimentary protoliths of the> 3.75 Ga Nuvvuagittuq Supracrustal Belt (Québec, Canada). Gondwana Res. 23, 574–594. https://doi.org/10.1016/j.gr.2012.11.005.

Olszewski, W.J., Wirth, K.R., Gibbs, A.K., Gaudette, H.E., 1989. The age, origin, and tectonics of the Grão Pará Group and associated rocks, Serra dos Carajás, Brazil: Archean continental volcanism and rifting. Precambrian Research 42, 229–254. https://doi.org/10.1016/0301-9268(89)90013-2.

Rego, E.S., Busigny, V., Lalonde, S.V., Philippot, P., Bouyon, A., Rossignol, C., Babinski, M., Zapparoli, A.C., 2021. Anoxygenic photosynthesis linked to Neoarchean iron formations in Carajás (Brazil). Geobiology 00, 1–16. https://doi.org/10.1111/gbi.12438.

Ribeiro da Luz, B., Crowley, J.K., 2012. Morphological and chemical evidence of stromatolitic deposits in the 2.75 Ga Carajás banded iron formation, Brazil. Earth Planet. Sci. Lett. 355, 60–72. https://doi.org/10.1016/j.epsl.2012.08.028.

Rogers, J. J. W., Santosh, M., 2003. Supercontinents in Earth History. Gondwana Res. 6, 357-368. https://doi.org/10.1016/S1342-937X(05)70993-X.

Rossignol, C., Rego, E.S., Narduzzi, F., Teixeira, L., Ávila, J.N., Silva, M.A.L., Lana, C., Philippot, P., 2020. Stratigraphy and geochronological constraints of the Serra Sul Formation (Carajás Basin,

Amazonian Craton, Brazil). Precambrian Res. 351, 105981. https://doi.org/10.1016/j.precamres.2020.105981.

Rossignol, C., Antonio, P.Y.J., Narduzzi, F., Rego, E.S., Teixeira, L., de Souza, R.A., Ávila, J.N., Silva, M.A.L., Lana, C., Trindade, R.I.F., Philippot, P., 2021. Unraveling one billion years of geological evolution of the southeastern Amazonia Craton from detrital zircon analyses. Geoscience Frontiers (in press), 101202. https://doi.org/10.1016/j.gsf.2021.101202.

Rouxel, O.J., Bekker, A., Edwards, K.J., 2005. Iron isotope constraints on the Archaean and Paleoproterozoic ocean redox state. Science 307, 1088–1090. https://doi.org/10.1126/science.1105692.

Salminen, J., Oliveira, E. P., Piispa, E. J., Smirnov, A. V., Trindade, R. I. F., 2019. Revisiting the paleomagnetism of the Neoarchean Uauá mafic dyke swarm, Brazil: Implications for Archean supercratons. Precambrian Res. 329, 108-123, https://doi.org/10.1016/j.precamres.2018.12.001.

Siepierski, L., Ferreira Filho, C.F., 2016. Spinifex-textured komatiites in the south border of the Carajás ridge, Selva Greenstone belt, Carajás Province, Brazil. J. S. Am. Earth Sci. 66, 41–55. https://doi.org/10.1016/j.jsames.2015.12.011.

Smirnov, A.V., Evans, D.A.D., Ernst, R., Soderlund, U., Li, Z.-X, 2013. Trading partners: tectonic ancestry of southern Africa and Western Australia, in Archean supercratons Vaalbara and Zimgarn. Precambrian Res. 224, 11–22. https://doi.org/10.1016/j.precamres.2012.09.020.

Tallarico, F.H.B., Figueiredo, B.R., Groves, D.I., Kositcin, N., McNaughton, N.J., Fletcher, I.R., Rego, J.L., 2005. Geology and SHRIMP U-Pb geochronology of the Igarapé Bahia deposit, Carajás copper-gold belt, Brazil: an Archean (2.57 Ga) example of iron-oxide Cu-Au-(U-REE) mineralization. Econ. Geol. 100, 7–28. https://doi.org/10.2113/100.1.0007.

Tarling, D. H., Hrouda, F., 1993. The Magnetic Anisotropy of Rocks, Chapman and Hall, London, 217p.

Tauxe, L., 2002. Paleomagnetic Principles and Practice, Kluwer Academic Publishers.

Tauxe, L., 2009. Essentials of Paleomagnetism. University of California Press. 512p.

Tavares, F.M., Trouw, R.A.J., da Silva, C.M.G., Justo, A.P., Oliveira, J.K.M., 2018. The multistage tectonic evolution of the northeastern Carajás Province, Amazonian Craton, Brazil: Revealing complex structural patterns. J. S. Am. Earth Sci. 88, 238–252. https://doi.org/10.1016/j.jsames.2018.08.024.

Teixeira, J.B.G., Eggler, D.H., 1994. Petrology, geochemistry, and tectonic setting of Archaean basaltic and dioritic rocks from the N4 iron deposit, Serra dos Carajás, Pará, Brazil. Acta Geol. Leopoldensia 17, 71–114.

Teixeira, N. A., Campos, L. D., de Paula R. R., Lacasse, C., M., Ganade, C. E., Monteiro, C. F., Lopes, L. B. L., Oliveira, C. G., 2021. Carajás Mineral Province - Example of metallogeny of a rift above a cratonic lithospheric keel. J. S. Am. Earth Sci. 108, 103091. https://doi.org/10.1016/j.jsames.2020.103091.

Trendall, A.F., 2002. The significance of iron-formation in the Precambrian stratigraphic record. Int. Assoc. Sedimentol. Spec. Publ. 33, 33–66. https://doi.org/10.1002/9781444304312.ch3.

Trendall, A., Blockley, J., 1970. The iron formations of the Precambrian Hamersley Group, Western Australia with special reference to the associated crocidolite. In: Western Australia Geological Survey Bulletin 119, pp. 1–366.

Trendall, A.F., Basei, M.A.S., De Laeter, J.R., Nelson, D.R., 1998. SHRIMP zircon U–Pb constraints on the age of the Carajás Formation, Grão Pará Group, Amazon Craton. Journal of South American Earth Sciences 11, 265–277. https://doi.org/10.1016/S0895-9811(98)00015-7.

van der Voo, R., 1990. The reliability of paleomagnetic data. Tectonophysics 184, 1–9. https://doi.org/10.1016/0040-1951(90)90116-P.

Vasquez, M.L., Carvalho, J.M.A., Sousa, C.S., Ricci, P.S.F., Macambira, E.M.B., Costa, L.T.R., 2008. Mapa Geológico do Pará em SIG. Serviço Geológico Brasileiro - CPRM.

Viehmann, S., Bau, M., Hoffmann, J.E., Münker, C., 2015. Geochemistry of the Krivoy Rog Banded Iron Formation, Ukraine, and the impact of peak episodes of increased global magmatic activity on the trace element composition of Precambrian seawater. Precambrian Res. 270, 165–180. https://doi.org/10.1016/j.precamres.2015.09.015.

Wirth K.R., Gibbs A.K., Olszewski W. 1986. U-Pb zircon ages of the Grão Pará Group and Serra dos Carajás Granite. Revista Brasileira de Geociências, 16: 195-200.

Zahirovic, S., Müller, R.D., Seton, M., Flament, N., 2015. Tectonic speed limits from plate kinematic reconstructions. Earth. Planet. Sci. Lett. 418, 40-52. https://doi.org/10.1016/j.epsl.2015.02.037.

Zegers, T.E., De Wit, M.J., Dann, J., White, S.H., 1998. Vaalbara, Earth's oldest assembled continent? A combined structural, geochronological, and palaeomagnetic test. Terra Nova 10, 250–259. https://doi.org/10.1046/j.1365-3121.1998.00199.x.

Zuchetti, M., 2007. Rochas máficas do Supergrupo Grão Pará e sua relação com a mineralização de ferro dos depósitos N4 e N5, Carajás, PA (Unpubl. Ph.D. thesis, Nº 7). Universidade Federal de Minas Gerais, Brasil, p. 16.